Biophysical interactions between engineered nanoparticles and biomimetic model membranes: nanotoxicology and synthetic biology applications

Marcos Arribas Pérez

Submitted in accordance with the requirements
for the degree of Doctor of Philosophy

UNIVERSITY OF LEEDS

The University of Leeds

School of Chemistry

September 2021

Declaration

The candidate confirms that the work submitted is their own, except where work which has formed part of jointly authored publications has been included. The contribution of the candidate and the other authors to this work has been explicitly indicated below. The candidate confirms that appropriate credit has been given within the thesis where reference has been made to the work of others.

The work in Chapter 3 of the thesis has appeared in publication as follows:

Arribas Perez, M., Moriones, O. H., Bastus, N. G., Puntes, V., Nelson, A., and Beales, P. A. (2019) Mechanomodulation of Lipid Membranes by Weakly Aggregating Silver Nanoparticles, Biochemistry ***58****, 4761-4773.*

Contribution of the authors:

- Arribas Perez, M.: Collected and analysed the data and wrote the manuscript
- Moriones, O. H.: Synthesised the nanoparticles, and acquired TEM images
- Bastus, N. G.: Synthesised the nanoparticles, and acquired TEM images
- Puntes, V.: Edited and proofread the manuscript.
- Nelson, A.: Edited and proofread the manuscript.
- Beales, P. A.: Provided supervision, edited and proofread the manuscript.

The work in Chapter 5 of the thesis is currently submitted for peer-reviewed publication (Langmuir). A preprint version of the manuscript is available at the preprint server ChemRxiv as follows:

Arribas Perez, M., and Beales, P. (2021) Biomimetic Curvature and Tension-Driven Membrane Fusion Induced by Silica Nanoparticles. ChemRxiv.
DOI: 10.26434/chemrxiv.14414540.v1

Contribution of the authors:

- Arribas Perez, M.: Collected and analysed the data and wrote the manuscript
- Beales, P. A.: Provided supervision, edited and proofread the manuscript.
- TEM images were collected by Dr Nicole Hondow from the School of Chemical and Process Engineering, University of Leeds)

Acknowledgements

I would like to thank Dr Paul Beales, firstly, for giving me the opportunity to work within his group and secondly, for his constructive guidance, support, help and patience throughout the last 4 years. I also want to acknowledge Prof. Andrew Nelson for his academic advice, and his kindness and always positive attitude.

I would like to extend my gratitude to Dr Sally Boxall and Dr Ruth Hughes, from the Bio-imaging and flow cytometry facility of the University of Leeds, a great deal of this thesis could not have been done without their hard work, and to David Fogarty, from the School of Chemistry, for helping me to fight against the fluorimeter when it decided not to work.

Of course, to Dr Andrew Booth and (nearly Dr.) Rashmi Seneviratne for their continuous help, for creating a friendly work environment and for making me feel included since the first day, thanks a million. I also like to thank, Dr Sanobar Kahn for training me during the first months, to Zexi Xu, to Juan Martinez and his music, and to everyone else who has been part of Beales group and lab 3.14 during these years. Finally, special acknowledgement to Jason Rowley and Simran Channa, for our deserved Friday trips to the pub.

También quiero dar las gracias a mis padres, Belén y Carlos, y a mi hermano, Raúl, por su constante apoyo y por darme todas las oportunidades que he tenido en la vida que me han permitido llegar hasta aquí.

Para terminar, a Paloma, la mejor compañera que he podido tener durante este tiempo, gracias por todo, por tu apoyo, tu ayuda, tu paciencia, tus ánimos, tu cariño y, en definitiva, gracias por hacer cada día mucho más bonito y feliz.

Abstract

Engineered nanoparticles (NPs) are nanoscale materials with unique physicochemical properties compared to bulk materials which provide novel and still largely unknown ways of interaction with biological systems. Since the gateway to the cell is the plasma membrane, understanding the interplay between NPs and membranes is a primary step towards understanding the behaviour of nanomaterials within biological systems. In this thesis, advanced spectroscopy and fluorescence microscopy techniques are employed to study the responses of large unilamellar lipid vesicles (LUVs) and giant unilamellar lipid vesicles (GUVs), respectively, to the interaction with silver NPs (AgNPs) and silica NPs (SiO_2 NPs).

Beyond the physicochemical properties of NPs and the membrane, the conditions of the medium also play a fundamental, but often overlooked, role in the NP-membrane interactions. Here, we provide evidence of the influence of the ionic strength of medium on the colloidal stability and membrane interactions of AgNPs, showing that at physiological ionic strength conditions AgNPs form small aggregates which display enhanced membrane activity. In a following investigation, we show that albumin proteins suspended in the medium adhere to the surface of SiO_2 NPs reducing the adhesion energy between the NPs and the membrane and consequently inducing major changes in the interaction mechanisms.

The ability of NPs to interact with lipid membranes also offer the prospect of using these nanomaterials in synthetic biology to develop membrane remodelling tools simpler and more robust than natural protein complexes. As an example, here we present 30 nm SiO_2 NPs as a protein-free membrane fusion system. We propose a mechanistic model to explain the NP-triggered fusion according to which the non-specific interaction between 30 nm SiO_2 NPs and lipid vesicles generates the right membrane curvature and tension conditions needed for the membranes to fuse. Finally, we use these NPs to build phase separated GUVs by fusing two single-phase vesicles. This represents a proof of increased membrane complexity achieved *via* membrane fusion. Moreover, membrane intermediate states during these fusion events reveal interesting phase dynamics involving the formation of transient asymmetric domains and interleaflet coupling processes. These initial observations can inspire future research programs focused on the development of novel-NP-based strategies to mimic protein functions.

Table of Contents

Abbreviations

AgNPs: Silver nanoparticles.

AuNPs: Gold nanoparticles.

BSA: Bovine serum albumin.

CF: 5(6)-carboxyfluorescein.

Chol: Cholesterol.

CMC: Critical Micelle Concentration.

DiD:1,1'-dioctadecyl-3,3,3',3'-tetramethylindodicarbocyanine,4-chlorobenzene-sulfonate salt.

DiO: 3,3’-dioctadecyloxacarbocyanine perchlorate.

DLS: Dynamic Light Scattering.

DOPC: 1,2-dioleoyl-sn-glycero-3-phosphocholine.

DOPE: 1,2-dioleoyl-sn-glycero-3-phosphoethanolamine.

DPPC: 1,2-dipalmitoyl-sn-glycero-3-phosphocholine.

FRAP: Fluorescence Recovery After Photobleaching.

FRET: Föster Resonance Energy Transfer.

GP: Generalized Polarization.

GPMVs: Giant Plasma Membrane Vesicles.

GUVs: Giant Unilamellar Vesicles.

HEPES: 4-(2-hydroxyethyl) -1- piperazine ethanesulfonic acid.

ITO: Indium titanium oxide.

Laurdan: 6-dodecanoyl-2-dimethylaminonaphthalene.

L_β: Solid or Gel phase.

L_d: Liquid disordered phase.

L_o: Liquid ordered phase.

LSPR: Localised Surface Plasmon Resonance.

LUVs: Large Unilamellar Vesicles.

MLVs: Multilamellar Vesicles.

NBD: Nitrobenzoxadiazole

NBD-DOPE:1,2-dipalmitoyl-sn-glycero-3-phosphoethanolamine-N-(7-nitro-2-1,3-benzoxadiazol-4-yl) (ammonium salt)

NPs: Nanoparticles.

Npy: Naphtho[2,3-a]pyrene (Naphthopyrene).

PC: Phosphatidylcholine.

PE: Phosphatidylethanolamine.

POPC: 1-palmitoyl-2-oleoyl-sn-glycero-3-phosphocholine

PS: Phosphatidylserine.

Rh-DOPE:1,2-dioleoyl-sn-glycero-3-phosphoethanolamine-N-(lissamine Rhodamine-B sulfonyl) (ammonium salt).

SD: Standard deviation

SiO_2 NPs: Silica nanoparticles.

SiO_2NPs@BSA: Silica nanoparticles coated with bovine serum albumin.

SM: Sphingomyelin.

SNPs-18: Silica nanoparticles LUDOX SM-30 (18 nm diameter).

SNPs-18@BSA: Silica nanoparticles LUDOX SM-30 (18 nm diameter) coated with bovine serum albumin.

SNPs-30: Silica nanoparticles LUDOX TM-50 (30 nm diameter).

SNPs-30@BSA: Silica nanoparticles LUDOX TM-50 (30 nm diameter) coated with bovine serum albumin.

TEM: Transmission electron Microscopy.

T_m: Melting temperature.

TRITC: Tetramethylrhodamine isothiocyanate.

UV-Vis: Ultraviolet-Visible.

List of figures

List of tables

Supplementary movies

Supplementary Movie 5.1
Sequential fusions of homogeneously labelled GUVs (Rhodamine-DOPE used as fluorescence dye). First fusion *via* gentle merging pathway and second fusion *via* hemifusion-fusion pathway (colour code scale indicated fluorescence intensity).

Supplementary Movie 5.2
Fusion of homogeneously labelled GUVs *via* direct full fusion (Rhodamine-DOPE used as fluorescence dye) (colour code scale indicated fluorescence intensity).

Supplementary Movie 5.3
Fusion of GUVs lumen mediated by SiO_2 NPs *via* hemifusion-fusion pathway (Magenta and green fluorescence correspond to DiD, DiO and TRITC-dextran, respectively).

Supplementary Movie 5.4
Fusion of differently labelled GUVs mediated by SiO_2 NPs *via* direct full fusion pathway (Red and green fluorescence correspond to Rhodamine-DOPE and DiO, respectively).

Supplementary Movie 5.5
Fusion of differently labelled GUVs mediated by SiO_2 NPs *via* hemifusion-fusion pathway. (Red and green fluorescence correspond to Rhodamine-DOPE and DiO, respectively).

Supplementary Movie 5.6
Fusion of differently labelled GUVs mediated by SiO_2 NPs *via* gentle merging pathway. (Red and green fluorescence correspond to Rhodamine-DOPE and DiO, respectively).

Supplementary Movie 6.1
Fusion of a L_d DOPC GUV labelled with Rh-DOPE and a L_o DPPC/Chol (7:3) GUV labelled with naphthopyrene to generate a final phase separated GUV.

Supplementary Movie 6.2
Fusion of a L_d DOPC GUV labelled with Rh-DOPE and a L_o DPPC/Chol (7:3) GUV labelled with naphthopyrene. GUVs become hemifused and show transient asymmetric domains and interleaflet coupling.

Supplementary Movie 6.3
Fusion of a L_d DOPC GUV labelled with Rh-DOPE and a L_o DPPC/Chol (7:3) GUV labelled with naphthopyrene. L_o dye is excluded from the hemifusion diaphragm before fusion.

Supplementary Movie 6.4
Fusion of a L_d DOPC GUV labelled with Rh-DOPE and a L_o DPPC/Chol (7:3) GUV labelled with naphthopyrene. L_d dye is excluded from the hemifusion diaphragm before fusion.

Chapter 1:
Introduction

This thesis focuses on the study of the response of lipid membranes to the contact with engineered nanoparticles. The following chapter aims to give readers the basic background information on biological membranes, engineered nanomaterials and important factors governing the interactions between them. Finally, we introduce the possibility of using nanomaterials as protein mimics in bottom-up synthetic biology.

1.1 Biological membranes

Biological membranes are extremely important for the life of cells. The plasma membrane acts as a semi-permeable barrier that separates the extracellular medium from the cytosol and maintains the cellular homeostasis [1]. Moreover, biomembranes play a crucial role in cell signalling, control the cellular transport of substances, and, in eukaryotic cells, form specialised intracellular compartments, called organelles, each of them with a particular inner environment, which enable eukaryotic cells to perform numerous biochemical reactions simultaneously and very efficiently [2].

1.1.1. Structure of biological membranes and lipids

In 1972, Singer and Nicolson proposed the fluid mosaic model to describe the structure of cell membranes [3]. This model is still accepted and defines biological membranes as dynamic and fluid lipid bilayers with proteins inserted or bound to their surface (Fig. 1.1). The principal component of biological membranes are phospholipids, which are amphiphilic molecules, or amphiphiles, composed of a hydrophilic phosphate head group and two hydrophobic acyl chains. The most common type of phospholipids in eukaryotic membranes are glycerophospholipids. These molecules have a headgroup formed by an alcohol derivative attached to a phosphate which in turn is linked to the hydrophobic backbone formed by a diacylglycerol (Fig 1.1) [4]. Glycerophospholipids are classified according to their headgroup. Typical glycerophospholipids found in biological membranes are phosphatidylcholine (PC) and phosphatidylethanolamine (PE), both zwitterionic at physiological pH, and phosphatidylserine (PS) which is negatively charged. Another physiologically relevant type of phospholipids located in biomembranes are sphingolipids, which are built from ceramide instead of diacylglycerol. The most abundant sphingolipid in eukaryotic cells is sphingomyelin (SM) [1, 4, 5]. Although phospholipids are normally classified by the structure of their hydrophilic headgroup, membrane lipids also differ in the length and degree of saturation of their hydrophobic acyl chains. Besides phospholipids, sterols constitute a major type of lipid found in biomembranes. The more abundant sterol in animal membranes is cholesterol [4, 5]. The final class of lipids comprised in biomembranes are glycolipids, which are analogous to sphingolipids but in this case, the ceramide backbone is linked to a sugar instead of a phosphate-linked head group [1].

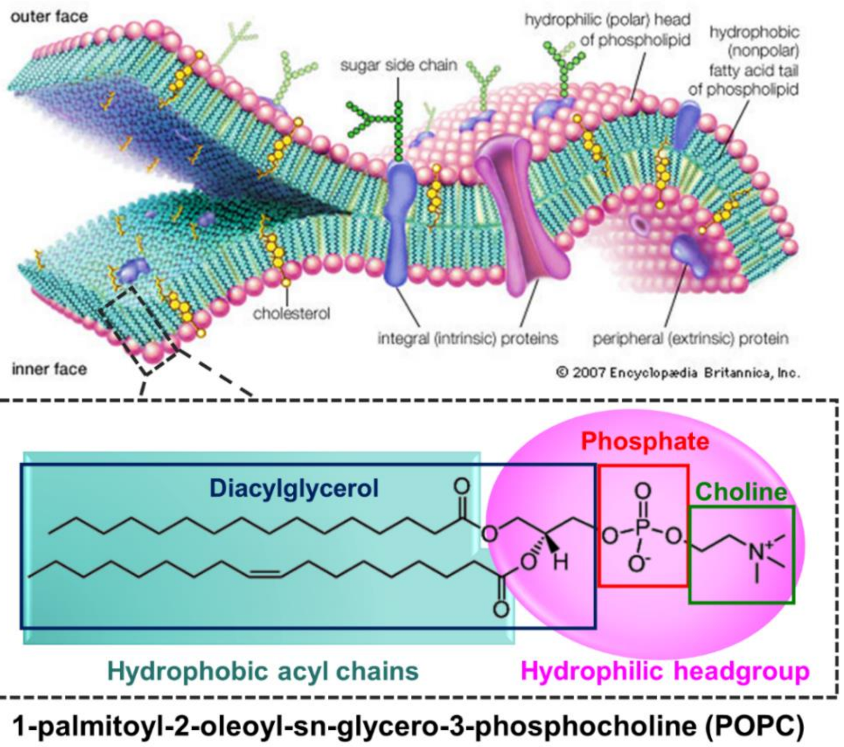

Figure 1.1. Schematic representation of a cell plasma membrane and chemical structure of a membrane phospholipid (POPC). *(Figure adapted from Encyclopædia Britannica, Inc.)*

1.1.2. Membrane asymmetry

Biological membranes exhibit differences in the lipid content of each leaflet. This property, known as membrane asymmetry, is conserved across organisms of all living kingdoms, from bacteria to animal and plant cells, and plays a fundamental role in numerous cellular functions [6]. The asymmetric distribution of phospholipid headgroups in cell membranes was experimentally proven for the first time in the early 1970s in human red blood cells [7] and was later confirmed in several cell types [8]. In mammalian cells, the membrane of the endoplasmic reticulum shows symmetric lipid distribution, but the plasma membrane and the membranes of other organelles, such as Golgi and endosomes, are asymmetric, with the inner leaflet rich in PS and PE while PC, SM and glycolipids are predominant in the outer monolayer (Fig. 1.2) [4, 7-9].

The first studies proved the asymmetric distribution of just phospholipid headgroups, but the membrane asymmetry does not only involve the lipid headgroups. In a recent publication, Lorent *et al.* have demonstrated that the plasma membrane of human erythrocytes is also asymmetric in the degree of saturation of the acyl chains, with the inner leaflets enriched in lipids with polyunsaturated acyl chains (Fig. 1.2) [9]. These findings imply that each leaflet has not only a different chemical composition but also different biophysical properties. The acyl chain asymmetry can therefore have significant implications on several biophysical properties of the membrane, including membrane order, fluidity, and curvature, as well as on the insertion of transmembrane proteins in the bilayer [9]. Nonetheless, there is still a considerable lack of knowledge about the biophysical properties of asymmetric membranes, mainly because most studies employ symmetric model membranes due to their ease of production and longer stability.

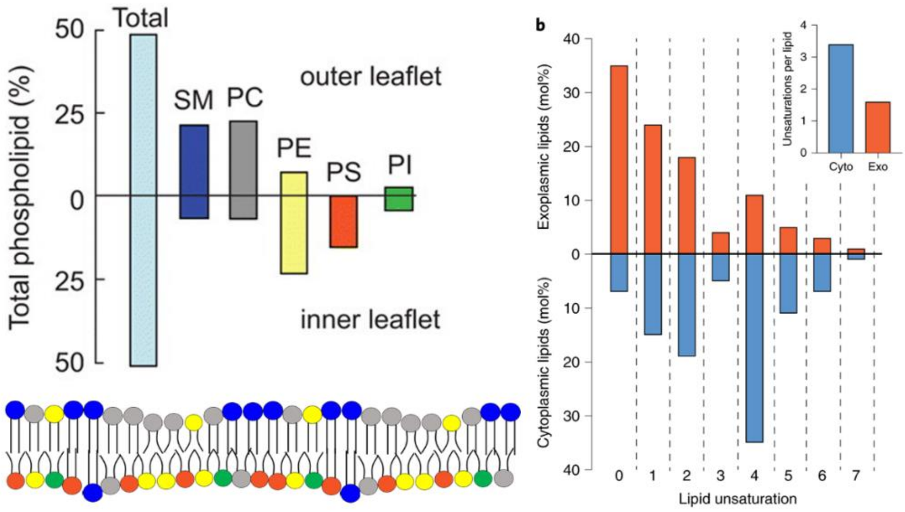

Figure 1.2. Asymmetric distribution of lipids in biological membranes. The bar plots show the transbilayer distribution of phospholipids across the human erythrocyte membrane by type of headgroup (left) and number of acyl chain unsaturations (right). (Figure adapted from references 6 and 7)

1.1.3. Membrane fluidity

Cell membranes are not rigid and static shells but fluid structures where the individual lipids are moving constantly. One of the most important lipid movements that occur within a membrane is the transversal diffusion or “flip flop” which refers to the ability of lipids to migrate from one leaflet of the membrane to the other one [10]. Spontaneous interleaflet lipid flip-flop is thought to be a very slow process since it requires the transient location of the hydrophilic lipid headgroup in the hydrophobic region of the membrane. *In vivo*, lipid flip-flop is regulated and catalysed by the enzymes flipases, which transport lipids from the outer to the inner leaflet, and flopases, which move the lipids in the opposite direction [6, 11].

Lipids also move laterally within the leaflets through the membrane plane *via* lateral diffusion. This lateral diffusion is indeed the principal type of lipid movement that happens within a cell membrane and occurs much faster than the flip-flop. The lipid lateral diffusion can result in membrane lateral heterogeneities where particular types of lipids, usually SM and cholesterol, gather together into membrane domains.

1.1.4. Amphiphile self-assembly and lipid phases

In aqueous solutions, amphiphiles can spontaneously self-assemble into supramolecular structures if their concentration is above a threshold called critical micelle concentration (CMC) [12]. This self-assembly is driven by the hydrophobic effect which forces the molecules to expose their hydrophilic head to the water while the hydrophobic tails are hidden from the aqueous solution [13]. The type of structure that amphiphilic molecules form in aqueous environments depends on their packing parameter (P):

$$\textbf{Equation 1.1} \qquad P = V/A_0 l$$

where V is the hydrophobic volume, A_0 is the interface area occupied by the head group and l is the acyl chain length [14]. Amphiphiles with only one tail, where A_0 is considerably larger than V/l, have a conical geometry (type I lipids) and are likely to form spherical or cylindrical micelles ($P \leq 1/2$) (Fig.1.3a-b). Lipids with two acyl chains have larger hydrophobic volume and can be considered as a cylinder (type 0 lipids), where $V = A_0 l$. This molecular geometry has a packaging parameter of $1/2 < P \leq 1$, which favours the formation of lamellar phases or lipid bilayers (Fig.1.3c). A final scenario occurs when the packing parameter is larger than 1 ($P > 1$), in this case the lipids are inverted cone-shaped (type II lipids) and tend to adopt inverse hexagonal and cubic geometries (Fig.1.3d). Biological membranes are formed mainly by cylinder-shaped phospholipids, however, they also contain lipids that favour other geometries. Those non-bilayer lipids have a significant effect on the membrane curvature and the lateral stress profile and are thought to be involved in membrane remodeling processes [15]. Moreover, non-lamellar phases have become extremely popular in nanomedicine to develop lipid nanoparticle-based drug delivery systems [16].

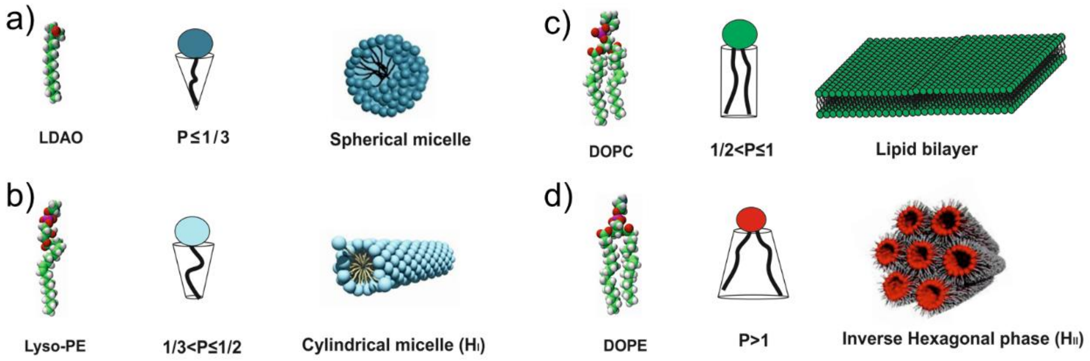

Figure 1.3. Molecular shape, packing parameter and favoured self-assembly geometry of different amphiphiles. a) Detergents, such as LDAO, have a conical shape which favours the formation of spherical micelles**.** b**)** Lyso-phospholipids, i.e., lyso-PE, are represented as truncated cones and tend to self-assemble into cylindrical micelles. c**)** DOPC is a cylindrical-shaped phospholipid that self-assembles into lipid bilayers. d**)** DOPE is a phospholipid with a small head group that tends to adopt inverted structures such as inverse hexagonal phase.

Lipid bilayers can exhibit different levels of order depending on their lipid composition and the temperature. These two parameters determine how densely packed the lipids will arrange within the membrane. Above a given temperature threshold, called melting temperature (T_m), phospholipid membranes (without cholesterol) undergo reversible thermotropic phase transitions from the liquid crystalline or liquid disordered phase (L_d), where lipids are loosely packed and show maximal lateral diffusion, to the solid or gel phase (L_β) where lipids are immobile and densely packed with their acyl chains completely extended (Fig. 1.4) [17, 18]. Phospholipids with long and saturated acyl tails have higher T_m than lipids with short and unsaturated acyl tails, hence at physiologically relevant temperatures the former will arrange into the L_β phase while the latter will form L_d membranes.

When cholesterol is present in the membrane, a third membrane phase can appear. This phase is called liquid ordered phase (L_o) and it is an intermediate between L_β and L_d, where lipids are densely packed but they still can diffuse laterally, although at a slower rate than in the L_d phase (Fig. 1.4) [17, 18]. Cholesterol can induce stiffening of liquid disordered membranes while it makes gel phase membranes more fluid. In ternary lipid mixtures, liquid disordered and liquid ordered phases often coexist in the membrane giving rise to membrane domains. In this situation, cholesterol molecules interact preferentially with saturated lipids and consequently, the regions of the membrane rich in saturated lipids are enriched with cholesterol and form L_o domains. In cell membranes, L_o domains are thought to be composed essentially of sphingolipids and cholesterol, although other phospholipids and glycolipids with long acyl chains, such as DPPC, can also form L_o phases in the presence of cholesterol [17, 19]. The L_o domains, often called lipid rafts, are thought to be involved in many cellular signalling and trafficking pathways [20]. However, while the formation of membrane domains in model membranes is well documented, the lipid raft concept associated with the formation of nanodomains in cell membranes is still very controversial since there is no strong experimental evidence of their existence and relevance. The membrane phase also influences other physical properties of the membrane such as membrane thickness, with L_β and L_o domains being thicker than L_d domains, membrane curvature and bending rigidity [21-23].

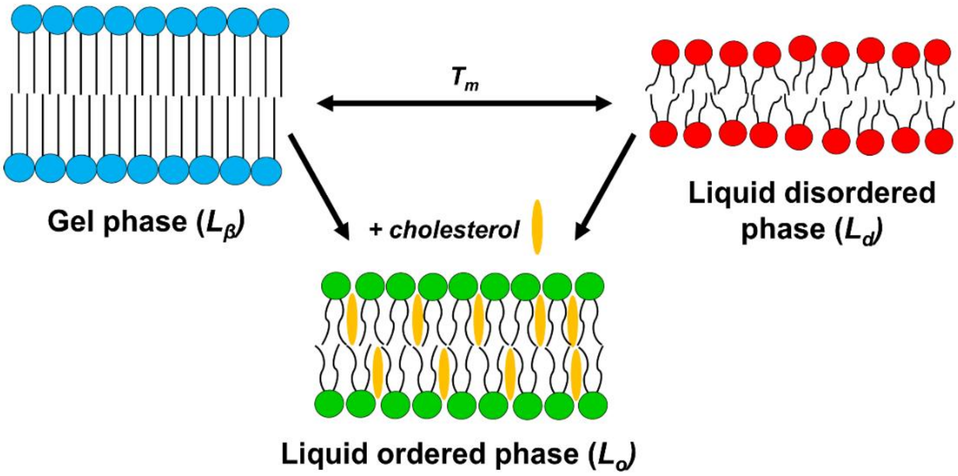

Figure 1.4. Membrane phase transitions**.** Above a given melting temperature and in absence of cholesterol, lipid membranes undergo reversible phase transitions from solid ordered gel phase (L_β) to disordered liquid phase (L_d). Membranes with cholesterol can adopt a liquid ordered phase (L_o) which is an intermediate between L_β and L_α phases.

1.1.5. Lateral stress profile and membrane stored elastic stress

The lateral stress profile (*P(z)*) results from the distribution of repulsive and attractive forces between lipid molecules at different depths (*z*) of a membrane monolayer. For each lipid monolayer the lateral pressure profile shows three different regions: i) a repulsive component in the headgroup region derived principally from electrostatic, steric and hydrational repulsions; ii) a strong attractive force generated by the hydrophobic effect at the hydrophobic-hydrophilic interface; iii) a repulsive force in the hydrophobic region due to high steric repulsions [5, 15, 24] (Fig. 1.5). The strong hydrophobic effect occurring in the hydrophobic-hydrophilic interface is the most important force for the structural stability of the membrane because it holds the lipids together and prevents the exposure of the hydrophobic tails to the aqueous environment, which is energetically unfavourable [15].

The integral of the lateral stress profile across the lipid monolayer is known as the net lateral tension. For a monolayer at equilibrium, the net lateral tension must be zero ($\int P(z)dz=0$). The spontaneous curvature of the monolayer (c_0) is proportional to the torque (*T*) acting on it, given by the first moment of the stress profile [24]:

$$\textbf{Equation 1.2} \qquad T = \int zP(z)dz = 0 = -\kappa_b c_0$$

where κ_b is the bending modulus. When the monolayer is formed exclusively by cylindrical-shaped type 0 lipids which, as was mentioned before, tend to form bilayers spontaneously, the net torque is zero and the flat monolayer remains stable. However, the presence of non-bilayer lipids produces a non-zero torque, which provides a preferred spontaneous curvature to the monolayer. Type I lipids promote positive spontaneous curvature whereas type II lipids favour negative spontaneous curvature (inverse hexagonal structures).

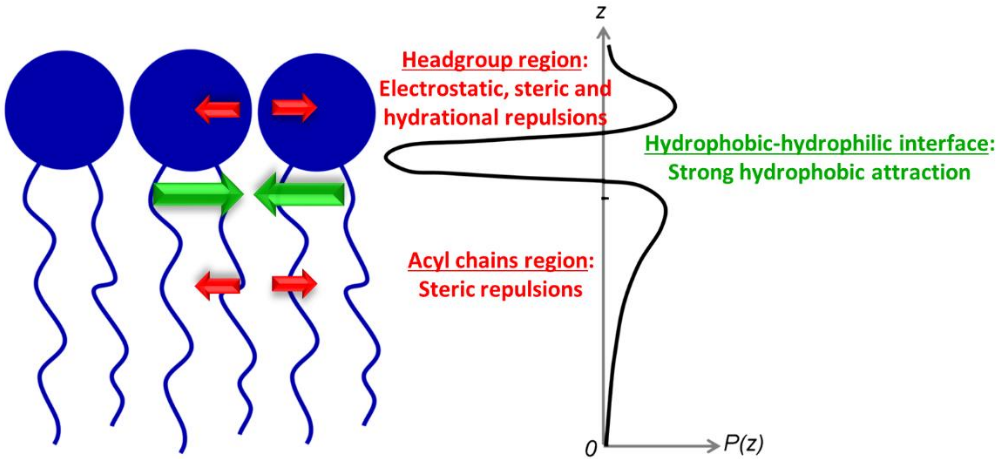

Figure 1.5. Lateral pressure profile of a phospholipid monolayer**.** Repulsive forces dominate at the hydrophilic headgroups and the hydrophobic acyl chains regions whereas a strong attractive force driven by the hydrophobic effect governs the hydrophobic-hydrophilic interface.

In lipid bilayers, the intrinsic wish of non-bilayer lipids would lead to monolayer separation (void formation), which implies an enormous energetic cost. To prevent such an unfavourable process, the lipid molecules are reshaped and forced to adopt flat curvatures to maintain the back-to-back arrangement of the two lipid monolayers (Fig. 1.6) [24]. This gives rise to a stored elastic stress in the membrane, which produces a lateral expansion of the bilayer and hence a wider separation between the head groups as well as increased exposure of the hydrophobic chains to the aqueous environment [13]. The stored elastic stress in the bilayer is expected to increase with the proportion of non-bilayer lipids. Nonetheless, the membrane bilayer can only hold a limited stored stress above which the hydrophobic effect at the hydrophobic-hydrophilic interface is not strong enough to maintain the bilayer structure the lipids experience a transition into inverse phases. The formation of inverse phases due to increased elastic stress is thought to be biologically relevant and has been proposed to be important during membrane fusion events [25].

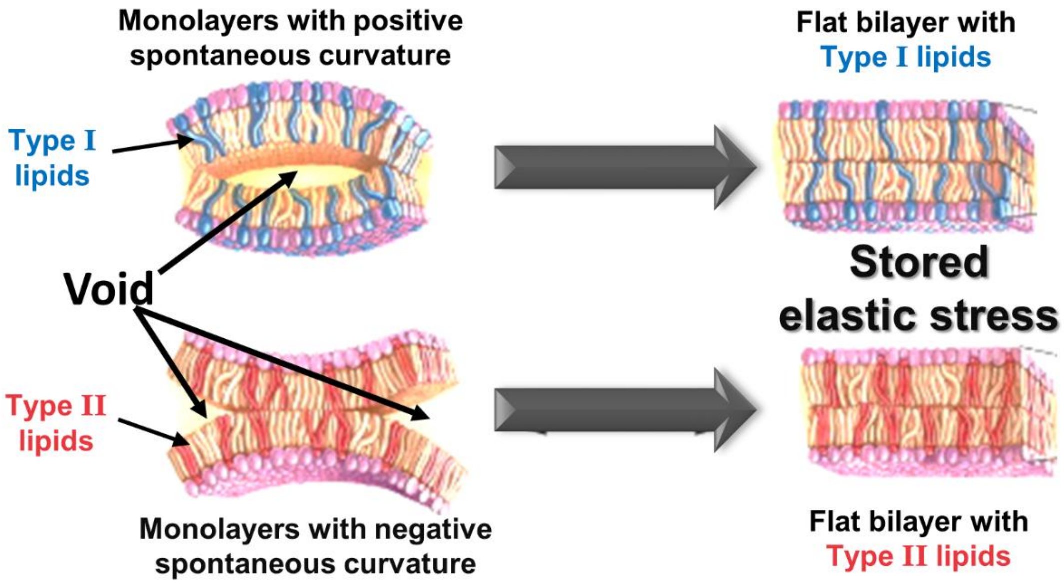

Figure 1.6. Stored elastic stress. The inclusion of non-bilayer lipids of type I or II in the membrane induces their monolayers to have a preferred spontaneous curvature, positive or negative respectively, which would generate energetically unfavourable voids in the membrane. However, in the lipid bilayer monolayers adopt a flat configuration against their "whish" which result in stored elastic stress. (Figure modified from reference 25).

In cell membranes, the membrane asymmetry implies that in a flat configuration, the lateral pressure profile of each monolayer may be different and therefore one of the monolayers will be subjected to greater elastic stress than the other. The stressed monolayer produces a membrane spontaneous curvature (C_0) which balances the lateral pressure in the bilayer, and consequently redistribute the stored elastic energy equally between the two monolayers (Fig. 1.7) [15].

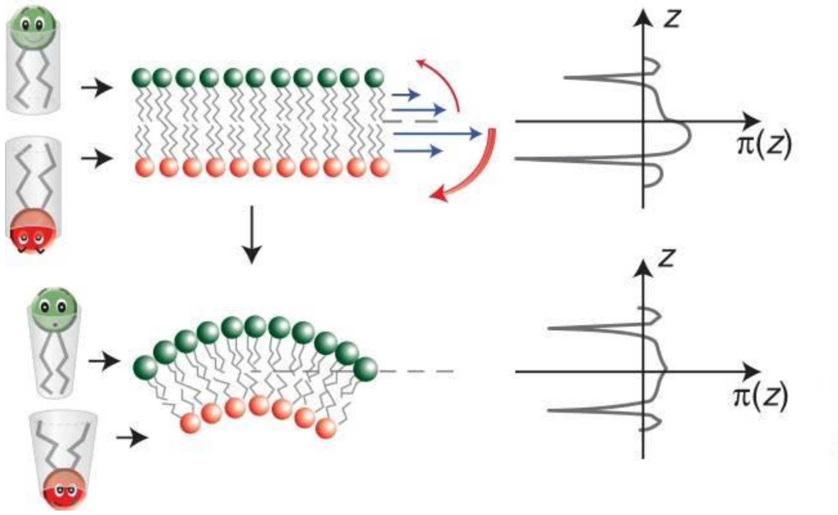

Figure 1.7. Membrane spontaneous curvature derived from membrane asymmetry**.** In lipid bilayers with compositional differences between each leaflet, the lateral pressure profile is unevenly distributed. To balance the stored elastic stress, the monolayer subjected to greater elastic stress bends and eventually, the bilayer lateral pressure profile reaches the equilibrium. (Figure reproduced from reference 13).

1.1.6. Membrane curvature and elasticity

Cell membranes are subjected to forces applied in different directions by biomolecules, essentially proteins, surrounding cells and other external compounds and materials, such as drugs or nanoparticles, which might generate membrane deformations. In 1973, Wolfgang Helfrich proposed a theoretical model of membrane elasticity in which the biomembrane resistance to deformation depends on two main elastic properties: stretching and bending [26]. This model assumes that the membrane is a two-dimensional elastic sheet and its thickness is marginal compared with its lateral surface dimension [2]. The elastic contribution per unit area to the free energy of the membrane (E) is defined by the Helfrich Hamiltonian:

$$\textbf{Equation 1.3} \qquad E = E_b + E_{st}$$

The term E_b is the free energy per unit area due to membrane bending and E_{st} is the free energy per unit area due to membrane stretching. The stretching term refers to the surface tension of the membrane. The change in free energy per unit area due to stretching can be expressed as:

$$\textbf{Equation 1.4} \qquad E_{st} = \left(\frac{\kappa_A}{2}\right)\left(\frac{\Delta A}{A_0}\right)^2$$

where κ_A is the area expansion modulus, ΔA is the change in membrane area and A_0 is the initial membrane area. The stretching term is often ignored in *Equation 1.3* because lipid bilayers are strongly resistant to stretching, due to the energetically unfavourable exposure of the hydrophobic lipid chains to water that stretching would produce [11, 27].

The most significant contribution to the membrane free energy is therefore the bending energy. The three-dimensional geometrical shape adopted by two-dimensional membranes (assuming infinitesimal thickness) can be described by their two principal curvatures, C_1 and C_2, which equate to the inverse of the principal radii of curvature ($1/R_1$ and $1/R_2$) (Fig. 1.8) [12]. These curvatures are perpendicular to each other and their combination defines the mean curvature (H) and the Gaussian curvature (G) at a particular point of the membrane:

$$\textbf{Equation 1.5} \qquad H = \frac{1}{2}(C_1 + C_2)$$

$$\textbf{Equation 1.6} \qquad G = C_1 \times C_2$$

The bending energy is dependent on these two curvatures as well as the elastic moduli associated with them, the bending modulus (κ_b) and the Gaussian modulus (κ_G), which indicate the energy cost per unit area needed to change the mean and Gaussian curvatures, respectively. The bending energy can be then expressed as:

$$\textbf{Equation 1.7} \qquad E_b = \tfrac{1}{2}\kappa_b(2H - C_0)^2 + \kappa_G G$$

The Gaussian term of the equation is only relevant when the membrane experiences a topological transition (i.e., fusion, fission and poration), otherwise its integral over the whole membrane surface does not change with the shape and the Gaussian elasticity term can be neglected [2, 12].

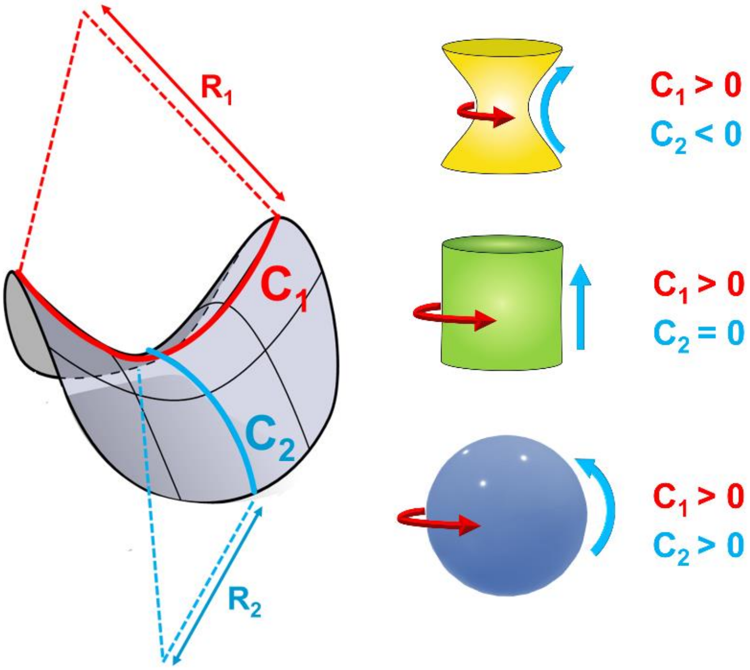

Figure 1.8. Schematic representation of principal membrane curvatures (C_1 and C_2) in different geometrical shapes.

1.1.7. Biomimetic model membranes

A frequent limitation of biochemical, biophysical and cell biology studies is the enormous complexity of biological systems. To deal with this issue, it is fundamental to find ways to reconstitute simpler *in vitro* systems easier to control. One example of such simplified systems are biomimetic (or artificial) model membranes, which are synthetic lipid bilayers where the lipid composition can be selected, the lipids can be modified, for instance labelled with a fluorescent dye, and the environmental conditions (pH, osmolarity, temperature, etc.) can be controlled [28]. Importantly, artificial model membranes retain fundamental physical and chemical characteristics of cell membranes and thus are extremely useful tools to gain information on the structure, functions and mechanical and dynamical properties of biological membranes as well as on their interactions with proteins, drugs and nanomaterials. The most commonly used artificial model membranes include supported lipid bilayers (SLBs), lipid droplets and lipid vesicles. This later system is the type of model membrane employed in this thesis. Additionally, giant plasma membrane vesicles (GPMVs) where the membrane is taken directly from an actual cell plasma membrane are becoming increasingly popular in the last years.

Lipid vesicles are spherical, free-standing model membranes with an encapsulated aqueous compartment extensively used in several research fields including biophysics, biochemistry, synthetic biology, toxicology, etc. Depending on the preparation method and the lipid composition, lipid vesicles can display different properties including the number of membranes, surface charge, and vesicle size. Based on the number of bilayers, vesicles are classified into multilamellar vesicles (MLVs) and unilamellar vesicles. The latter category is the most biologically relevant and is in turn subdivided according to the vesicle size into small (not used in this project), large and giant unilamellar vesicles (Fig. 1.9) [29].

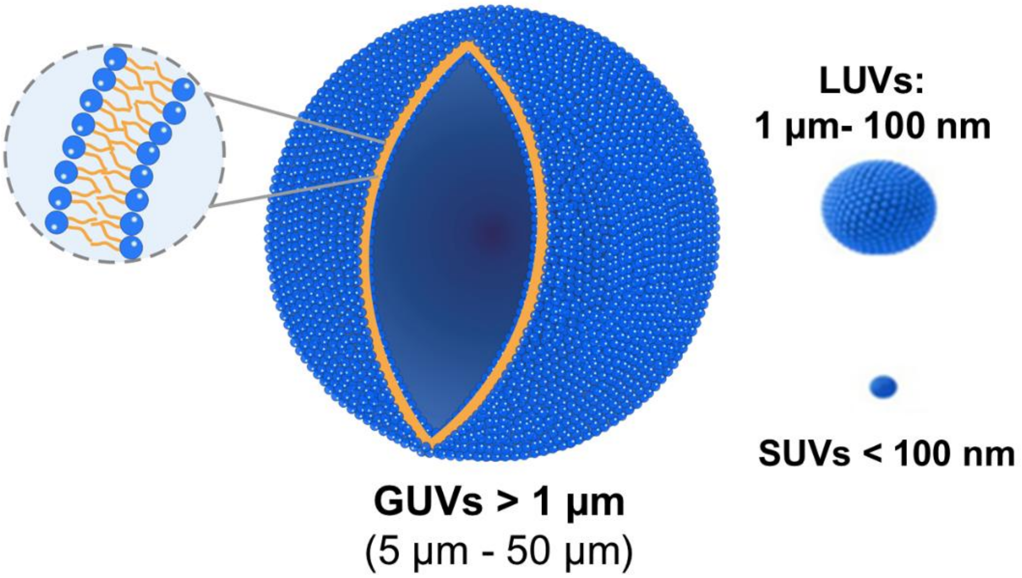

Figure 1.9. Classification of unilamellar lipid vesicles. From the biggest to smallest: Giant Unilamellar Vesicles (GUVs) larger than 1 µm (usually 5 -50); Large Unilamellar Vesicles (LUVs) between 1 µm and 100 nm; Small Unilamellar Vesicles (SUVs) smaller than 100 nm.

1.1.7.1. Large unilamellar vesicles

Large unilamellar vesicles (LUVs) are liposomes with a diameter between 100 nm and 1 µm, which is below the resolution of conventional optical microscopy. Hence, LUVs are usually employed in ensemble experiments based on spectroscopy, light scattering and calorimetry methods which provide information about the averaged behaviour of the vesicles in the sample, making easier and faster the acquisition and analysis of statistical data [2]. Due to their great efficiency to encapsulate hydrophilic molecules, LUVs are frequently used in membrane permeability assays. Moreover, LUVs are extensively employed for cryo-electron microscopy and other common techniques used in structural studies, such as small-angle neutron scattering (SANS) and small-angle X-ray scattering (SAXS). Notably, LUVs are of great interest in nanomedicine as they can be used as vectors of both hydrophilic drugs encapsulated in their lumen and hydrophobic compounds inserted in their membrane [29].

1.1.7.2. Giant unilamellar vesicles

Giant unilamellar vesicles (GUVs) are cell-sized biomimetic membrane systems that are visible *via* optical microscopy techniques at the single vesicle level [2, 30]. Hence, GUVs can be studied using a variety of microscopy-based methods that provide information about a wide range of biophysical properties of membranes [30]. Moreover, single vesicle analysis reveals transient intermediate states impossible to distinguish in LUVs. Importantly, GUVs can encapsulate biological machineries which reproduce biochemical reactions occurring naturally in living cells. Thus, GUVs are common model architectures used in bottom-up synthetic biology as plasma membrane mimics to replicate complex biological systems in a simpler context. This allows to gain a better understanding of fundamental cellular processes and to develop novel concepts and biotechnologies [30-34]. In addition, the possibility of recreating minimal protocells makes GUVs extremely important in origins-of-life and cellular evolution research [35].

1.2 Engineered nanoparticles

At the end of the 20th century, scientists zoomed into the nanoworld and found an unexplored source of technological innovations. In the early 2000s, nanotechnology already moved from academic laboratories towards commercialisation. Since that moment, it has experienced a rapid and continuous development that has led to an exponential growth in the use of engineered nanoparticles (NPs) in a wide range of industries including construction materials, electronics, textiles, and pharmaceutics.

Officially, engineered nanoparticles are defined as materials with at least one external dimension in a size range between 1 nm and 100 nm [36]. Compared to bulk material, the nanoscale provides enhanced surface reactivity, high surface to volume ratio and other novel physicochemical properties as well as the ability to enter individual cells and gain access to their inner biochemistry. Nanomaterials are therefore very promising tools in biomedicine and biotechnology to develop biosensing and bioimaging technologies, drug delivery systems, and diagnostic devices.

However, NPs can also produce cytotoxic effects which range from mild cellular injuries to cell death. The cytotoxicity of NPs is often related to the generation of reactive oxygen species (ROS), often due to the release of ions from the NP surface, which produce oxidative stress in the cells and lead to inflammatory responses and mitochondrial perturbations related linked to the release of pro-apoptotic factors and programmed cell death [37-40]. The interaction of NPs with cells can also induce protein depletion and DNA damages which alter fundamental signalling pathways and gene expression [37-40]. Additionally, another principal cytotoxicity pathway arises from the interaction between NPs and the plasma membrane which often produce membrane perturbations. These membrane defects can result in severe cell damage even if this contact does not lead to the cellular uptake of NPs [37, 40-42].

Depending on their composition, NPs can be classified as organic nanomaterials (liposomes, dendrimers and carbon-based nanomaterials, etc.) or inorganic nanoparticles (metals, metal oxides, quantum dots, etc). In addition, these two groups of NPs can be combined to form another class of nanomaterials known as nanocomposites [43]. According to the Nanotechnology Consumer Products Inventory (CPI), metal and metal oxides are the nanomaterials most employed in commercially available products [44]. The research presented in this thesis is focused on two types of inorganic nanomaterials, silver NPs (AgNPs) and silica NPs (SiO_2 NPs).

1.2.1 Silver nanoparticles

Noble metal NPs, especially AgNPs, are the most widely used nanomaterials in consumer products [44, 45]. The remarkable interest raised by AgNPs is principally due to their antimicrobial activity and their unique optical properties which make these nanomaterials very attractive for biomedical and biotechnological applications [46, 47 48].

Silver and silver salts have been used for centuries as antimicrobial agents for the treatment of burns, wounds and bacterial infections [49]. Currently, AgNPs are routinely employed to sterilise medical equipment and other consumer products including clothes, food storage bags and refrigerator surfaces. Several studies have proven the highly efficient bactericidal activity of AgNPs against the gram-negative bacteria *Escherichia coli* [50-53]*.* AgNPs have also shown bactericidal activity against gram-negative *Pseudomonas fluorescens* [54]*,* and more remarkably against gram positive bacteria resistant to broad-spectrum antibiotics, such as *Staphylococcus aureus* and *Staphylococcus epidermidis* [55]*.* Besides its antibacterial properties, AgNPs have exhibited antifungal effects against human pathogenic fungi of the genus *Candida* [56], as well as antiviral activity against human immunodeficiency virus (HIV) [57], hepatitis B virus (HBV) [58] and H1N1 influenza A virus [59].

The extraordinary optical properties of AgNPs arise from their localised surface plasmon resonance (LSPR), which is a collective coherent oscillation of the free electrons (electron cloud) on the metal surface that occurs when it is excited by light at a specific wavelength (Fig. 1.10). The LSPR results in strongly enhanced light absorption and scattering properties at that particular wavelength [60-62]. The light scattering at the same frequency as the incident light radiation is known as Rayleigh light scattering. The enhanced Rayleigh scattering displayed by AgNPs makes them much brighter and resistant to photobleaching than common fluorescent dyes, allowing stronger light excitation energy and longer working times [60]. The enhanced Rayleigh scattering can be successfully exploited in a range of biophysical methods, biological sensing, imaging, medical diagnosis and cancer theranostics. The LSPR of AgNPs also enhances the Raman scattering of surrounding molecules up to 10^{14} times. This property is known as surface-enhanced Raman scattering (SERS). Spectroscopy and microscopy methods based on SERS can be applied for antigen localisation and quantification, detection of microorganisms in blood and *in vivo* recognition of cancer cells [62, 63]. Although important advances have been made in the detection of analytes, such as antigens, antibodies, enzymes and nucleotides, in solution and cell cultures, the application of these biosensing methods *in vivo* is more challenging and still in development but SERS diagnosis studies and SERS image-guided surgery have shown very promising results [62, 63].

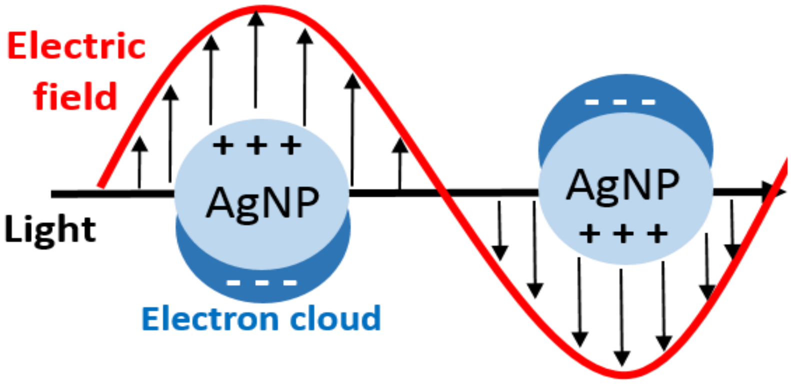

Figure 1.10. Schematic representation of localised surface plasmon resonance of AgNPs

1.2.2 Silica nanoparticles

SiO_2 NPs are one of the most popular nanomaterials in biomedical investigations. Natural crystalline silica NPs, such as quartz and cristobalite found in coal mine dust for instance, are known to be highly toxic and induce lung diseases such as chronic obstructive pulmonary disease, lung cancer and silicosis [64, 65]. On the contrary, amorphous SiO_2 NPs have shown better biocompatibility and enormous versatility in terms of pharmacological and biotechnological applications. Amid these applications, SiO_2 NPs are being extensively studied as delivery systems of drugs and peptides in cancer therapies, proteins and genes in cell and molecular biology studies and dyes and contrast agents in molecular imaging and diagnostic procedures [66].

Amorphous SiO_2 NPs offer numerous advantageous properties for biomedical applications. Firstly, they can be produced on a large scale at a low cost [66]. Also, the size and shape of SiO_2 NPs can be precisely controlled within a wide range of sizes. The accurate control of these physical properties is extremely important since they are the primary factor that controls their biological activity and potential toxicity. The hydrophilic surface of these nanomaterials favours prolonged blood protected circulation [66]. Moreover, the surface of SiO_2 NPs presents silanol groups (Si-OH) which facilitate the functionalisation of their surface *via* physical adsorption or covalent conjugation of different chemical compounds, polymers, dyes and targeting ligands [66, 67]. These surface functionalisations can modify the surface charge of the particle, improve their stability and biocompatibility and provide controllable release of drugs, proteins, and other small molecules conjugated to the NP surface or encapsulated within hollow SiO_2 NPs. In addition, amorphous SiO_2 NPs can present pores in their surface which are normally exploited for the adsorption of the molecular cargo. According to the porosity of their surface, amorphous SiO_2 NPs are classified into mesoporous SiO_2 NPs and non-porous SiO_2 NPs. The SiO_2 NPs used in the present thesis are within the latter group.

1.2.3 Nanoparticle-biomembrane interactions

The use of NPs in biomedicine implies their direct contact with cells. The potential pharmacological and biomedical applications of nanomaterials often rely on their ability to gain access to the intracellular environment and reach specific subcellular targets. In this context, the first barrier that NPs encounter is the plasma membrane of cells and subsequently the biomembranes that delimit the intracellular compartments. Normally. the internalisation of large macromolecules into the cell occurs via receptor-mediated endocytosis, however, it has been observed that some NPs can penetrate artificial model membranes without involving any specific receptor-mediated interaction [68]. This suggests that the NPs uptake can be driven just by physicochemical interactions, nevertheless during the process they can lead to cytotoxicity by damaging the plasma membrane and thereby inducing the loss of cellular homeostasis [69, 70]. Hence, it is crucial to understand how biomembranes behave when exposed to NPs and which are the physicochemical processes governing the interactions between NPs and biomembranes. Such non-specific physical interactions are extremely complex and involve several forces acting together at the nanoparticle-membrane interface (nanobio interface).

The nature of the NP-biomembrane interactions and their potential toxicity do not only depend on the composition of the NPs but are strongly influenced by their physicochemical properties [71, 72], the conditions of the medium [71, 73] and the composition and biophysical properties of the membrane [74, 75] (Fig. 1.11). Due to the large number of parameters influencing the NP behaviour in biological systems and the complexity of such systems, understanding these interactions is extremely challenging. Consequently, reductionist approaches, usually based on biomimetic model membrane systems, are commonly employed to investigate the interplay between NPs and biomembranes.

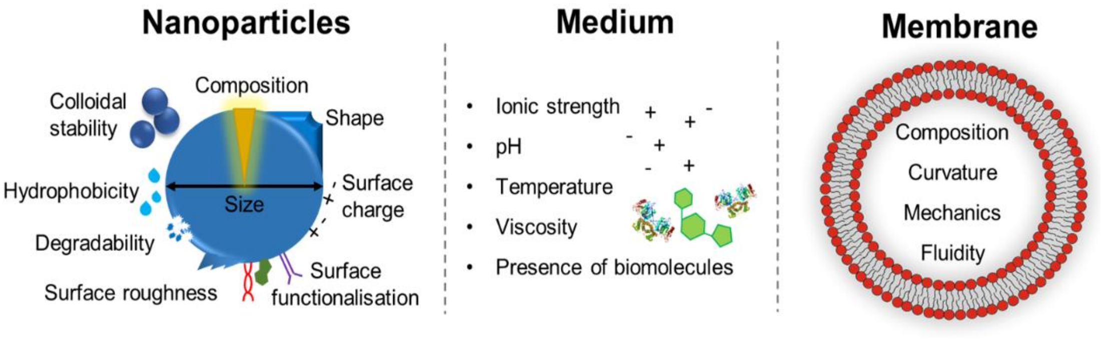

Figure 1.11. Principal factors that affect the NP-membrane interactions. The interactions between NPs and lipid membranes are influenced by the composition and intrinsic characteristics of the NPs, the conditions of the surrounding medium and the biophysical properties and lipid composition of the membrane. (Figure inspired in reference 66)

The mechanism of interaction between engineered nanoparticles and lipid membranes is determined by a balance between the adhesion energy (*w)*, which attracts the NPs towards the membrane, and the membrane's resistance to deformation, which opposes the membrane wrapping around the spherical NPs, defined by the elastic properties of the membrane. Assuming a tensionless membrane, the ratio between the bending rigidity (κ_b) of the membrane and the adhesion energy defines a critical diameter (d_c) above which the NP is spontaneously wrapped by the membrane: [76]

$$\textbf{Equation 1.8} \qquad d_c = 2\sqrt{\frac{2\kappa_b}{w}}$$

According to this simple model, a nanoparticle of a given size will be completely wrapped by the membrane only if the adhesion energy is high enough to overcome the energy cost needed to bend the membrane. The relationship between NP size and membrane wrapping has been proved experimentally. For example, cryo-electron microscopy and tomography images have shown that SiO_2 NPs with a diameter larger than 30 nm are totally wrapped by DOPC membranes and internalised into large unilamellar vesicles LUVs, while SiO_2 NPs of 15 nm remain attached to the LUV surface but are not engulfed by the membrane [77]. Fluorescence confocal microscopy studies have also shown similar results [78, 79]. However, there are intermediate states where NPs only get partially wrapped by the membrane. The degree of wrapping is thought to be limited by the membrane tension, which represents an additional energy cost that has to be overcome by the adhesion energy to achieve full wrapping [68, 75, 80, 81]. In addition, NPs can show cooperative behaviour once adsorbed to the membrane which can enhance their ability to produce membrane deformations and become wrapped. An example of NP cooperative behaviour has been recently shown by Contini *et al.* who reported that gold nanoparticles (AuNPs) with a diameter equal to or below 10 nm undergo cooperative absorption and can form tubular deformations in the membrane, while the adsorption and ability to bend membranes of larger AuNPs is significantly reduced [80].

The adhesion energy is often difficult to evaluate because it is the result of a combination of several forces acting together at the nanoparticle-membrane interface, including hydration, van der Waals, electrostatic, and steric interactions [71, 82]. Besides the size and composition of the NPs, the forces acting at the nanobio interface are also influenced by other properties of the NPs such as the shape, surface charge or hydrophobicity. Chithrani *et al* observed higher cellular uptake of spherical gold nanoparticles (AuNPs) into HeLa cells than rod-shaped AuNPs [83]. Moghadam *et al* showed that AuNPs and titanium dioxide (TiO_2) NPs with positive surface charge significantly increase the permeability of DOPC membranes while negatively charged TiO_2 NPs barely induce any dye leakage [84]. Dubavik and co-workers compared the uptake of amphiphilic and hydrophilic cadmium telluride quantum dots (CdTe QDs) into GUVs and GPMVs and observed that only amphiphilic CdTe QDs penetrated the vesicles [85]. They also tested the internalization of these particles into Chinese Hamster Ovary cells and reported that both types of QDs were internalized, nonetheless, they noticed that amphiphilic QDs penetrated directly through the cell membrane while hydrophilic QDs were internalized via endocytosis [85].

The membrane charge also modulates the NP-membrane adhesion strength. In a recent publication by Zuraw-Weston *et al*, the authors show that the adhesion energy can be tuned by including different fractions of lipids positively charged (DOTAP) or negatively charged (DOPS) in the membrane [75]. They found that below a threshold fraction of DOPS or DOTAP, AuNPs and SiO_2 NPs, respectively, adsorb onto the surface of the vesicles but do not produce any major perturbation in the membrane. In this scenario, the NPs can be partially wrapped by two different membranes and thus act as an adhesive bridge that mediates GUV-GUV adhesion. In contrast, when the charged lipid fraction in the membrane reaches or exceeds the threshold value, the NPs are wrapped by the membrane showing cooperative behaviour and induce a series of perturbations in the GUVs which eventually lead to complete vesicle destruction [75]. The interaction mechanisms shown in this publication will be further discussed and compared with our results in **Chapter 4** and **Chapter 5** of this thesis.

Finally, the properties of the surrounding medium also have a profound impact on the stability and surface properties of NPs and thus modulate their adhesion energy and biological activity [71, 73, 86]. For instance, the ionic strength of the medium is known to induce aggregation and degradation of some types of NPs [87-89], however, less attention has been put to its effect on the interaction with lipid membranes. Depending on the type of nanoparticle, the ionic strength can reduce or enhance the affinity of the NPs for the membrane. For instance, the adhesion of cationic polystyrene NPs to zwitterionic PC GUVs decreases as the concentration of NaCl in the medium increases [90]. On the contrary, 10 nm AuNPs have been recently shown to induce significant dye leakage from DOPC LUVs only when the interaction occurs in a solution containing NaCl [80].

Moreover, physiological media contain a myriad of biomolecules that have a great impact on the biological behaviour of NPs. When NPs are immersed in such complex biological fluids, many different molecules compete to adsorb onto the surface of the NPs. Consequently, the NP surface becomes rapidly covered by biomolecules, principally proteins, forming a biomolecular adsorption layer around the nanoparticles, known as biomolecular corona [91]. Since the proteins are the primary component of biomolecular coatings and little is still known about the contribution of other biomolecules, such as lipids, sugars or nucleic acids, the biomolecular corona is commonly considered to be a protein corona. The structure and composition of the protein corona as well as the state of the proteins that form it is not yet clear and shows great variability [92]. For example, the analysis of protein coronas formed on SiO_2 NPs and polystyrene NPs have revealed more than 100 different types of proteins among which the most abundant are albumin, apolipoproteins, and hemoglobin subunits [91, 93, 94]. Protein coronas are thought to be dynamic structures where some proteins bind irreversibly to the NP surface (hard corona) but others with a weaker binding affinity (soft corona) show a dynamic and reversible attachment and detachment from the protein corona [71, 92, 95, 96]. The degree of surface coverage and binding affinity for the NP surface depends on both the type of protein and the properties of the NPs [91, 97, 98].

Independently of the composition, thickness and organisation of the corona, it is universally accepted that protein coronas induce profound changes in the surface properties of bare NPs and also that proteins adsorbed onto the NP surface can undergo conformational changes which can lead to the exposure of new peptide sequences (epitopes) or altered protein function [71, 96]. These effects influence the NP biointeractions in two different but complementary ways. On one hand, protein coronas significantly affect the non-specific interactions of NPs with lipid membranes as they can lower the surface energy of the NPs, screen their surface charge and hinder potential surface functionalisations. On the other hand, the adsorbed proteins, either in their native configuration or in altered conformations, can potentially interact with membrane receptors and activate different cellular responses [96]. Therefore, protein (or biomolecular) coronas likely produce great impacts on the potential toxicity of NPs and their viability for biomedical applications.

1.3 Synthetic Biology

Biotechnology relies on the production and utilisation of biological organisms. Such organisms are extremely complex and present redundant components which makes them difficult to control and less energetically efficient. Thus, simpler systems, easier to study and manipulate are desirable. In this context, synthetic biology emerges as a new interdisciplinary field, which merges biology, physics and engineering. Synthetic biology is then a young discipline within biotechnology involved in the design and construction of minimal biological entities as well as in the redesign of natural biological systems for functional purposes but also to improve our understanding of different biological components and systems.

The field of synthetic biology uses two approaches: top-down and bottom-up. The former involves the modification of living cells to equip them with new functionalities. For instance, the cellular genome can be reprogrammed to design new metabolic and signalling pathways within the cell [99]. The bottom-up approach, on the contrary, aims to reconstruct cellular elements from non-living building blocks. A central and exceptionally challenging objective of bottom-up synthetic biology is building a living synthetic cell from a minimal set of functional elements [100-102]. Artificial cell projects adopt modular engineering strategies for the assembly of cell-like minimal systems within the synthetic cell (Fig. 1.12). Most studies propose the following elementary characteristics that such minimal cells must have [100-102]:

- Compartmentalisation.
- Storage, processing and replication of information.
- Metabolism and signalling.
- Spatiotemporal integration and coordination.
- Sensing and communication with the environment.
- Growth and division.

Lipid vesicles, especially GUVs, are the most common architecture used to mimic the plasma membrane and delimit the boundary of artificial cells. Thus, lipid vesicles themselves provide one of the key features of living systems, compartmentalisation, and serve as the elementary building block which will host the rest of components of the synthetic cell. Examples of biological entities reconstituted inside GUVs include cytoskeleton components, DNA nanostructures, cell-free protein expression systems (PURE), small unilamellar vesicles and bacteria [103].

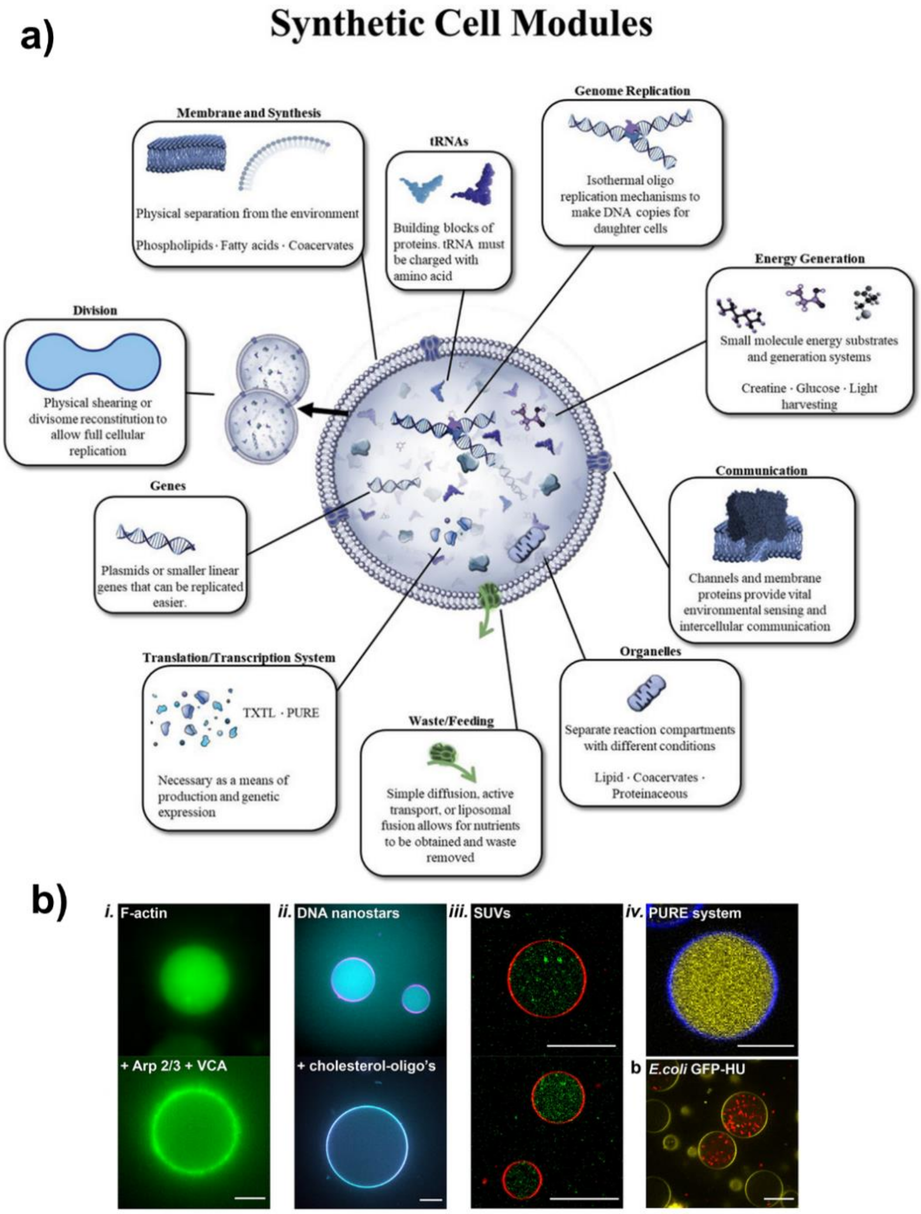

Figure 1.12. Building blocks of artificial cells. a) Modular components of a synthetic cell. (Figure taken from reference 96). b) Actin cytoskeleton, DNA nanostructures, SUVs, PURE system and *E. coli* cells encapsulated within GUVs. (Images taken from reference 99)

1.3.1. Engineered nanoparticles for Synthetic Biology

A difficulty often encountered when trying to reconstitute protein complexes inside an artificial cell is that different enzymes and proteins need particular environmental conditions to be structurally stable and functional. In addition, many of those proteins, particularly transmembrane proteins, are very difficult to express and purify. This limitation might be circumvented by the incorporation of inorganic engineered nanoparticles to the artificial cell toolbox as protein mimics because NPs are usually cheaper to produce and more stable and robust than natural proteins.

Albeit the structure and function of proteins are usually very precise, proteins and NPs can present similarities in terms of size, charge, shape, and surface functional groups [104]. While some protein functions are very specific and difficult to imitate, others mediate common biochemical reactions or physical processes easier to mimic. For example, AuNPs with different surface functionalisations have exhibited various enzymatic activities [105, 106]. Besides enzymatic activity, the ability of NPs to interact with lipid membranes might confer nanomaterials the capacity to perform other protein activities including membrane remodelling and shape transformations, exchange of substances between the lumen of the artificial cell and the environment and cell-cell (vesicle-vesicle) adhesion [75, 107, 108]. In living cells, these processes are performed by specific and highly regulated protein complexes, however, NPs have the potential to induce similar modifications in the membrane than natural protein complexes which in principle would lead to similar outcomes. To test this hypothesis, in the present thesis we investigate the potential ability of SiO_2 NPs to mediate membrane fusion.

The life of cells is largely dependent on membrane fusion processes. Eukaryotic cells require sequential fusion events to transport substances between membrane-bound organelles, to release molecules to the extracellular environment or to incorporate nutrients *via* endocytosis [109, 110]. In artificial cells, membrane fusion is employed as a growth mechanism as well as to deliver new biochemical species into the cellular compartment [101]. Fusion events in living cells are intricate phenomena that require the coordinated action of multicomponent protein complexes. The main molecular machinery that performs membrane fusion in eukaryotic cells is the SNARE protein complex. SNARE proteins (and other viral fusion proteins) mediate membrane fusion by driving a delicate balance of membrane curvature and tension between two closely apposed membranes [111-113]. Hence, according to our hypothesis, NPs able to produce membrane curvature and at the same time increase the membrane tension might have a latent fusogenic activity.

As introduced in **Section 1.2.3**, the interaction between NPs and lipid membranes is governed by the balance between the adhesion energy and the membrane's resistance to deformation (*Equation 1.8*), determined by its elastic properties. This relationship determines a critical NP diameter above which the NPs can be wrapped by the membrane. The interaction between SiO_2 NPs and lipid membranes is known to be particularly sensitive to the NP size, thus by tuning the size of the NPs, the effect that they produce on lipid membranes can be considerably modified. In 2012, Zhang *et al* showed that SiO_2 NPs of 18 nm diameter interact with DOPC giant unilamellar vesicles (GUVs) inducing high tension, solidification and rupture of lipid membranes, whereas larger SiO_2 NPs of 78 nm and 182 nm are wrapped by the membrane [79]. In that study they propose that a cross-over between both effects will be observed when the membrane adhesion and curvature elastic energies become equal, that is when the size of the SiO_2 NPs equals the critical diameter. Introducing typical values of bending rigidity of DOPC membranes (19-24 $\kappa_B T$)[114, 115] and the adhesion energy between SiO_2 and phosphocholine (PC) membranes (0.5 and 1 mJ/m^2) [116] in *Equation 1.8* renders a critical diameter in the range of 25-40 nm. We hypothesise that SiO_2 NPs within this critical size range (30 nm SiO_2 NPs) will provide a balance between membrane curvature and membrane tension analogous to the physical membrane perturbations induced by natural membrane fusion complexes and therefore will be able to mediate fusion of lipid membranes.

1.4 Project outline

The general purpose of this thesis is to study the interactions of inorganic engineered nanoparticles with model lipid membranes with two principal objectives:

1) To gain insight into how the physical perturbations that inorganic nanomaterials cause to the structural, mechanical and dynamical properties of lipid membranes are influenced by the medium conditions.
2) To evaluate the potential of nanomaterials to mimic membrane remodelling functions of natural protein complexes.

To reach these goals, the response of artificial model membranes, LUVs and GUVs, to the interaction with NPs will be analysed using advanced spectroscopy and fluorescence microscopy techniques, respectively. A detailed explanation of the experimental methods and the theoretic basis behind them is provided in **Chapter 2**.

Two chapters of the thesis will be dedicated to each point (Fig. 1.13). More specifically, within the first one we will explore the impact of the ionic strength of the medium (**Chapter 3**) and the presence of proteins (**Chapter 4**) on the interplay between NPs and lipid membranes. The second part of the thesis will focus on studying the mechanisms by which SiO_2 NPs trigger membrane fusion (**Chapter 5**) and a proof-of-concept study where NP-triggered fusion is used to generate phase separated membranes (**Chapter 6**).

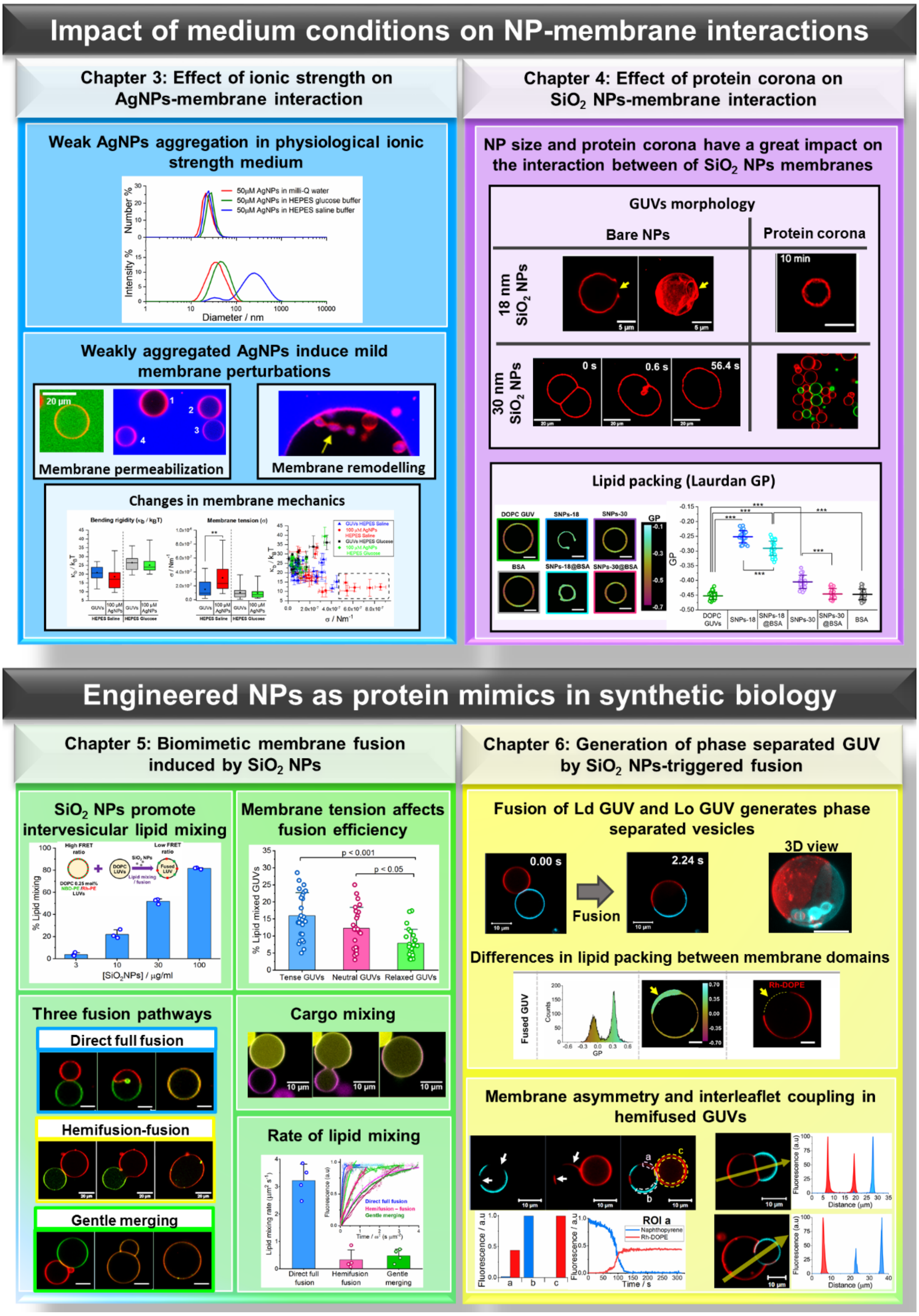

Figure 1.13. Thesis results at glance.

Chapter 2:
Materials and methods

This chapter outlines the methods used repeatedly throughout this thesis. The first section in this chapter gives theoretical background on fundamental analytical methods used for the study of membrane biophysics and NP-membrane interactions. The next sections describe the materials and the detailed experimental procedures employed in the work presented in **Chapters 3, 4, 5** and **6**.

2.1 Theory and instrumentation

2.1.1 Dynamic light scattering

Dynamic light scattering (DLS) is a technique employed to determine the size or size distribution of particles in suspension. DLS is therefore very important to characterise the size of NPs and LUVs as well as to assess the colloidal stability of NPs in suspension.

The DLS instrument commonly consists of a He-Ne laser at 633 nm which is directed to the sample cuvette and a photon detector situated at a particular scattering angle (normally 90º or 173º) to measure the scattered light (Fig. 2.1). The size measured by DLS is called hydrodynamic radius (or hydrodynamic diameter) and is defined as the radius (or diameter) of a sphere with the same diffusion coefficient as the sample under investigation [117]. In suspension, particles diffuse through Brownian motion and this movement results in fluctuations of the laser light intensity. These fluctuations in the scattered intensity are processed using the autocorrelation function ($G(\tau)$), which compares the intensity of the signal (I) at an initial time (t) with its intensity after a time delay (τ) (Fig. 2.1):

$$\textbf{Equation 2.1} \qquad G(\tau) =< I(t)I(t+\tau) >$$

If the intensity of the signal at the initial time is compared with the intensity at a very short time later, the correlation between them is strong. However, when the initial intensity is compared with the intensity of the signal at a longer time, the correlation is lower. Thus, the autocorrelation of the signal drops with time until there is no correlation. For monodisperse suspensions of particles undergoing Brownian motion, the autocorrelation function decreases exponentially with the time delay [118]:

$$\textbf{Equation 2.2} \qquad G(\tau) = A\left(1 + Be^{-2Dq^2\tau}\right)$$

where *A* and *B* are the baseline and the intercept of the autocorrelation function respectively, *D* is the diffusion coefficient and *q* is the magnitude of the scattering vector given by:

$$\textbf{Equation 2.3} \qquad q = (4\pi n/\lambda)sin(\theta/2)$$

where *n* is the refractive index of the medium, *λ* is the wavelength of the laser and *θ* is the scattering angle. Large particles diffuse relatively slowly through the medium resulting in a slower fluctuating intensity signal as compared to the small particles, which diffuse faster [118]. Therefore, the decay of the signal for large particles happens at longer times than for small particles. For polydisperse samples the autocorrelation function includes the sum of the exponential decays of the different particle sizes:

$$\textbf{Equation 2.4} \qquad G(\tau) = A\left(1 + B\sum e^{-2Dq^2\tau}\right)$$

Finally, the diffusion coefficient (*D)* obtained from the autocorrelation function, can be used to calculate the hydrodynamic radius (*R*) of the particles, applying the Stokes-Einstein equation:

$$\textbf{Equation 2.5} \qquad D = \frac{k_B T}{6\pi\eta R}$$

where *T* is the temperature in Kelvin (K), k_B is the Boltzmann constant and *η* is the viscosity of the solvent.

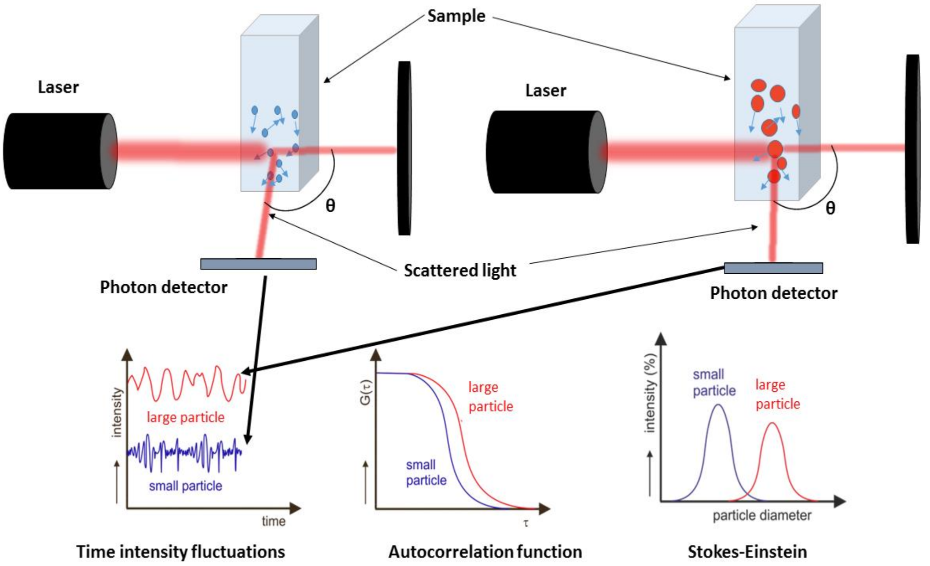

Figure 2.1. Schematic representation of DLS and data processing of particles of different sizes. The laser light is directed to the sample and the particles scatter the light which is then detected by a photon detector placed at a scattering angle θ. The Brownian motion of the particles results in fluctuations of the light intensity. The rate of time intensity fluctuations is processed using the autocorrelation function and the Stokes-Einstein equation to determine the particle size.

The size distribution of particles obtained by DLS is relative to the intensity of the light scattered. The distribution by intensity provides good results for monodisperse particles, but for polydisperse samples with particles of different sizes or aggregates, a size distribution by number gives information about the proportion of particles of each size comprised in the sample. To convert the distribution by intensity into distribution by number, DLS uses the Mie theory which describes the light scattering produced by spherical particles of all sizes and optical properties [119]. To do this conversion, Mie theory considers the difference between the refractive index of the dispersant and the particles [117]. According to Rayleigh's approximation, the intensity of scattering is proportional to the sixth power of the particle diameter (d^6), thus the size by number graph for a sample with two populations of particles of 10 nm and 100 nm equal in number will show two identical peaks. However, the peak at 100 nm in the size by intensity plot will be a million times higher than the one at 10 nm (Fig. 2.2) [119].

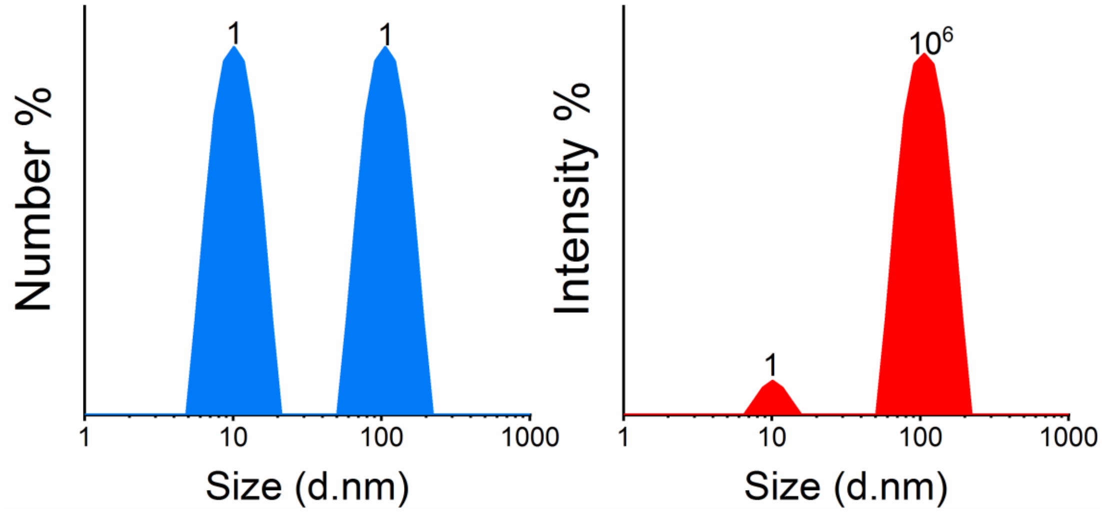

Figure 2.2. Size distribution by intensity and by number of a sample containing particles of 10 nm and 100 nm equal in number. (Figure adapted from reference 119)

2.1.2 Doppler electrophoretic light scattering analysis

Doppler electrophoretic light scattering analysis (DELSA) is a method that allows to measure the zeta (ζ) potential of particles in suspension. In this thesis, (and in NP studies in general) the zeta potential is used as an estimation of the surface charge of colloidal NPs.

When suspended in aqueous media, most particles acquire an electric charge which in turn affects the distribution of ions in their vicinity forming an electrical double layer [120]. In the inner region of the electrical double layer, called Stern layer, a high concentration of counterions is strongly bound to the surface of the particle. The outer region of the electrical double layer is the diffuse layer, where the distribution of ions (co-ions and counterions) is determined by electrostatic forces and thermal motion [120]. Within this layer, there is a boundary known as shear or slipping plane which separates the ions that remain tightly attached to the particle (stationary phase) from the ions which are free in the bulk solution (mobile phase) [121]. The potential at the slipping plane is the ζ potential (Fig. 2.3).

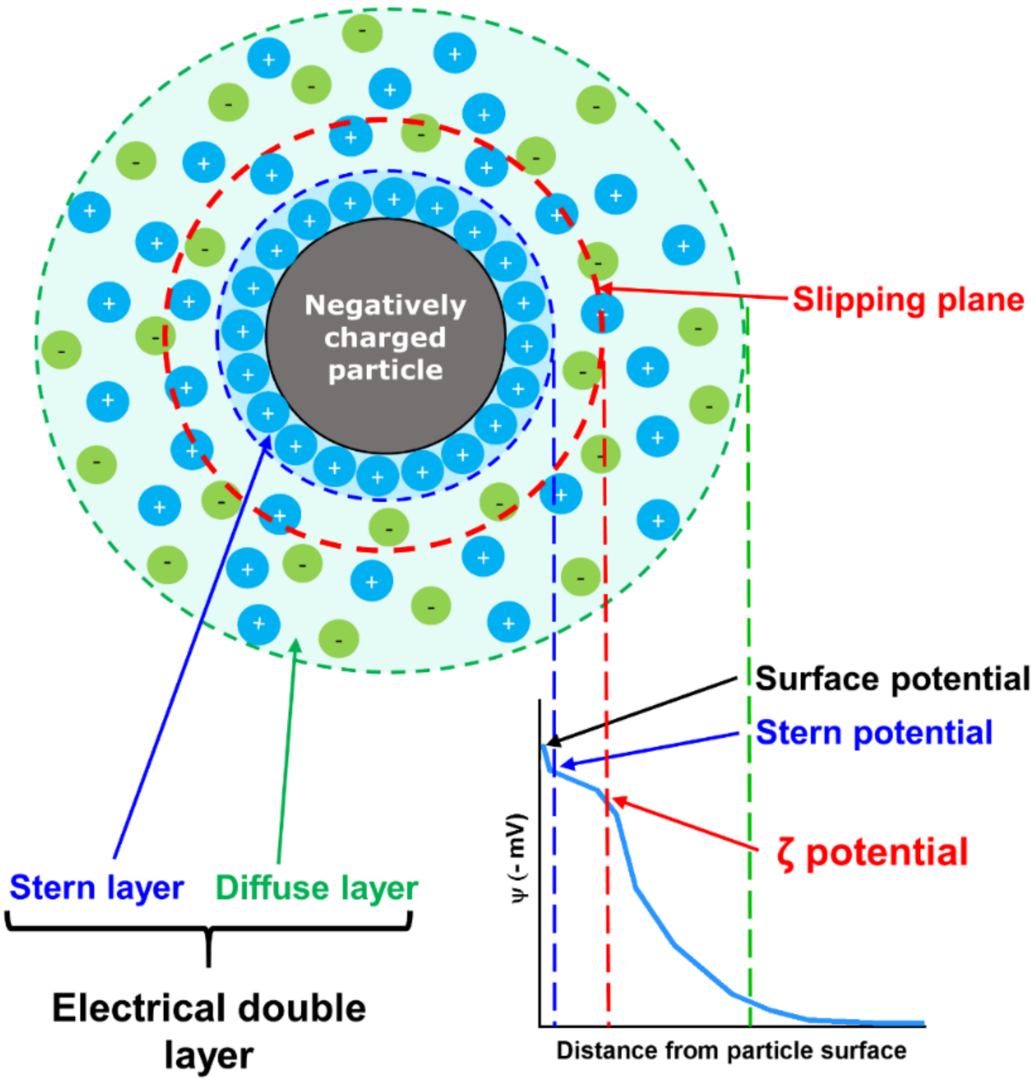

Figure 2.3. Schematic representation of the electric double layer formed around a particle suspended in an aqueous solution.

DELSA uses microelectrophoresis to estimate the ζ potential of the particles in suspension. Electrophoresis is an electrokinetic process that causes the movement of charged particles in solution when an external electric field is applied. In practice, the sample is placed in a special cuvette that has an electrode at either end and after the electric field is applied, the particles move towards the oppositely charged electrode. During the process, the sample is irradiated by a laser beam and the movement of the particles induces shifts in the frequency of the scattered light (Δf) which are used to calculate the velocity (υ) at which the particles move [121]:

$$\textbf{\textit{Equation}}\ \mathbf{2.6} \qquad \Delta f = \frac{2\upsilon\ \sin(\theta/2)}{\lambda}$$

where θ is the scattering angle and λ is the laser wavelength. In a typical optical configuration for DELSA measurements, the detector is placed at a scattering angle of 17° and the light source is a He-Ne laser with a wavelength of 633 nm.

The particle velocity can then be used to estimate the electrophoretic mobility (U_e) of the particles under an applied electric field (E) *[122]*:

$$\textbf{\textit{Equation}}\ \mathbf{2.7} \qquad U_e = \frac{\upsilon}{E}$$

Finally, the electrophoretic mobility is converted into ζ potential (ζ) by using Henry's equation *[121, 122]*:

$$\textbf{\textit{Equation}}\ \mathbf{2.8} \qquad U_e = \frac{2\ \varepsilon\ \zeta\ \ F(\kappa a)}{3\eta}$$

where ε is the dielectric constant; η is the viscosity of the medium and *F(κa)* is the Henry function. When the particles are suspended in an aqueous solution with moderate electrolyte concentration and the particle radius is larger than the thickness of the double layer, *F(κa)* takes the value of 1.5 (3/2) *[122]*. This is known as the Smoluchowski approximation of Henry's equation and it is the most commonly used equation to calculate the ζ potential of the particles *[121]*. Using the Smoluchowski approximation, Henry's equation *(Equation 2.8*) is simplified to:

$$\textbf{\textit{Equation}}\ \mathbf{2.9} \qquad U_e = \frac{\varepsilon\ \zeta}{\eta}$$

2.1.3 Ultraviolet-Visible spectroscopy

Ultraviolet-Visible (UV-Vis) spectroscopy is a widely used technique that offers a myriad of possibilities to perform both quantitative and qualitative sample analysis based on colorimetric measurements. For instance, in this thesis UV-Vis spectroscopy is used to determine the lipid concentration in LUVs samples and the absorbance peak of AgNPs is an indicator of their size and aggregation state. UV-Vis spectroscopic methods measure the light absorbed by an analyte within the ultraviolet (200-350 nm) and visible (350-700 nm) regions of the electromagnetic spectrum.

Light can be considered to behave either as waves propagating in an electromagnetic field or as particles with discrete amounts of energy, called photons. The interaction of these photons with matter leads to the phenomena of light absorption and emission [123]. The result of this interaction depends on the energy of the photon and the electronic state of the molecules radiated. In an atom or a molecule, the electrons can travel in different orbitals characterised by well-defined energy levels, hence the energetic state of the electrons determine in which orbital they are placed. The absorption of UV or visible light by a molecule can induce the promotion of electrons from the highest occupied molecular orbital (HOMO) to the lowest unoccupied molecular orbital (LUMO). However, for this transition from the electronic ground state to an excited state to happen, the energy of the photon absorbed must be equal to the energy gap between the orbitals [124]. The energy of the photon (E) is related to the frequency (ν) and the wavelength (λ) of the electromagnetic radiation by the Plank-Einstein relation:

$$\boldsymbol{Equation\ 2.10} \qquad E = h\nu = \frac{hc}{\lambda}$$

where h is the Planck constant and c is the speed of light.

The wavelength at which the light absorbed by an analyte reaches its maximum can be easily determined by recording its absorption spectrum using UV-Vis spectroscopy. When a sample is irradiated with an incident beam of light of intensity I_0, part of the light is absorbed and the rest is transmitted [124]. The transmitted beam will have lower intensity (I) than the original beam. The absorbance (A) is then calculated as:

$$\boldsymbol{Equation\ 2.11} \qquad A = log\left(\frac{I_0}{I}\right)$$

Both I_0 and I are measured in watts (W), hence, the absorbance is a unitless parameter. Usually, a reference sample with the same solvent and cuvette type is used as baseline to account for any absorbance that is not due to the analyte. In this case, I_0 in *Equation 2.11* is the intensity of the light transmitted through the reference sample. The absorbance of the sample is proportional to the amount of HOMO to LUMO excitations occurring in it, or what is the same, the number of absorbing molecules in the sample. This allows to calculate the concentration of analyte (c) in the sample from its absorbance using the Beer-Lambert law [124]:

$$\boldsymbol{Equation\ 2.12} \qquad A = \varepsilon c l$$

where l is the path length of the cuvette containing the sample and ε is the molar extinction coefficient, also known as molar absorptivity, which indicates how strongly a substance absorbs light at a specific wavelength.

The light absorbance is measured using an UV-Vis spectrophotometer. In its simpler configuration, this instrument consists of a UV-Vis light source, a monochromator, a sample compartment and a photodetector. The most common light sources are deuterium lamps for the UV range of wavelengths and tungsten halogen lamps for visible light. The monochromator breaks the spectrum of wavelengths produced by each lamp into individual wavelengths. The light at the selected wavelength passes through the sample and the transmitted light goes to the photodetector, commonly photomultiplier tubes or silicon photodiodes [124, 125] (Fig 2.4). The instrument employed in this project was a Cary 100 UV Vis spectrophotometer.

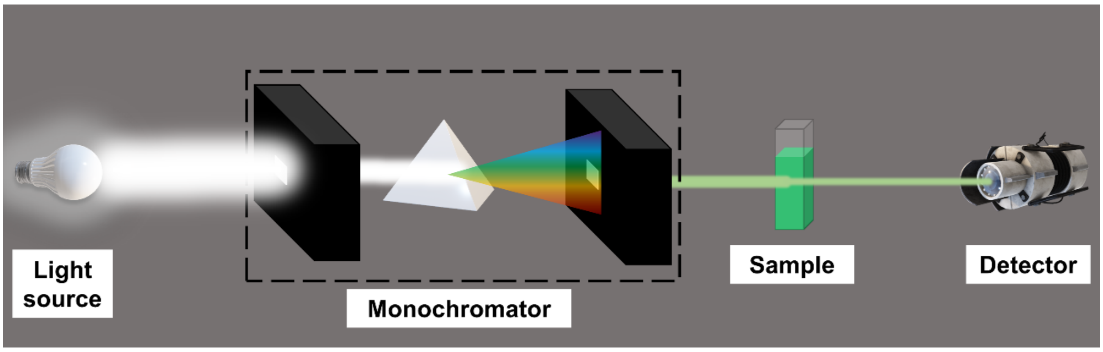

Figure 2.4. Schematic diagram of the basic components of a UV-Vis spectrophotometer.

2.1.4 Fluorescence spectroscopy

Fluorescence is another type of interaction between light and matter resulting from the ability of some molecules, known as fluorophores, to absorb and emit photons. The absorption peak of a fluorophore is equivalent to its maximum excitation wavelength. Nearly instantaneously to being excited, the fluorophore emits light (fluorescence) at longer wavelengths, thus with less energy, than the excitation beam.

The fluorescence process begins with the excitation of an electron from the electronic ground singlet state (S_0) to a high vibrational level of a singlet excited state (S_1) by a light beam at the maximum excitation wavelength. Once excited, the molecule releases some energy via non-radiative processes, such as vibrational relaxation or heat release. This non-radiative relaxation is called internal conversion and induces the electron to pass from higher vibrational levels in the excited state to the lowest vibrational level of the excited state. Next, the electron relaxes from the lowest vibrational level of the excited state to the ground singlet state releasing a photon, hence emitting fluorescence. The released photon is lower in energy than the incident beam due to energy being previously lost through internal conversion. This energy loss between excitation and emission is known as the Stokes shift [126]. The processes occurring during the absorption of light and fluorescence emission by a fluorophore is illustrated by the Jablonski diagram (Fig. 2.5).

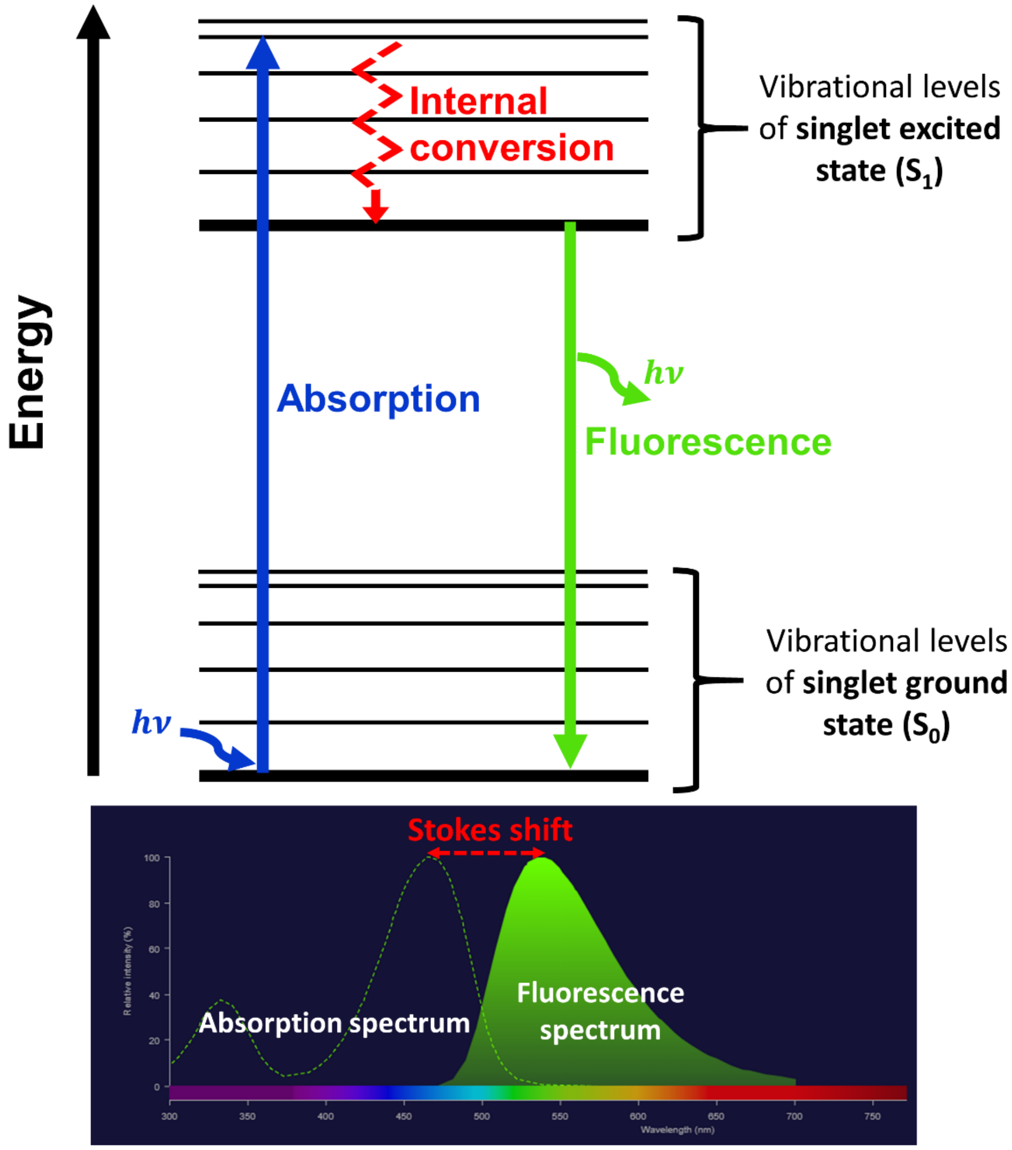

Figure 2.5. Jablonski diagram and example of absorption and fluorescence spectra of a fluorophore (NBD). The absorption of light (*hv*) induces the excitation of an electron from the electronic ground state to a high vibrational level of an electronic excited state (blue arrow). The molecule initially relaxes through non-radiative processes (internal conversion) and the electron passes from higher vibrational levels in the excited state to the lowest vibrational level of the excited state (red dashed arrow). The electron finally relaxed back to the ground state emitting a fluorescence (green arrow). The released photons are lower in energy, hence of higher wavelength, than the incident light as shown in the absorption/fluorescence spectra of the fluorophore NBD. This loss of energy is called Stokes shift.

Fluorescence spectroscopy methods are extensively used in ensemble experiments to analyse changes in membrane permeability and lipid packing produced by NPs interacting with LUVs. The fluorescence intensity is measured with a fluorescence spectrophotometer or fluorometer (Fig. 2.6). The instrument used in this thesis was a FluoroMax-Plus fluorometer (Horiba Scientific). The first part of a fluorometer is similar to the UV-Vis spectrophotometer and is formed by an UV-Vis light source and a monochromator to select the adequate excitation wavelength. The most common light sources used in fluorescence spectroscopy are low-pressure mercury lamps and xenon arc lamps, although light-emitting diodes (LEDs) and lasers are gaining popularity. The light beam is then directed to the sample which consequently emits fluorescence in the UV, visible or infrared (IR) region of the electromagnetic spectrum. The light emitted is passed through a second monochromator situated at 90º respect to the excitation beam, which selects the emission wavelength of interest and removes the excitation light from the signal. The fluorescence intensity at the selected wavelength is finally detected using either photomultiplier tubes or silicon photodiodes [124, 126].

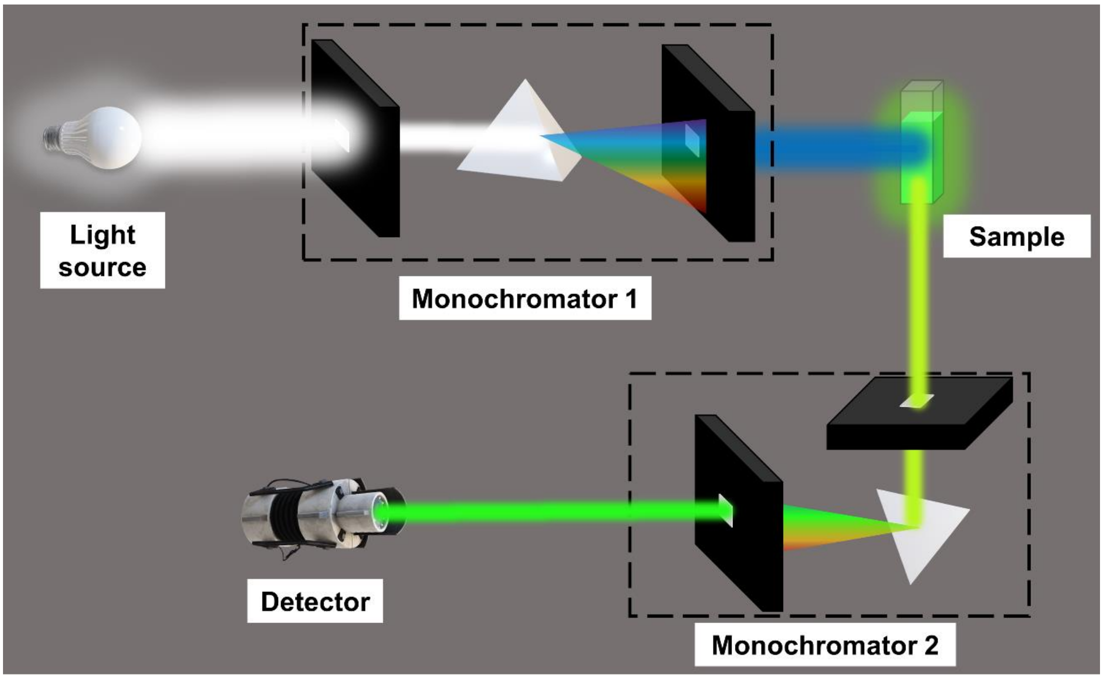

Figure 2.6. Schematic diagram of the basic components of a fluorometer.

2.1.4.1. Förster resonance energy transfer

Förster resonance energy transfer (FRET) is a phenomenon, originally described by Theodor Förster, which involves the transfer of energy between two different and compatible molecules, commonly referred to as FRET pairs. To be compatible, the fluorescence emission spectrum of the first fluorescent dye (donor) must overlap at least partially the absorption, or excitation, spectrum of the second molecule (acceptor). This implies that the acceptor and donor ground and excited electronic states are of the same magnitude of energy and some of their vibrational levels are in resonance [127]. Besides, the lower vibrational levels of the excited state in the acceptor are of lower energy than in the donor, thus the energy transferred is high enough to induce the excitation of the acceptor [127]. FRET assays are used in membrane fusion studies to detect merging between LUVs labelled with a FRET pair and unlabelled LUVs, as will be explained later in **Section 2.3.5**. Although in most FRET applications the acceptor is a fluorophore, this is not mandatory. The non-fluorescent acceptors act as fluorescence quenchers of the donors. Classic methods to evaluate membrane permeability, such as the carboxyfluorescein leakage assay described in **Section 2.3.4**, are examples of quenching-based experiments.

The first stage of FRET is the same described for fluorescence: the absorption of light by the donor fluorophore induces the elevation of an electron to a higher excited singlet state. After the initial internal conversion, the electron returns from the lowest vibrational level of the excited state to the ground electronic state, however, this transition does not produce the emission of a photon. Rather than originating fluorescence emission, in FRET processes the energy of the excited donor molecule is transferred to a neighbour acceptor molecule through a non-radiative long-range dipole-dipole coupling mechanism [126, 128]. Consequently, an electron in the acceptor jumps to a higher excited state. The relaxation of the electron to the ground electronic state is accompanied by fluorescence emission if the acceptor is fluorescent (Fig. 2.7), whereas if the acceptor is not fluorescent the energy is dissipated as heat [126].

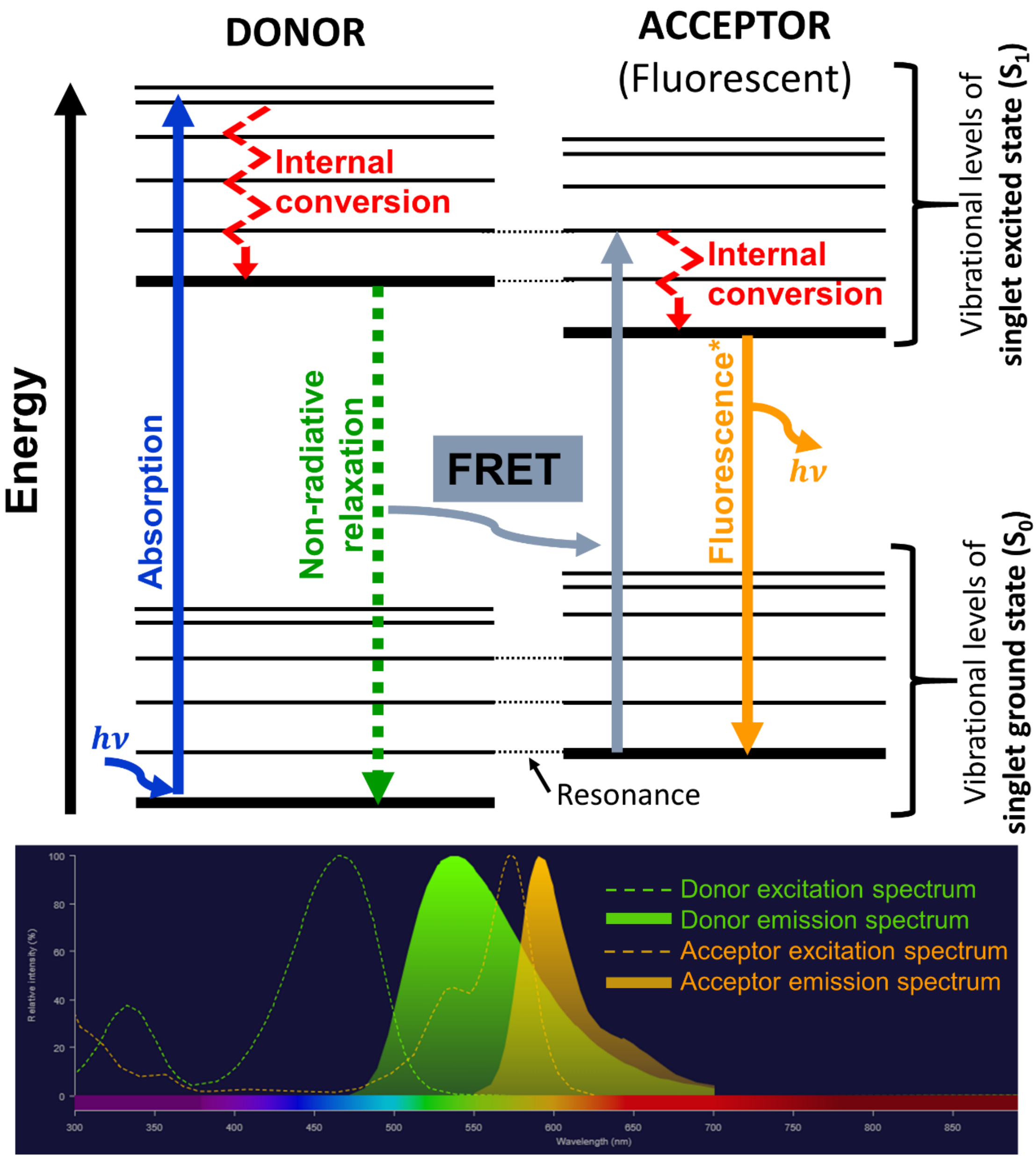

Figure 2.7. Jablonski diagram of FRET process and example of excitation and emission spectra of a FRET pair (NBD-Rhodamine). After excitation, the donor dye instead of emitting fluorescence, transfers its energy to the acceptor through FRET and the excited electron returns to the ground state. Consequently, an electron of the acceptor molecule passes to an electronic excited state. Finally, the excited electron returns to the ground state and the acceptor molecule emits fluorescence. The bottom plot shows the overlap of the fluorescence emission of the FRET donor with the excitation spectrum of the FRET acceptor needed for FRET to occur.

In addition to the spectral overlap, the FRET efficiency (*E*) is also highly dependent upon the distance between the donor and the acceptor [126, 128]:

$$\textbf{Equation 2.13} \qquad E = \frac{R_0^6}{R_0^6 + r^6}$$

where *r* is the distance between the donor and the acceptor and R_0 is the Förster distance in Å, which is defined as the distance where FRET efficiency is 50% and can be estimated using the following equation [126]:

$$\textbf{Equation 2.14} \qquad R_0 = 0.211(\kappa^2 n^{-4} \phi_D J(\lambda))^{1/6}$$

where *n* is the refractive index of the medium, κ^2 is a dimensionless factor ranging between 0 and 4 which indicates the relative dipolar orientation of the two molecules; ϕ_D is the quantum yield of the donor which refers to the ratio of photons absorbed to photons emitted by a fluorescent dye; and $J(\lambda)$ (in units of M^{-1} cm^{-1} nm^4) is the spectral overlap integral [126, 128]. Thus, *Equation 2.13* shows that the further is the donor from the acceptor the lower is the FRET efficiency whereas if the distance between the donor and the acceptor is below R_0, the efficiency increases considerably. FRET processes are usually limited to distances ranging from 1 to 10 nm [128, 129]. The FRET efficiency can be experimentally determined by comparing the maximum fluorescence intensity of the donor in the absence of acceptor (D_D) and when the acceptor is present (D_{DA}):

$$\textbf{Equation 2.15} \qquad E = 1 - \frac{D_{DA}}{D_D}$$

A further parameter used for evaluating experimentally FRET processes occurring in the sample of interest is the FRET ratio (F) which serve to monitor relative changes in the FRET efficiency under different conditions:

$$\textbf{Equation 2.16} \qquad F = \frac{A_{DA}}{D_{DA}}$$

where A_{DA} is the maximum fluorescence intensity of the acceptor when both the donor and the acceptor are present in the sample. The FRET ratio only can be used when the acceptor is a fluorescent dye.

2.1.5 Confocal laser scanning microscopy

Confocal laser scanning microscopy is an optical imaging technique that uses spatial filters (pinholes) to eliminate out-of-focus light or glare of fluorescently labelled specimens thicker than the plane of focus [130]. This allows to collect bidimensional (2D) images at different focal planes, or sample depths, that can be overlapped to reconstruct three-dimensional (3D) images. The elimination of out-of-focus glare also provides high-resolution images of samples labelled with multiple fluorophores and hence it is extensively used for studying biological systems [131].

In a typical confocal microscope configuration, a laser system is used as excitation source and two pinhole apertures, situated in a conjugated focal (confocal) plane to each other and with a scanning plane on the specimen, define the sample thickness that will be scanned. The light emitted by the laser passes through a first pinhole aperture, is reflected by a dichromatic mirror and is focused to a point of the specimen by a microscope objective. The dichromatic mirror reflects light of wavelengths shorter than a determined value whereas light of longer wavelength is transmitted [131]. A confocal microscope usually has different dichromatic mirrors for specific excitation lasers and fluorescence emission spectra to adjust the light source to the excitation wavelength of the fluorophore of interest and collect the emitted fluorescence within the desired wavelength range. Once the light reaches the sample, the fluorophores excited emit fluorescence at a higher wavelength than the excitation light. The fluorescence emitted go back through the dichromatic mirror and just the light emitted from the desired focal plane passes through the second pinhole to the photomultiplier detector, while the out-of-focus light is blocked [130] (Fig. 2.8).

Confocal microscopy is a very powerful technique for both qualitative and quantitative analysis of biological systems. For instance, in terms of membrane studies, it provides qualitative information about the morphology and topology of membranes, lipid phase separation and potential localisation of proteins and other fluorescently labelled molecules in the membrane. In addition to qualitative properties, a myriad of techniques based on confocal imaging are extensively used for the quantitative study of permeability, fluidity and mechanical properties of the membrane. Two of these quantitative methods, fluorescence recovery after photobleaching (FRAP) and flickering spectroscopy, are explained in detail in the following sub-sections.

All confocal microscopy experiments shown in this thesis were performed in a Zeiss LSM-880 inverted laser scanning confocal microscope with a Plan-Apochromat 40x/1.4 Oil DIC M27 objective lens (NA = 1.4).

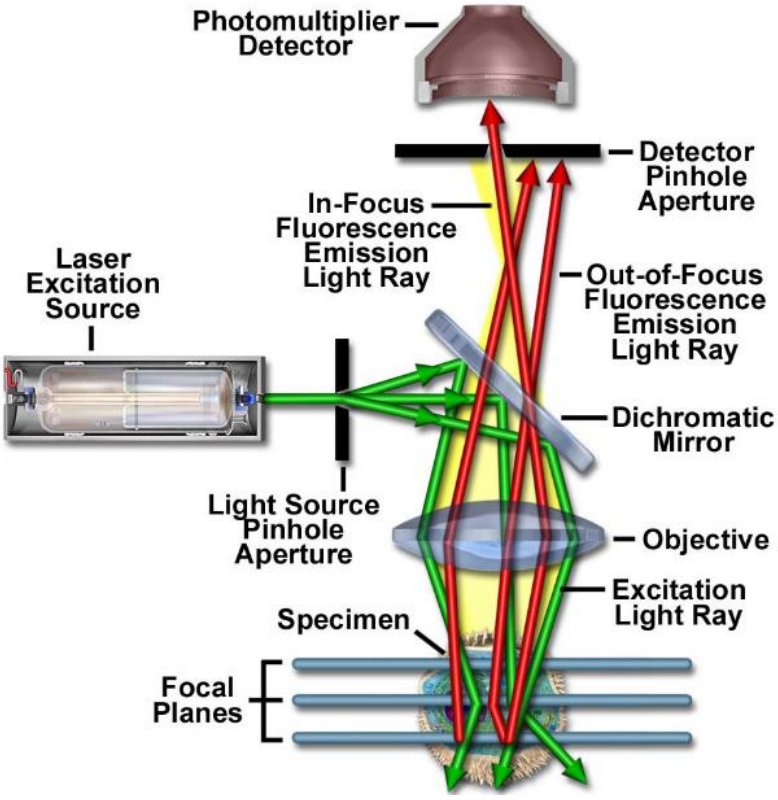

Figure 2.8. Schematic diagram of the basic configuration of a confocal laser scanning microscope along with the pathway of the excitation laser (green) and the fluorescence emission (red). (Figure reproduced from reference 130).

2.1.5.1 Fluorescence recovery after photobleaching

Fluorescence recovery after photobleaching (FRAP) is a powerful confocal microscopy-based method to study the mobility and interactions of fluorescent biomolecules and compounds in biological and biomimetic systems at the micrometre scale. FRAP is commonly used in membrane biophysics investigations to determine the lateral diffusion coefficient of lipids within the membrane. Along with molecular diffusion, the basic principle behind FRAP is the fluorescence photobleaching. When a fluorophore is excited by a high-intensity laser, its excited electrons tend to change their spin state from an excited singlet state to an excited triplet state (T_1) through a process called intersystem crossing. Fluorophores in the triplet excited state can easily react with other molecules in the system leading to a chemical product that is no longer fluorescent, in other words, a photobleached fluorophore [132].

In a FRAP experiment, a region of interest (ROI) in a fluorescently labelled sample is initially irreversibly bleached with a high-intensity laser pulse. This results in a considerable loss of fluorescence intensity in the photobleached ROI. After the photobleaching, the rate of fluorescence recovery in the ROI is monitored by imaging the sample with a low-intensity laser to avoid further photobleaching [133, 134]. The fluorescence is recovered because the unbleached fluorophores surrounding the bleached region diffuse into the ROI whereas the bleached molecules diffuse out and get diluted in the sample [132]. The fluorescence intensity in the ROI over time is normalised against the fluorescence intensity prior to bleaching in the same region of the sample. The normalised fluorescence intensity is plotted against time to obtain a recovery curve characteristic of FRAP. The final fluorescence intensity is usually slightly lower than before the bleach because a proportion of the molecules in the sample is photobleached (Fig. 2.9).

To quantify the diffusion rate of the molecules in the sample, the recovery curves must be fitted to a theoretical FRAP model. The fluorescence recovery within circular ROIs is accurately described by the Soumpasis equation [135].

$$\textbf{Equation 2.17} \qquad f(t) = A\left\{exp\left(-\frac{2\tau_D}{t}\right)\left[J_0\left(\frac{2\tau_D}{t}\right) + J_1\left(\frac{2\tau_D}{t}\right)\right]\right\}$$

where t is time, A is the fluorescence recovery level, τ_D is the characteristic recovery time, and J_0 and J_1 are modified Bessel functions of the first kind. Finally, the diffusion coefficient (D) can be calculated from the recovery times and the radius of the bleached region (ω) using:

$$\textbf{Equation 2.18} \qquad D = \frac{\omega^2}{4\tau_D}$$

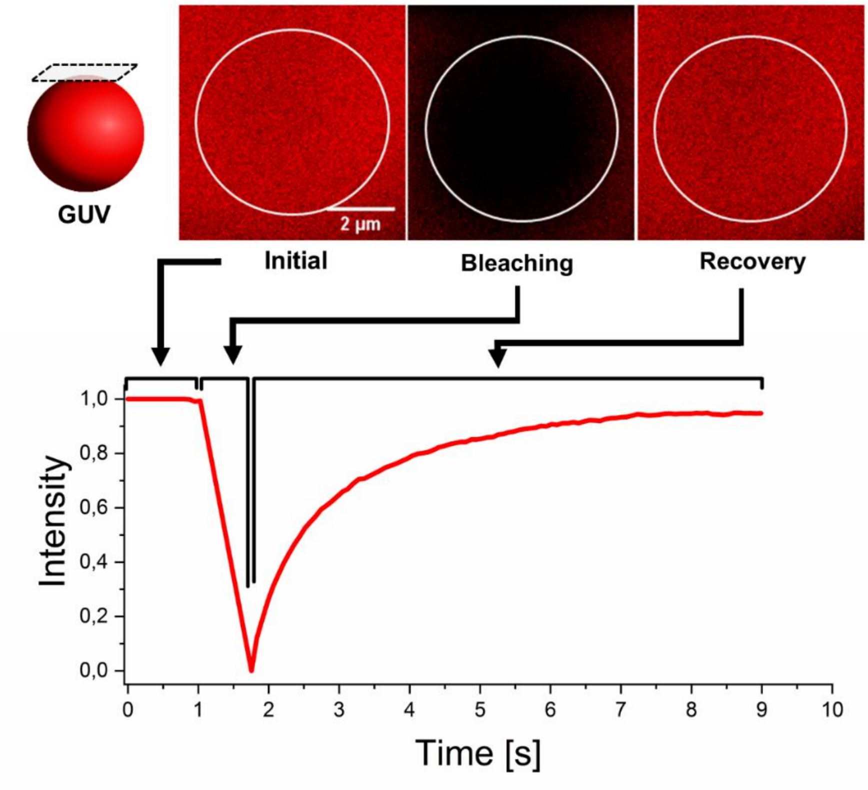

Figure 2.9. Confocal micrographs of FRAP experiment performed on the top pole of a GUV and fluoresce recovery curve**.** The white circle in the micrographs indicates the region of interest (ROI). Initially, the ROI shows a maximum fluorescence intensity. The fluorophores in the ROI are then bleached using a high-intensity laser pulse. After bleaching, the fluorescence is gradually recovered via lateral diffusion of fluorescent lipids into the ROI.

2.1.5.2 Flickering spectroscopy

Flickering or fluctuation spectroscopy is a non-invasive image analysis technique based on the analysis of the thermal shape fluctuations of lipid membranes originated from the Brownian motion of water molecules around the membrane [136]. It was firstly used by Brochard and Lennon in 1975 to describe the flicker phenomena of red blood cells [137], and since then it has become one the most popular methods to gain information about the mechanical properties of lipid membranes [114, 115, 138].

In 1984 Helfrich and Servuss calculated the membrane fluctuation spectrum for small thermal undulations using a quasi-planar continuous bilayer approximation [139]. According to Helfrich's formulation, the elastic energy (*E*) needed to deform a membrane depends on two main mechanical parameters, the membrane tension (σ) and the bending rigidity (κ), and is given by:

$$\boldsymbol{Equation\ 2.19} \qquad E = \frac{1}{2}\int \left\{\sigma\big(\nabla h(x,y)\big)^2 + \kappa(\nabla^2 h(x,y))^2\right\} dx\, dy$$

where $h(x,y)$ is the height of the membrane relative to a fixed horizontal plane in the point of coordinates (x, y), or what is the same, the displacement of the membrane contour respect its average position. By transforming the displacement into Fourier space and assuming equipartition of energy, the mean square amplitude of each fluctuation mode ($\langle | h(q)^2 \rangle$), also known as fluctuation spectrum, can be related to the membrane tension and bending rigidity by:

$$\boldsymbol{Equation\ 2.20} \qquad \langle |h(q)|^2 \rangle = \frac{k_B T}{L^2(\sigma q^2 + \kappa q^4)}$$

where L^2 is the area of the membrane, q the wavevectors ($q=(q_x+q_y)^{1/2}$), k_B the Boltzmann's constant and T the absolute temperature.

In addition to the quasi-planar model shown above, alternative quasi-spherical models which expand the membrane fluctuations into spherical harmonics are also commonly used to describe the thermal fluctuations of lipid vesicles. However, Pecreaux *et al.* [140] pointed out that when only the equatorial plane (y =0) of a lipid vesicle is being analysed (as it is the case of video microscopy), only the fluctuations in this plane are accessible and the quasi-planar and quasi-spherical formulations of the fluctuation spectrum are equivalent for all but the lowest fluctuation modes. The fluctuation spectrum in the equatorial plane of the vesicle is then given by:

$$\textbf{Equation 2.21} \qquad \langle |h(q_x, y=0)|^2 \rangle = \frac{1}{L}\frac{k_B T}{2\sigma}\left(\frac{1}{q} - \frac{1}{\sqrt{\frac{\sigma}{\kappa} + q^2}}\right)$$

Experimentally, the shape fluctuations of the membrane can be observed in GUVs using optical microscopy methods, commonly phase contrast [22, 115, 141] and confocal microscopy [114, 115, 142]. Hence, the first step of flickering spectroscopy is collecting videos of single GUVs imaged at their equatorial plane. Then the contour of the GUV is extracted from the videos to analyse the fluctuations of the membrane respect its mean shape over time. Detailed descriptions about the contour detection algorithm can be found elsewhere [114, 143]. Briefly, in the case of fluorescence confocal microscopy images, the position of the membrane is detected with subpixel resolution by finding the radial maximum intensity profile, expressed in polar coordinates $r(\varphi)$, from every frame of the time-series.

The radial profiles show the fluctuations of the distance from the centre of the GUV to the membrane, and the amplitude of the membrane fluctuations is calculated relative to the mean radius of the vesicle. Then the amplitude of the fluctuations is Fourier transformed to calculate the mean square amplitude of each Fourier mode. Finally, the values of the bending rigidity and membrane tension can be obtained by fitting the experimental fluctuation spectrum with *Equation 2.21.*

2.2 Materials

2.2.1 Lipids

The main lipids used in this research are 1,2-dioleoyl-sn-glycero-3-phosphocholine (DOPC), 1,2-dipalmitoyl-sn-glycero-3-phosphocholine (DPPC), cholesterol (from ovine wool), 1,2-dioleoyl-sn-glycero-3-phosphoethanolamine-N-(lissamine rhodamine B sulfonyl) (ammonium salt) (Rh-DOPE,) and 1,2-dioleoyl-sn-glycero-3-phosphoethanolamine-N-(7-nitro-2-1,3-benzoxadiazol-4-yl) (ammonium salt) (NBD-DOPE) were purchased from Avanti Polar Lipids Inc. (Alabaster, USA) . The molecular structure of the main lipids used in this research is represented in Figure 2.10.

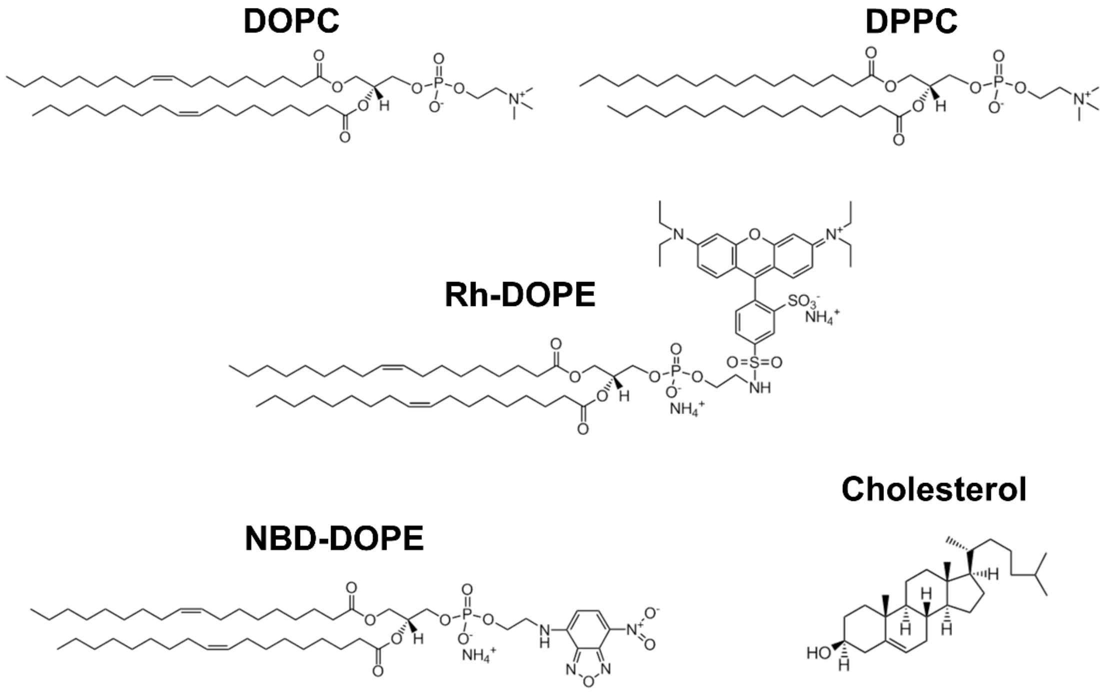

Figure 2.10. Molecular structure of DOPC, DPPC, Rh-DOPE, NBD-DOPE and cholesterol.

2.2.2 Nanoparticles

Silver nanoparticles (AgNPs) were provided by collaborators from the “Inorganic Nanoparticles Group” from the Institut Català de Nanociència i Nanotecnologia (ICN2) (Barcelona, Spain). Silica nanoparticles (SiO_2 NPs) LUDOX SM-30 and LUDOX TM-50 were purchased from Sigma-Aldrich Co. (Gillingham, UK).

2.2.3 Buffers

Most of the experiments in this thesis were performed in a buffer resembling the ionic strength of physiological media made of 20 mM HEPES and 150 mM NaCl. Some experiments were conducted in a low ionic strength buffer containing 20 mM HEPES but 300 mM glucose instead of NaCl to maintain the same osmolality of the medium. The osmolality of the buffer was measured with a 3320 Micro-Osmometer (Advanced Instruments, Norwood, UK). All buffers were adjusted to pH 7.4 with NaOH. HEPES, NaCl, glucose, and NaOH were obtained from Sigma-Aldrich Co. (Gillingham, UK).

2.2.4 Miscellaneous materials

Indium titanium oxide (ITO) coated glass slides (surface resistivity 8–12 V sq^{-1}), $AgNO_3$, sucrose, bovine serum albumin (BSA), 5(6)-carboxyfluorescein and tetramethylrhodamine isothiocyanate (TRITC)-dextran 70 kDa were purchased from Sigma-Aldrich Co. (Gillingham, UK). Microscope µ-slide 8 well glass bottom chambers (Ibidi GmbH) were purchased from Thistle Scientific Ltd (Glasgow, UK). 3,3'-dioctadecyloxacarbocyanine perchlorate (DiO), 1,1'-dioctadecyl-3,3,3',3'-tetramethylindodicarbocyanine, 4-chlorobenzenesulfonate salt (DiD), 6-Dodecanoyl-2-Dimethylaminonaphthalene (Laurdan), cascade blue-dextran 10 kDa and TRITC-dextran 40 kDa were purchased from ThermoFisher Scientific Ltd. (Loughborough, UK). Naphtho[2,3-a]pyrene (naphthopyrene) was obtained from Tokyo Chemical Industries UK Ltd (Oxford, UK).

2.2.4.1. 5(6)-Carboxyfluorescein

The hydrophilic fluorescent dye 5(6)-carboxyfluorescein (CF), a mixture of 5-carboxyfluorescein and 6-carboxyfluorescein (Fig. 2.11), is a common tool to study changes in membrane permeability as well as to investigate the controlled content release from drug carries. This is due to its self-quenching ability at high concentrations.

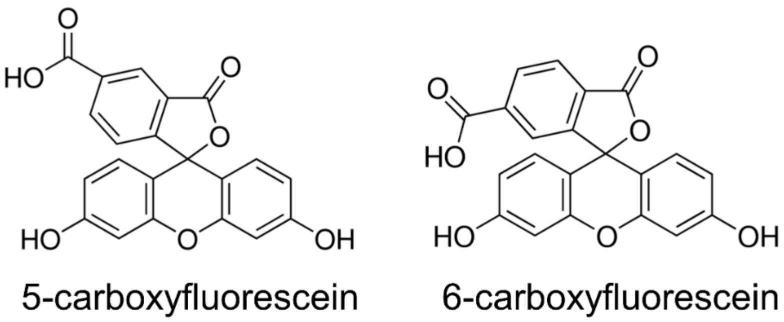

5-carboxyfluorescein 6-carboxyfluorescein

Figure 2.11. Chemical structure of 5- and 6-carboxyfluorescein.

The mechanism of CF fluorescence quenching inside lipid vesicles was first investigated by Chen and Knutson [144]. They showed that when encapsulated at a high concentration (200 mM) in DPPC liposomes, CF undergoes self-quenching, losing 97-98% of its fluorescence signal. They attributed the self-quenching to the formation of non-fluorescent CF dimers. These dimers, apart from not being fluorescent themselves, quench the fluorescence of the solution through Förster resonance energy transfer from the fluorescent CF monomers.

2.2.4.2. Environment-sensitive fluorophore Laurdan

Laurdan is a naphthalene derivative firstly synthesised in 1979 by Weber and Farris [145]. Laurdan is a polar-sensitive fluorophore: upon excitation in polar solvents, its dipole moment increases producing a reorientation of the surrounding polar molecules which results in a red shift of the fluorescence emission of the probe [134, 146].

Laurdan has been extensively used in membrane biophysics to assess the lipid packing within the membrane [147]. Laurdan localises in the hydrophilic/hydrophobic interface region of the membrane [148], showing maximum fluorescence at 490 nm or 440 nm depending on the membrane hydration (Fig. 2.12). Thus, an emission peak at 490 nm implies a hydrated and disordered membrane, while an emission maximum at 440 nm indicates a more ordered membrane where lipids are tightly packed and fewer water molecules are located near the dye. The fluorescence intensity at 440 nm (I_{440}) and 490 nm (I_{490}) is used to calculate a quantitative indicator of membrane order called generalized polarization (GP) [148], which increases with the order of the membrane:

$$\textbf{\textit{Equation}}\ \mathbf{2.22} \qquad GP = \frac{I_{440} - I_{490}}{I_{440} + I_{490}}$$

The GP of membranes labelled with Laurdan can be determined via fluorescence spectroscopy measurements [149, 150] or by spectral imaging [150-152].

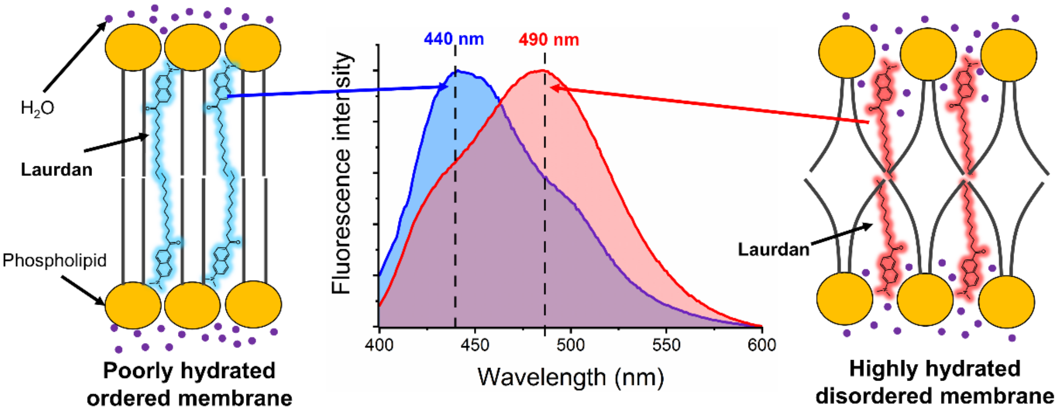

Figure 2.12. Schematic representation of Laurdan molecules within membranes with different levels of hydration along with characteristic fluorescence emission spectra in each condition.

2.3 Experimental procedures

2.3.1 Preparation of large unilamellar vesicles

LUVs were prepared by lipid thin film hydration followed by extrusion. Initially, a vial of 100 µl of the desired lipid mixture was dried from chloroform under vacuum overnight to get a lipid thin film. The lipid film was then rehydrated with 500 µl of the desired buffer and vortexed to form a suspension of vesicles polydisperse in size and lamellarity. Next, to break the multilamellar vesicles (MLVs) and form unilamellar liposomes, the sample was frozen in liquid nitrogen, thaw in a water bath at 60° C and vortexed. This freeze-thaw-vortex cycle was carried out 5 times. The sample was subsequently extruded 11 times by passing through a 400 nm pore size polycarbonate membrane using either an Avanti mini-extruder (Avanti Polar Lipids) or a LiposoFast extruder (Avestin Inc.) to obtain a homogeneous population of 400 nm LUVs. The size of the LUVs was determined by DLS and the lipid concentration by a standard phosphorus assay.

2.3.2 DLS and DELSA

DLS and DELSA experiments were performed with a Malvern Zetasizer Nano ZS (Malvern Panalytical, Malvern, UK). DLS was used to determine the size of LUVs, AgNPs and SiO_2 NPs as well as for evaluating the stability and aggregation state of NPs under different medium conditions. 200 µl of sample was placed in a microcuvette and each sample was measured three times (unless otherwise specified) at a fixed 173° back-scattering angle. The hydrodynamic size was reported as the average of the three readings. The results were processed using the Malvern Zetasizer software to obtain the hydrodynamic diameter from the analysis of the autocorrelation function of the light intensity scattered by the suspended particles in solution.

The ζ potential of NPs in solution was determined by DELSA. Approximately 1 ml of sample was introduced in a special cuvette for ζ-potential measurements (cuvette DTS1070, Malvern Panalytical, Malvern, UK). Each sample was measured three times at a fixed 17° back-scattering angle. The ζ potential was calculated from the measured electrophoretic mobility using the Smoluchowski approximation. The data were analysed with the Malvern Zetasizer software.

2.3.3 Phosphorus assay

The phospholipid concentration in the LUVs samples was determined using the phosphorus assay, which consists in digesting the organic sample into inorganic phosphorus. A phosphorus standard solution was used to prepare six calibration test tubes (0 µmol, 0.0325 µmol, 0.065 µmol, 0.114 µmol, 0.163 µmol, and 0.228 µmol) to use as calibration curve and three replicates of LUVs sample were made by adding 70 µl aliquots of the LUVs sample to sample test tubes. The digestion process begins with the addition of 450 µl of H_2SO_4 (8.9 M) to each tube before heating at 215° C for 25 min. After cooling the samples at room temperature, 150 µl H_2O_2 were added and the samples were heated at the same temperature for a further 30 min. The samples were cooled again before adding 3.9 ml of mili-Q water. Finally, 500 µl of both 2.5% (w/v) ammonium molybdate tetrahydrate and 10% (w/v) ascorbic acid were added and the tubes were sealed and vortexed before heating at 100° C for 7 min. The absorbance of the samples was measured at 820 nm using a Cary 100 UV Vis spectrophotometer and the concentration of lipid in the LUVs sample was estimated from the calibration curve made with the standard samples.

2.3.4 5(6)-carboxyfluorescein leakage assay

The leakage assay is a technique widely used in cytotoxicity studies for the detection of changes in membrane permeability upon interaction with potential membrane disruptors such as peptides, proteins, drugs or nanoparticles with lipid membranes. It is based on the fluorescence self-quenching that CF undergoes at high concentrations. In the context of this thesis, LUVs encapsulating self-quenched CF were exposed to NPs. The interaction of the NPs with the lipid membrane can lead to pore formation and even complete rupture of the LUVs which results in the release of the CF to the external medium where it gets diluted and hence, its fluorescence signal increases significantly (Fig. 2.13).

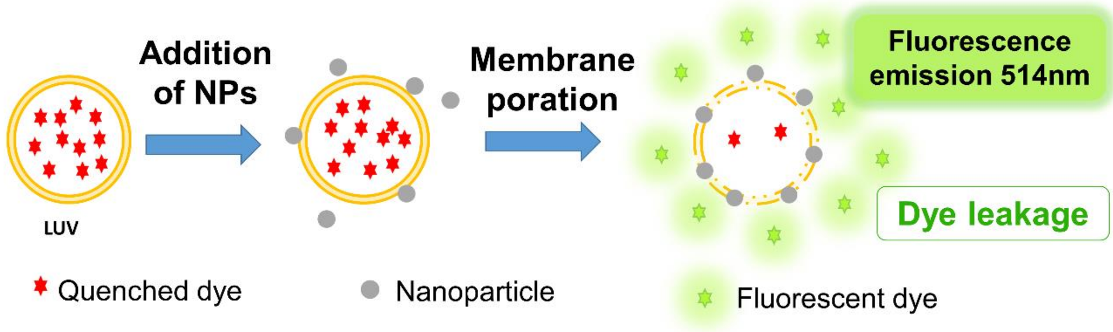

Figure 2.13. Schematic representation of CF leakage from a lipid vesicle. Inside the LUVs CF is self-quenched. The addition of NPs produces membrane pores and leads to the release of the dye from the vesicle to the external medium where it gets diluted and become fluorescent.

LUVs were prepared as explained in *Section 2.3.1.* To load the vesicles with CF, the lipid film was rehydrated with 500 µl of 20 mM HEPES, 120 mM CF, pH 7.4. After the extrusion, the sample was passed through a Sephadex G-25 column to remove the unencapsulated CF via size exclusion chromatography, obtaining DOPC LUVs with self-quenched CF encapsulated. Samples were prepared by suspending the LUVs in isotonic buffer at a final phospholipid concentration of 0.1 µM. Each sample was exposed to different concentrations of NPs and the fluorescence intensity was measured from 500 nm to 600 nm (excitation at 492 nm) using a fluorometer. The results were calculated from the fluorescence intensity values at 514 nm (I_n) and are presented as the normalized fraction of dye leakage. To calculate the fraction of dye release, a sample of LUVs non-treated with NPs was used as baseline signal which was subtracted from the emission spectrum (I_0) and values for complete dye leakage (I_{max}) were obtained by adding 50 µl of the surfactant Triton X-100 (10% w/v) which causes the lysis of the LUVs. The normalized fraction of CF leakage (L) is given by:

$$\boldsymbol{Equation\ 2.23} \qquad L_n = \frac{I_n - I_0}{I_{max} - I_0}\ x\ 100$$

2.3.5 Intervesicular lipid mixing measured by FRET

The Förster Resonance Energy Transfer (FRET) between NBD and rhodamine (Rh) was used to measure the lipid mixing between LUVs upon exposure to SiO_2 NPs, which is an indicator of membrane fusion and hemifusion. For these experiments, LUVs labelled with 0.25 mol% NBD-DOPE and 0.25 mol% Rh-DOPE as well as non-labelled LUVs were prepared *via* lipid thin film hydration followed by extrusion. The two sets of LUVs were mixed in a 1:4 ratio (20 µM labelled LUVs and 80 µM non-labelled LUVs) and incubated for 30 minutes with different concentrations of SiO_2 NPs. In addition, samples of LUVs non-treated with SiO_2 NPs were used as negative control and samples of LUVs labelled with 0.05 mol% NBD-DOPE and 0.05 mol% Rh-DOPE were used as full lipid mixing control. The fluorescence intensity of the samples was measured between 500 nm and 650 nm, using the excitation wavelength of NBD (460 nm). The maximum fluorescence intensity of NBD (D_{AD} at 530 nm) and Rh (A_{AD} at 590 nm) was used to calculate the FRET ratio (F) of each sample using *Equation 2.16*. The membrane fusion between the two populations of LUVs leads to final fused vesicles with a mixed membrane where the distance between the fluorophores increases and consequently the FRET ratio decreases. The percentage of lipid mixing was then calculated by normalising the FRET ratios of each sample (F_n) between the baseline samples of LUVs untreated with SiO_2 NPs (F_0) and the full lipid mixing controls (F_{full}):

$$\textbf{Equation 2.24} \qquad \%\ Lipid\ mixing = \frac{F_n - F_0}{F_{full} - F_0}\ x\ 100$$

Moreover, the fluorescence intensity of NBD (donor) at 530 nm when the acceptor Rh is present (D_{DA}) and absent (LUVs labelled only with 0.25 mol% NBD-DOPE) (D_D) was measured to calculate the FRET efficiency (E) using *Equation 2.16*.

2.3.6 Electroformation of giant unilamellar vesicles

In 1986, Angelova and Dimitrov observed that electric fields can induce swelling of lipids films and developed a method to prepare Giant Unilamellar Vesicles (GUVs) based on applying direct current (DC) electric fields to dried lipid films rehydrated in water solutions [153]. This protocol, known as electro-swelling or electroformation, was later improved using alternating current (AC) electric fields which reduce the formation of gas bubbles and increase the production rate of GUVs [154, 155].

GUVs were prepared using the electroformation method. First, 15 µl of lipid solution (0.7 mM) were deposited as a thin layer over the conductive side of two ITO coated glass slides and then dried under a nitrogen stream. The ITO slides were then assembled into an electroformation chamber each in contact with a copper tape and separated by a 1.6 mm Teflon gasket (Fig. 2.14). The chamber was filled with a 300 mM sucrose solution (300 mOsm kg^{-1}) and connected to a function generator to apply an AC electric field. The frequency of the electric field was set at 10 Hz and the voltage was gradually increased from 1 V peak-to-peak (Vpp) to 5 Vpp over 15 minutes and maintained at 5 Vpp for two hours. Finally, the frequency was gradually reduced to 0.1 Hz over 10 minutes to facilitate the closure and detachment of GUVs from the slide. For mixtures of lipids with melting transition temperatures (T_m) below 15 ºC the electroformation was carried out at room temperature, otherwise, the GUVs were electroformed at a temperature above the transition temperature of the lipid with the highest T_m in the mixture. After electroformation, the GUVs were suspended in isotonic (unless otherwise specified) buffer.

To prepare GUVs loaded with fluorescent dextran, the sucrose solution was doped with 0.5 mg/ml of TRITC-dextran and the electroformation was carried out at 35 ºC using the same settings detailed above. After electroformation, 200 µl of the GUVs were diluted with 800 µl of isotonic buffer. The diluted GUVs were then centrifuged for 5 minutes at 100*g,* so the GUVs sink to the bottom of the tube and the free dextran remains in the supernatant. Then, 600 µl of the supernatant were carefully removed from the tube and 600 µl of isotonic buffer were added to the GUVs. The sample was centrifuged again (5 min at 100*g*), 600 µl of the supernatant were removed and 600 µl of isotonic buffer were added again to resuspend the GUVs.

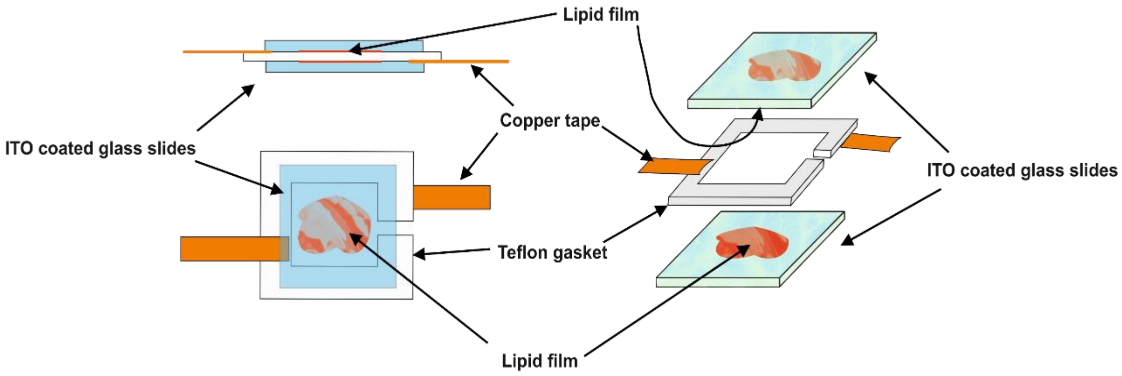

Figure 2.14. Schematic representation of an electroformation chamber.

2.3.7 Detection of changes in morphology and permeability of GUVs

Confocal laser scanning microscopy was used to monitor changes in the permeability and the morphology of GUVs induced by NPs. Table 2.1 shows the excitation laser and the fluorescence emission range for every dye used in confocal microscopy experiments in this thesis. Before beginning the experiments, the glass surfaces of the 8-well microscope chamber slides are treated with 5% BSA solution in mili-Q water for 10 minutes and then rinsed with Milli-Q water and dried under a nitrogen stream to prevent GUVs from adhering and rupturing onto the glass.

Table 2.1. Dyes used in confocal microscopy experiments

Fluorescent dye	Excitation laser	Emission range
Naphthopyrene	Diode 405 nm	410-503 nm
Cascade blue	Diode 405 nm	410-483 nm
CF	Argon 488 nm	493-556 nm
DiO	Argon 488 nm	493-553 nm
TRITC	DPSS 561 nm	570-625 nm
Lissamine Rhodamine (Rh-DOPE)	DPSS 561 nm	566-630 nm
DiD	HeNe 633 nm	638-750 nm

To identify morphological changes in the vesicles produced by the NPs, 200 μl of GUVs were initially deposited into a well of the microscope slide. Then the NPs were carefully added to the GUVs and their morphology was monitored by taking snapshots or by collecting time series to follow the process over time.

To study changes in membrane permeability, a membrane-impermeable fluorescent dye (fluorescent dextran or CF) is added to the 200 μl GUVs suspension, consequently, the bulk solution becomes fluorescent whereas the lumen of the GUVs remains uncoloured. The tile scanning option was used to image large areas of the sample and facilitate the acquisition of statistical data (Fig. 2.15). These scans were acquired before and after incubating the GUVs with the NPs. The fluorescence intensity in the lumen of GUVs was quantified and normalised using *Equation 2.23* where now L_n is the percentage of dye that leak into a particular GUV, I_0 is the average pixel intensity of the dye in the lumen of the GUVs before adding the NPs, I_n is the average pixel intensity of the dye in the lumen of the GUV analysed and I_{max} is the average pixel intensity of the dye in the bulk solution. Only GUVs with a normalised fluorescence intensity in their lumen higher than 20% were considered permeable to the fluorescent molecules in the external medium. The images were analysed using the Fiji extension of ImageJ software (National Institutes of Health, Bethesda, MD) and the proportion of GUVs affected by the NPs was determined by manual counting.

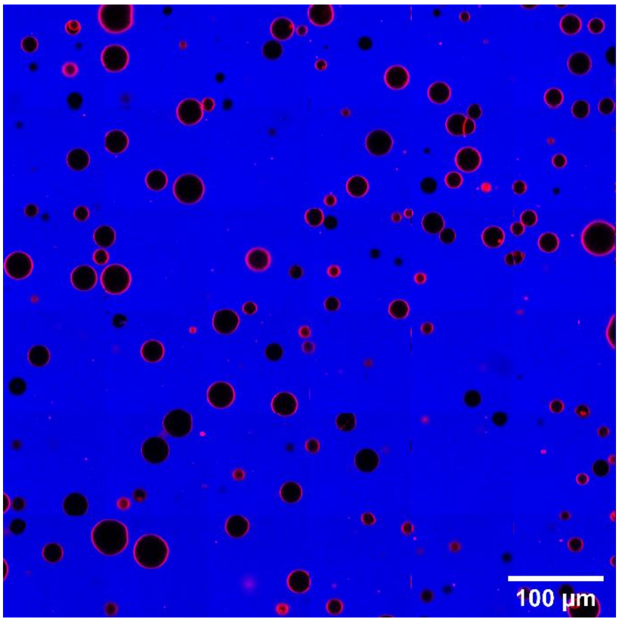

Figure 2.15. Example of confocal microscopy tile scan image of GUVs (red) with cascade blue-dextran molecules in solution (background blue fluorescence).

2.3.8 Imaging of membrane fusion and estimation of lipid mixing rate

Two populations of GUVs differently labelled were prepared by electroformation. Then 100 µl of each GUV population were mixed and, once the GUVs have sunk to the bottom of the imaging-slide well, 25 µg/ml SiO_2 NPs were added. Confocal microscopy time series were recorded to follow the fusion process over time. Images were analysed with Fiji to measure the fluorescence intensity of each dye in different regions of the membrane of the GUVs.

To estimate the lipid mixing rate, we monitored the fluorescence increase over time of one of the dyes while it invades the GUV initially labelled with the other fluorophore. The fluorescence was normalised to the maximum intensity reached after fusion. The data were fitted to an exponential function ($f(x) = A(1-exp(-t/\tau))$) where A is the change in fluorescence, t is the time passed since the lipids begin to mix and τ is the time constant. The rate of lipid mixing was calculated as the diffusion coefficient (*Equation 2.18*), where ω is now the radius of a circle with a surface area equivalent to the GUV analysed. The analysis of the images and the data was performed with Fiji and Origin Pro.

2.3.9 Acquisition and analysis of FRAP data

The potential changes in the fluidity of the membrane of GUVs induced by the NPs were investigated using FRAP. FRAP experiments were performed on the top pole of GUVs before and after adding the NPs. A circular ROI of 5 ± 0.5 µm diameter was exposed to 5 bleaching scans at 100% laser power and the recovery was monitored by recording time series of 100 frames. The recovery curves were fitted with Origin Pro using the fluorescence recovery model shown in *Equation 2.17* and from the recovery times, the diffusion coefficient is calculated using *Equation 2.18*. The movement of GUVs during the data acquisition might provide faster fluorescence recovery times than the one due solely to lipid diffusion. To minimise this issue, only measurements where the GUVs remained stationary during the bleaching and recovery process were included in the data analysis and the diffusion coefficient is given as the average of at least 15 individual measurements. In addition, this issue affects equally to control and non-control samples so the obtained data allows to detect relative changes in lipid diffusion coefficient between the (non-control) samples and the controls.

2.3.10 Acquisition and analysis of flickering spectroscopy data

The mechanical properties of GUVs were determined using flicker spectroscopy. After electroformation, the GUVs were suspended in a hyperosmotic buffer (315 mOsm kg^{-1}) (1 vol GUVs: 4 vol buffer) and incubated overnight at 4º C to osmotically relax the tension of the membrane. Confocal microscopy time series of 1000 frames and a resolution of 1024 x 1024 pixels were taken at the equatorial plane of single GUVs before and after exposure to the NPs. The confocal pinhole aperture was adjusted to 0.7 µm and, to increase the scan speed, single GUVs were zoomed in upon to the maximum magnification that allows imaging of the whole vesicle. The contour detection and fluctuation analysis were performed using an algorithm developed in MATLAB (The MathWorks) kindly provided by Prof. Pietro Cicuta and co-workers at the University of Cambridge, UK. This programme analyses each frame of the time series and quantifies the membrane tension and bending rigidity by fitting the fluctuation power spectrum of the membrane with *Equation 2.21*.

2.3.11 Laurdan spectral imaging

GUVs labelled with 0.5 mol% Laurdan were prepared by electroformation. The spectral imaging is acquired using the lambda mode of the Zeiss LSM880 confocal microscope, which allows split the fluorescence emission spectrum of a dye into up to 34 spectral intervals recorded in individual detection channels. Laurdan was excited with the 405 nm laser and the fluorescence detection range was set between 410 nm and 550 nm with a spectral step of 8.9 nm per channel. Snapshots of Laurdan labelled GUVs were acquired before and after exposure to NPs. The images were analysed with a Fiji plugin developed by Sezgin *et al* [151], setting 440 nm and 490 nm as maximum emission wavelengths to calculate the GP values as shown in *Equation 2.22*.

Chapter 3:

Effect of the ionic strength of the medium on the interaction between silver nanoparticles and lipid membranes

3.1 Introduction

Silver nanoparticles (AgNPs) are very appealing for industrial and biomedical applications due to their antimicrobial activity and their unique optical properties (see **Section 1.2.1**) but have also shown significant toxicity against different eukaryotic cell types. The mechanisms of AgNPs-induced cytotoxicity are still unclear and vary depending on the physicochemical properties of the NPs, their concentration and the exposure time, but also on the cell type they encounter [64]. For instance, Kim *et al.* observed that AgNPs induce cytotoxic effects in HeLa cells, Chinese Hamster Ovary cells, mouse preosteoblast MC3T3-E1 cells and rat adrenal medulla PC12 cells, with the two latter being most affected [156].

The interaction of AgNPs with the plasma membrane is essential for their biomedical activity but is also the initial step of the toxicity pathway. This interaction often leads to the internalisation of the NPs into the cell and can induce loss of membrane integrity [69, 70]. Once internalised, AgNPs could cross and damage other sub-cellular membranes, such as the inner mitochondrial membrane generating mitochondrial respiratory chain dysfunction and originating endogenous reactive oxygen species (ROS) [69, 70, 157, 158]. In addition, AgNPs are very susceptible to changes in the medium composition that can lead to corrosion, aggregation and oxidation processes which change their physicochemical properties and therefore their biological activity and cytotoxic effect [157].

In this chapter, we investigate how changes in the ionic strength of the medium influence the surface charge and colloidal stability of AgNPs as well as their effect on the biophysical properties of lipid membranes. In this manner, we can relate how modifications of AgNPs produced by changes in the ionic strength of the medium influence their ability to interact with lipid membranes.

3.2 AgNPs tend to aggregate in physiological ionic strength buffer

The citrate coated AgNPs used in this study were synthesised by collaborators from the *Institut Català de Nanociència y Nanotecnologia* (Barcelona, Spain), using the seeded-growth method [159]. These AgNPs were nanospheres with a diameter of 22.4 ± 2.5 nm as determined by transmission electron microscopy (TEM) (Fig. 3.1).

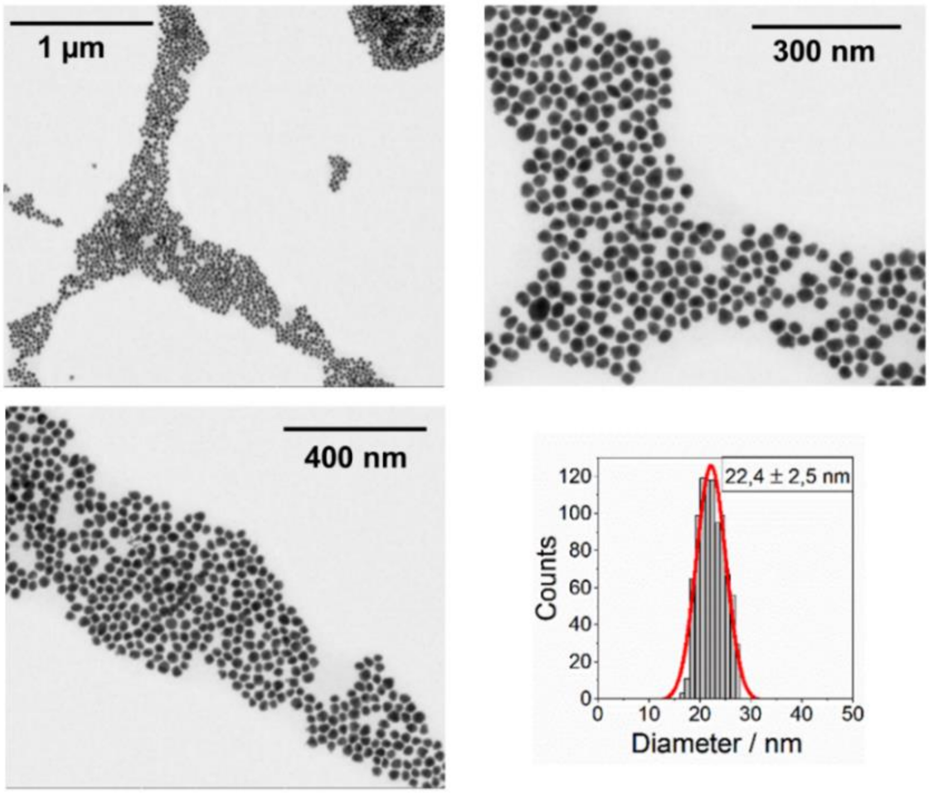

Figure 3.1. TEM images of spherical AgNPs. The data presented in this figure were acquired and analysed by collaborators from the Institut Català de Nanociència y Nanotecnologia (ICN2) in Barcelona.

Nonetheless, when suspended in biological media, the physicochemical properties of AgNPs can change as a result of dissolution and aggregation processes, as well as adsorption of biomolecules to the NP surface, which have an important influence on the biological activity of the NPs [160]. The aggregation of AgNPs can be easily detected using UV-vis spectrophotometry. The maximum absorption peak of the UV-vis spectrum of AgNPs corresponds with the LSPR peak. The absorbance spectrum of AgNPs suspended in water shows a single peak, typical of monodisperse AgNPs, at 417 nm (Fig 3.2). However, the LSPR is very sensitive to changes in the physicochemical properties of AgNPs produced by the medium. For instance, aggregation processes are known to produce a sharp decrease and broadening in the LSPR peak, an increase of absorbance at longer wavelengths and, sometimes, the appearance of secondary peaks [47]. This aggregation pattern is observed when the AgNPs are suspended in HEPES-buffered saline solution (Fig. 3.2).

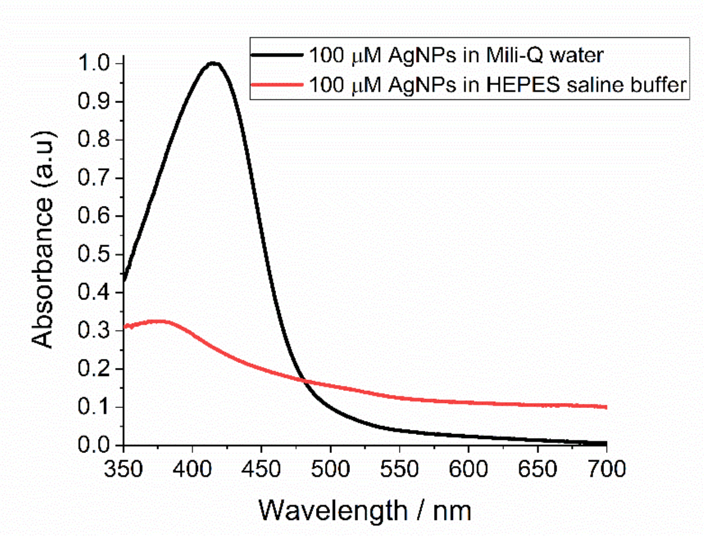

Figure 3.2. UV-vis spectrum of AgNPs suspended in mili-Q water and HEPES saline buffer. The LSPR peak of AgNPs in mili-Q water corresponds to 417 nm. In HEPES saline buffer the drop of LSPR peak and the increase in absorbance at longer wavelengths is an indicator of aggregation.

Additionally, the colloidal stability AgNPs in physiological and low ionic strength buffers was also tested by comparing the hydrodynamic size of AgNPs suspended in milli-Q water with their hydrodynamic size when suspended in the buffer of interest. The size distribution by intensity shows that the hydrodynamic diameter of AgNPs suspended in HEPES glucose buffer (43.5 ± 0.9 nm) does not differ significantly from the results in milli-Q water (40.2 ± 1.0 nm), hence the NPs are highly monodispersed and stable in this buffer. The bigger size obtained by DLS compared to TEM is expected because, while TEM measures only the physical size of the core NPs, DLS measures the hydrodynamic size which, in addition to the NP core, takes into account the stabiliser coating and the electrical double layer around the NPs [161, 162]. On the contrary, the rise of the ionic strength of the medium to physiological levels leads to aggregation as indicated by the appearance of a secondary peak around 200 nm in the DLS intensity distribution. However, the size distribution by number at this AgNPs concentration (50 µM), and incubation time (30 min) does not show differences with respect to the distributions in mili-Q water and HEPES glucose buffer, therefore most of the AgNPs are still monodisperse (Fig. 3.3).

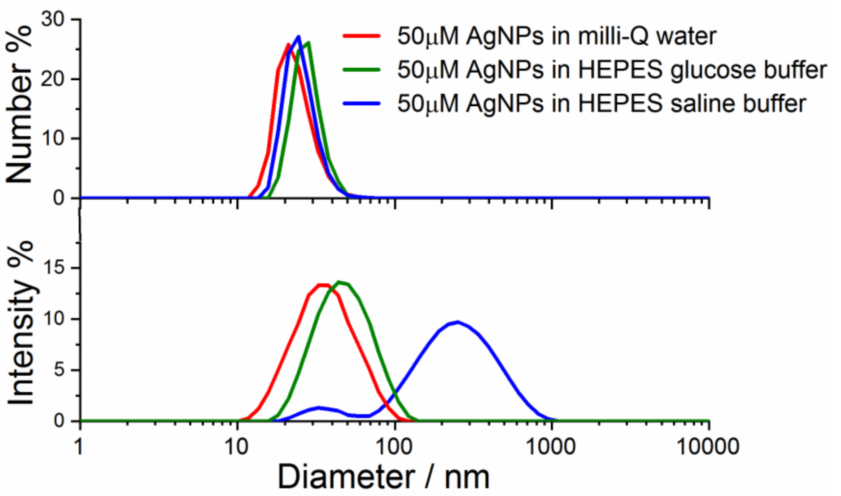

Figure 3.3. DLS data of 50 µM AgNPs suspended in mili-Q water, HEPES saline and HEPES glucose buffer for 30 minutes. The size distribution by number (top graph) shows a monodisperse distribution of AgNPs with peaks around 25 nm. The size distribution by intensity (bottom graph) is similar for AgNPs dispersed in mili-Q water and HEPES glucose buffer, whereas in HEPES saline buffer AgNPs show a tendency to form aggregates.

Doppler electrophoretic light scattering analysis (DELSA) was used to determine the ζ potential of AgNPs in different solutions. Similar to the hydrodynamic size, the ζ potential of AgNPs is comparable in milli-Q water and HEPES glucose buffer, -28.0 ± 6.08 mV and -21.2 ± 9.20 mV respectively, whereas in HEPES saline buffer the surface charge of AgNPs becomes less negative (-8.99 ± 15.18 mV) (Table 3.1). This less negative ζ potential is the reason behind the aggregation tendency in HEPES saline buffer. According to the Derjaguin-Landau-Verwey-Overbeek (DLVO) theory, the colloidal stability of NPs in suspension is determined by the balance between attractive forces, mainly Van der Waals forces, and electrostatic double-layer repulsions [14, 71, 163]. In low ionic strength medium, the negative surface charge provided by the citrate coating stabilises the AgNPs suspension by electrostatic double-layer repulsions. However, in HEPES saline buffer the high concentration of ions produces a screening of the surface charge that compresses the electrical double layer around the AgNPs [89, 164, 165]. Consequently, the electrostatic repulsions between AgNPs become weaker and their aggregation tendency increases.

Table 3.1. ζ potential of AgNPs in different media

MEDIUM	ζ-potential
Mili-Q water	-28.0 ± 6.08 mV
HEPES glucose buffer	-21.2 ± 9.20 mV
HEPES saline buffer	-8.99 ± 15.18 mV

DLS was also employed to monitor the temporal evolution of the hydrodynamic size of AgNPs suspended in low ionic strength (100 µM AgNPs) and physiological ionic strength buffers (50 µM, 100 µM and 250 µM AgNPs) for 2 hours by taking measurements every 60 seconds. The aggregation kinetics of colloidal suspensions can be fast when there is not a repulsive barrier between the particles and every collision between particles leads to attachment, or slow when the particles encounter a repulsive energy barrier and only a fraction of collisions are effective. The probability of effective collisions is indicated by the attachment efficiency (α). It can be estimated by normalising the slow aggregation rate constant (k_s) to the aggregation rate constant in the fast aggregation regime (k_{fast})[88]:

$$\textbf{\textit{Equation}}\ \mathbf{3.1} \qquad \alpha = \frac{k_s}{k_{fast}}$$

The fast aggregation rate constant can be estimated using Smoluchowski coagulation theory, where k_B is Boltzmann's constant, T is the temperature and η is the viscosity of the medium [120].

$$\textbf{\textit{Equation}}\ \mathbf{3.2} \qquad k_{fast} = \frac{4k_B T}{3\eta}$$

The slow aggregation rate constant is calculated from the experimental data. The increase in hydrodynamic diameter (D_h) of AgNPs at early time was analysed using a linear least-squares regression, and the slope ($(dD_h(t))/dt)_{t\to 0}$) is used for calculating k_s [88]:

$$\textbf{\textit{Equation}}\ \mathbf{3.3} \qquad \frac{1}{D_{h0}}\left(\frac{dD_h(t)}{dt}\right)_{t\to 0} = k_s N_0 \left[1 + \frac{\sin(D_{h0}q)}{2D_{h0}q}\right]$$

In low ionic strength, the hydrodynamic size of AgNPs does not change with time, whereas the aggregation profile of AgNPs in HEPES saline buffer shows a relatively fast initial increase in hydrodynamic diameter that slows down after about 10 minutes (Fig. 3.4). As expected, the more concentrated samples exhibit faster growth, forming larger aggregates. Analysis of the early, linear stage of aggregate growth was used to calculate the average aggregation rate constant (k_s) for AgNPs in HEPES saline buffer, which in turn lead to calculate an average attachment efficiency of AgNPs in this medium of: α = 0.016 ± 0.003. The low value of α is typical of a weakly aggregating regime where less than 2% of collisions result in aggregation. Given this value of α, the AgNPs must overcome a 4.1 k_BT energy barrier (E_b) in a collision in order to stick to each other.

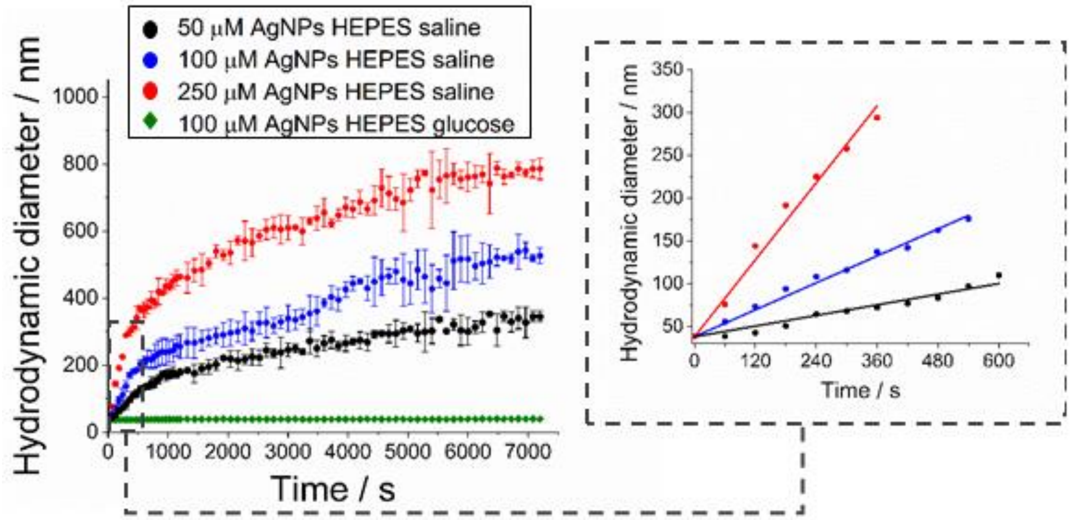

Figure 3.4. Aggregation kinetics of AgNPs. In HEPES saline buffer the hydrodynamic diameter increases with time and NP concentration. Data are presented as the mean (dots) ± SD (error bars) of three independent measurements. The inset plot to the right is the enlarged early time aggregation used for calculating the aggregation rate constant (ks).

3.3 The ionic strength of the medium modulates the effect of AgNPs on the membrane permeability

The optical properties of AgNPs occasionally lead to interferences in spectroscopy-based methods, especially in wavelengths near the LSPR peak. Although the maximum absorption peak of these AgNPs (417 nm) is far from the working wavelength of 5(6)-carboxyfluorescein (λ_{ex} 492nm; λ_{em} 514nm), the aggregates have different optical properties and might enhance or weaken the fluorescence signal of 5(6)-carboxyfluorescein (CF).

To assess whether the fluorescence emission of CF is affected by the presence of AgNPs in the sample, the fluorescence intensity of CF at various concentrations was compared with the intensity of the same samples after the addition of 100 µM AgNPs. No significant difference in fluorescence intensity of CF was observed before and after the addition of AgNPs (Fig. 3.5).

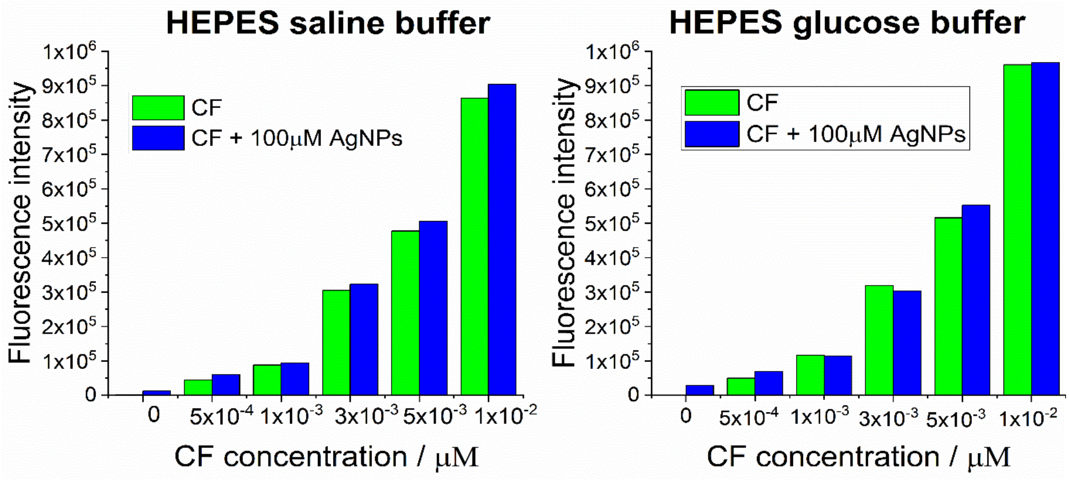

Figure 3.5. Comparison of fluorescence intensity signal of CF samples at different concentrations in the presence and absence of 100 µM AgNPs.

Therefore, the effect of AgNPs on the membrane permeability was initially investigated by quantifying the release of CF from DOPC LUVs. The CF-loaded LUVs (400 nm diameter) were suspended in isotonic HEPES saline buffer or HEPES glucose buffer reaching a final phospholipid concentration of 0.10 ± 0.02 µM. The LUV suspensions were then exposed to various concentrations of AgNPs (1 µM, 3 µM, 10 µM, 30 µM and 100 µM) and the fluorescence intensity at 514 nm was measured every 15 minutes during a total time of 90 minutes. In both media, concentrations of AgNPs below 10 µM do not induce any change in membrane permeability. In HEPES glucose buffer, the highest concentrations of AgNPs (30 µM and 100 µM) induce just a marginal dye release which does not increase significantly over time, remaining below the 10%. On the other hand, in physiological ionic strength buffer, the exposure of LUVs to 10 µM AgNPs produce a minimal dye leakage, but at higher AgNPs concentrations the dye release begins to be more extensive, reaching a maximum leakage of nearly 15% and 30% after 30 minutes of exposure to 30 µM and 100 µM AgNPs, respectively. At that moment, the dye release levels off and remains stable for the next 60 minutes (Fig. 3.6).

These results evidence a strong influence of the medium conditions on the interaction between AgNPs and zwitterionic phospholipid membranes and suggest that only weakly aggregated AgNPs are able to interact with the membrane. Given the dependence of AgNPs aggregation upon concentration and time when suspended in physiological ionic strength buffer, at the same incubation time, the highest concentrations of AgNPs lead to more and larger aggregates. These aggregates are however still in suspension and able to interact with the vesicles and permeate their membrane, whereas single NPs do not change the permeability of the membrane. At longer times, the aggregates gradually grow bigger until they reach a size where are expelled from the solution and no longer able to interact with the suspended vesicles.

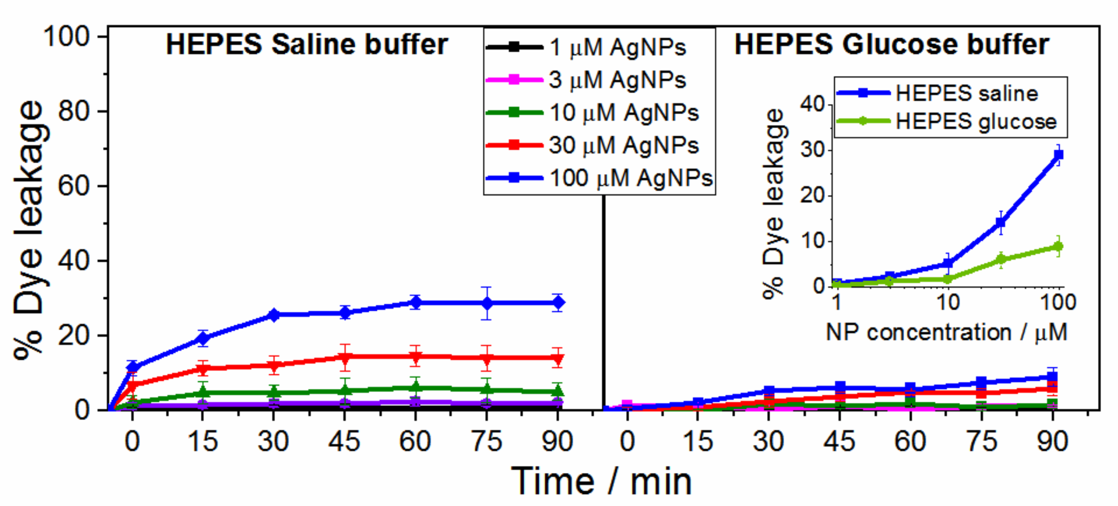

Figure 3.6. Leakage of CF from DOPC LUVs induced by AgNPs. In HEPES saline buffer AgNPs induce a higher dose-dependent leakage CF from LUVs than in HEPES glucose buffer. Inset shows the dye leakage percentage as a function of NP concentration after 90 minutes of incubation. Data are presented as the mean (dots) ± SD (error bars) of three independent measurements

The release of the dye from the lumen of the vesicles can be a consequence of different processes, from the opening of small membrane pores to the complete lysis of the liposomes. The mechanism behind the change in membrane permeability was identified using confocal microscopy to directly observe the influx of hydrophilic macromolecules (10 kDa cascade blue dextran) into GUVs after 20 ± 5 minutes of exposure to 50 µM, 100 µM and 250 µM AgNPs. Additionally, control experiments were carried out adding equivalent volumes of milli-Q water to the GUVs to test the effect of a potential osmotic shock.

Confocal microscopy observations firstly confirmed the regulating role of the medium composition on the AgNPs-membrane interactions. In low ionic strength buffer, the incubation of GUVs with AgNPs barely produces any change in their permeability to dextran 10 kDa. On the contrary, at physiological ionic strength, the exposure to AgNPs induces a dose-dependent increase in GUVs permeable to 10 kDa dextran. The GUVs permeable to fluorescent dextran do not experience dramatic morphological changes, such as vesicle burst or large membrane holes (Fig. 3.7 a). This rise in the proportion of permeable GUVs is statistically significant at the three concentrations of AgNPs tested, but it does not exceed 15% even at the highest AgNPs concentration (Fig. 3.7 b). The osmotic shock controls discard a contribution of changes in the osmotic pressure to the effects observed. The diffusion of large hydrophilic macromolecules, such as 10 kDa dextran, into the lumen of GUVs is an indicator of the formation of membrane pores, which can vary in size and lifetime [90, 166, 167].

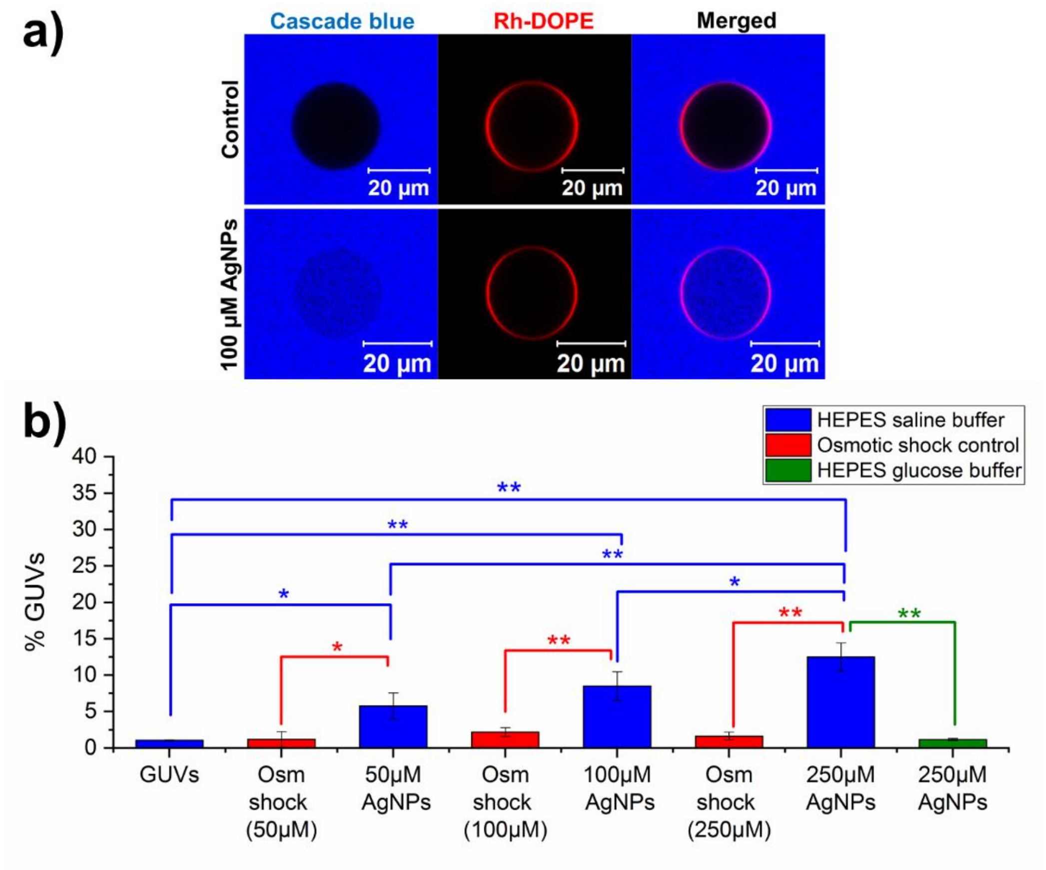

Figure 3.7. Effect of AgNPs in the permeability of DOPC GUVs. a) DOPC GUV labelled with Rh-DOPE before (upper panel) and GUV permeable to 10 KDa Cascade blue dextran after exposure to 100 µM AgNPs (lower panel). **b)** The proportion of GUVs permeable to 10 kDa dextran upon exposure to AgNPs in physiological ionic strength medium (blue bars), low ionic strength medium (green bar) and osmotic shock controls (red bars). Data obtained from analysing 700 ± 75 GUVs (from 5 different samples) for each condition. Bar plot indicates mean ±SD. Statistical significance was tested using a one-way ANOVA with Bonferroni multiple comparisons test ($^{*}p \leq 0.05$, $^{**}p \leq 0.01$).

To get further information about the characteristics of the pores, the permeability of GUVs to 10 kDa dextran was compared with their permeability to the much smaller dye CF (0.376 kDa). Using confocal microscopy, we analysed the specific level of leakage in every GUV observed (Fig. 3.8 a). The proportion of GUVs permeable to CF molecules after exposure to 100 μM AgNPs is nearly three times higher than to bigger dextran molecules (Fig. 3.8 b). This difference is a consequence of the nanoscale size of the pores which allow easier and faster transmembrane diffusion of small molecules and limit the passage of big macromolecules across the membrane. Moreover, the distribution of permeable GUVs according to their level of leakage shows that nearly 40% of the permeable GUVs were fully filled (> 80% dye leakage) with CF after exposure to 100 µM AgNPs. In contrast, less than the 20% of GUVs permeable to 10 kDa dextran showed more than 60% of leakage, of which just a marginal proportion was fully leaked (Fig. 3.8 c). The fact that most of the GUVs observed were just partially filled with the fluorescence extravesicular medium indicates that the nanosized pores formed are transient and the membrane can recover its integrity and block the diffusion of hydrophilic macromolecules.

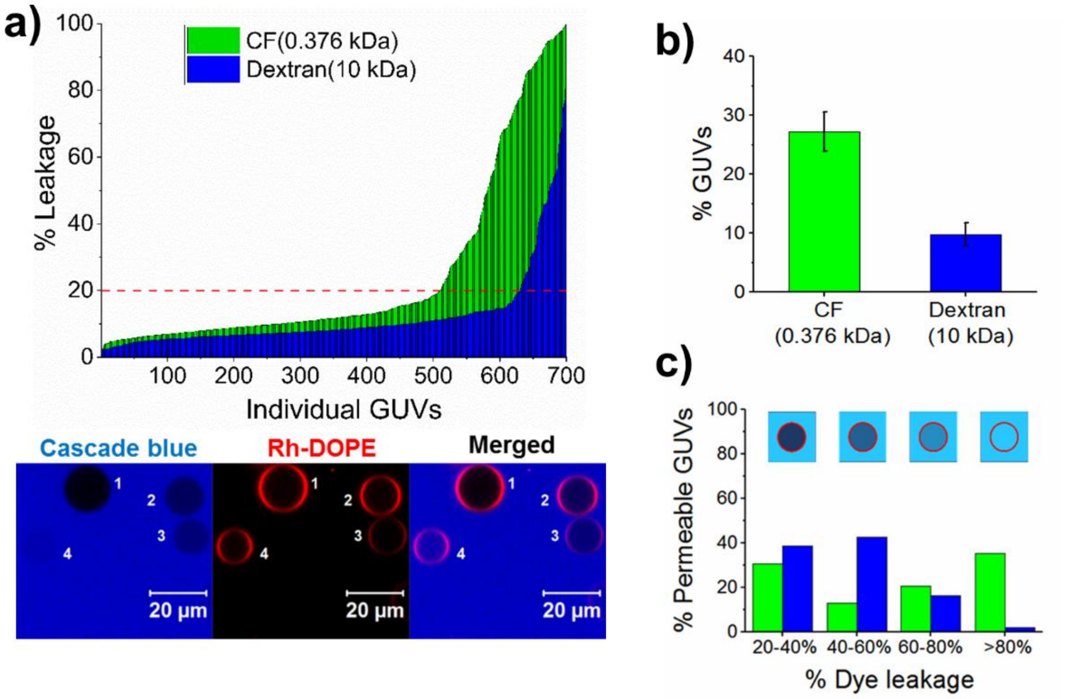

Figure 3.8. Influx of CF and 10 kDa dextran into DOPC GUVs after exposure to 100 µM AgNPs. a) Percentage of CF and dextran leaked into the lumen of each GUV analysed. The red dashed line indicates the level (20%) above which GUVs are considered permeable. Confocal micrograph shows GUVs with different degrees of permeability to 10 kDa cascade blue dextran: unleaked GUV (1), partially leaked GUVs (2 and 3) and fully leaked GUV (4). b) Proportion of GUVs permeable to CF and 10 kDa dextran (mean ± SD of 5 different samples). c) Distribution of permeable GUVs according to their level of leakage (cartoon represents GUVs with different levels of dye leakage). Data obtained from the analysis of 700 GUVs (from 5 different samples) for each different condition.

In addition to aggregation, the conditions of the medium can also induce dissolution of AgNPs that leads to the release of Ag^+ ions which might also induce changes in the physicochemical properties of lipid membranes. To assess whether the membrane perturbations observed in physiological ionic strength buffer are produced by the release of Ag^+ or by the AgNPs themselves, control experiments were performed adding $AgNO_3$ to the GUVs at concentrations equivalent to the AgNPs. The results summarised in figure 3.9 indicate that Ag^+ ions do not induce changes in membrane permeability and therefore the leakage observed in the previous experiments is exclusively induced by weakly aggregated AgNPs.

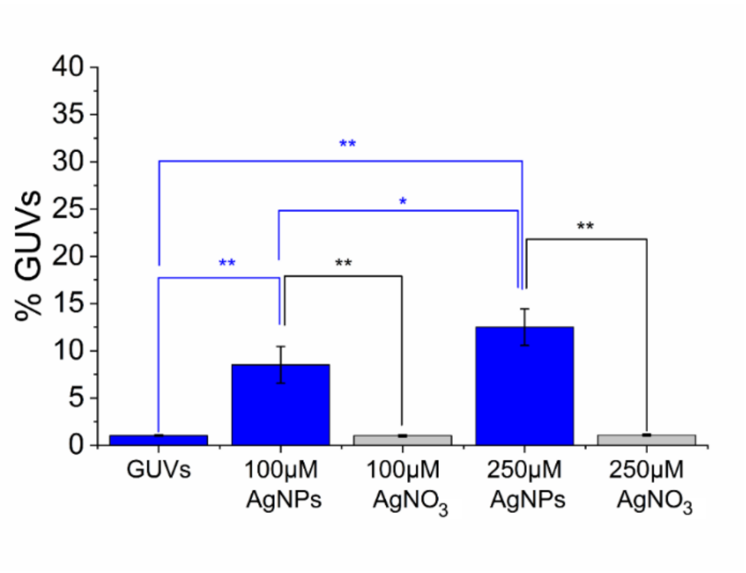

Figure 3.9. Effect of AgNPs and $AgNO_3$ in the permeability of DOPC GUVs to 10 kDa dextran. The presence of Ag^+ ions does not induce changes in the permeability of GUVs. Data obtained from the analysis of 700 ± 50 GUVs for each different condition. Data obtained from analysing 700 ± 75 GUVs (from 5 different samples) for each condition. Bar plot indicates mean ±SD. The statistical significance was tested using a one-way ANOVA with Bonferroni multiple comparisons test ($^*p \leq 0.05$, $^{**}p \leq 0.01$).

3.4 AgNPs induce formation of intraluminal vesicles in physiological ionic strength conditions

Confocal microscopy also revealed that AgNPs can form membrane invaginations and intraluminal vesicles (ILVs) in a small proportion of the GUVs when suspended in high ionic strength buffer (Fig. 3.10). These ILVs are small vesicles filled with extravesicular medium within the lumen of the GUVs. The formation of ILVs is extremely fast, however potential intermediate states in the form of pearling tubes were observed. This phenomenon has been previously reported by Yu and Granick, who observed that aliphatic amine NPs encapsulated within DOPC GUVs adsorb onto the membrane and induce the protrusion of large tubes followed by pearling events [107]. Similarly, Montis *et al*. observed that cationic gold nanorods (AuNR) produce tubular protrusions that breakup into pearls in POPC GUVs [168].

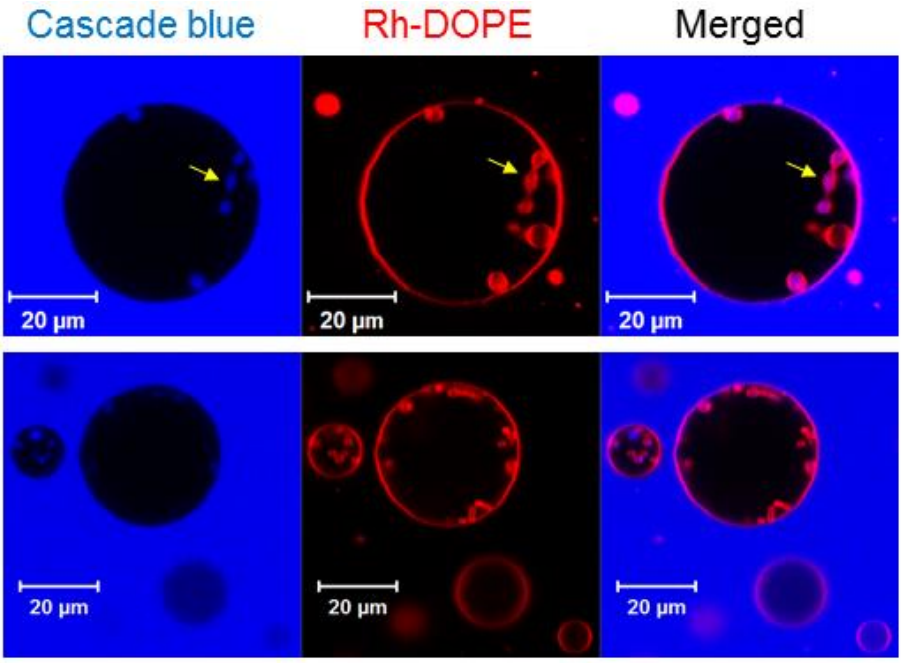

Figure 3.10. DOPC GUVs with intraluminal vesicles (ILVs) and pearling tubular structures (yellow arrows) filled with bulk solution (10 kDa dextran labelled with cascade blue) after exposure to AgNPs.

The experimental procedure and data analysis used for these experiments were the same employed for the estimation of dye leakage into GUVs. ILVs were not seen in low ionic strength buffer, hence this effect is also influenced by the composition of the medium. At physiological ionic strength, the proportion of GUVs with ILVs observed is low but statistically significant with respect to the GUVs before exposure to AgNPs and the osmotic shock controls. However, the ILVs formation does not vary significantly with the concentration of AgNPs, representing in all cases between the 5% and 6% of GUVs observed (Fig. 3.11). The size and the number of ILVs per GUV observed are highly variable, but this variability is also independent from the concentration of AgNPs.

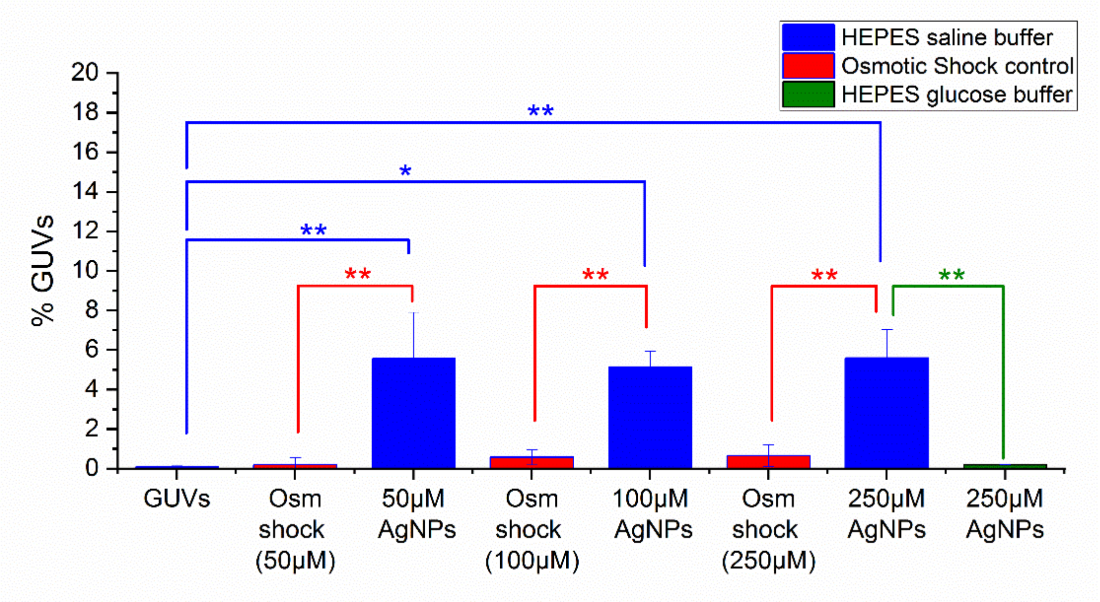

Figure 3.11. Proportion of GUVs with ILVs after exposure to AgNPs. In HEPES saline buffer, the proportion of GUVs with ILVs is low and similar at the three concentrations of AgNPs explored. Insignificant proportion of GUVs with ILVs was observed in the Osmotic shock controls and HEPES glucose buffer. Data obtained from analysing 700 ± 75 GUVs (from 5 different samples) for each condition. Bar plot indicates mean ±SD. The statistical significance was tested using a one-way ANOVA with Bonferroni multiple comparisons test (*$p \leq 0.05$, **$p \leq 0.01$).

These results suggest that the formation of ILVs is a stochastic event that has already reached its maximal extend at 50 μM AgNPs. We propose that this effect could be related to the aggregation of AgNPs in physiological conditions. The aggregation of NPs is a stochastic process that may lead to a large number of aggregates polydisperse in size and shape. Molecular dynamics studies have shown that the configuration NPs adopt to form clusters or aggregates modifies their ability to bend lipid membranes [169, 170]. According to these simulations, the formation of ILVs could be a result of the assembly of AgNPs aggregates on the GUV membrane. Nonetheless, only aggregates with a particular shape, size and orientation would be able to efficiently bend the membrane to induce tubular membrane invaginations and form ILVs.

ILVs are not observed after exposure to $AgNO_3$, thus the membrane remodeling processes are not induced by the release of Ag+ ions near the membrane but only by slightly aggregated AgNPs (Fig 3.12).

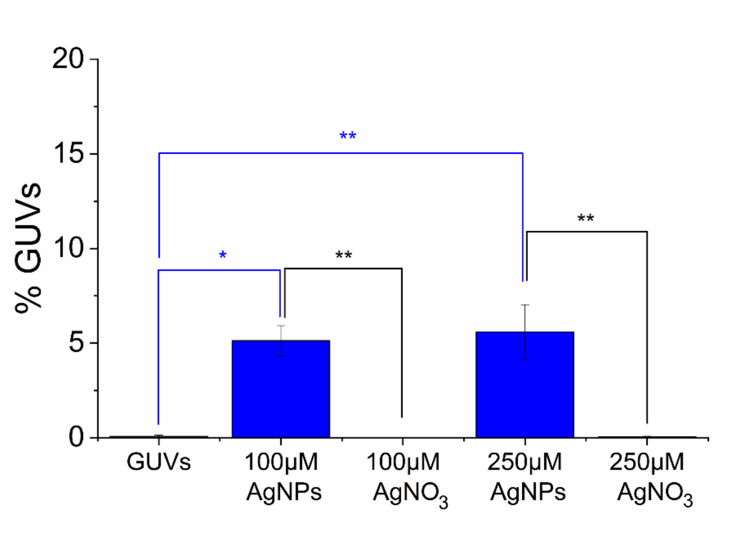

Figure 3.12. Proportion of GUVs with ILVs after exposure to AgNPs and $AgNO_3$. Ag^+ ions do not induce ILVs formation. Data obtained from analysing 700 ± 75 GUVs (from 5 different samples) for each condition. Bar plot indicates mean ±SD. Statistical significance tested using a one-way ANOVA with Bonferroni multiple comparisons test ($*p \leq 0.05$, $**p \leq 0.01$).

3.5 AgNPs slightly decrease the membrane fluidity in physiological ionic strength conditions.

The impact of AgNPs on the lipid lateral diffusion through the membrane was studied using FRAP. The experiments were conducted before and after incubation of DOPC GUVs with 100 µM AgNPs in both physiological and low ionic strength buffers. An example of the recovery curves obtained is presented in Figure 3.13, showing that full fluorescence recovery (around 90%) is achieved in all cases.

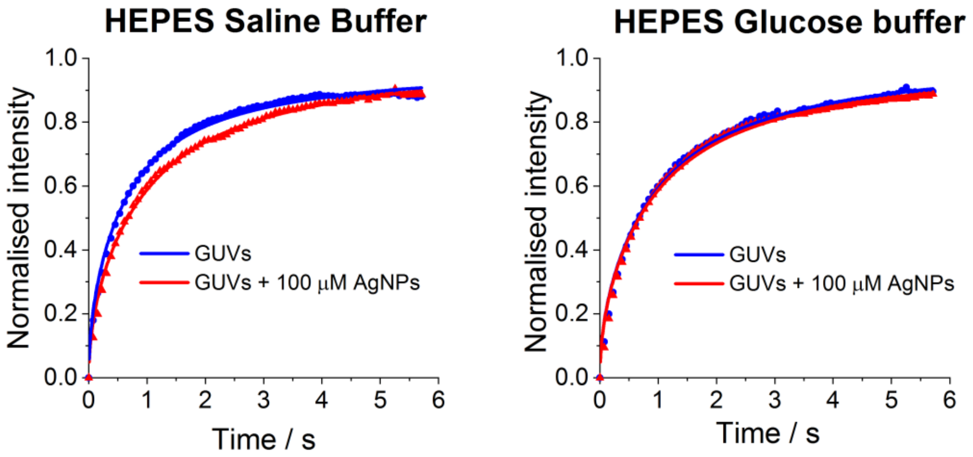

Figure 3.13. FRAP recovery curves of GUVs before and after exposure to 100 µM AgNPs in HEPES saline buffer and HEPES glucose buffer.

Figure 3.14 shows the distribution of GUVs by their diffusion coefficient. At physiological ionic strength, the diffusion coefficient of the DOPC membrane after exposure to 100 µM AgNPs drops by an average of 16%, from 3.02 ± 0.34 µm s^{-1} to 2.54 ± 0.31 µm s^{-1}, whereas the exposure to 100 µM $AgNO_3$ do not modify the lipid lateral mobility (2.99 ± 0.27 µm s^{-1}). This subtle impact of AgNPs in the fluidity of the membrane could be originated by generic adsorption interactions of AgNPs on the membrane. In striking contrast to the low probability effects of poration and ILV formation seen in previous experiments, the decrease in membrane fluidity occurs across all GUVs observed, hence the change in the membrane fluidity is not the initial mechanism that gives rise to the membrane perturbations seen in previous sections.

In low ionic strength buffer, AgNPs barely modify the lipid lateral mobility. Interestingly, the mean diffusion coefficient of DOPC in these conditions (2.54 ± 0.31 µm s^{-1}) is lower than in HEPES saline buffer. Previous fluorescence correlation spectroscopy (FCS) studies have reported that sugars reduce the lipid lateral diffusion in a concentration-dependent manner *[171]*. Hence, we attribute the lower membrane fluidity in low ionic strength buffer to the high concentration of glucose in the medium.

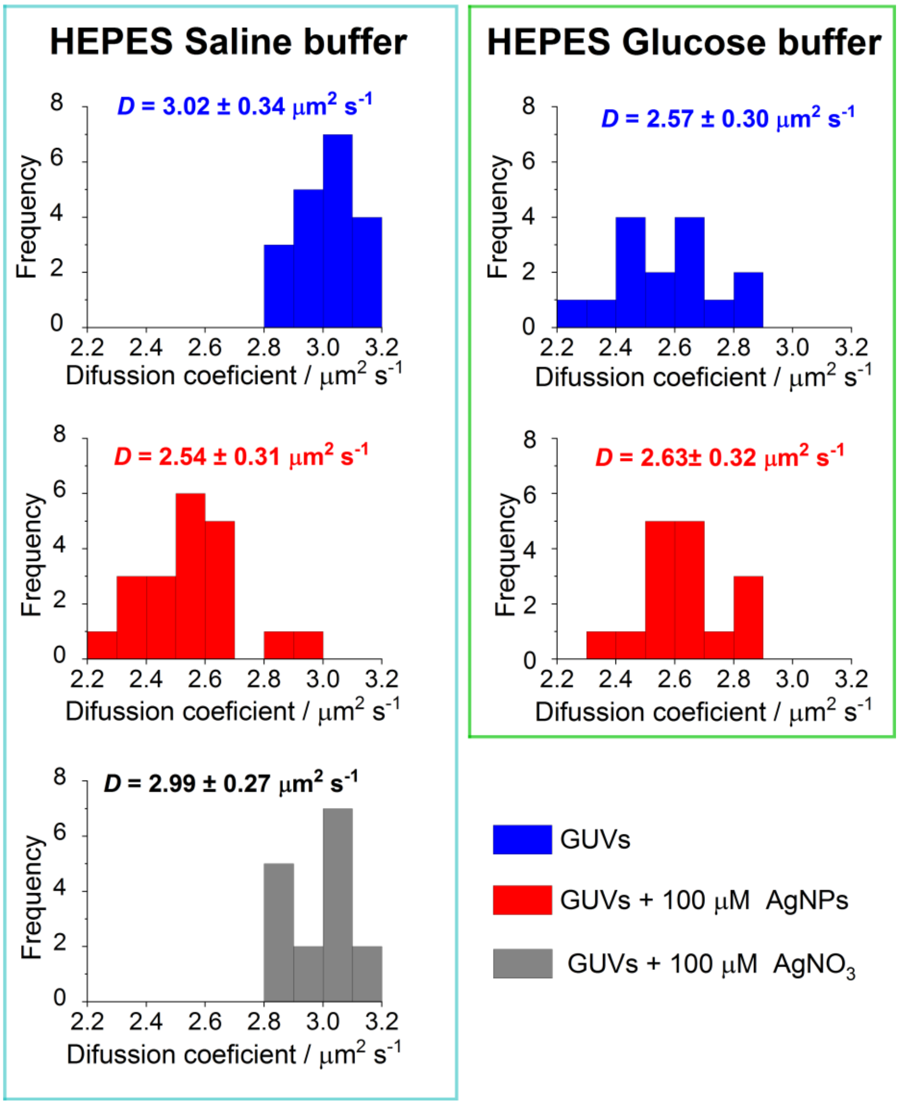

Figure 3.14. Distribution of diffusion coefficients obtained from FRAP recovery curves. D values indicate the mean diffusion coefficient calculated in each condition. In HEPES saline buffer, AgNPs induce a slight but statistically significant decrease in lipid lateral diffusion. The exposure to $AgNO_3$ (bottom left panel) does not modify the lipid lateral diffusion. In low ionic strength medium, the membrane fluidity of DOPC GUVs is lower than in HEPES saline and does not change after incubation with AgNPs.

3.6 AgNPs affect the mechanical properties of a sub-population of GUVs in physiological ionic strength buffer.

The ability of AgNPs to adsorb to the membrane and occasionally produce membrane remodeling events suggests that these NPs might also modify the mechanical properties of the membrane. The membrane tension (σ) and bending modulus (κ_b) of GUVs were quantified by analysing the thermal fluctuations of the membrane using flicker spectroscopy. This technique has a limitation in the spatiotemporal resolution which does not allow to calculate accurately the mean amplitude of the membrane fluctuations ($\langle|h(q)|^2\rangle$) of high-tension GUVs within a wavenumber (q) range broad enough [172]. To circumvent this issue, the GUVs were incubated overnight in hyperosmotic buffer to reduce the mean membrane tension. This osmotic relaxation increases the amplitude of the membrane thermal fluctuations making the analysis of the flicker spectrum more reliable. Additionally, the osmolarity of the AgNPs suspension was balanced with sucrose until isotonic to the experimental medium to prevent changes in the osmolarity of the medium during the experiment.

As expected, in low ionic strength buffer AgNPs do not induce any change in either the tension or the bending rigidity of the membrane. However, in physiological ionic strength conditions, the addition of 100 µM AgNPs to the osmotically relaxed GUVs induces subtle changes in the mechanical properties of the membrane and widens the distribution of both the tension and the bending rigidity values. The exposure of GUVs to AgNPs produces a rise in the mean membrane tension which, in spite of not being a drastic change, is statistically significant ($p < 0.01$) (Fig. 3.15 a). This increase in membrane tension is accompanied by a small decrease in bending rigidity, nevertheless, the latter does not show statistical significance (Fig. 3.15 b). Interestingly, these changes in membrane mechanics are not produced by slight shifts in every GUV in the sample but arise from significant changes in membrane tension and bending rigidity of a sub-population of the GUVs analysed (Figure 3.15 c).

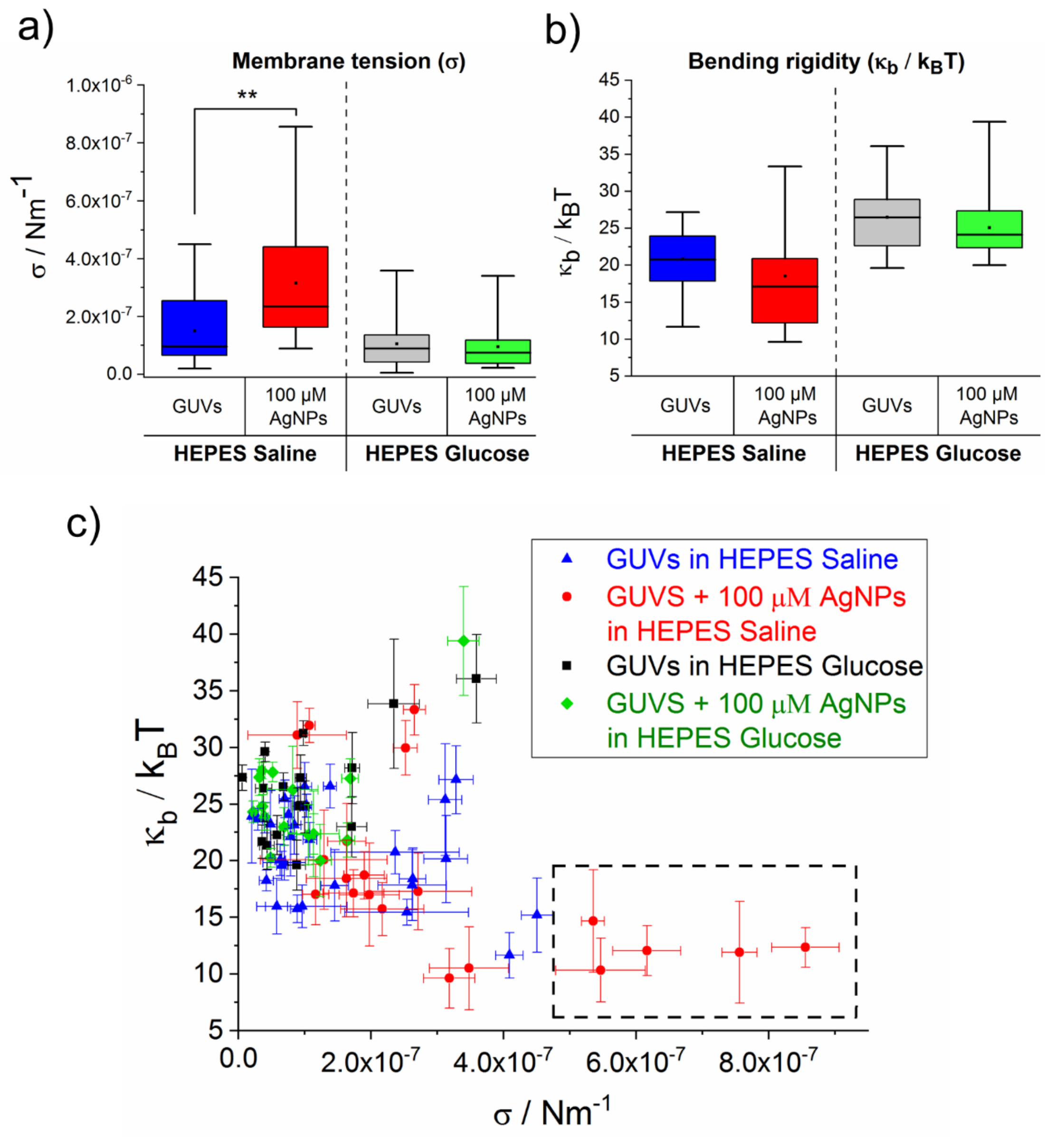

Figure 3.15. Mechanical properties of osmotically relaxed GUVs in HEPES saline and HEPES glucose buffer before and after exposure to 100 µM AgNPs. a) In HEPES glucose buffer, the membrane tension (σ) does not vary after exposure to 100 µM AgNPs whereas in HEPES saline a statistically significant change in membrane tension is observed ($^{**}p \leq 0.01$, ANOVA with Bonferroni multiple comparisons test) b) In HEPES saline buffer, AgNPs induce a broader distribution and a slight shift in bending rigidity (κ_b). In HEPES glucose buffer, the bending rigidity barely changes. c) The plot of bending rigidity against membrane tension shows that most of the GUVs analysed have similar membrane tension (>5x10-7 Nm-1) and bending rigidity (15–35 k_BT). However, after exposure to AgNPs, a sub-population of GUVs in HEPES saline (dashed box) experiences a significant increase in membrane tension (<5x10-7 Nm-1) and a small decrease in membrane bending rigidity (10-15 k_BT).

These results could be directly linked to the formation of membrane pores, invaginations and ILVs described in previous sections, which also occur in a small proportion of the GUVs population. A recent study has shown that the formation of ILVs by the endosomal sorting complex required for transport (ESCRT) produces a significant increase in membrane tension of GUVs originated by the removal of excess membrane surface area [173]. Furthermore, the increase of the membrane tension is known to favour the membrane poration [174-176], and therefore could favour the membrane permeation effect induced by AgNPs.

Finally, we observed that the membrane tension and bending rigidity of GUVs do not vary after exposure to 100 μM $AgNO_3$ (Fig. 3.16). Therefore, we can confirm that the changes in the mechanical properties of the membrane at physiological ionic strength conditions are not induced by the presence of Ag^+ but by the interaction of weakly aggregating AgNPs with the membrane.

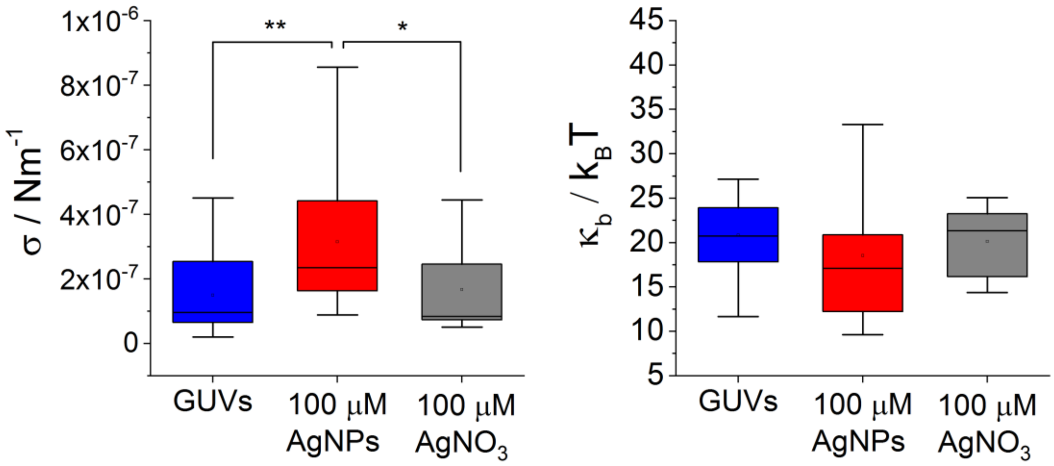

Figure 3.16. Comparison between the effect of AgNPs and $AgNO_3$ in the mechanical properties of DOPC GUVs. Exposure to $AgNO_3$ does not change the mechanical properties of GUVs. The membrane tension of GUVs after exposure to 100 μM AgNPs is significantly higher than the membrane tension of pre-treated GUVs ($^{**}p \leq 0.01$) and GUVs treated with 100 μM $AgNO_3$ ($^{*}p \leq 0.05$). The statistical significance was tested using a one-way ANOVA with Bonferroni multiple comparisons test.

3.7 Discussion

The results presented in this chapter firstly evidence a significant impact of the medium conditions on the surface charge and colloidal stability of AgNPs. The behaviour of nanomaterials in biological systems is governed by their physicochemical properties, nonetheless, these properties are susceptible to change once the NPs enter biological media. The citrate coating of AgNPs gives them a negative surface charge and stabilises the colloidal suspension in low ionic strength media through electrostatic double-layer repulsions. However, the high concentration of ions in physiological conditions modifies the ζ potential of AgNPs and promotes their aggregation. In this medium, Na^+ ions screen the negative surface charge and reduce the inter-particle repulsive force to a thermally accessible energy barrier of 4.1 k_BT, thereby facilitating the concentration-dependent aggregation of AgNPs [163, 177]. The analysis of the aggregation kinetics of AgNPs indicates a weak aggregation regime with 1.6% of AgNPs collisions resulting in an aggregation event and where most of the aggregates are still in suspension at the experimental incubation times.

Several previous investigations have focused on the effect of the attachment of proteins to the NP surface (protein corona) on the biological activities of NPs [178-184], however, comparatively less attention has been paid to other properties of the medium, such as pH or ionic strength, which can also alter the physicochemical properties of NPs and their biointeractions. Our data show that in physiological ionic strength conditions, AgNPs induce subtle but important effects on the physicochemical properties of the membrane, whereas in low ionic strength buffer the membrane maintains its integrity after exposure to AgNPs. Therefore, the buffer conditions modify the interactions of AgNPs acting at the nanobio interface and hence modulate their interaction with membranes. Control experiments also show that any membrane perturbation observed is not caused by the dissolution of Ag^+ ions from the AgNPs.

At pH 7.4, the DOPC membrane carries a slight negative charge [185]. Thus, in low ionic strength environments, electrostatic repulsion between AgNPs and the DOPC bilayer may dominate over other attractive forces, preventing significant interaction. However, when the ionic strength increases, the screening of the surface charge of AgNPs decreases electrostatic repulsive forces between the NPs and the membrane, increasing the likelihood of more significant interaction. In addition, the loss of colloidal stability and weak aggregation behaviour of AgNPs makes them less soluble and more surface-active, further increasing membrane interactions. This modulatory effect of the ionic strength of the medium on the AgNPs-membrane interaction has been reported earlier by Wang *et al*, who, using quartz crystal microbalance with dissipation (QCM-D), found that the deposition rates of AgNPs on DOPC supported lipid bilayers (SLBs) increases when the concentration of salt in the medium rises [186]. A similar electrostatically mediated interaction was reported by Li and Malmstadt for cationic polystyrene NPs (PNPs) which interact weakly with the membrane as the ionic strength of the medium increases [90].

In physiological conditions, we observe that AgNPs induce changes in membrane permeability and can form membrane invaginations such as ILVs. Several studies have shown the ability of eukaryotic, bacterial and virus proteins as well as antibacterial peptides and NPs to change the morphology of the membrane and form invaginations and ILVs without the need of cellular endocytic mechanisms or external sources of energy [107, 142, 168, 187-190]. Generally, the interaction of single proteins or particles is not strong enough to induce these large deformations of the membrane and thus many molecules or particles must cooperate to bend the membrane [169, 188]. For instance, the clustering of Gb3-binding B subunit of the bacterial Shiga toxin (STxB) can induce membrane invagination in artificial model membranes, however, these invaginations are not observed when the clustering is inhibited [187]. In a recent study, Contini *et al* showed a cooperative behaviour of 10 nm AuNPs adsorbed onto DOPC and POPC LUVs [80]. These AuNPs can form linear clusters perpendicular to the lipid bilayer which induce tubular deformations of the membrane towards the lumen of the liposome. Moreover, in the same study they reported that the presence of NaCl in the medium increases considerably the leakage of calcein from LUVs produced by 10 nm AuNPs, however, they do not show whether the aggregation tendency of the NPs increases or not in saline buffer [80]. From our observations, we propose that single AgNPs are not able to bend the membrane, nonetheless the formation of NP clusters of a particular size, shape and orientation relative to the lipid bilayer will increase their ability to deform the membrane and produce tubular invaginations and ILVs.

Membrane remodeling processes, such as invaginations and ILVs, remove excess membrane, which, along with the pressure generated by the AgNPs that adhere onto the membrane, increases the membrane tension and can lead to membrane poration [90]. The increase in membrane tension is also known to be the driving force for the opening of pores which will in turn produce membrane permeation, causing the membrane translocation of impermeable dextran probes and the relaxation of the membrane tension. The lifetime of membrane pores is usually short because as the membrane tension relaxes, the line tension at the pore edge drives the closure of the pore [174, 191]. The size of the pore defines the minimum size of the molecules that can diffuse across the membrane. The higher permeability to carboxyfluorescein (0.37 kDa) than to dextran (10 kDa) observed in our experiments represents the presence of nanoscale pores in the membrane as a result of the AgNPs. Furthermore, the fact that most of the GUVs observed were not fully leaked indicates these pores are transient.

In general, toxicology studies focus on terminal effects where the analytes induce severe damages in the plasma membrane or other cellular components that lead to cell death. However, other subtle effects in the physicochemical properties of the membrane can also have biological importance. Cells are able to sense mechanical stimuli and convert them into biochemical signals to adapt to their microenvironment [192]. Mechanical forces can modify the elastic and dynamical properties of the membrane, which in turn can lead to conformational changes in membrane proteins, such as ion channels [193], G-protein coupled receptors (GPCRs) [194-196] and integrins [197]. These proteins trigger metabolic cascades that induce different cellular responses such as cell migration, differentiation, and proliferation [198, 199]. For instance, in endothelial cells the plasma membrane senses haemodynamical forces generated by the blood and activates downstream signalling pathways related to inflammatory responses, regulation of blood pressure or coagulation processes [200]. Another important example of mechanical sensing and transduction is the Hippo pathway, which controls organ growth by regulating cell proliferation [201]. The mechanical stress applied to the plasma membrane modulates the actin cytoskeleton and activates GPCRs. This begins a complex signal pathway that eventually activates the proto-oncogenes proteins YAP/TAZ which translocate from the cytoplasm to the nucleus and induce cell proliferation [202]. Prolonged mechanical stress can lead to an overexpression of YAP/TAZ which promotes unregulated cell proliferation and eventually oncogenesis [201, 202]. Thus, even small changes in the mechanical and dynamical properties of the membrane, such as the ones produced by AgNPs, can induce multiple cellular responses which lead to a myriad of processes encompassing from inflammatory responses to the development of serious diseases.

3.8 Conclusions

To summarise, here we show the significant impact that the ionic strength of the medium has on the physicochemical properties of AgNPs and their interactions with biomembranes (Fig. 3.17). From our results, we propose that monodisperse AgNPs are non-interacting and could be safely exploited as imaging contrast agents for diagnosis and cancer theranostics. However, the aggregation of AgNPs would lead to two different possibilities: i) large aggregates precipitate and are expelled from the solution and do not interact with the membrane. These large aggregates are expected to be highly toxic because they are more difficult to be transported in the blood and can be accumulated in certain organs before reaching their specific targets and produce severe damage [203]. ii) smaller aggregates become more membrane-active than monodisperse AgNPs increasing the tension of the membrane and opening pores. The formation of transient pores offers opportunities in transfection technologies but at the same time raises nanotoxicology concerns.

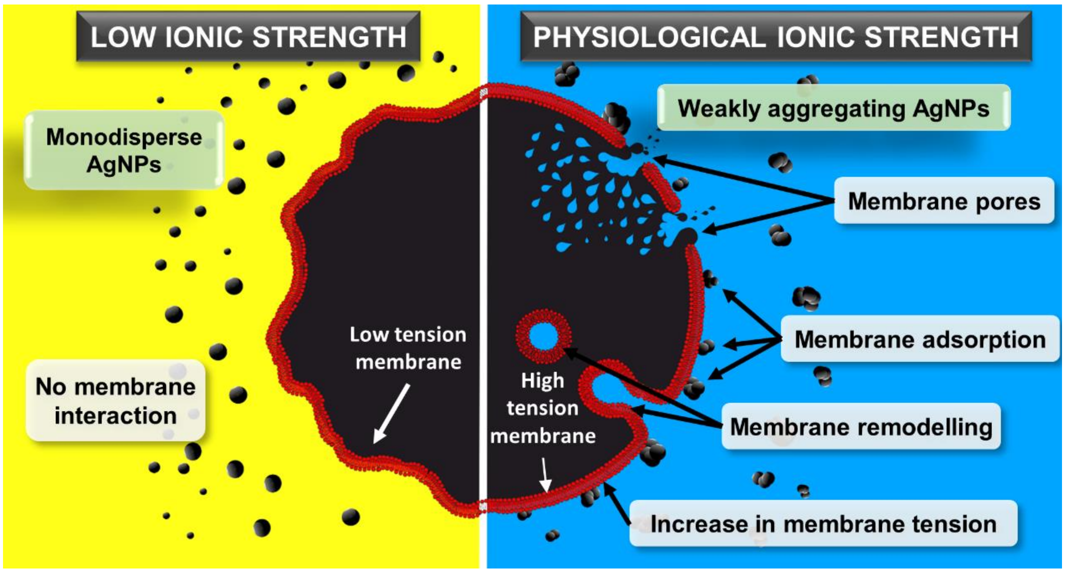

Figure 3.17. Summary of AgNPs behaviour in low and physiological ionic strength media and their effects of the biophysical properties of lipid membranes

In the next chapter, we will continue exploring the influence of the medium conditions on the interaction between NPs and lipid membranes, particularly the effect of a simplified protein corona formed around the NPs. For that study we will use silica nanoparticles, which are known to strongly interact with biomimetic model membranes, to facilitate the detection of changes in the interaction mechanisms induced by the proteins adsorbed to the NP surface.

Chapter 4:

Impact of serum albumin corona on the interaction between silica nanoparticles and lipid membranes

4.1 Introduction

Silica nanoparticles (SiO_2 NPs) are highly bioactive nanomaterials. The interaction between SiO_2 NPs and lipid membranes has been reported to be dependent on the NP size. Cryo-electron microscopy and tomography images have shown that SiO_2 NPs with a diameter larger than 30 nm are completely wrapped by DOPC membranes and internalised into large unilamellar vesicles LUVs, while SiO_2 NPs of 15 nm remain attached to the LUV surface but are not engulfed by the membrane [77]. This size-controlled interaction has also been seen in GUVs imaged with fluorescence confocal microscopy [78, 79].

While the strong interaction of SiO_2 NPs might result in highly toxic consequences, it also provides an excellent opportunity to develop novel biomedical devices. The use of NPs for biomedical purposes implies their inoculation into the organism where they encounter the blood serum and other biological fluids. As mentioned in **Section 1.2.3**, under such conditions, biomolecules (lipids, nucleic acids, proteins, etc,) adsorb onto the NP surface creating a biomolecular corona [92, 96]. Proteins are considered the most relevant component of these coronas to the point that most studies consider coronas composed exclusively of these biomolecules. The protein corona can alter and even completely screen the intrinsic surface properties of the bare NPs and hence confer a new biological identity to the nanoparticles which determines their biointeractions [71, 92, 96, 98, 204].

In this chapter, we investigate the influence of a model bovine serum albumin corona on the fundamental interaction mechanisms between SiO2 NPs of two different sizes (18 nm and 30 nm) with DOPC membranes. First, we characterise the SiO2 NPs with and without corona using TEM, DLS and DELSA. Then, we evaluate the effect of those NPs in the permeability of LUVs and finally we use confocal microscopy to identify morphological transitions experienced by GUVs after being exposed to the SiO2 NPs with and without protein corona as well as to quantify changes in lipid packing from Laurdan spectral imaging data.

4.2 Characterisation of SiO_2 NPs with and without a serum albumin corona

In this work, we employed two types of commercial amorphous SiO_2 NPs, LUDOX SM-30 and LUDOX TM-50. TEM images show that both types of SiO_2 NPs are roughly spherical but they differ in their size: the first type has an average diameter of nearly 18 nm (17.8 ± 4.8 nm) and the mean diameter of the second class is around 30 nm (30.8 ± 3.9 nm) (Fig. 4.1a-b). A similar size distribution is observed by DLS, although the hydrodynamic diameters measured by DLS are larger (24.9 ± 0.9 nm for LUDOX SM-30 and 43.0 ± 1.4 nm for LUDOX TM-50) than the actual diameters observed in the TEM images. For clarity purposes, in this chapter LUDOX SM-30 NPs and LUDOX TM-50 NPs will be referred to as SNPs-18 and SNPs-30, respectively. DLS also show that both kinds of SiO_2 NPs are colloidally stable in the experimental HEPES saline buffer (20 mM HEPES, 150 mM NaCl, pH 7.4) for at least 48 h (Fig. 4.2a-b). The SiO_2 NPs are negatively charged as determined by DELSA. The measured ζ potential indicates that SNPs-30 are slightly more negatively charged (-18.2 ± 1.8 mV) than SNPs-18 (-15.8 ± 0.4 mV) (Fig. 4.2c).

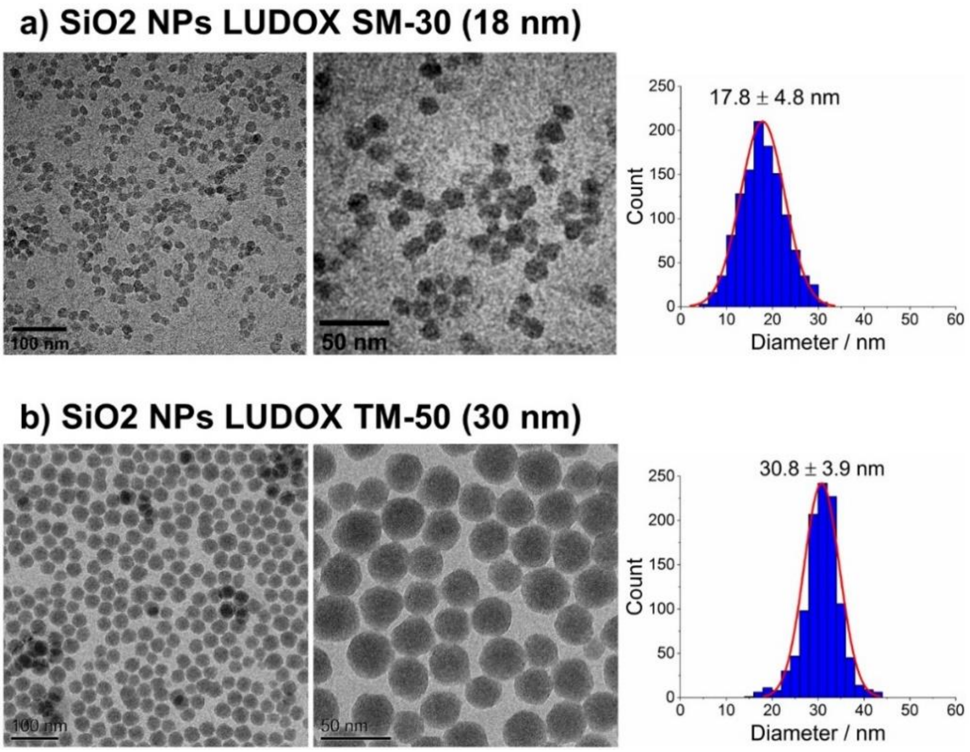
a) SiO2 NPs LUDOX SM-30 (18 nm)

b) SiO2 NPs LUDOX TM-50 (30 nm)

Figure 4.1 Transmission electron microscopy images of SiO_2 NPs and analysis of their size distribution. a) SiO_2 NPs LUDOX SM-30 have an average diameter of 17.8 ± 4.8 nm. b) SiO_2 NPs LUDOX TM-50 have an average diameter of 30.8 ± 3.9 nm. (TEM images were collected by Dr Nicole Hondow, School of Chemical and Process Engineering, University of Leeds)

We next evaluated the influence of the adsorption of serum albumin to the surface of SiO_2 NPs in their size, surface charge and colloidal stability. Albumin is the most abundant protein in blood serum, representing more than 50% of the total serum proteins, and has been reported to be a major component of protein coronas formed around SiO_2 NPs when suspended in biological media [93, 94]. Bovine serum albumin (BSA) was employed to recreate a simplified version of a protein corona formed around SiO_2 NPs. The concentration of BSA (100 mg/ml) used to prepare the protein-coated SiO_2 NPs solutions is comparable to the total concentration of proteins in blood serum. We prepared initial stocks of 10 mg/ml SiO_2 NPs suspended in a solution of 100 mg/ml BSA in HEPES saline buffer. The stock solutions were incubated at 4 ºC for 24 hours (unless otherwise specified) and then diluted into experimental samples at the desired concentrations. From this point, the SiO_2 NPs with the BSA corona will be denoted as SiO_2NPs@BSA, SNPs-18@BSA or SNPs-30@BSA.

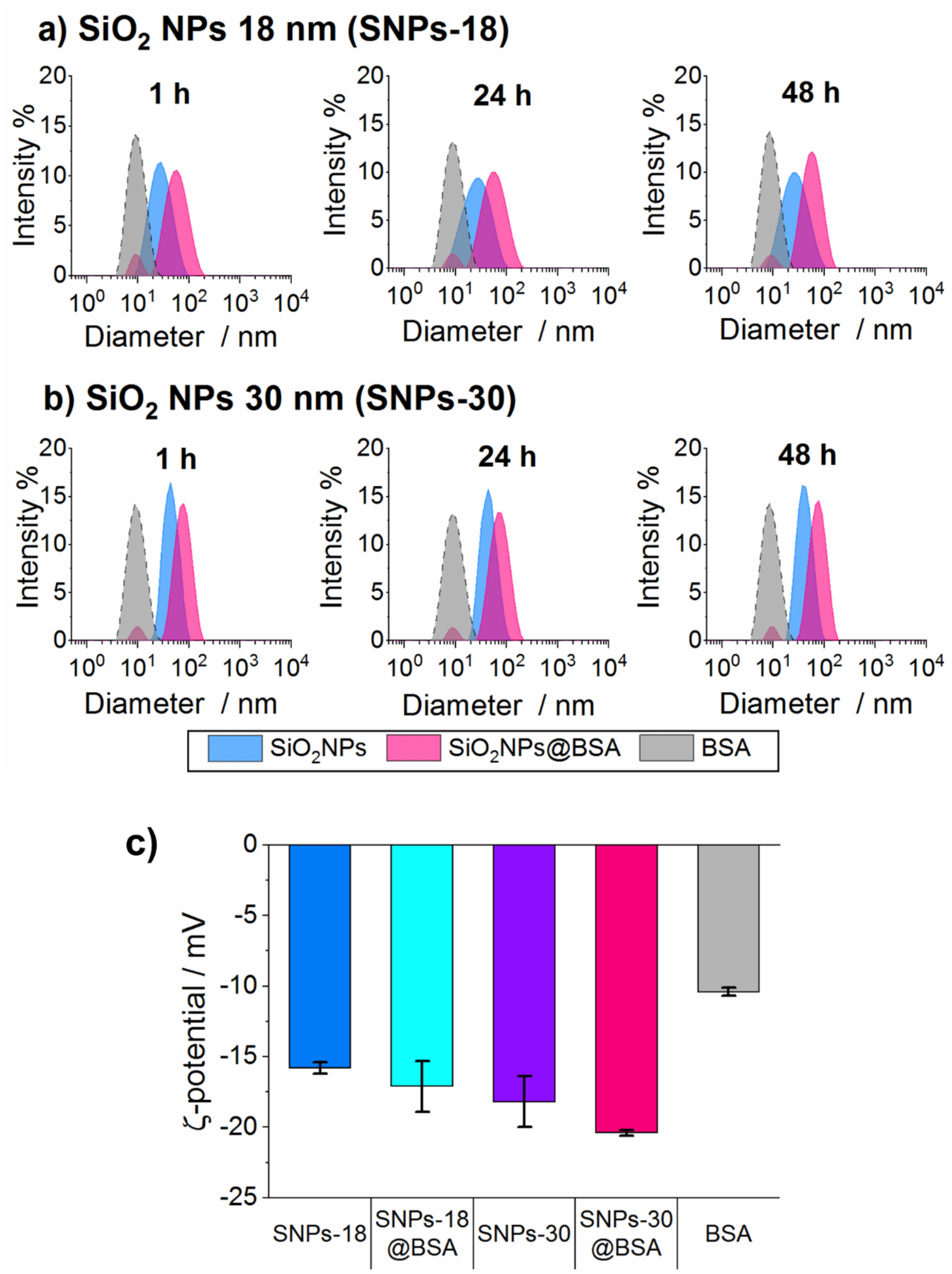

Figure 4.2. Hydrodynamic diameter and ζ potential of SiO$_2$ NPs with and without BSA corona. a) Hydrodynamic diameter of bare SNPs-18 (blue), SNPs-18@BSA (magenta) and free BSA control (grey) after 1 h, 24 h and 48 h of incubation in the buffer. b) Hydrodynamic diameter of bare SNPs-30 (blue), SNPs-30@BSA (magenta) and free BSA control (grey) after 1 h, 24 h and 48 h of incubation in the buffer. BSA molecules adhere to both types of NPs producing an increase in their hydrodynamic diameter. The small peak in the SiO$_2$NPs@BSA samples corresponds to free BSA molecules that are not attached to the NP surface. c) ζ potential of SiO$_2$ NPs with and without BSA corona as well as free BSA control. The ζ potential of SNPs-30 is slightly more negative than SNPs-18. The BSA corona induces mild changes in the ζ potential of both types of SiO$_2$ NPs which becomes more negative. Free BSA molecules show lower ζ potential (also negative) than SiO$_2$ NPs and SiO$_2$NPs@BSA samples. Bar plot indicates mean ±SD of 3 independent measurements.

We measured the hydrodynamic diameter of the SiO_2 NPs after 1 h, 24 h and 48 h of incubation in the BSA solution (Figure 4.2 a-b). After 1 h in the BSA solution, the hydrodynamic diameter of SNPs-18 rises from around 25 nm to 58.8 ± 2.6 nm (Fig. 4.2a). SNPs-30 show similar behaviour with an increment from around 40 nm to 82.9 ± 3.1 nm (Fig. 4.2b). The increase in the hydrodynamic size of the SiO_2 NPs arises from the adhesion of BSA to the SiO_2 NP surface creating a protein corona. Some small NP clusters are also likely to form in presence of BSA but there are no signs of large aggregates. The small peaks displayed in the SiO_2NPs@BSA samples correspond to free BSA molecules in solution. As observed for the bare SiO_2 NPs, the hydrodynamic size of SNPs-18@BSA and SNPs-30@BSA also remains stable for at least 48 hours (Fig. 4.2a-b).

The formation of a protein corona is initially dominated by the binding affinity between the NP surface and the proteins [92, 95]. The stable protein corona around the NPs detected in the DLS data indicates a high affinity between BSA and the surface of the SiO_2 NPs. Once the surface of the NPs has been coated with proteins, the protein corona can grow but the process is now governed by protein-protein interactions [95]. The binding affinity of BSA proteins for the BSA-coated SiO_2 NPs will be lower than for the bare SiO_2 surface, hence not all proteins in solution are included in the corona but a proportion of them remains free in solution. This explanation agrees with a previous study of protein corona formation on SiO_2 which reported a high binding affinity between BSA and SiO_2 NPs and the reduction of the binding affinity between bovine serum proteins and SiO_2 NPs with a preformed protein corona [93].

The BSA corona also produces mild changes in the surface charge of the SiO_2 NPs, which become more negatively charged. The ζ potential of SiO_2 NPs measured after incubating them for 24 h in BSA solution was SNPs-18@BSA = -17.1 ± 1.8 mV and SNPs-30@BSA = -20.4 ± 0.2 mV (Fig. 4.2c).

4.3 BSA-corona modify the effect of SiO_2 NPs on the permeability of LUVs

CF leakage assay was employed to investigate the effect of SiO_2 NPs and SiO_2NPs@BSA in the permeability of 400 nm DOPC LUVs. CF loaded LUVs were prepared *via* extrusion as stated in **Sections 2.3.1** and **2.3.4.** The LUVs were suspended in isotonic buffer and incubated for 30 min with the appropriate SiO_2 NPs. A wide range of NP concentrations was tested for each type of SiO_2 NPs with and without BSA corona, covering from 10^{-4} µg/ml to 300 µg/ml.

Both SNPs-18 and SNPs-30 induce a dose-dependent leakage of CF from the LUVs (Fig. 4.3a-b). The dye release begins to be noticeable at NPs concentrations between 0.01 µg/ml and 0.1 µg/ml and then increases progressively as the NP concentration is raised, until it reaches a maximum level of approximately 55% at 10 µg/ml SNPs-18 and 3 µg/ml SNPs-30. From this point, CF leakage percentage observed in samples of SNPs-30 at higher concentrations remains stable at around 55% (Fig. 4.3b), while more concentrated samples of SNPs-18 show lower leakage (40-45%) than the observed at 10 µg/ml SNPs-18 (Fig. 4.3a).

The leakage decrease at the highest concentrations of SNPs-18 is unexpected and suggest that the NPs are somehow impeding the release of contents from the LUVs. Vakurov *et al*. studied the interaction of SiO_2 NPs with supported DOPC monolayers using Scanning Electron Microscopy and observed that the SiO_2 NPs organise themselves forming a thin monolayer that adheres to and fully covers the lipid monolayer surface [205]. Based on this observation, we propose a hypothesis to explain our results. When the LUVs are exposed to high SNPs-18 concentrations (>10 µg/ml), the SNPs-18 initially form pores in the membrane and the CF is released from the lumen of the LUVs. However, as time passes the NPs would cover completely the surface of the LUVs forming a sealing shell that reduces the rate of dye leakage. As a result, after 30 minutes these samples with high SNPs-18 concentration would show lower leakage than samples where the SNPs-18 are less concentrated. Samples of SNPs-30 do not show the drop of leakage at high concentrations but a plateau which indicates that the maximum leakage that these NPs induce has been reached at 3 µg/ml. This subtle difference in the leakage data likely indicates that SNPs-30 have a different interaction mechanism and so the protective shell formed by the SNPs-18 might not happen with larger NPs.

The presence of a protein corona modifies the effect of the SiO_2 NPs on the permeability of the LUVs. SNPs-18@BSA induce higher CF leakage from the LUVs than SNPs-18. In the concentration range between 0.01 µg/ml and 3 µg/ml the leakage produced by SNPs-18@BSA is just slightly higher than in samples of SNPs-18 without BSA corona. At higher concentrations, SNPs-18@BSA do not show the reduction of leakage observed for the SNPs-18 but the dye release keeps increasing, reaching values of nearly 80% CF release at 300 µg/ml (Fig. 4.3a). The BSA corona might be preventing the formation of the NP sealing shell around the LUVs so the leakage is not suppressed at high concentrations.

On the contrary, the BSA corona reduces the leakage induced by the larger SNPs-30. This suggests that the BSA corona might be weakening the interactions of these NPs with the membrane. This leakage reduction is especially noticeable between 0.01 µg/ml and 30 µg/ml. In samples of 30 µg/ml and higher concentrations, the dye release produced by SNPs-30@BSA is closer to that observed in SNPs-30 samples (Fig. 4.3b). The different effect of the BSA corona on the leakage produced by each type of SiO_2 NPs is a further indicator of different interaction mechanisms at play depending on the size of the NP.

Additionally, we performed control measurements of samples where the LUVs were exposed to free BSA at concentrations equivalent to the BSA concentration in the SiO_2NPs@BSA samples. We detect that free BSA also induces CF leakage in a concentration-dependent manner, beginning to produce marginal leakage at 10 µg/ml

BSA and reaching 25% CF leakage at 3 mg/ml. In SiO_2NPs@BSA samples most of the proteins are expected to have adhered to the SiO_2 NPs surface, but there is an excess of free BSA that might contribute to the leakage observed in those samples. Nevertheless, the contribution of free BSA to the leakage is expected to be nuanced since most of the proteins are adhered to the NPs.

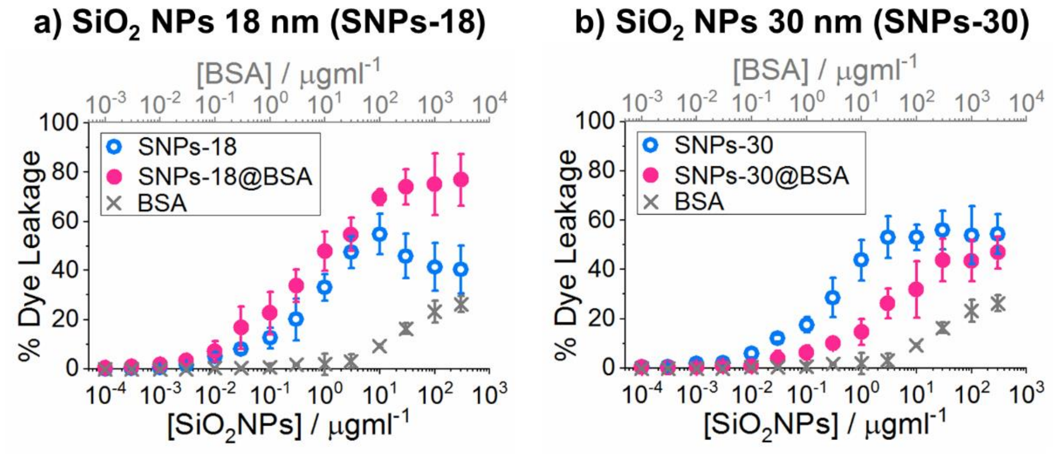

Figure 4.3. CF leakage from DOPC LUVs after 30 minutes of incubation with SiO_2 NPs with and without BSA corona at a wide range of concentrations. a) Leakage induced by SNPs-18 (blue open circles) and SNPs-18@BSA (magenta circles). b) Leakage induced by SNPs-30 (blue open circles) and SNPs-30@BSA (magenta open circles). Gray crosses in a and b indicate leakage induced by free BSA (concentration of BSA indicated in the upper axis, only valid for samples of free BSA and SiO_2 NPs with BSA corona). Data indicate mean ±SD of 3 replicates.

4.4 NP size and BSA corona change significantly the interaction between SiO_2 NPs and GUVs

Confocal microscopy was used to visualise morphological changes experienced by DOPC GUVs labelled with 0.5 mol% Rh-DOPE after interacting with SNPs-18, SNPs-18@BSA, SNPs-30 and SNPs-30@BSA. Additionally, using spectral imaging on GUVs labelled with 0.5 mol% Laurdan we measured the generalised polarisation (GP) of this polar-sensitive dye to detect changes in lipid packing within the membrane of the GUVs caused by the different types of SiO_2 NPs. All experiments were carried out at a SiO_2 NP concentration of 25 μg/ml. Control experiments confirmed that neither the morphology of the GUVs nor the lipid packing (Fig. 4.8) is affected by the presence of BSA in the medium at the concentration (0.25 mg/ml) at which they are found in the SNPs-18@BSA and SNPs-30@BSA samples.

Upon interaction with SNPs-18, the GUVs become wrinkled and show permanent microsized pores (Fig. 4.4). The formation of these large pores by this type of SiO_2 NPs has been already reported by Zhang *et al*, who also showed that this effect was accompanied by a considerable decrease in lipid lateral diffusion [79]. They proposed that the interaction of the SiO_2 NPs with the membrane produces a change in the tilt angle of the P^{-}-N^{+} dipole in the PC headgroup of the lipids which would produce a denser lipid packing and consequently decrease the membrane fluidity and increase the membrane tension [79]. This increased lateral tension generates elastic stress which is released by the fracture of the membrane which leads to the formation of single microsized holes in the GUVs.

Laurdan imaging data show that SNPs-18 induce a large increase in average GP of the DOPC GUVs, from around -0.45 to nearly -0.25 after exposure to SNPs-18 (Fig 4.8) This confirms that SNPs-18 produce a tighter packing of the lipids within the membrane, however, the average GP of the GUVs is still within the GP range corresponding to liquid disordered membrane [150, 151]. In our experiments, Laurdan is equally distributed along the inner and outer leaflet of the membrane so the GP values we observe correspond to the mean values of both monolayers. However, SNPs-18 adhere primarily to the outer leaflet so the effect of the SNPs in the packing density of the lipids might be stronger in the outer leaflet than in the inner monolayer. In that case, the barely changed GP of the inner monolayer would mask a less negative or even positive GP value corresponding to the outer leaflet.

Therefore, SNPs-18 potentially generate an asymmetric lipid packing between the membrane leaflets with the lipids in the outer monolayer more densely packed than in the inner leaflet. This asymmetry might explain the final morphology adopted by the GUVs. At the edge of the microsized pores, we observe enhanced fluorescence intensity due to the high curvature adopted by the membrane, which appears to be rolled up (Fig. 4.4). This rolled-rim pot-shaped GUV has been proposed to be stabilised by the asymmetric distribution of the lipids within the membrane [206]. According to a theoretical model developed by Sakuma and co-workers, the membrane asymmetry generates negative spontaneous curvature which competes with the line tension at the rim of the pore. Consequently, the membrane adopts a rolled-up structure that stabilises the pore edge [206].

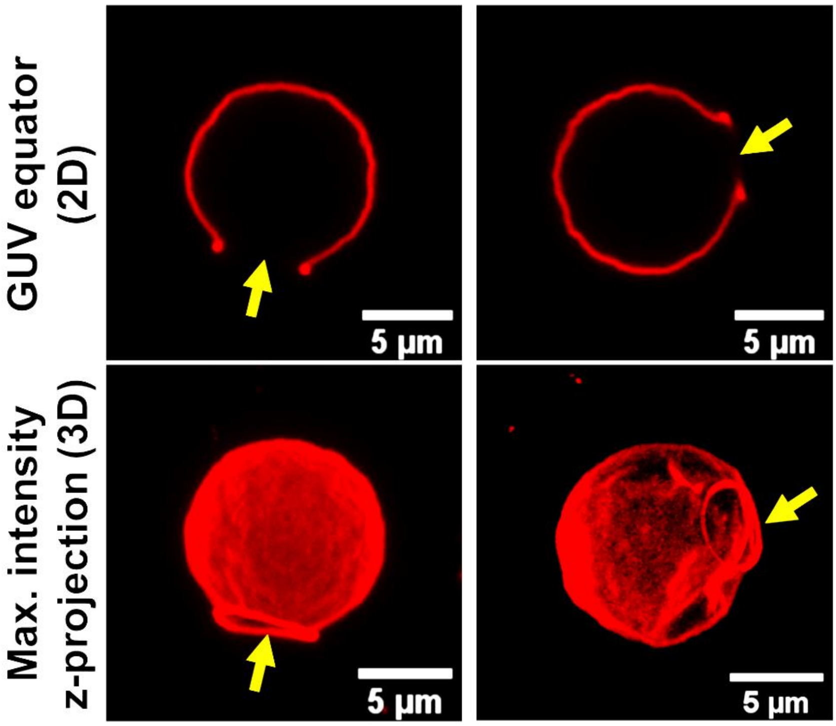

Figure 4.4. Confocal microscopy images of DOPC GUVs labelled with Rh-DOPE after exposure to 25 µg/ml SNPs-18. Left micrographs show the GUVs at the equator plane and images on the right show three-dimensional maximum intensity projections. Yellow arrows indicate the permanent microsized pores produced by the SNPs-18 on the GUVs.

The presence of a BSA corona around the SNPs-18 deeply modifies their interaction with DOPC GUVs. SNPs-18@BSA do not form large pores in the membrane but produce a progressive shrinkage of the GUVs. Real-time confocal microscopy images show that the size of the GUVs decreases while their membrane becomes thicker and its fluorescence more intense (Fig 4.5a-c). The analysis of the vesicle size against time shows a progressive shrinkage which suggests that the adhesion of SNPs-18@BSA to the GUVs induces a slow gradual rearrangement of the membrane. At the end of the process, the apparent radius of the vesicles is between 30% and 70% smaller compared to the radius of the initial GUVs. In most of the observed events, the apparent shrinking rate varies between 1 $\mu m^2/s$ and 6 $\mu m^2/s$, but we observe two isolated events that show significantly faster (10 $\mu m^2/s$ and 20 $\mu m^2/s$) apparent shrinking rate (Fig 4.5c).

Occasionally the GUVs seem to collapse, nevertheless, this final breakdown is only apparent (Fig 4.5a, bottom panel). Three-dimensional z-projections indicate that the GUVs exposed to SNPs-18@BSA do not fully collapse and retain an approximately spherical shape (Fig 4.5d). During the collection of confocal microscopy time series, GUVs are initially imaged at their equatorial plane, however, while the vesicles shrink, they can move out from the confocal plane. Consequently, the images are no longer taken at the GUV equator but closer to its upper pole where its diameter is smaller and the vesicles can appear to have collapsed. This also contributes to the variability of the apparent shrinking rate observed between different events (Fig. 4.5c), since the movement of the GUVs out from the confocal plane would produce an apparent size reduction rate faster than the actual rate of vesicle shrinkage induced by the SNPs-18@BSA.

The increase in membrane thickness and fluorescence intensity likely denotes that SNPs-18@BSA are wrapped and generate highly curved sub-micrometre membrane invaginations. Moreover, nanosized pores are expected to be formed on the membrane allowing the contents in the lumen to be expelled from the GUVs while they shrink. The average Laurdan GP of the GUVs after exposure to SNPs-18@BSA indicates that the lipids become densely packed in the highly curved membrane (Fig 4.8). The lipid packing of the GUVs after interacting with SNPs-18@BSA (GP= -0.29) is however lower on average than the induced by the bare SNPs-18 (GP= -0.25).

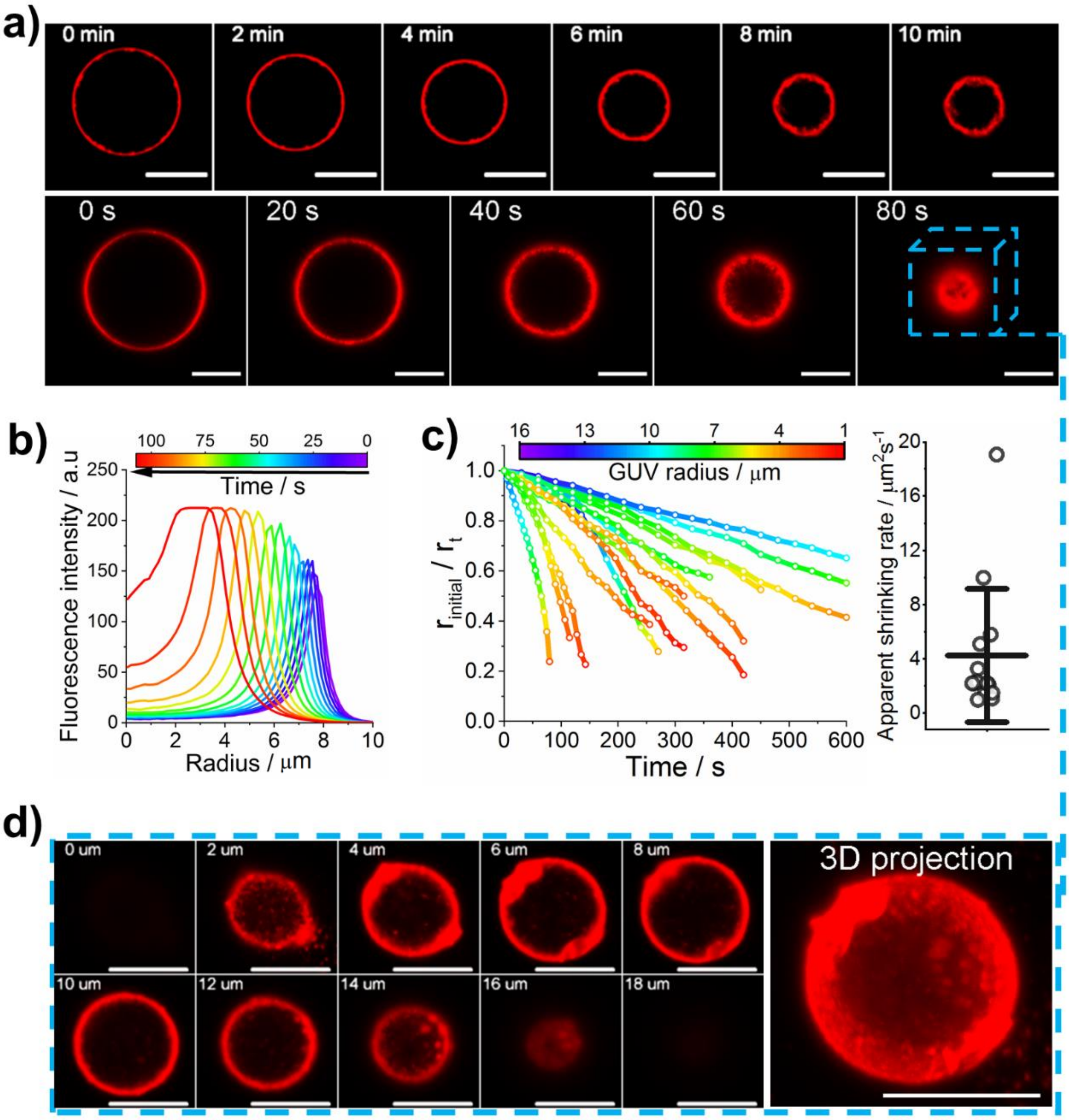

Figure 4.5 a) Confocal microscopy time series of DOPC GUVs labelled with Rh-DOPE show a gradual shrinkage of the vesicles accompanied by an increase in membrane thickness and fluorescence intensity. b) Example of radial integrated fluorescence intensity measurement of a GUV interacting with SNPs-18@BSA. The radius of the GUV decreases with time (see colour bar) and the fluorescence intensity increases. The wider curves at longer times indicate a thicker membrane. c) Apparent shrinking of individual GUVs. The y-axis represents the normalised GUV radius at each time point and the colour of the lines indicate the actual radius of the GUV (see colour bar). Plot on the right shows the apparent shrinking rate distribution (mean ± SD). d) Confocal microscopy images of a GUV after SNPs-18@BSA-induced shrinkage at different focal planes (z-planes) and three-dimensional maximum intensity projection. The GUV appears damaged but still maintains its spherical shape.

The interaction between SNPs-30 and GUVs is extremely interesting and demonstrates the striking importance of the NP size in the interaction between SiO_2 NPs and lipid membranes. As introduced in **Section 1.3.1**, these NPs are within the critical size range (25-40 nm) at which the adhesion energy, which drives NPs towards the lipid membrane, equates the elastic energy, which determines the resistance of the membrane to be deformed. Zhang *et al* suggested that SiO_2 NPs within this size range are expected to induce a cross-over between tension-driven and curvature-driven interaction regimes [79]. Since natural protein complexes trigger membrane fusion by generating a balance of membrane curvature and tension [109, 111, 207], we proposed that SiO_2 NPs with a diameter of 30 nm might be able to mimic the activity of those protein complexes and induce fusion of artificial lipid membranes.

Real-time confocal microscopy images show that when SNPs-30 interact with two closely localised GUVs, the vesicles fuse generating a final GUV with a membrane composed of a mixture of the lipids in the initial vesicles (Fig. 4.6). The SiO_2 NPs-triggered fusion mechanisms and the fusion efficiency of 30 nm SiO_2 NPs will be studied in more detail in the next chapter of this thesis. Nonetheless, these initial observations clearly confirm the ability of SNPs-30 to trigger fusion of apposing GUVs and therefore validate our initial hypothesis. Moreover, Laurdan spectral imaging shows that SNPs-30 induce a mild but statistically significant increase in the average GP of the Laurdan molecules embedded in the membrane (GP= -0.40) (Fig. 4.8). This increased membrane order, although more moderate than that induced by SNPs-18, could still increase the membrane tension and facilitate the contact between closely localised membranes. [79, 111, 208-210]. In addition, changes in the membrane order can lead to localised lipid packing defects which have been previously considered as an initial step required for two adjacent membranes to fuse [108, 211, 212].

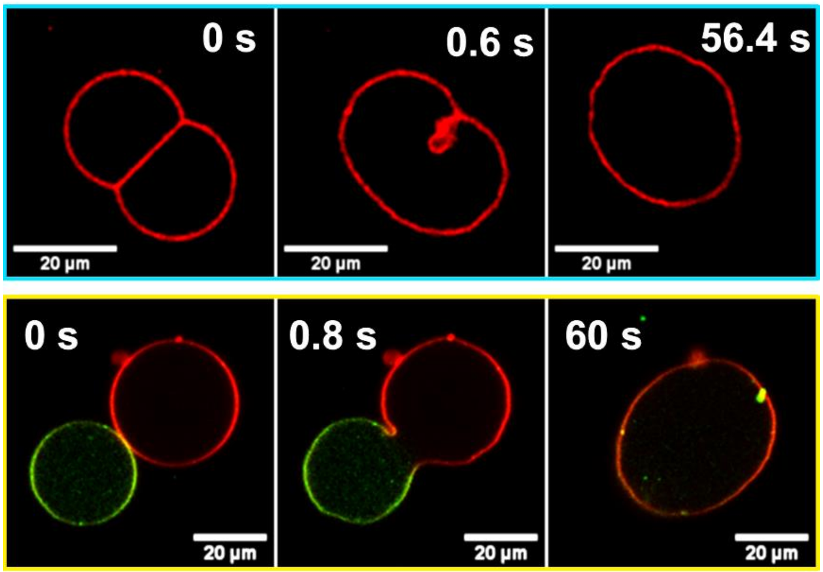

Figure 4.6. Confocal microscopy time series of DOPC GUVs undergoing fusion after interaction with 25 µg/ml SNPs-30. In the top panel both GUVs are labelled with Rh-DOPE and in the bottom panel, one GUV is labelled with Rh-DOPE (red) and the other with DiO (green). Both dyes colocalise in the membrane of the final fused GUV.

The BSA corona suppresses the fusogenic ability of SNPs-30. The interaction between SNPs-30@BSA promotes the adhesion of the GUVs which gather forming clusters of tens of vesicles (Fig. 4.7). The GUVs maintain their integrity and neither membrane perturbations nor fusion events are observed. Although the interaction between the SNPs-30@BSA and GUVs does not lead to fusion events, the experiments with homogeneously labelled vesicles might be hindering a potential lipid transfer between the adhered GUVs due to the formation of fusion intermediate states where only the outer monolayers of the membranes are fused. Experiments mixing populations of GUVs, one labelled with Rh-DOPE and the other with the green dye DiO (1 mol%) were used to detect such lipid transfer between the GUVs, which would lead to the colocalization of both dyes in the membrane of the same GUV. After 30 minutes of incubation with 25 µg/ml, we again observe clusters of vesicles composed of both types of GUVs but we do not detect any transfer of lipids between the oppositely labelled GUVs (Fig. 4.7). The mean Laurdan GP of the GUVs remains unchanged after exposure to SNPs-30@BSA (GP= -0.45) (Fig. 4.8). Hence, the adhesion of SNPs-30@BSA to the membrane is unable to induce any packing defects.

These results, together with the reduced CF leakage seen before, suggest the BSA corona weakens the interaction between SNPs-30 and lipid membranes. The first stage of the fusion produced by SNPs-30 implicates the close apposition of the neighbouring GUVs. SNPs-30@BSA seem to retain this ability but the protein corona prevents the generation of the membrane perturbations (packing defects, curvature and lateral tension) required for the GUVs to fuse.

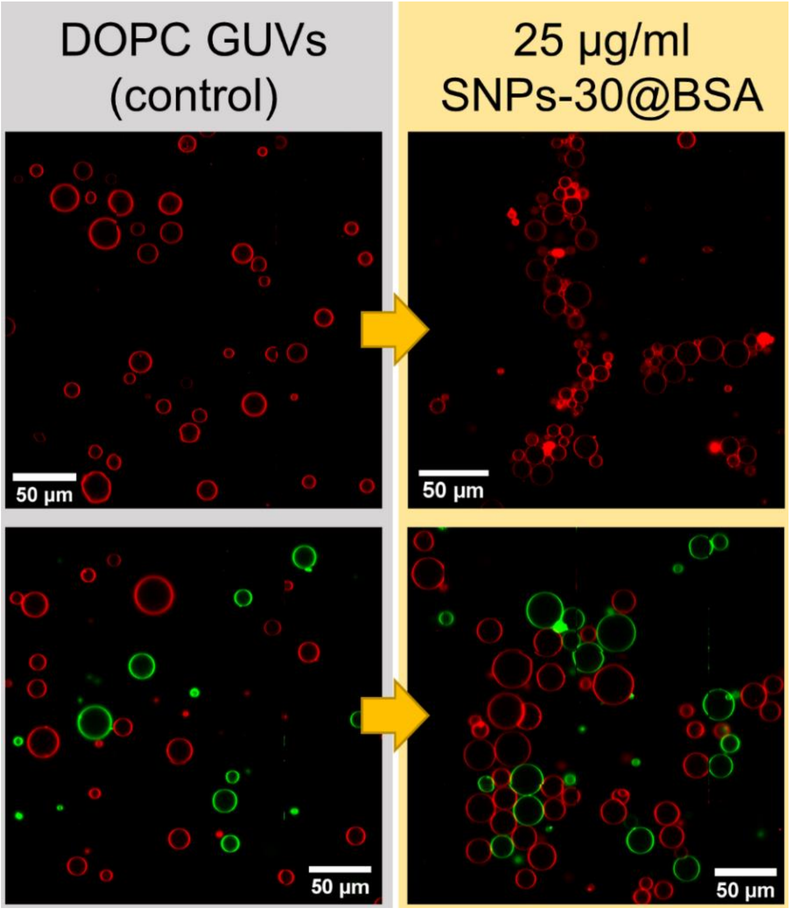

Figure 4.7. Confocal microscopy images of DOPC GUVs before and after incubation with SNPs-30@BSA for 30 min. In the top images GUVs are labelled with Rh-DOPE and in the bottom images, one population of GUVs is labelled with Rh-DOPE (red) and the other with DiO (green). After incubation with SNPs-30@BSA, the GUVs gather into clusters but maintain their integrity and do not fuse. No lipid mixing between the differently labelled GUVs is detected.

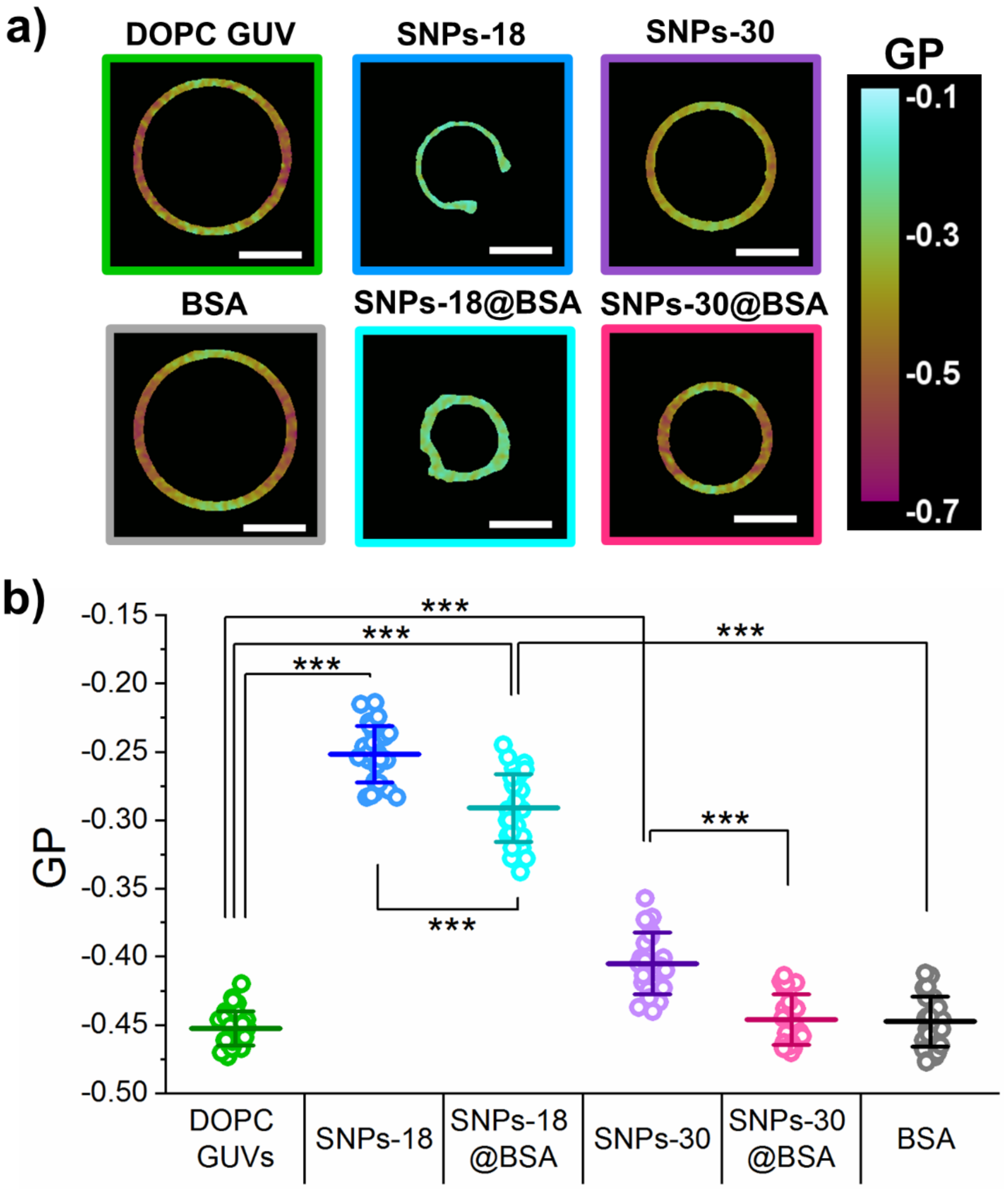

Figure 4.8 Spectral imaging of DOPC GUVs labelled with Laurdan before and after exposure to 25 µg/ml SiO_2 NPs with and without BSA corona. a) Examples of Laurdan GP maps of GUVs under the different experimental conditions. b) Distribution of average Laurdan GP of the GUVs before and after 30 min incubation with the different SiO_2 NPs with and without BSA corona as well as after incubation with 0.25 mg/ml BSA. Data presented as mean ± SD, circles indicate each individual measurement (DOPC GUVs: n=35/ SNPs-18: n=26 / SNPs-18@BSA: n=29/ SNPs-30: n=25/ SNPs-18@BSA: n=26 / BSA: n=26). Statistical significance tested using a one-way ANOVA with a post-hoc Bonferroni test (***p< 0.001)

4.5 Discussion

Here we studied the interplay between SiO_2 NPs of two different sizes (SNPs-18 of 18 nm and SNPs-30 of 30 nm) and DOPC vesicles and how the presence of a protein corona coating the NPs alters those interactions. Our results first corroborate the well-known influence of the NP size on these interactions [77-79]. Bare SiO_2 NPs of both sizes interact strongly with lipid membranes as indicated by the high proportion of CF released from LUVs after exposure to SiO_2 NPs. The two types of SiO_2 NPs induce similar dye leakage from DOPC LUVs, however, this data suggests completely different interaction mechanisms later revealed by confocal imaging of GUVs. SNPs-18 induce microsized permanent pores in the GUVs and a considerably tighter packing of the lipids in the membrane whereas SNPs-30 promote fusion of closely localised GUVs and a milder increase in Laurdan GP.

The biomedical interest of SiO_2 NPs makes it important to understand the behaviour of these nanomaterials when they come in contact with biological media. Cell membranes rarely encounter bare nanomaterials but NPs coated by biomolecules present in biological fluids. The main and more extensively studied component of such coatings are proteins, which form the protein corona [95]. The adsorption of proteins to the NP surface and the reversibility of the process is determined by the binding affinity of the proteins for the nanomaterial [98]. This binding affinity depends principally on the type of protein and the surface properties of the NPs and their size [91, 96, 97].

To mimic the protein coverage experienced by NPs in biological media we incubated the SiO_2 NPs with BSA proteins. This leads to a very simplified protein corona made exclusively of BSA which provides information about changes in the interaction between both types of SiO_2 NPs and the lipid membranes induced by the surface coating of the NPs with proteins but this does not necessarily correspond to what would happen *in vivo,* where much more complex coronas composed of different proteins as well as other biomolecules cover the surface of NPs.

The formation of the BSA corona around the SiO_2 NPs is detected as an increase in the hydrodynamic diameter of the NPs, which approximately doubles the hydrodynamic size of the bare SiO_2 NPs. The size of the SiO_2NPs@BSA remains stable for at least 48 hours. This stable protein corona likely indicates a high affinity of BSA by the SiO_2 NPs where they get strongly bound covering their surface completely. This complete surface coverage of SiO_2 NPs by strongly bound proteins has been reported previously [93, 98]. The free BSA observed in SiO_2NPs@BSA samples correspond to proteins that cannot access the NP surface. Once all the NP surface has been covered by BSA molecules, the adhesion of excess proteins to the corona is controlled by protein-protein interactions which are weaker than the affinity of BSA towards SiO_2 NPs [95]. The more external layer of the protein corona (often called soft corona) is thought to be very dynamic with their proteins getting exchanged with free proteins in the surrounding environment [96]. In our samples, since only one type of protein (BSA) is present the dynamic exchange between free proteins and the more external BSA molecules of the corona would reach an adsorption-desorption equilibrium which maintains the BSA corona apparently stable.

The BSA corona surrounding the SiO_2 NPs modifies their membrane activity, but the effect is different between the two types of SiO_2 NPs investigated. These results imply that although the protein corona gives a new identity to the NPs, the size of the pristine SiO_2 NPs still defines the interaction mechanism to some extent. The membrane permeability assays indicate that the BSA corona enhances the dye leakage from the LUVs produced by the smaller particles of 18 nm. On the contrary, SNPs-30@BSA cause a lower dye release than the bare SNPs-30.

The differential interaction of bare SiO_2 NPs and SiO_2NPs@BSA with lipid membranes becomes unequivocally evident in view of how they affect the morphology of GUVs and the lipid packing of their membrane. Unlike SNPs-18, which produce large permanent pores, SNPs-18@BSA induce a gradual shrinkage of the GUVs which eventually result in considerably smaller vesicles with a thick crumpled membrane. These final GUVs conserve a spherical shape with an aqueous lumen encapsulated unlike the pot-shaped GUVs with large permanent pores generated by SNPs-18. SNPs-18@BSA keep the ability to induce tighter packing of the lipid shown by the pristine SNPs-18, but this effect is slightly weakened by the BSA corona.

Zuraw-Weston *et al.* performed a study where they modulated the adhesion strength of NPs to the membrane by changing the surface charge of the membrane [75]. At the strong adhesion regime, they observed a multistage vesicle destruction process. In the first stage of that process, the NPs get wrapped by the membrane inducing a gradual shrinkage of the GUVs as well as highly curved structures of their surface. The vesicles that shrank faster surpass a tension threshold that makes them advance to the next step of the destruction process that consists of the opening of a large permanent pore similar to the ones induced by the SNPs-18 [75]. Thus, comparing their results with what we observed in our study, a possible explanation to our results is that the contact of SNPs-18 with the GUVs drives them to rapidly shrink (faster than the temporal resolution of the confocal microscope) and consequently transition into the permanent pore configuration, apparently skipping the first stage. In the case of SNPs-18@BSA, the BSA corona would slow down the shrinkage rate and prevent the membrane tension to reach the lysis tension threshold, thus arresting the process at the first destruction stage. However, in our results, SNPs-18 do not show any evidence of a multistage interaction process but the vesicle shrinkage and pore opening happen suddenly resembling a first-order phase transition. We believe that this effect does not involve wrapping processes but is due to the condensation of the lipid headgroups of the outer leaflet of the membrane where the SNPs-18 adhere, which induce an increase in membrane tension that drives the opening of the pore and an asymmetric lipid packing which helps to stabilise the pore edges. The BSA corona modifies the interaction mechanisms so NPs can now get wrapped by the membrane creating highly curved membrane structures and inducing a gentle shrinkage of the GUVs.

The BSA corona around SNPs-30 seems to diminish the ability of these particles to interact with lipid membranes. SNPs-30@BSA induce the adhesion of GUVs which gather forming clusters but the BSA corona suppresses the fusogenic activity and the ability to induce changes in the lipid packing of the GUVs. In this case, the BSA corona likely reduces the adhesion energy of the NPs to the membrane and impedes the generation of membrane perturbations needed to trigger the fusion process. An analogous weakening effect of the protein corona on the bioactivity of SiO_2 NPs was reported by Lesniak *et al*., who observed that the protein corona hampers the adhesion of 50 nm SiO_2 NPs to the plasma membrane of live cells and consequently reduce the NP uptake levels [204]. NPs of different chemical compositions, such as gold and polystyrene, have also exhibited reduced membrane activity when coated with protein coronas [178, 213]. On the contrary, Churchman et al. reported that the protein corona improves the colloidal stability of otherwise aggregated zinc oxide NPs (ZnO NPs) and this enhances their interaction with DOPC membranes [179].

From a toxicological perspective, it is generally accepted that protein coronas improve the biocompatibility of NPs and thereby reduce their potentially hazardous effects [214]. For instance, it has been observed that protein coronas protect cells from the cytotoxic effect induced by bare positively charged polystyrene NPs [215]. The adsorption of proteins can also minimise the toxicity by preventing the aggregation and degradation that some types of NPs experience when suspended in aqueous solutions [216-218]. On the contrary, the protein corona has been reported to increase the cellular uptake of AgNPs which, once internalised in the cells, produce severe cytotoxic effects [183, 219]. Moreover, occasionally the protein corona can affect the stability of the NPs and promote aggregation [98], which is expected to increase the toxicity of nanomaterials.

The knowledge about the impact of protein coronas on the NP-membrane interactions and the potential cytotoxicity arising from them still presents considerable gaps. The myriad of parameters influencing the non-specific biomolecular coating of nanomaterials leads to highly complex and variable structures formed under different experimental conditions which makes it difficult to extract unified conclusions. In addition, different types of membranes and cell lines can react distinctively to the NP contact. Understanding how biomolecular coronas form and their relevance in the NP stability, reactivity and biocompatibility is thereby an extremely challenging task that needs the combination of different experimental perspectives. In this context, reductionist studies represent a first step that provides elementary information on structural and dynamical aspects of the assembly of different biomolecular coronas, as well as their influence on the stability and membrane activity of NPs.

4.6 Conclusions

The results shown here manifest the great impact that the size and protein corona have on the interaction between SiO_2 NPs and lipid membranes. Using BSA to form a model protein corona of controlled composition, we observe that the corona weakens the interaction of SiO_2 NPs with the membrane leading to outcomes completely different to the ones produced by pristine SiO_2 NPs. Bare SNPs-18 produce large permanent pores on DOPC GUVs as well as a significantly tighter packing of the lipids in the membrane. When a BSA corona is formed around those NPs, they are wrapped by the membrane, forming sub-micrometre highly curved structures and transient nanosized pores in the GUVs which consequently suffer a gradual shrinkage. The BSA corona reduces considerably the ability of SNPs-30 to interact with lipid membranes and suppresses their fusogenic activity. The different membrane responses produced by the two types of SiO_2NPs@BSA indicate that the size of the bare NPs still determines the interaction mechanism with the membrane.

The fusogenic activity of 30 nm SiO_2 NPs will be explored in depth in the next chapter, where we will analyse the intermediate states that membranes adopt during SiO_2 NPs-triggered fusion and propose a mechanistic explanation for the process.

Chapter 5:
Biomimetic membrane fusion induced by silica nanoparticles

5.1 Introduction

Membrane fusion is a key communication and transport process in living cells that is highly desirable to replicate in artificial cell systems to modify their membrane composition, volume, surface area and shape as well as to control chemical compartmentalisation and trigger targeted chemical processes. Mechanistic models for membrane fusion involve a series of sequential intermediate steps. The process begins with the docking of two membranes. This is followed by the destabilisation of the lipids by inducing these membranes to curve towards each other and increasing their local lateral tension. This leads to the hemifusion of the contacting outer leaflets followed by the final formation and expansion of a full fusion pore, which completes the process [207, 220].

In living cells, membrane fusion is regulated and catalysed by the coordinated action of protein complexes, among which the SNARE proteins are possibly the best known. [110] However, protein-free membrane fusion can be achieved *in vitro* using other chemical stimuli, including particular membrane compositions [209, 221], membrane-anchored DNA [222], peptides [223, 224] and multivalent ions [225] or by physical stimuli such as optically heated gold nanoparticles [226-228] or electric pulses [229]. All these fusion strategies (including proteins) share the ability to induce one or more changes in membrane tension, curvature, fluidity, or other biophysical properties of the membrane which can lower the energy barrier to membrane fusion with varying degrees of efficiency. The ability of engineered nanoparticles (NPs) to deform membranes and facilitate remodelling processes can also be exploited in synthetic biology to efficiently trigger and control membrane fusion. An example of a NP-based fusion system has been recently presented by Tahir *et al*. who designed amphiphilic nanoparticles composed of a gold core functionalized with a mixed monolayer of alkanethiol ligands able to perform calcium-triggered membrane fusion [108].

Here, we investigate the potential for 30 nm diameter SiO_2 NPs as artificial membrane fusion machinery. The efficiency of these SiO_2 NPs in promoting lipid mixing, considered an essential consequence of membrane fusion events, in populations of LUVs is studied using a Förster Resonance Energy Transfer (FRET) assay. However, this method is insufficient to investigate the mechanisms involved in fusion events. For this reason, we perform further confocal microscopy studies GUVs, which allow time-resolved investigation of the trajectories of fusion events between individual pairs of GUVs. Direct imaging of kinetic pathways of membrane fusion permits the identification of intermediate fusion states and quantification of the rate of lipid mixing between fusing GUVs in order to propose a mechanistic interpretation of the process.

5.2 Intervesicular lipid mixing quantified by FRET

The fusogenic activity of 30 nm SiO_2 NPs was initially evaluated by a lipid mixing assay based on FRET [230]. DOPC LUVs labelled with both NBD-DOPE and Rh-DOPE are mixed with probe-free DOPC LUVs at a 1:5 ratio and exposed to different concentrations of SiO_2 NPs for 30 min. The values for full lipid mixing are obtained from samples containing only LUVs labelled with 0.05 mol% NBD-DOPE and Rh-DOPE, which represent the maximum dilution of the probes in the membrane that can be reached in our experiments.

The samples not treated with SiO_2 NPs show reduced NBD intensity and high Rh-DOPE fluorescence emission because both fluorophores are closely colocalised in the labelled LUVs leading to a maximum FRET ratio. However, the exposure to SiO_2

NPs induces a decrease in FRET ratio (increased NBD fluorescence and reduced Rh-DOPE intensity), which is indicative of dose-dependent lipid mixing between vesicles (Fig. 5.1a-b). Our results show that nearly 50% lipid mixing is reached when the LUVs are incubated with 30 µg/ml SiO_2 NPs and around 80% lipid mixing happens when LUVs are exposed to 100 µg/ml SiO_2 NPs (Fig. 5.1c). The presence of SiO_2 NPs in solution promotes the exchange of lipids between labelled and unlabelled LUVs, hence the distance between the donor and acceptor fluorophores increases as they get diluted into the unlabelled membranes and the FRET signal drops. These results must be interpreted carefully since the changes in the FRET signal are not exclusively produced by fusion but can result from other processes such as hemifusion [231] and rupture of the vesicles [232].

The complete fusion of liposomes upon interaction with SiO_2 NPs would lead to a population of larger vesicles. Hence, we used DLS to measure changes in the hydrodynamic size of LUVs after exposure to SiO_2 NPs with the aim to assess whether SiO_2 NPs induce complete fusion of LUVs. We observe that the size distribution of LUVs increases after incubation with 30 µg/ml and 100 µg/ml SiO_2 NPs for 30 min from 347.40 ± 14.05 nm to 482.90 ± 52.02 nm and 564.10 ± 23.23 nm, respectively, thus a large proportion of the LUVs in the sample has fused into larger vesicles (Fig. 5.1d). Assuming that vesicle volumes are conserved during fusion events, these increases in vesicle size distributions are equivalent to, on average, 2.7 vesicles (30 µg/ml) and 4.3 vesicles (100 µg/ml) fusing with one another to form the larger vesicle population. These estimates are consistent with the 50% and 80% lipid mixing values reported by FRET at these NP concentrations when starting from an initial 1:4 mixture of labelled to unlabelled vesicles.

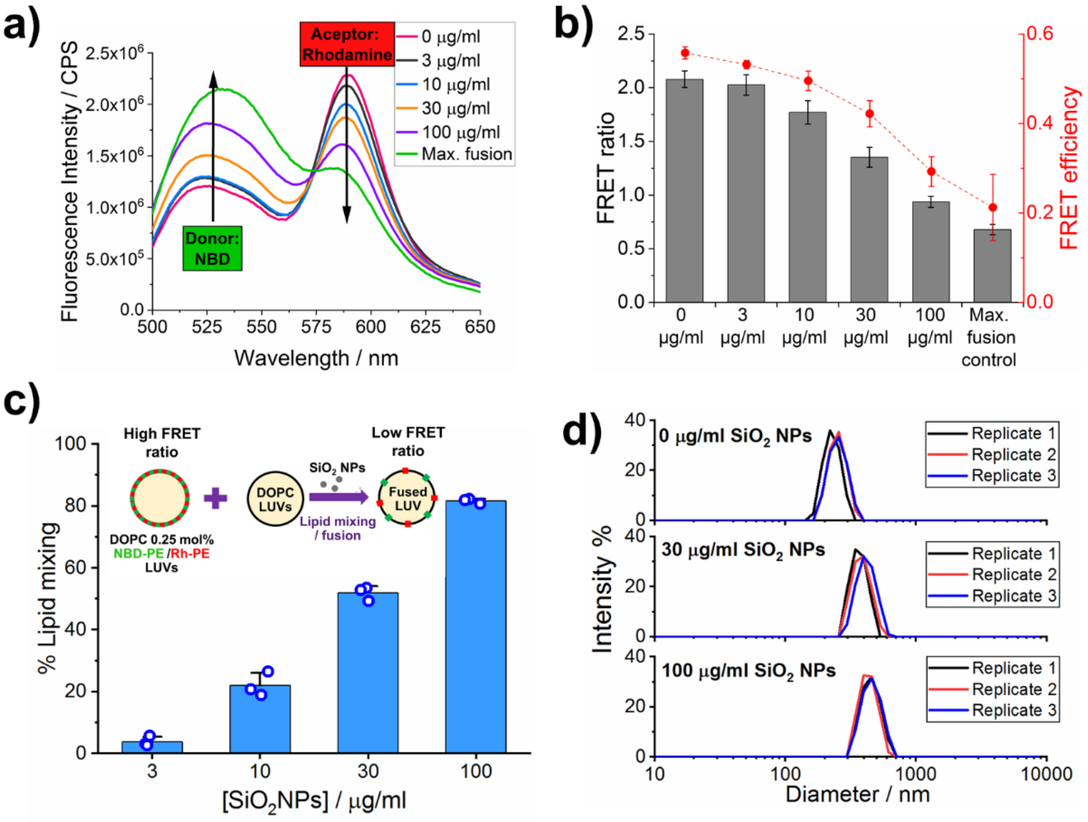

Figure 5.1. Fusogenic activity of SiO_2 NPs evaluated by FRET and DLS. a) Example of fluorescence emission spectrum of DOPC LUVs labelled with 0.25 mol% Rh-DOPE and NBD exposed to different concentrations of SiO_2 NPs for 30 min (Max fusion control sample made of LUVs labelled with 0.05 mol% Rh-DOPE and NBD). b) Average FRET ratio and FRET efficiency at a range of SiO_2 NP concentrations after 30 min incubation with LUVs. c) Percentage of lipid mixing induced by SiO_2 NPs. Lipid mixing is detected as a decrease of FRET ratio in samples containing unlabelled DOPC LUVs and DOPC LUVs labelled with NBD-DOPE and rhodamine-DOPE (inset). The lipid mixing rises as the LUVs population is exposed to increased concentrations of SiO_2 NPs. d) Hydrodynamic size distribution of DOPC LUVs before (0 µg/ml SiO_2 NPs) and after exposure to 30 µg/ml and 100 µg/ml SiO_2 NPs for 30 minutes measured by DLS. After incubation with SiO_2 NPs the size of the LUVs increases. Data in b and c presented as mean ±SD of 3 replicates.

5.3 SiO_2 NPs mediate fusion of GUV membranes and contents

As anticipated in the previous chapter (**Section 4.4)**, 30 nm SiO_2 NPs promote fusion of DOPC GUVs. Initial confocal microscopy movies of GUVs labelled with 0.5 mol% Rh-DOPE (Rh-GUVs) after exposure to 25 µg/ml SiO_2 NPs show that not all the fusion events mediated by SiO_2 NPs occur in the same manner but various processes, involving distinct morphological changes of GUVs, can lead to membrane fusion.

Figure 5.2a shows a sequence of two fusion processes occurring between two apposed GUVs, one of them with a third GUV inside. Initially, one of the GUVs begins to shrink and its membrane is apparently transferred to the neighbour GUV which progressively gets bigger. At the same time, the third GUV, which was inside the growing one, is expelled from the lumen. These two GUVs remain attached to each other and slowly get smaller until eventually their membranes fuse resulting in a single final GUV (Supplementary Movie 5.1). During the process, we observe spots in the GUV surface with a fluorescence signal considerably brighter than the rest of the membrane. This enhanced localised fluorescence intensity is attributed to highly curved regions of the membrane induced by the NPs adhering to the GUV surface and being wrapped by the membrane [79, 233]. The nanoscale membrane curvature induces an increased membrane area, and therefore number of fluorophores, per pixel in the x-y plane of the image, which translates into a brighter fluorescent signal. If NPs get fully wrapped by the membrane, they can lead to fission processes that pull the membrane which engulfs the NPs out from the GUV membrane [78, 233]. These fission processes explain the fluorescence signal observed in the lumen of the GUVs in Figure 5.2a. A different mechanism is observed in Figure 5.2b, where the fusion occurs after the sudden breakage of the membrane at one end of the GUV contact region. The membrane at the contact region gets trapped in the lumen of the fused GUV and quickly rearranges to form an intraluminal vesicle (Supplementary Movie 5.2).

We observe increased fluorescence intensity at the rim of the membrane interface which separates the GUVs (Fig. 5.2a-b). This locally enhanced intensity likely denotes that three bilayers are contacting at these points (Y-like junction), one bilayer from each GUV and a mixed bilayer formed at the interface, commonly named hemifusion diaphragm. In such Y-like junctions, the membranes are under high curvature stress and the lipids get condensed. The formation of fusion intermediate states will be further discussed in the following sections.

To observe whether the contents of the DOPC GUVs mix upon vesicle fusion, we carried out additional experiments mixing a population of GUVs encapsulating a sucrose solution with a second GUV population containing a mixture of sucrose and fluorescent 70 kDa TRITC-dextran (TRITC-filled GUV). The analysis of the fluorescence intensity of the GUV cargo during the fusion process indicates a complete mixing of the lumens once the GUVs fuse (Fig. 5.2c, Supplementary movie 5.3). Before the GUVs fully fuse, there is a lipid transfer between the GUVs which results in the simultaneous swelling of the fluorescently loaded vesicle and shrinking of the contiguous GUV. This swelling requires the entry of non-fluorescent content into the TRITC-filled GUV which causes a gradual dilution of the TRITC in the lumen and explains the gradual drop of its fluorescent observed before fusion. By comparing the fluorescence intensity in the lumen of the TRITC-filled GUV with its volume at the different time points, we clearly observe that the increase of the TRITC-filled GUV volume is proportional to the drop of the fluorescence intensity in its lumen (Fig 5.2c). However, it is unclear whether the swelling is driven by the net influx of contents into the TRITC-filled GUV from the shrinking GUV, from the outer medium or both, through transient nanopores opened in the membrane. During the swelling process, we do not observe transfer of TRITC-dextran from the growing GUV to the shrinking GUV until the fusion pore opens. Once the GUVs fuse, the lumens of the two GUVs mix completely, consequently the fluorescent dextran molecules get diluted in the final lumen and the fluorescent intensity of the GUV cargo decreases steeply (Fig. 5.2c).

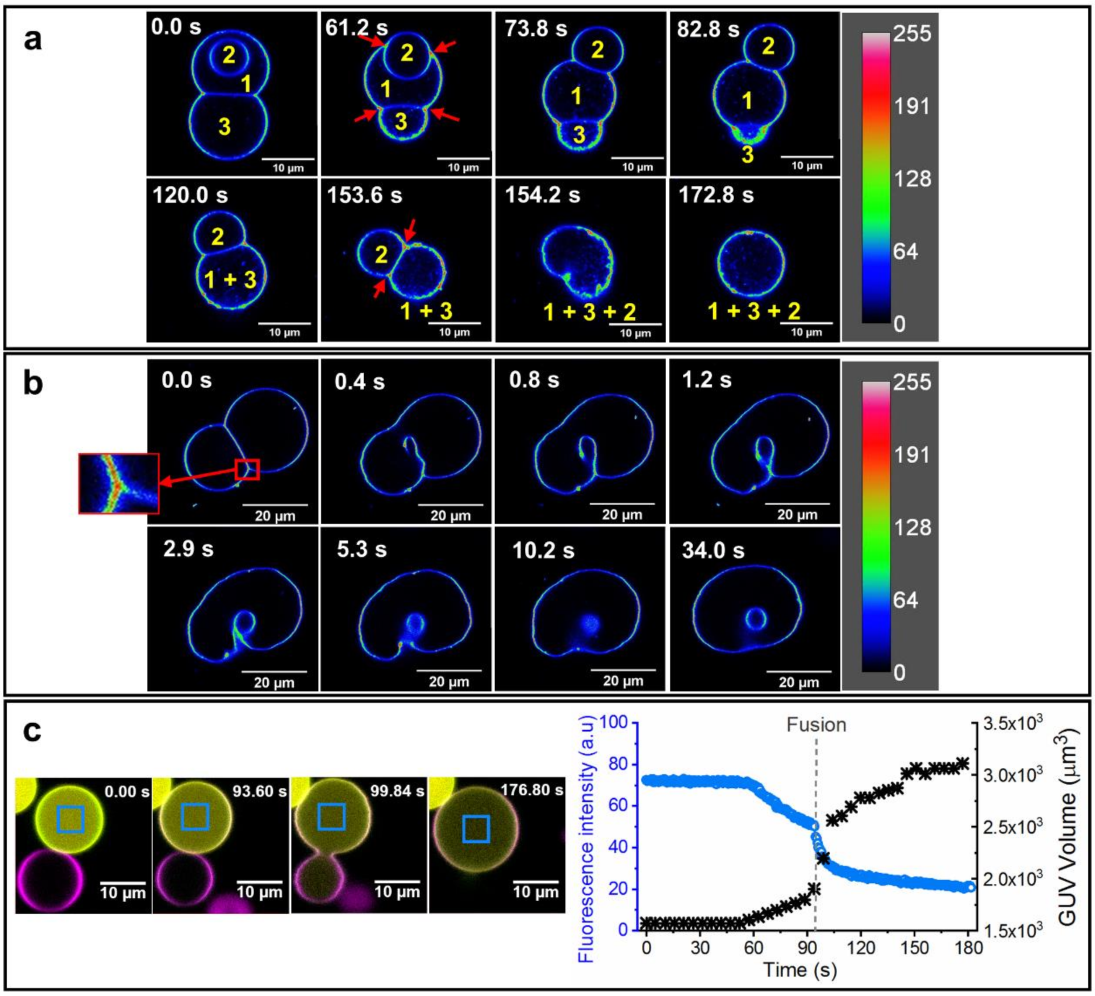

Figure 5.2. Confocal microscopy images of GUVs fusion triggered upon exposure to 25 µg/ml SiO_2 NPs. In panels a and b, GUVs are labelled with Rh-DOPE and its fluorescence is presented as a pseudocolour associated with the intensity as indicated in the colour code scale. a) Initially two GUVs are docked (1 and 3) and the first one has a third vesicle inside (2). As time progresses, the GUV 3 gradually merges into the GUV 1 and at the same time, GUV 2 is ejected. The resulting 1+3 GUV and GUV 2 remain attached and the former start shrinking. Eventually, the GUVs fuse originating a single final GUV 1+3+2. b) The boundary membrane which separates the two GUVs suddenly breaks at one end and the GUVs fuse. A membrane fragment gets trapped in the lumen of the new GUV and forms an intraluminal vesicle. Red arrows indicate regions of enhanced fluorescence intensity at the edges of the docking regions. c) Micrographs showing lumen mixing during fusion. One of the GUVs, labelled with 1 mol% DiO (green) is loaded with sucrose and TRITC-dextran 70 kDa (yellow) and the other is labelled with 1 mol% DiD (magenta) and its lumen contains only sucrose (non-fluorescent). The plot shows the fluorescence intensity of TRITC-dextran (blue circles, blue y-axis) in the region of the GUV lumen indicated by the blue box in the micrographs as well as the volume of the TRITC-filled GUV (black crosses, black y-axis) against time. The drop in fluorescence intensity before fusion corresponds with the swelling of the GUV. After fusion, the lumens of the two GUVs mix inducing a sharp drop of fluorescent intensity in the lumen of the resultant GUV.

5.4 Fusion efficiency is influenced by membrane tension

Membrane tension is known to be a crucial biophysical parameter for the progress of membrane fusion events [111, 113, 234-236]. Hence, we investigated the effect of the membrane tension in the fusion process triggered by SiO_2 NPs. The first step to assess the influence of membrane tension in the fusion process was to modify the tension of the GUVs after electroformation by incubating them in hypertonic, isotonic or hypotonic buffer overnight to obtain “relaxed”, “neutral”, or “tense” GUVs, respectively. Then, to quantify the proportion of GUVs undergoing fusion in the sample we mixed equally tense Rh-GUVs and DiO-GUVs (DOPC labelled with 1 mol% DiO) in a 1:1 volume ratio before adding the SiO_2 NPs (25 µg/ml). Finally, after incubating the GUVs with the NPs for 30 min we took tile scans and counted the proportion of GUVs with both dyes colocalised in the membrane (lipid mixed GUVs).

The images of vesicles incubated in isotonic buffer show an average proportion of lipid mixed and fused GUVs of 12.25 % from the total number of GUVs. The osmotic relaxation of the GUVs reduces the mean proportion of lipid mixed GUVs in the samples to 7.90 %, while in the samples of osmotically tensed GUVs the average percentage of vesicles fusing rises to 15.96 % (Fig. 5.3a). The tile scans were taken from 5 independent samples for each condition. These data denote a clear impact of the membrane tension on the fusion process induced by the SiO_2 NPs. Similar results were obtained by FRET spectroscopy on LUVs samples (Fig. 5.3b). The membrane tension of the LUVs was osmotically modified using the same strategy than for GUVs.

Besides promoting the fusion process itself, membrane tension can also facilitate the close apposition of two GUVs by favouring partial NP wrapping over complete engulfment [80]. At the interface between two GUVs, SiO_2 NPs might get partially wrapped by both membranes and promote their adhesion. This idea is supported by a recent study which has shown that gold nanoparticles and silica nanoparticles partially wrapped by the membrane can promote the adhesion of GUVs, while complete wrapping induces vesicle tubulation and collapse [75].

Note that from the confocal microscopy images we are only counting the fusion events occurring between oppositely labelled GUVs, but fusions between GUVs labelled with the same dye are also taking place. In our samples, a Rh-GUV has the same probability to fuse with a DiO-GUV than with another Rh-GUV, and the same applies for a DiO-GUV. Therefore, the proportion of GUVs undergoing fusion in our samples is, in theory, double than the quantified in the images. Also note that the proportion of fused GUVs is likely lower than that observed in LUV experiments due to the much larger GUVs exhibiting limited diffusion compared to LUVs, significantly reducing the number of collision events between these vesicles, which are required to facilitate membrane adhesion and fusion.

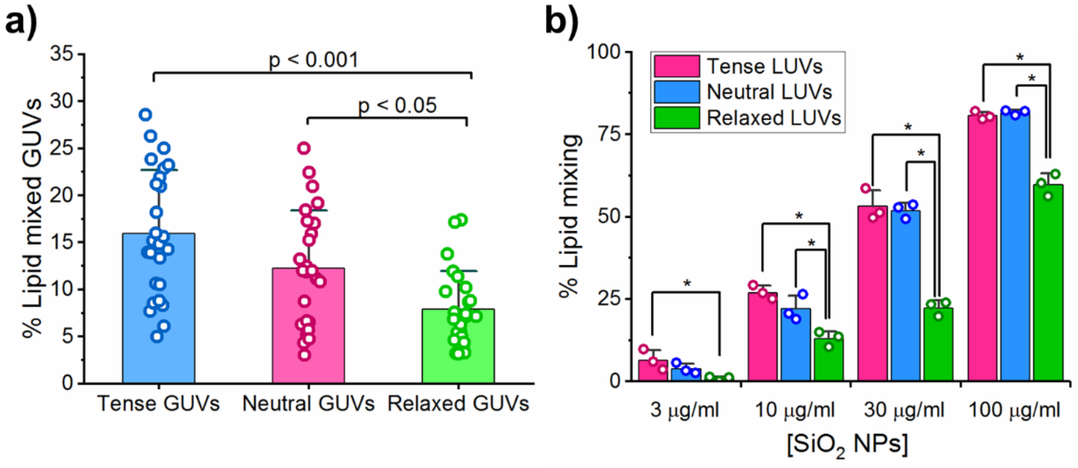

Figure 5.3. Impact of membrane tension on the efficiency of SiO_2 NPs-triggered fusion. a) Percentage of lipid mixed GUVs observed in confocal microscopy images depending on the membrane tension after incubation with 25 µg/ml SiO_2 NPs. The bars show the mean and the error bars the standard deviation. The overlayed circles represent the proportion of lipid mixed GUVs in each image analysed (Tense GUVs = 26 images; Neutral GUVs = 25 images; Relaxed GUVs = 24 images). b) Effect of membrane tension on the percentage of lipid mixing of LUVs samples after exposure to SiO_2 NPs for 30 min measured by FRET. The bars show the mean, the error bars the standard deviation and circles indicate each individual measurement. The statistical significance in a and b was tested using a one-way ANOVA with a post-hoc Bonferroni test (in b) $^*p < 0.05$).

5.5 SiO_2 NPs induce fusion of GUVs via three different pathways

With the aim of getting a further mechanistic insight into the processes leading to membrane fusion, we perform additional real-time confocal microscopy experiments to record single fusion events between Rh-GUVs and DiO-GUVs. These experiments provide information about intermediate states as well as the kinetics of the fusion process by detecting the lipid mixing between GUV pairs.

First, we localise GUV pairs composed of one Rh-GUV and a DiO-GUV which show only red and green fluorescence, respectively. After SiO_2 NPs are added to the sample, we monitor changes in fluorescence intensity in each channel over time at the interface between vesicles and the more distal regions of each GUV. Our observations show that once SiO_2 NPs interact with a pair of GUVs, the vesicles adopt different intermediate states characterised by the degree of lipid mixing before their eventual fusion. The fusion process begins with a localised merging of the outer leaflets of the apposed GUVs as a result of high local curvature and lipid packing defects induced by the SiO_2 NPs. The resulting structure would be a fusion stalk where the inner monolayers of the neighbouring membranes form a bilayer in a small region where the GUVs are docked. The outer leaflets thus reorganise themselves into a highly bent monolayer, which would be expected to begin to merge [237]. From this point, depending on the different intermediate states and morphological transitions that GUVs experience, we identify three main fusion pathways mediated by SiO_2 NPs.

Direct Full Fusion. In the first pathway, no or marginal intervesicular lipid exchange is observed before the GUVs fuse. The membrane breaks at one edge of the interface and the GUVs suddenly fuse. Immediately following fusion, the lipids from the original vesicles are observed to be not yet mixed, and the new GUV shows two easily distinguishable hemispheres, one green and one red, which then mix rapidly in the newly merged membrane (Fig. 5.4, Supplementary Movie 5.4). The interaction of

SiO_2 NPs with the membrane of the GUVs would induce membrane defects which generate large elastic stress at the rim of the docking region. The stalk presumably originates at the edge of the boundary region but the persistent elastic stress would conceivably compel the membrane to break, forming a pore that would be anticipated to expand laterally along the perimeter of the docking zone. Consequently, the membrane region that was separating the individual GUVs would get trapped inside the new GUV and therefore reorganise to avoid exposure of hydrophobic lipid tails, forming an intraluminal vesicle (Fig. 5.4 and 5.2b).

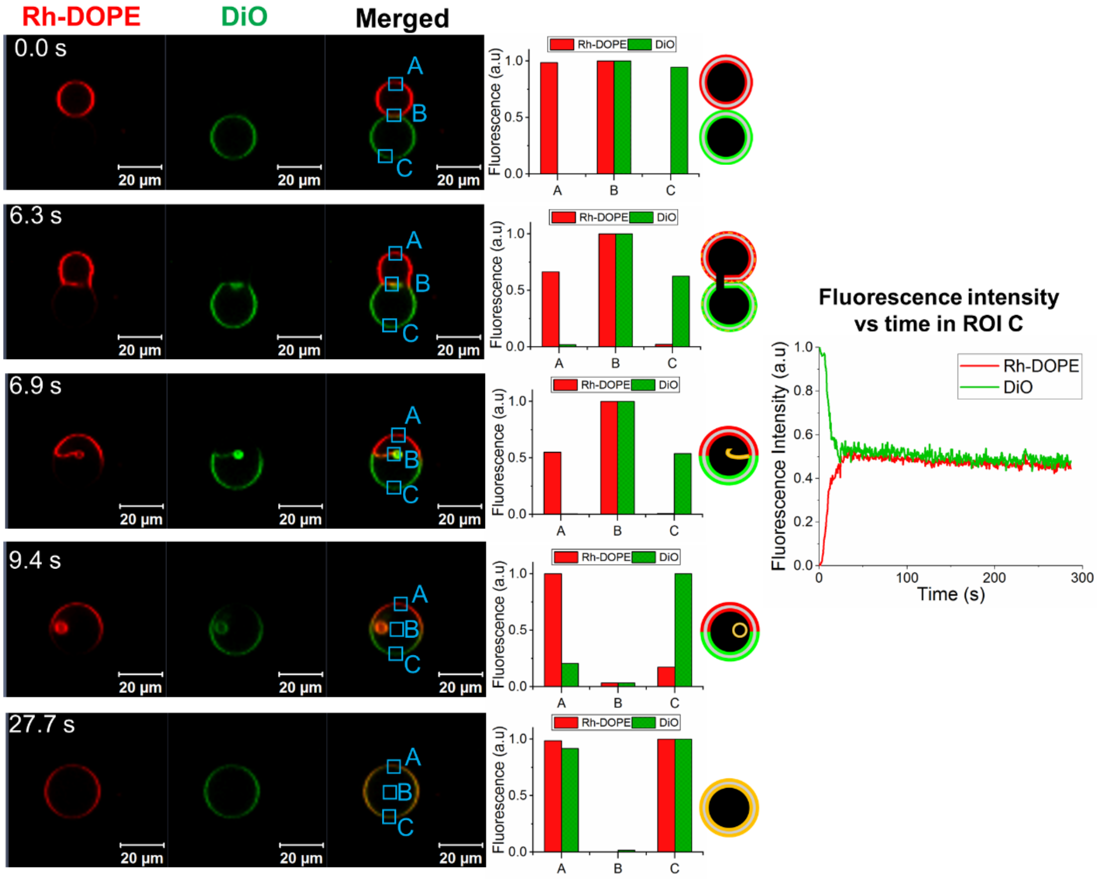

Figure 5.4. Fusion of GUVs *via* the direct full fusion pathway. Confocal microscopy images show the state of the GUVs at particular stages of the process. DOPC GUVs are labelled with Rh-DOPE (red) and DiO (green). The bar plots show the fluorescence intensity of each dye measured at the ROIs indicated by the blue boxes. Cartoons are schematic representations of the lipid mixing and topological transformations occurring at that particular time point. The bar plots indicate that lipid mixing occurs after the GUVs fuse. The membrane boundary gets trapped in the final GUV and reorganise originating an intraluminal vesicle. The line plot displays the evolution of the fluorescence intensity in both channels over time at the ROI C.

A similar fusion mechanism was reported by Tanaka *et al.*, who observed that trivalent lanthanum ions (La^{3+}) induce the fusion of DOPC GUVs [238]. They propose that the outer monolayer of the membranes merge at one edge of the region, where membranes are in contact, and this destabilises the packing of the lipid tails that causes the breakage of the membrane, leading to fused GUVs with an intraluminal vesicle. Moreover, previous studies on vacuole fusion mediated by the SNARE complex have proposed that the formation of an intraluminal vesicle during the fusion occurs when the fusion pore forms at one point on the rim of the stalk and expands laterally along the perimeter entrapping a membrane fragment, which becomes an intraluminal vesicle [239, 240]. In one of these studies, Mattie and colleagues showed that the expansion of the stalk into a hemifusion diaphragm inversely correlates with intraluminal fragment formation [240].

Hemifusion – fusion. In this pathway, a gradual bidirectional exchange of lipids between the contacting GUVs is detected before the eventual fusion of the vesicles (Fig. 5.5, Supplementary Movie 5.5). This second fusion pathway resembles the classic fusion model in which the expansion of the stalk into a hemifusion diaphragm precedes the formation of the fusion pore [25, 208]. A hemifusion diaphragm is an intermediate state where the outer monolayers of the fusing GUVs are merged and the inner monolayers form a mixed bilayer at the contact region.

The hemifusion intermediate is detected by the presence of both dyes in the same GUV [209, 241]. Although the resolution of the confocal microscope does not allow us to see whether the dyes are located in the inner or the outer monolayer of the membrane, their fluorescence intensity is indicative of their presence in one or both leaflets of the bilayer. Before the fusion begins, the fluorescence intensity of Rh-DOPE is maximum in the Rh-GUV (bilayer intensity= 1; inner monolayer intensity=0.5; outer monolayer intensity=0.5), where it is present in both membrane leaflets, whereas no Rh-DOPE fluorescence is observed in the initial DiO GUV. When the GUVs become hemifused, as only the lipids in the outer monolayer are mixed, the Rh-DOPE molecules in the outer monolayer of the Rh-GUV diffuse into the outer monolayer of the opposing GUV. Consequently, the dye gets diluted across the merged outer monolayer of the two GUVs. Assuming that the two vesicles have the same size, the relative intensity of Rh-DOPE in the Rh-GUV will now represent 75% of the initial intensity (bilayer intensity= 0.75; inner monolayer intensity=0.5; outer monolayer intensity=0.25) and the relative intensity of Rh-DOPE in the DiO-GUV will be 25% (bilayer intensity= 0.25; inner monolayer intensity=0; outer monolayer intensity=0.25). This is equivalent to saying that when the GUVs are hemifused, the Rh-DOPE fluorescence intensity in the DiO GUV represents the 33% of its fluorescent intensity in the Rh GUV. Depending on the relative sizes of the GUVs this value can vary, but if only the outer monolayers are fused it is always expected to be lower than 50%. The same explanation applies to the fluorescence of DiO but in the opposite direction.

The analysis of the fluorescence intensity in different regions of the GUVs indicate that the lipids of the outer leaflets mix completely before the GUVs fuse, as observed in Figure 5.5 (frame t=239.4 s). The enhanced fluorescence intensity displayed by both dyes at the GUV interface is probably due to lipid condensation at the rim of the hemifusion diaphragm, where the membrane is expected to be highly curved. Images at longer times indicate a further level of lipid mixing, suggesting some extent of interleaflet lipid exchange. Eventually, a fusion pore opens and expands quickly through the hemifusion diaphragm and the GUVs fuse completing a classic hemifusion-fusion pathway. The newly formed GUV progressively adopts the spherical shape typical of vesicles and the lipids get homogeneously distributed across the membrane. In this case, the final GUV does not show the single intraluminal vesicle characteristic from the direct full fusion pathway.

While the hemifusion is taking place, the GUVs slowly shrink and bright dots appear in their lumen, suggesting that lipids are being removed from the membrane by the SiO_2 NPs (Fig. 5.5). Cryo-EM studies have revealed that SiO_2 NPs completely wrapped by the membrane are internalised inside liposomes, showing a supported lipid bilayer coating removed from the membrane of the vesicle [77, 242]. A different investigation by Strobl *et al* showed that SiO_2 NPs are able to cross DOPC membranes and, during the process, they take small membrane sections with them, inducing the shrinkage of the GUV and a rise in its membrane tension [78]. This is very similar to what we observe in our experiments. Hence, the opening of the fusion pore would seemingly be driven by a further increase in membrane tension induced by SiO_2 NPs removing membrane surface area from the GUVs.

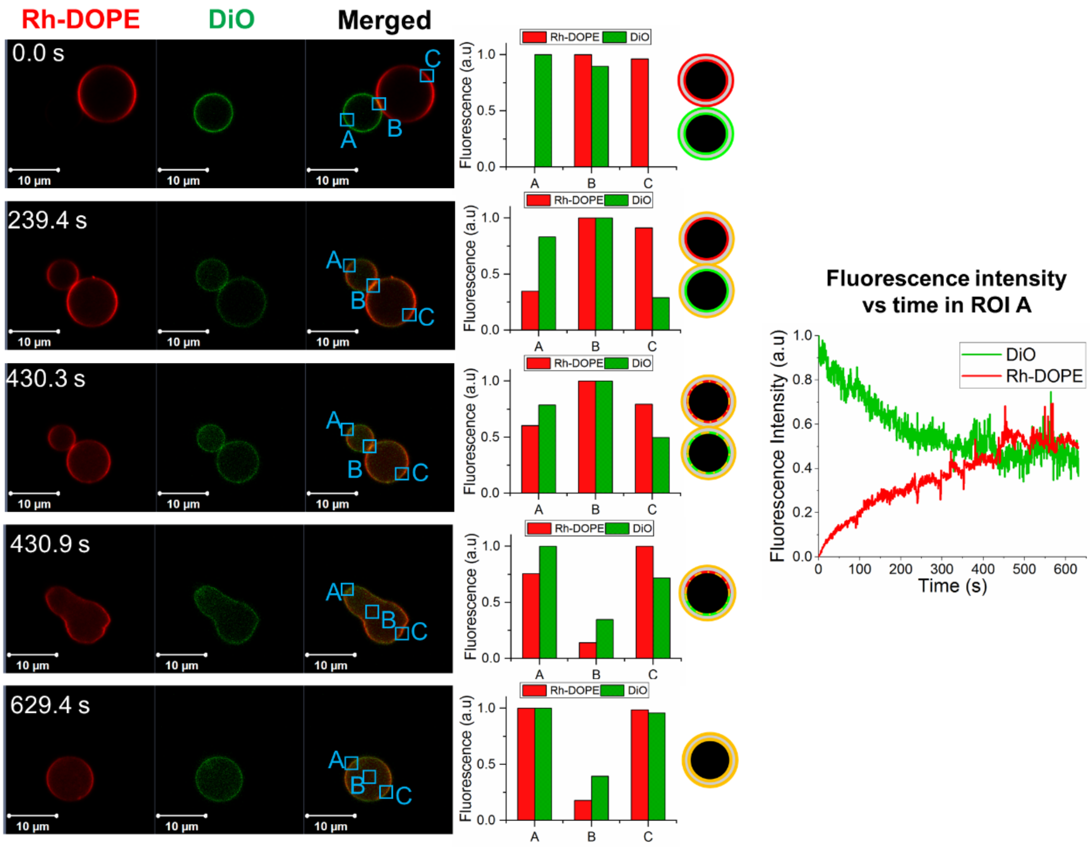

Figure 5.5. Fusion of GUVs *via* hemifusion-fusion pathway. Confocal microscopy images showing intermediate states of the fusion process. DOPC GUVs are labelled with Rh-DOPE (red channel) and DiO (green channel). The bar plots show the fluorescence intensity of each fluorophore measured at the ROIs indicated by the blue boxes. Cartoons are schematic interpretations of the data. The lipid mixing observed before the GUVs fuse indicates that a hemifusion intermediate has formed. Eventually the GUVs fuse. The fluorescence intensity observed in the lumen of the GUVs is likely to proceed from small patches of the membrane removed by the SiO_2 NPs. The line plot displays the evolution of the fluorescence intensity in both channels over time at the ROI A.

Gentle merging. The fusion processes are not always completed by the opening of a fusion pore at the hemifusion diaphragm. On these occasions, one of the GUVs is gradually absorbed by the other and their membranes fuse by a process that we have called gentle membrane merging (Fig. 5.6, Supplementary Movie 5.6). Like in the previous pathway, the fluorescence intensity analysis indicates an initial lipid mixing just in the outer monolayers followed by further lipid mixing in the inner monolayers. However, unlike the hemifusion-fusion pathway, during these events, there is an apparent full bilayer lipid mixing while the two GUVs are still separated. We hypothesise that the elastic stress at which the membranes are subjected is not high enough to drive the opening of a large fusion pore at the hemifusion diaphragm. The tension at the hemifusion diaphragm is presumably stably maintained and the elastic stress could be totally relaxed at the rim of the hemifusion diaphragm by enhanced flip-flop and the formation of transient nanosized pores. As the lipid bilayers mix, one of the apposed GUVs gets progressively smaller and its membrane is transferred to the neighbouring vesicle, which consequently grows until the shrinking GUV is completely engulfed and only one GUV with a fully mixed membrane survives. The result from these events is then a GUV formed by a mixture of the membranes from the two initial GUVs and whose volume equals the sum of the volumes of the initial vesicles (Figure 5.6).

We suggest that once the GUVs become hemifused, before the fusion pore can open, one of the vesicles would be stochastically disrupted by the NPs and that would allow the transfer of its membrane to the apposed GUV. This process would be potentially driven by differential Laplace pressure between the two vesicles as well as other unknown energy minimisation processes. However, from our observations, there is insufficient experimental evidence yet to claim a definitive mechanism that explains the gentle membrane merging events.

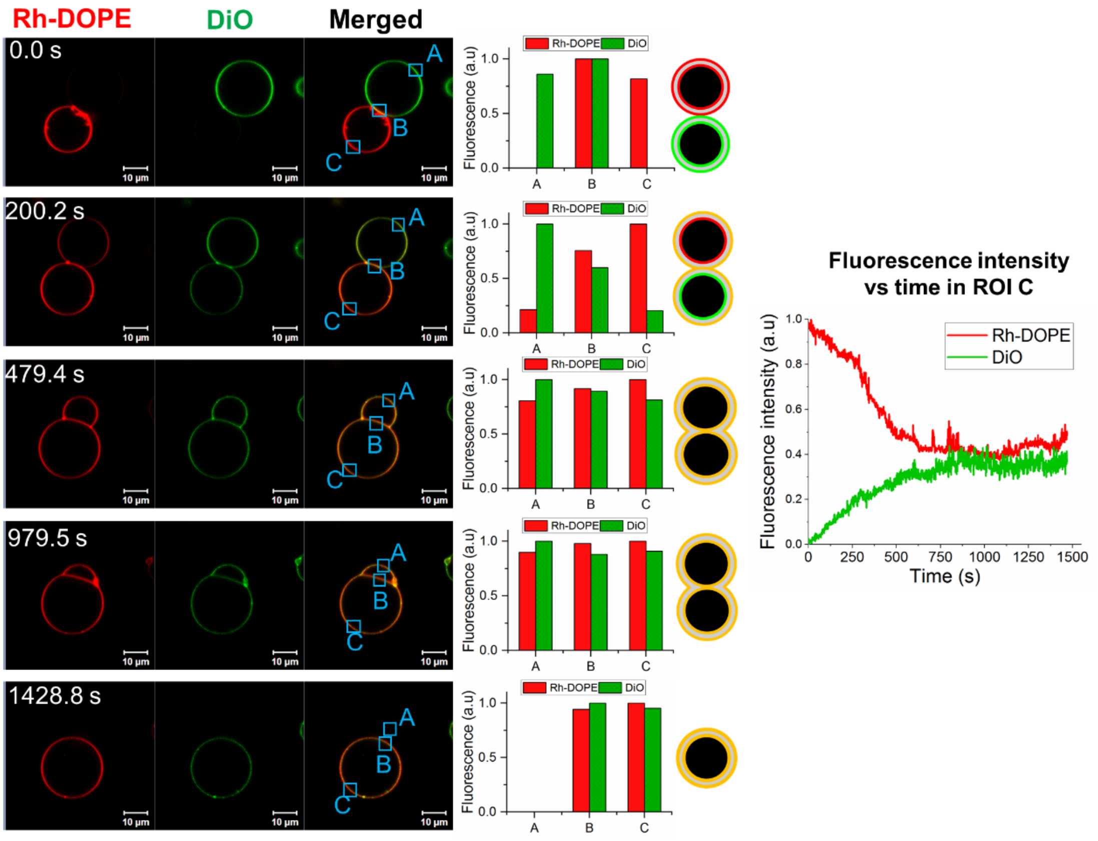

Figure 5.6. Fusion of GUVs *via* gentle merging pathway. Confocal microscopy images show the state of the GUVs at different stages of the process. The DOPC GUVs are labelled with Rh-DOPE (red channel) and DiO (green channel). The bar plots show the fluorescence intensity of each fluorophore measured at the ROIs indicated by the blue boxes. Cartoons are schematic interpretations of lipid mixing membrane configuration state at the stage of the process shown in the micrographs. The lipid mixing observed before the GUVs fuse indicates that a hemifusion intermediate has formed. One of the GUVs gradually shrinks and the other GUV grows consequently. At the same time, their membranes merge gently until forming a single GUV with a mixed membrane. The line plot displays the evolution of the fluorescence intensity in both channels over time at the ROI C.

We also measured the diameter of the GUVs at the beginning and the end of the fusion processes to calculate their volume. The change of GUV volume is reported as the ratio between the volume of the final fused GUV and the sum of the volume of the two initial GUVs:

$$\frac{Volume\ of\ final\ GUV}{Volume\ of\ initial\ GUV\ 1 + Volume\ of\ initial\ GUV\ 2}$$

If this ratio is 1, the volume of the two initial GUVs is conserved in the final GUV, while lower values indicate volume loss during the fusion process. During the direct full fusion and gentle merging pathways there is volume conservation (direct full fusion = 0.92 ± 0.03; gentle merging = 0.93 ± 0.05) (Fig. 5.7). These pathways generate a final GUV with a volume that is approximately equivalent to the sum of the volumes of the initial GUVs. On the other hand, during the hemifusion-fusion pathway there is a significant loss of volume in the final GUV in comparison to the GUVs at the beginning of the fusion process (0.63 ± 0.24) (Fig. 5.7). In this case, we also analysed the change in volume between the final GUV and the GUVs at the time just before the fusion pore opens (denoted as Hemifusion-fusion* in Figure 5.7)) and observed that the opening of the fusion pore is not associated with a volume reduction (0.96 ± 0.07) (Fig. 5.7), but the loss of volume occurs while the GUVs are hemifused, as observed in Figure 5.5 and Supplementary Movie 5.5.

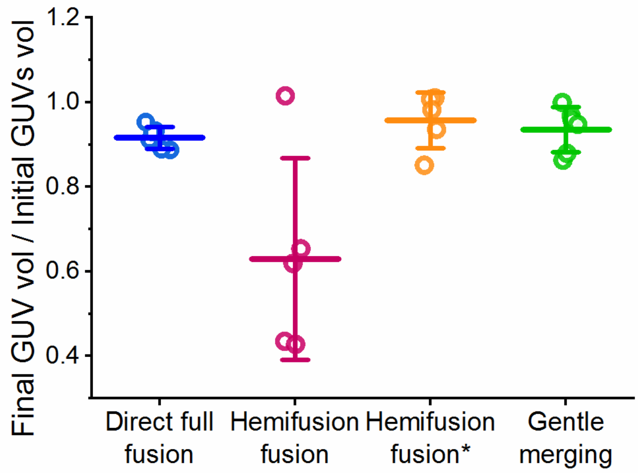

Figure 5.7. Ratio of change of GUVs volume after each fusion pathway (Mean ± SD).

5.6 The rate of lipid mixing is slower in fusion pathways involving hemifusion intermediates

Further analysis of the confocal time series allows quantification of the rate of lipid mixing in the different fusion pathways. For this analysis, we measure the increase in fluorescence intensity over time from the moment when one of the dyes begin to migrate into its neighbouring vesicle. The increase of fluorescence intensity over time was well described by an exponential decay function. The time constant obtained from the empirical exponential fitting was used to calculate the rate of lipid mixing along the membrane surface.

The results summarised in Figure 5.8 show a much slower lipid mixing rate when the fusion pathway involves the formation of a hemifusion diaphragm. The lipid mixing rate calculated from the direct full fusion events (3.22 ± 0.60 $\mu m^2\ s^{-1}$) is consistent with literature values for the lateral diffusion coefficient of DOPC [79, 243], therefore in this pathway the lipid mixing is driven solely by the lateral diffusion of lipids once the vesicles have fused.

In contrast, the lipid mixing rates estimated for the other two fusion pathways are considerably slower than DOPC lateral diffusion, with values of 0.33 ± 0.36 $\mu m^2\ s^{-1}$ for the hemifusion-fusion pathway and 0.48 ± 0.24 $\mu m^2\ s^{-1}$ for the gentle merging. Similar slow diffusion of lipids has been reported previously in protein-free and SNARE-mediated hemifused GUVs [223, 241]. We observe that full bilayer mixing can be reached while the GUVs are hemifused. This bilayer mixing may result from enhanced lipid flip-flop between the membrane leaflets which considerably reduces the rate of lipid mixing compared to lateral diffusion alone. The formation of a stable hemifusion diaphragm implies that the surface area of the inner leaflets of the membranes must be larger than that of outer monolayers. This requires the transport of lipids from the outer leaflet to the inner leaflet *via* flip-flop. The lipid flip-flop would be expected to be particularly enhanced at the rim of the hemifusion diaphragm. In this region, the significant negative curvature of the membrane likely generates a mechanical stress different in each monolayer and the membranes becomes highly unstable. The differential mechanical stress derived from increased membrane curvature as well as local membrane deformations are known to significantly increase the rate of interleaflet lipid transport. [244, 245] Moreover, molecular dynamics simulations have shown that lipid flip-flop is a preferential mechanism to reduce the instability at the junction site of three bilayers and maintain a metastable hemifusion diaphragm [246].

Another potential contribution to bilayer lipid mixing involves the formation of transient nanoscopic pores in the membrane, which allows short-lifetime pulses of lipid transfer between monolayers. Such interleaflet lipid exchange would relax the stress in the membrane by the net removal of lipids from the compressed outer monolayer to the expanded regions of the inner leaflets during the bidirectional diffusional exchange of lipids across the open pore.

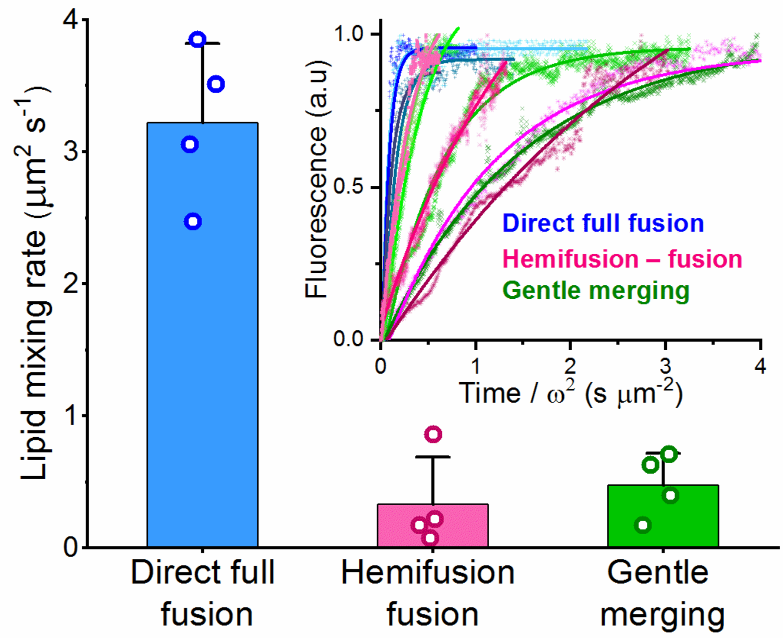

Figure 5.8. Rate of lipid mixing during each fusion pathway. The calculated average lipid mixing rate for the fusion events via direct full fusion is 3.22 ± 0.60 $\mu m^2\ s^{-1}$ whereas the hemifusion-fusion pathway and the gentle merging show reduced lipid mixing rates, 0.33 ± 0.36 $\mu m^2\ s^{-1}$ and 0.48 ± 0.24 $\mu m^2\ s^{-1}$, respectively (The bar plot show the mean ± SD with the individual datapoints overlayed). The inset plot shows the normalised fluorescence intensity of the dye when it begins to colonise a membrane where it was not present initially as a function of time per unit area. The curves of individual events were fitted using an exponential function (see methods) to estimate the rate of lipid diffusion.

5.7 Discussion

In this work, we introduce a protein-free membrane fusion platform based on the ability of 30 nm SiO_2 NPs to trigger membrane curvature and tension that mimics the physicochemical effects of natural protein complexes for membrane fusion. Initial FRET experiments performed in bulk LUV populations show a significant increase in intervesicular lipid mixing dependent on the concentration of SiO_2 NPs in solution. The fusogenic activity of SiO_2 NPs is confirmed by direct imaging of GUVs using confocal microscopy, which also allows to identify intermediate states adopted by the membranes during the fusion process.

Figure 5.9 summarises the proposed nanoscale molecular mechanisms that occur as SiO_2 NPs induce the contact and fusion of two membranes. Based on our observations, we propose a scenario where membrane tension is the principal driving force of the fusion events. This view agrees with previous studies, including theoretical models [175, 208], simulations [234, 235, 247] and experimental investigations [236, 248]. In our system, the fusion starts when SiO_2 NPs in suspension interact with closely localised GUVs. This interaction likely favours the close contact between the membranes of two GUVs by inducing local changes in membrane curvature. Molecular simulations have shown that any protein complex located between two opposing membranes generates a local membrane curvature that promotes the close approximation of the opposing leaflets needed to begin the fusion process [249]. Additionally, 30 nm SiO_2 NPs affect the membrane order and might induce lipid packing defects (See **Chapter 4**). The negative surface charge of SiO_2 NPs is predicted to cause a reorientation of the DOPC headgroup dipole generating an electrostatic condensation of the area per lipid in the outer membrane leaflet, which would generate an increase in membrane tension [250].

The fusogenic activity of SiO_2 NPs relies on its capacity to generate a membrane tension high enough to overcome different energy barriers during the fusion process. The energy required to initiate the fusion and form the fusion stalk has been estimated to be in the range of 20-35 k_BT [251, 252]. The rise in membrane tension generates elastic stress which, along with high local membrane curvature and lipid packing defects, can result in energetically unfavourable exposure of hydrophobic lipid tails to the aqueous medium. The elastic stress is released by the reorganisation of the membranes in the boundary between the GUVs so the exposed hydrophobic region of one membrane matches the hydrophobic region of the inner leaflet of the adjacent membrane [209]. This leads to the formation of the fusion stalk where the outer monolayers start merging.

After the stalk is formed, GUVs can follow three different pathways that lead to membrane fusion: i) direct full fusion, ii) hemifusion-fusion and iii) gentle merging. The direct full fusion is the fastest but more energetically demanding process. The opening of the fusion pore directly from the stalk implies an energy cost of around 100 k_BT [251]. Hence a significant increase in membrane tension would be needed for the membranes to fuse immediately after the stalk formation. Such a high energetic cost implies that the membrane tension acquired is not always sufficient to trigger this pathway. However, instead of aborting the process, the system finds an alternative route, the hemifusion intermediate, which is slower but requires less energy. The energy barrier for the expansion of the stalk into a hemifusion diaphragm varies between 15 and 35 k_BT depending on the lipid composition, the membrane tension and the spontaneous curvature [251, 253]. At this point, a further increase of the membrane tension can drive the opening and expansion of the fusion pore at the hemifusion diaphragm to complete the hemifusion-fusion pathway. If the energy needed for the opening and expansion of a fusion pore at the hemifusion diaphragm (35-40 k_BT) [251] cannot be overcome, the process finishes *via* gentle membrane merging. At this lower tension, the probability of a stochastic disruption of the membrane of one GUV before full fusion increases. Once one GUV is disrupted, it begins to shrink while the other grows and uptakes lipids from the disrupted one. This process is likely to be initially driven by a differential Laplace pressure inside each GUV, but other forces are needed for the process to advance until the membranes fully merge into a final bigger GUV.

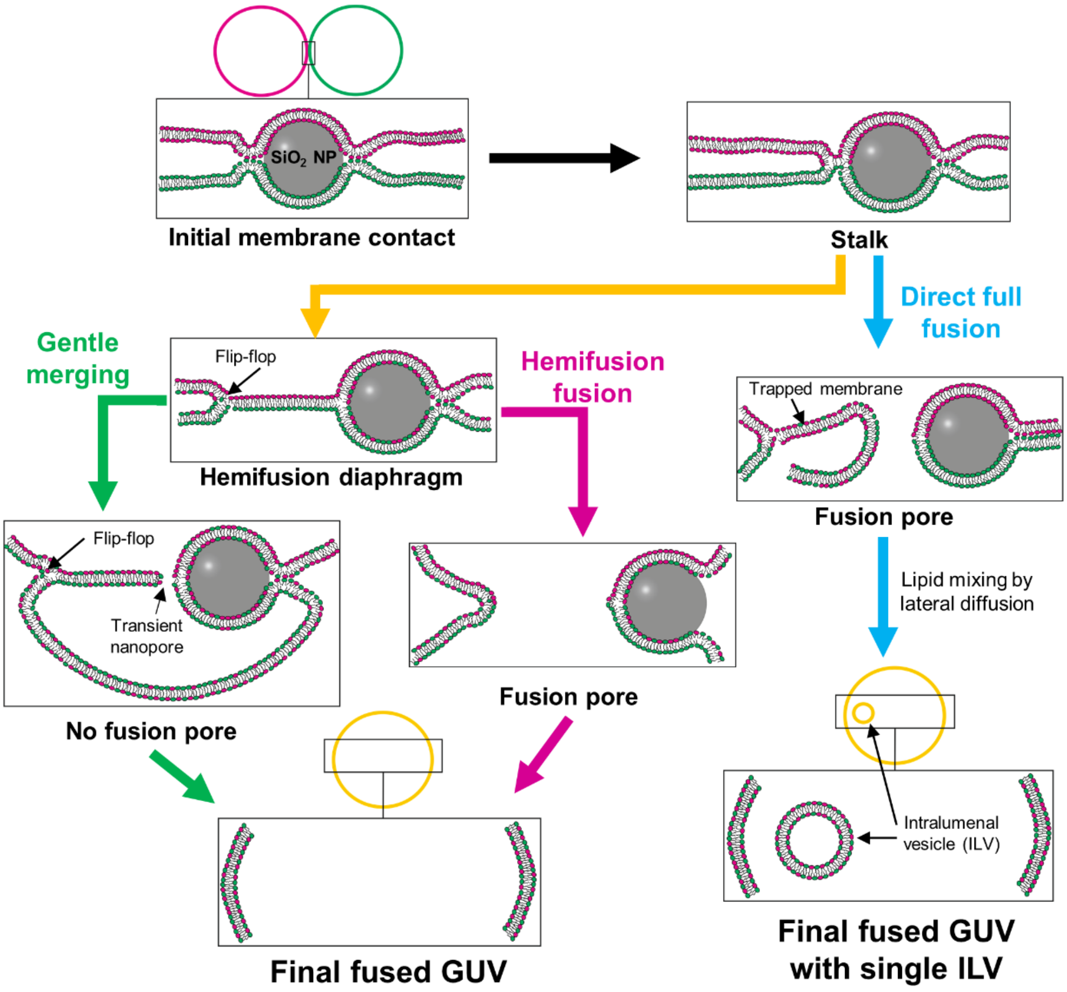

Figure 5.9. Schematic representation of membrane transitions occurring at the docking region during fusion events triggered by SiO_2 NPs. The SiO_2 NPs facilitate the initial contact between two membranes and induce high local curvature, increased tension and lipid packing defects. This promotes the formation of a stalk. At this point, a fusion pore can form directly from the stalk leading to a sudden full fusion of the GUVs. After the GUVs fuse, the lipids in the membrane mix *via* lateral diffusion and the membrane previously placed at the boundary is trapped in the lumen and forms an intraluminal vesicle (Sudden full fusion pathway). The stalk can also expand into a hemifusion diaphragm stabilised by enhanced lipid flip-flop at its rim. If a fusion pore opens at the hemifusion diaphragm the fusion process is completed (Hemifusion-fusion pathway). However, if this does not happen the hemifusion diaphragm persists stabilised by flip-flop and transient nanopores. In this case, one of the GUVs is gradually absorbed by the other one and their membranes gently merge (Gentle membrane merging pathway).

The effect of membrane tension in the fusion efficiency was evaluated in LUVs and GUVs using FRET and confocal microscopy, respectively. Our results show a higher proportion of vesicles fused or undergoing fusion when the tension of their membranes was osmotically increased and vice versa. Unfortunately, our experimental approach does not allow us to quantify the proportion of fusion events taking place through each different pathway, so different strategies might be considered in the future to overcome this limitation and get more information about biophysical parameters influencing which fusion pathway is going to be followed.

Beyond the balance of adhesion and bending energies, the size of the nanoparticle may also be important in obtaining fusogenic activity. In the study by Zuraw-Weston *et al.,* where they investigated the topological transitions experienced by charged GUVs upon interaction with oppositely charged NPs, they used smaller NPs than the SiO_2 NPs LUDOX TM-50 employed in our study, some of which with a radius (*r*) comparable to the thickness of the lipid bilayer [75]. Membrane rupture and GUV destruction were observed *for* $wr^2/\kappa_b > 0.6$ but membrane fusion was not reported [75]. Notably, we propose that $wa^2/\kappa_b \sim 2$ is required for membrane fusion, a regime that was not explored in the study by Zuraw-Weston *et al.* This suggests that there may be a size range optimal to induce membrane fusion such that the radius of curvature of the nanoparticle is not so great that the membrane ruptures during partial wrapping.

Since the effect that SiO_2 NPs of a given size produce in lipid membranes depends on the balance between adhesive forces and the elastic properties of the membrane, changes in the solution environment (such as ionic strength, pH, temperature), SiO_2 NPs surface functionalisation and membrane composition might affect the fusogenic activity of 30 nm SiO_2 NPs. Modifications of such parameters have not yet been investigated, but new experimental conditions might require changing the SiO_2 NP size to maintain the right balance between adhesion and bending energies needed to obtain fusogenic activity. In Chapter 4 we showed that the presence of a BSA corona coating these NPs suppresses their fusogenic activity. The BSA corona would lower the adhesion energy of SiO_2 NPs which consequently become unable to induce lipid packing defects, membrane curvature and increased membrane tension required to initiate the fusion events

A current major challenge in the study of membrane remodelling processes is understanding the role that Gaussian curvature plays in them. The experimental investigation of Gaussian curvature is very challenging and requires membrane systems whose topology can be tightly controlled [249]. The fact that the same fusogen can induce membrane fusion *via* different pathways represents an advantage for the study of membrane fusion mechanisms because it implies that by changing particular conditions (membrane composition, vesicle shape, ionic strength, divalent cations such as Ca^{2+}, *etc*.) the system could be tuned to favour a specific fusion pathway over the others and give information about the influence of specific parameters, such as membrane curvature and tension, in the fusion process. Also, these SiO_2 NPs are inexpensive to produce, can remain colloidally stable in solution for long periods of time and its surface can be easily functionalised to increase or decrease their affinity for the membrane [67]. Therefore, SiO_2 NPs are a promising synthetic biology tool for triggering membrane fusion in a broad range of experimental scenarios.

5.8 Conclusions

Here we have investigated the mechanisms by which SiO_2 NPs of 30 nm are able to mediate membrane fusion. The size of these NPs provides them with the ability to induce a combination of membrane curvature, increased membrane tension and lipid disorganisation which initiate fusion of closely localised membranes. The fusion mediated by SiO_2 NPs occurs *via* three different pathways characterised by the intermediate states adopted by the membranes during the process. According to our hypothesis, the tension acquired by the membranes is the principal factor that selects which fusion pathway is followed.

Our results offer the prospect of using SiO_2 NPs as a nanotechnological tool in synthetic biology to create more complex model membrane systems, which better mimic the properties of cell membranes. As a proof of concept, in the next chapter, we will use these SiO_2 NPs to generate phase separated membranes by fusing two single-phased GUVs and analysing the remarkable membrane reorganisation phenomena that occur during the process.

Chapter 6:
Phase separated GUVs generated by fusion

6.1 Introduction

Biological membranes are formed by a myriad of different lipids which provide them with particular biophysical properties and functionality. Such functionality is often associated to the formation of membrane domains where saturated phospholipids with long acyl chains and cholesterol accumulate and create the right conditions to recruit membrane proteins and initiate signalling pathways [20, 254-257].

The lateral organisation of lipids within membranes which leads to the formation of membrane domains is commonly studied in multicomponent model membranes, usually GUVs and GPMVs, which exhibit a behaviour reminiscent of living cell membranes [17, 257, 258]. Such multicomponent vesicles are usually prepared directly from solutions containing a mixture of the desired lipids. However, alternative methods to induce phase separation in initially homogeneous membranes can provide more precise control over the final composition of the vesicles and a better understanding of the domain formation process. Membrane fusion represents an effective strategy to fulfil this purpose. Bezlyepkina *et al* used electrofusion to generate three-component GUVs from simpler vesicles and determine the tie lines of ternary lipid mixtures in the final GUV [259]. Other studies have also employed membrane fusion to generate GUVs with liquid disordered (L_d) and liquid ordered (L_o) coexisting domains [227, 260].

In the previous chapter, we showed that 30 nm SiO_2 NPs effectively trigger fusion of DOPC membranes by imposing a balance between membrane curvature and increased lateral tension in the membranes. However, L_o membranes are more resistant to be deformed [138], consequently, the fusogenic activity of SiO_2 NPs might be reduced if one of the membranes participating in the fusion is in the L_o phase. In this chapter, we will test the ability of the same 30 nm SiO_2 NPs to mediate membrane fusion between a liquid disordered membrane and a liquid ordered membrane with the final aim to generate phase separated GUVs. Phase separation is detected using confocal microscopy to image GUVs labelled with phase partitioning dyes and Laurdan to determine the physical state of the membrane.

6.2 SiO_2 NPs mediate fusion between L_d and L_o GUVs

To test whether SiO_2 NPs of 30 nm can be used to generate phase separated GUVs by fusing single-phase vesicles, we mixed, in a 1:1 volume ratio, DOPC GUVs with GUVs composed of 7:3 mol ratio DPPC and cholesterol (Chol). The experiments were performed at room temperature, below the melting temperature of DPPC (T_m= 41ºC) so the DPPC/Chol (7:3) membranes adopt a liquid ordered phase. Then, we incubated the GUVs with 25 µg/ml SiO_2 NPs of 30 nm diameter and used fluorescence confocal microscopy to image the samples. To visualise the phase state of the membrane we incorporated Rh-DOPE (0.5 mol%) into the DOPC GUVs and naphthopyrene (Npy) (1 mol%) into the GUVs made of DPPC and cholesterol. These dyes are commonly used as membrane phase markers as Rh-DOPE preferentially partitions into the L_d phase of the membrane and Npy into L_o domains [261].

From confocal microscopy time series, we observe that 30 nm SiO_2 NPs promote fusion between a L_d GUV and a L_o GUV. These results demonstrate that the fusion ability of 30 nm SiO_2 NPs is not limited to just DOPC membranes but they are also effective when one of the membranes is stiffer, as in the case of DPPC/ Chol GUVs. Importantly, once fused the membrane of the new GUV lowers its free energy by remaining phase separated displaying large L_d and L_o micro-domains (Fig. 6.1, Supplementary movie 6.1). Our observations are consistent with previous studies on membrane phase separation in DOPC/ DPPC/ Chol GUVs [262]. Considering that the initial GUVs are of the same size, the final membrane composition of the fused GUV is predicted to be 50:35:15 DOPC/ DPPC/ Chol. At room temperature, this ternary lipid composition is in the liquid-liquid immiscibility region of the phase diagram where L_d and L_o domains coexist in the membrane [262]. The fused membrane shows a L_o domain rich in DPPC and cholesterol which is expected to be more densely packed, less fluid and thicker than DOPC-rich L_d domains. Three-dimensional images of the phase separated GUVs show some darker patches in the L_o phase which might indicate the formation of disordered domains within the L_o phase from which the L_o dye gets excluded (Fig. 6.1). The lipids segregate into large domains to minimise the line tension at the phase boundary generated by an energetically unfavourable exposure of the hydrophobic acyl chains which arises from a thickness mismatch at the boundary between L_d and L_o domains [263].

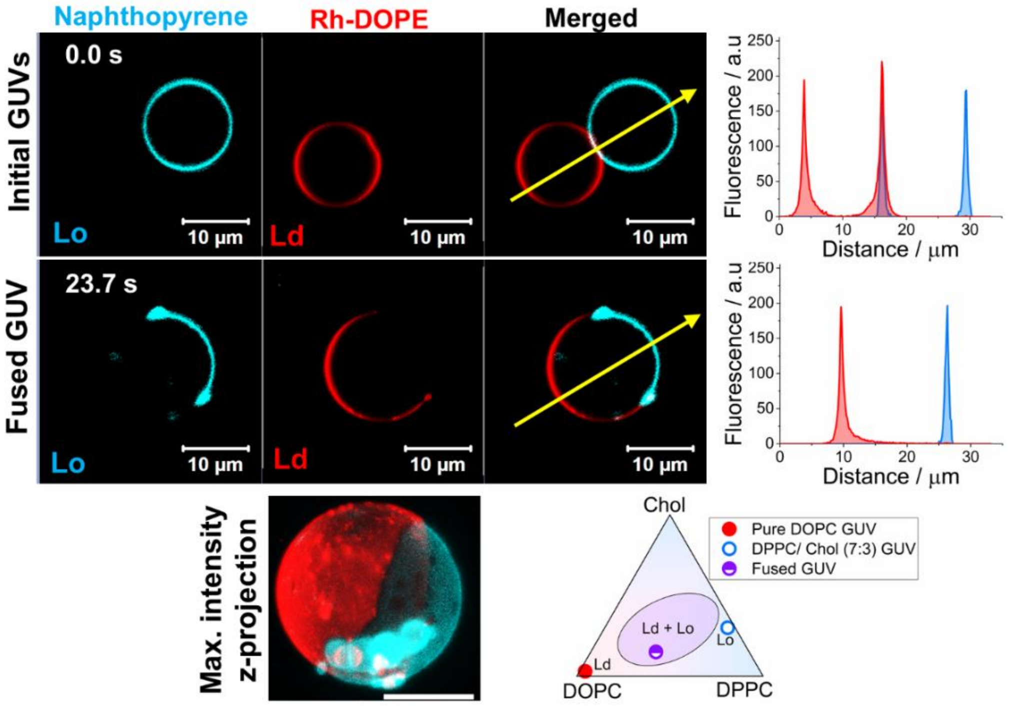

Figure 6.1. Confocal microscopy images of L_o and L_d GUVs before and after fusion. L_o DPPC/Chol (7:3) GUV is labelled with naphthopyrene (Npy) (cyan) and L_d DOPC GUV is labelled with Rh-DOPE (red). After fusion Npy partitions into the L_o phase and Rh-DOPE into the L_d phase. Plots in the right show the fluorescence intensity profile of Rh-DOPE (red) and Npy (blue) along the yellow arrow shown in the micrographs. Bottom image shows a 3-D maximum intensity projection of a phase separated fused GUV, dye excluding patches are observed in the L_o phase and potentially indicate disordered domains formed within the L_o phase. The phase diagram is not empirical, but an approximation for illustrative purposes to show the position of pure DOPC (red circle), DPPC/Chol (7:3) (blue circle) and the theoretical composition of a fused GUV assuming equal surface area of the initial vesicles (purple circle). The shaded region indicates the approximate liquid-liquid coexistence region.

Next, using the tile scan function of the confocal microscope, we quantified the proportion of phase separated GUVs generated after incubating the vesicles with the SiO_2 NPs to test whether the fusion efficiency is affected by the introduction of L_o membranes in the system. The images show an average of 11.2% GUVs phase separated, a very similar proportion to the fused GUVs observed in samples containing just pure DOPC GUVs (12.25 %) (Fig. 6.2). There are two plausible explanations for these results. The first one is that although the bending rigidity of L_o membranes is predicted to be from 1.25 times to even an order of magnitude higher than L_d membranes [21, 138], the adhesion strength of the 30 nm SiO_2 NPs to the PC bilayer is still sufficient to overcome the energy cost required to bend the membrane, and so the NPs can adhere to both DPPC/Chol and DOPC membranes and induce their fusion. The other possibility is that the bending of only one of the membranes (the DOPC one in this case) in the adhesion site is sufficient to trigger fusion,

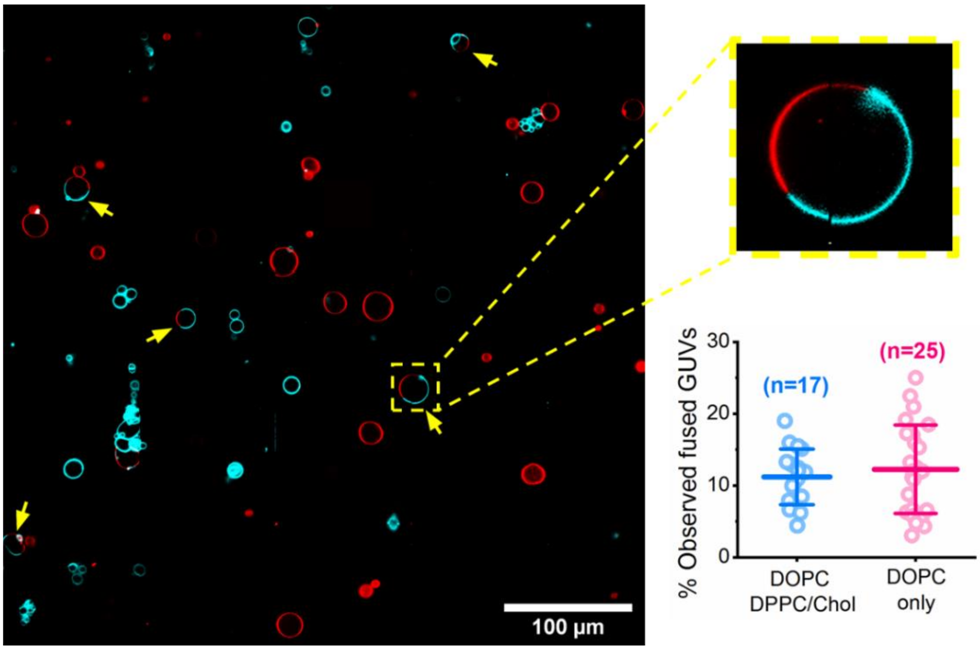

Figure 6.2. Example of confocal microscopy tile scan after incubating the GUVs with 25 µg/ml SiO_2 NPs. Yellow arrows highlight the phase separated GUVs. The top left image shows a zoomed-in phase separated GUV. The plot shows the percentage of fused GUVs observed in the tile scans in samples of DOPC GUVs mixed with DPPC/Chol (7:3) GUVs in a 1:1 volume ratio (blue) and in samples of DOPC GUVs where half of the GUVs are labelled with Rh-DOPE and the other half with DiO (magenta). Data are presented as mean ± SD, circles indicate the percentage of fused GUVs observed in each image (number of individual datapoints indicated in the plot). The proportion of observed fused GUVs in the two conditions does not show statistical difference (one-way ANOVA with a $p < 0.5$ post-hoc Bonferroni test)

Further analysis of the membrane phase was performed using Laurdan spectral imaging. In this case, the DOPC and the DPPC/ Chol (7:3) GUVs were labelled with 0.5% mol Laurdan. In addition, 0.1 mol% Rh-DOPE was also added to the DOPC lipid mixture as a L_d phase marker to show the correlation between L_d phase and GP values in fused GUVs. Mean Laurdan GP values of control DOPC GUVs are around -0.45, while the GP values of DPPC/ Chol GUVs are much higher, peaking at 0.30, as expected for more ordered membranes [151]. After fusion, the Laurdan GP map clearly shows two easily distinguishable regions in the membrane, which correspond to the L_o (positive GP values) and L_d (negative GP values) domains. The Rh-DOPE fluorescence signal in the fused GUV matches perfectly with the region of the membrane displaying negative GP values (Fig. 6.3).

Compared to the control DOPC GUVs, the L_d domains of the phase separated GUVs generated by fusion show significantly higher (less negative) average GP values (GP= -0.10), which indicates a denser lipid packing (Fig. 6.3). After fusion, the lipids in the new phase separated vesicle redistribute across the membrane, and the equilibrium lipid composition of each coexisting domain in the fused GUV is determined by the tie lines of the phase diagram. The lipid redistribution is governed by the gradient in the chemical potentials of the lipids which at equilibrium must be the same in each phase [259]. Consequently, in the equilibrium, the L_d phase of the fused GUV will no longer be a pure DOPC membrane but a DOPC-rich domain, and the same will occur with the L_o phase, which will be enriched in DPPC and cholesterol but not exclusively formed by these lipids. We therefore attribute the higher GP of the L_d domains of the phase separated GUVs to a lateral diffusion of DPPC molecules from the L_o domains to the disordered membrane phase. Additionally, cholesterol molecules are also expected to diffuse into the L_d phase, but to a lesser extent due to their slight preference for L_o domains [259]. In the L_d phase, cholesterol is known to produce a tighter packing of the DOPC lipids in the membrane [264, 265]. The redistribution of cholesterol is also envisaged to induce denser packing of the DPPC lipids in the ordered phase

[262, 266], however, the GP values observed in the L_o domains of the fused GUVs are slightly less positive than in the control DPPC/ Chol GUVs. This is due to the migration of DOPC molecules into the L_o domains, as dictated by the tie lines in the L_d-L_o coexisting region of the phase diagram. This capacity of low concentrations of DOPC molecules to disrupt the dense packing of DPPC lipids in gel-phase membranes and generate more disordered phases has been demonstrated using wide-angle X-ray scattering (WAXS)[266].

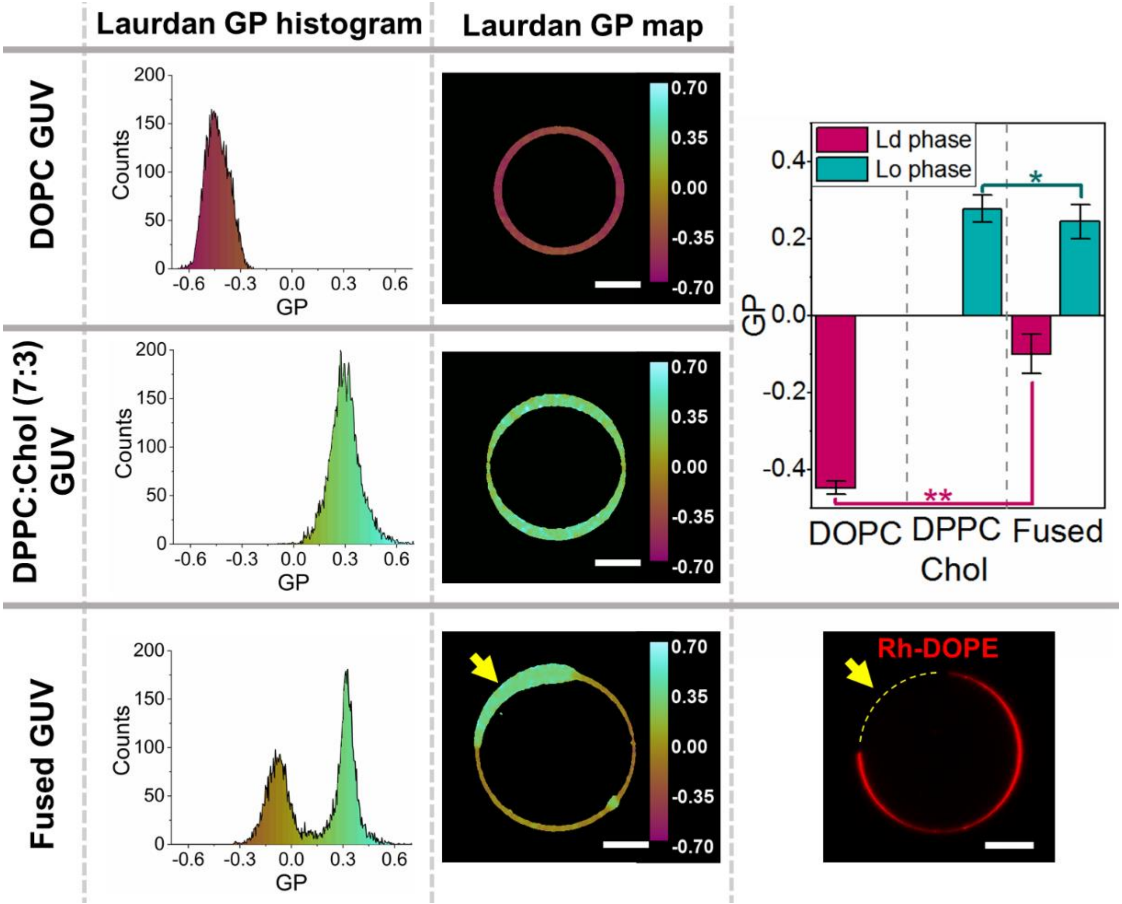

Figure 6.3. Laurdan GP maps and histograms of DOPC GUV (top) DPPC/Chol (7:3) GUV (middle) and fused phase separated GUV (bottom). Rh-DOPC fluorescence in fused GUV (bottom left image), which partitions into the L_d phase, matches with lower values of Laurdan GP while it is excluded from the L_o domain which shows positive GP values. Bar plot shows average GP values ± SD of L_d and L_o phase in DOPC GUVs (n= 26), DPPC/Chol (7:3) (n=16) GUVs and fused phase separated GUVs (n=26). The average GP value of the L_d phase is significantly less negative in the fused GUVs (GP= -0.10±0.05) than in the pure DOPC GUVs (GP= -0.45±0.02). The average GP of the L_o phase is slightly higher in the DPPC/Chol (7:3) GUVs (GP= 0.28±0.03) than in the fused phase separated GUVs (GP= 0.24±0.04). The statistical significance was tested using a one-way ANOVA with Bonferroni multiple comparisons test ($^*p \leq 0.05$, $^{**}p \leq 0.01$).

6.3 Fusion between L_o and L_d GUVs always involves opening of fusion pore

In the previous chapter, we identified three fusion pathways by which 30 nm SiO_2 NPs mediate fusion of pure DOPC membranes. We proposed that those pathways are controlled by the mechanical properties of the membranes undergoing fusion, hence changes in the lipid composition of one or both membranes might modify the fusion mechanisms. So, we employed real-time confocal microscopy to record single fusion events between DOPC GUV and DPPC/ Chol (7:3) GUVs. From 41 movies collected, 32 showed completed fusion events. The remaining videos (n=9) were discarded because either the dyes were considerably bleached before full fusion was observed due to the extended exposure to the laser beam (over 15 minutes) (n=7) or the GUVs lost their integrity during the process (n=2).

The analysis of the 31 complete fusion events showed differences compared to the fusion between pure DOPC membranes. In just over half of the movies (n=17) the GUVs experienced a direct full fusion where the fusion occurs before any lipid transfer between the GUVs is detected. In the other 15 observations, the opening of the fusion pore was preceded by a hemifusion intermediate state. A more thorough analysis and discussion of the hemifusion process will be given in the next section. Interestingly, the gentle membrane merging pathway seems to be suppressed when one of the GUVs has a L_o membrane. The reason for the absence of gentle merging membrane events is unclear. One possibility is that the transbilayer asymmetry at the hemifusion diaphragm, formed by a DOPC monolayer and a DPPC/ Chol monolayer, might make the membrane more unstable or increase the membrane tension and thus lower the energy barrier to the eventual opening of the fusion pore. Using flicker spectroscopy, Elani *et al.* demonstrated that asymmetric GUVs, with one leaflet composed of DOPC and the other with POPC, show a significantly increased membrane bending rigidity compared to symmetric bilayers [267]. Theoretical modelling and coarse-grained simulations have also suggested that imbalanced lipid packing in each leaflet of asymmetric membranes can generate a differential lateral stress which can have a strong impact on the mechanical properties of the membrane, including membrane tension, bending rigidity and spontaneous curvature [268].

The absence of gentle membrane merging events is not the only difference between the fusions of L_d and L_o GUVs compared with the fusion of two DOPC GUVs. In every direct full fusion event observed between two DOPC GUVs, the membrane at the contact region got trapped and reorganised into an intraluminal vesicle (ILV) once the vesicles fuse. On the contrary, the intraluminal membrane trapping was never observed when the DOPC vesicles underwent fusion through the hemifusion-fusion pathway. However, in fusions between DOPC GUVs and DPPC/ Chol GUVs the membrane trapping occurs (or not) independently of the fusion pathway followed. We detected this phenomenon in about 47% (8 out of 17) of the direct full fusions and 40% (6 out of 15) of the hemifusion-fusion events. The trapped membrane presents two behaviours which consist of either adopting a curved shape or getting progressively retracted towards its end still in contact with the GUV membrane (Fig. 6.4). Eventually, the intraluminal membrane fragment is reabsorbed back into the surface of the fused GUV. The time it takes for the membrane fragment to be reabsorbed shows high variability, ranging from minutes to less than a second (Fig. 6.4). This varying reabsorption speed might indicate that the membrane at the contact region is always trapped in the fused GUV but it cannot always be observed in the movies because it can occur faster than the frame rate acquisition of the confocal microscope, which in our movies ranges between 0.30 s/frame and 0.64 s/frame.

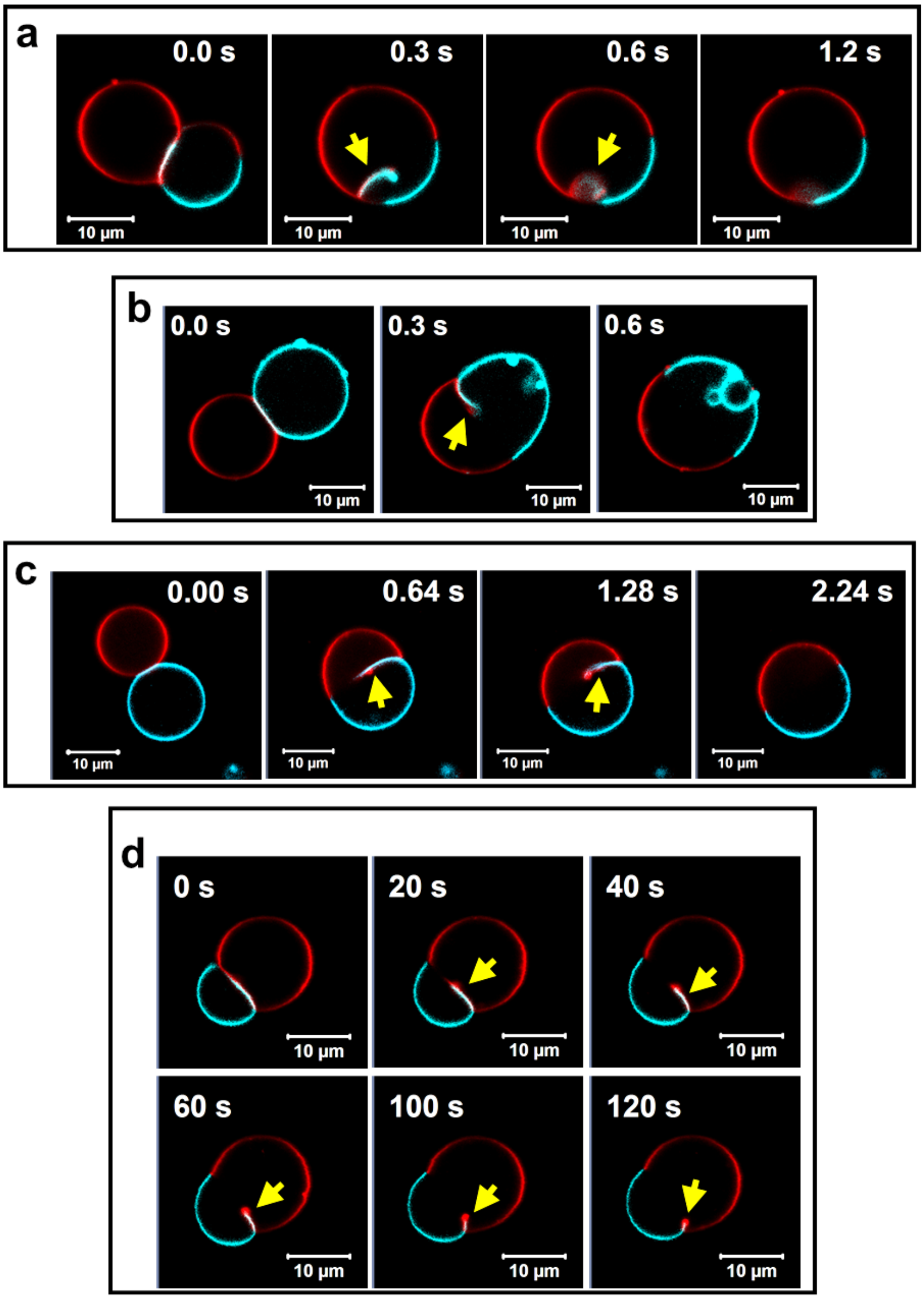

Figure 6.4. Confocal microscopy time-lapse images showing the fate of the membrane fragment trapped within fused GUVs. Once trapped inside the fused GUV, the membrane previously situated at the contact region adopts a curved shape (a) or retracts towards the GUV membrane (b-d). The retraction speed is highly variable ranging from less than a second (b), a few seconds (c) to even a couple of minutes (d). Yellow arrows denote trapped membrane fragments.

6.4 Asymmetric domains and interleaflet coupling in hemifused GUVs

As mentioned above, in nearly half of the fusion events observed the GUVs become hemifused as indicated by the diffusion of lipids from one GUV to the opposing vesicle. The reorganisation of the lipids in the hemifused GUVs reveals two remarkable biophysical phenomena: membrane asymmetry and interleaflet coupling. Figure 6.5 shows time-lapse confocal microscopy images of two GUVs during hemifusion along with fluorescence intensity data in different regions of their membranes. Maximum fluorescence intensity of rhodamine (Rh_{max}) corresponds to regions of the membrane where both leaflets are formed mainly by L_d DOPC lipids, whereas in L_o bilayers the fluorescence intensity of the L_o marker Npy is maximum (Npy_{max}). If the dyes were present in only one of the membrane monolayers, their fluorescence intensity would be 50% lower than those maximum values.

When the GUVs become hemifused, Rh-DOPE fluorescence emerges in a region of the L_o membrane. The Npy fluorescence intensity in that membrane region is simultaneously reduced to about half compared to its fluorescence in the rest of the membrane, Npy_{max} (Fig 6.5, Supplementary movie 6.2). Assuming that only the outer leaflets of the GUVs are fused, the fluorescence intensity levels suggest that the L_o marker is only present in the inner membrane leaflet while the outer monolayer is enriched with DOPC lipids transferred from the opposite GUV, which induce a phase transition from L_o to L_d indicated by the rise of rhodamine fluorescence. Hence, the structure in that region of the membrane corresponds to an asymmetric domain with an ordered DPPC/Chol inner leaflet and a disordered DOPC-rich outer monolayer.

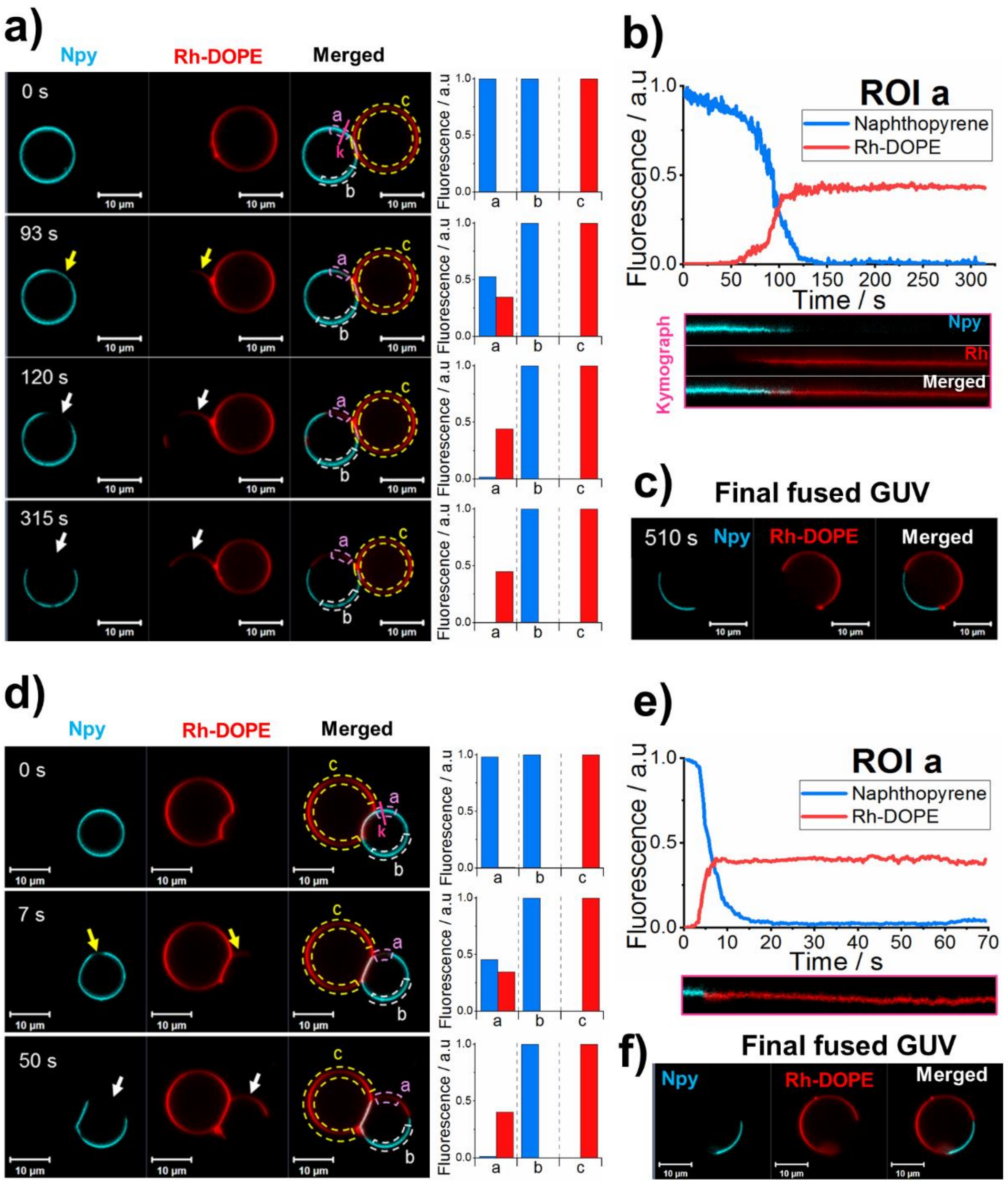

Figure 6.5. Asymmetric membrane domains and interleaflet coupling observed in hemifused GUVs. a) and d) Confocal microscopy time-lapse images of GUVs during hemifusion. Naphthopyrene (Npy) (cyan) and Rh-DOPE (red) are used as L_o and L_d markers, respectively. Yellow arrows indicate regions of the membrane where both dyes are colocalised (asymmetric domains) and white arrows indicate regions of the membrane where the L_o marker is completely excluded from the membrane due to interleaflet coupling. Bar plots show the normalised fluorescence intensity measured in the ROIs shown in the merged channel. Fluorescence intensity in “ROI b” and “ROI c” corresponds to the maximum intensity of Npy and Rh-DOPE, respectively, and fluorescence in the background is used as minimum intensity. “ROI a” shows an initial rise in fluorescence intensity of Rh-DOPE simultaneous to a reduction of Npy fluorescence to about half compared to its maximum intensity (93 s in a) and 9 s in d)). Later micrographs show a complete exclusion of Npy from that region of the membrane while the fluorescence intensity of Rh-DOPE in “ROI a” remains close to 0.5 at all times. b) and e) Normalised fluorescence intensity of Rh-DOPE (red line) and Npy (blue line) in “ROI a” against time. Kymographs show fluorescence levels over the dyes over time at the pink line indicated as k in the micrographs at t = 0 s in a) and d. c) and f) Phase separated GUV after fusion. The symmetry is apparently restored in the final fused GUVs

Strikingly, shortly after the formation of the asymmetric domain, the L_o marker is completely excluded from that region of the membrane while the fluorescence intensity of rhodamine remains just about 50% of Rh_{max} (Fig 6.5). The exclusion of Npy from the asymmetric domain likely responds to a loosening of the lipid packing in the DPPC/Chol inner monolayer induced by the L_d outer leaflet. Then, assuming none or minimal lipid transfer between the membrane leaflets, the resulting structure would be an asymmetric L_d domain where Rh-DOPE molecules partition into the DOPC-rich outer leaflet while the inner leaflet is composed of DPPC and cholesterol in a disorganised configuration, which compels the Npy molecules to diffuse laterally to regions where the lipids are more densely packed. This phenomenon by which one membrane monolayer modulates the physical properties of the opposite leaflet is known as interleaflet coupling. The analysis of the fluorescence intensity dynamics at the asymmetric domain clearly shows the transient colocalisation of the two dyes followed by the loss of Npy fluorescence (Fig 6.5b and e). In our observations, the time elapsed between Rh-DOPE fluorescence is initially detected in the L_o GUV and the Npy molecules are fully excluded from the asymmetric domain varies between approximately 10 and 100 s. The membrane asymmetry is only maintained while the GUVs are hemifused. Once the GUVs fully fuse, the membrane symmetry is apparently restored and the location of the fluorescent dyes in one monolayer matches its location in the opposite monolayer (Fig.6.5c and f).

The asymmetric membrane domains, detected by the Rh-DOPE fluorescence (Fig. 6.6 c-d), display Laurdan GP values between -0.2 and 0.2 which are intermediate between the pure DOPC and the DPPC/ Chol bilayers, in the GP map (Fig.6.6 a-b). These intermediate GP values can denote a mix of densely packed inner monolayer and less ordered outer monolayer or an intermediate packing lipid packing across the bilayer. However, these images do not allow us to discern whether the bilayers in the asymmetric domain are already coupled or not, because the L_o marker Npy and Laurdan cannot be imaged at the same time due to their spectral overlapping.

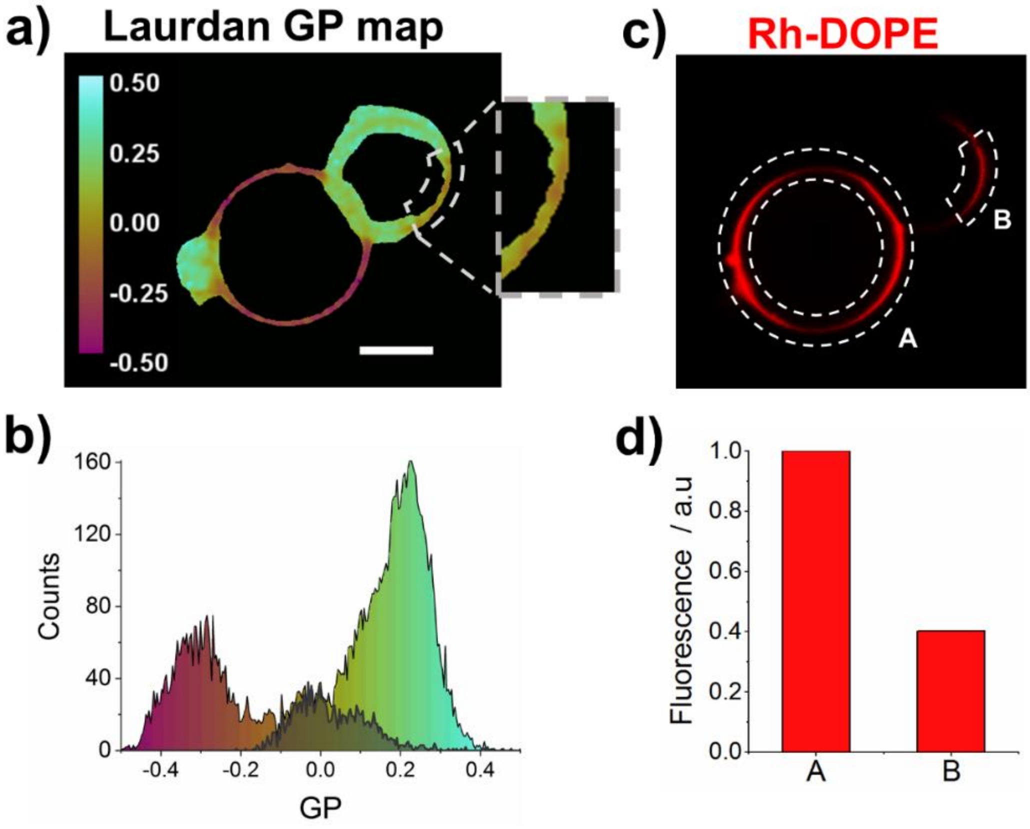

Figure 6.6. Comparison between Laurdan GP and Rh-DOPE fluorescence across the surface of hemifused GUVs. a) Laurdan GP map of hemifused GUVs. Zoomed region indicates a disordered domain within the initial L_o GUV. b) Laurdan GP histogram of image in shown in "a". Shaded region corresponds to the zoomed region in "a", which shows GP values intermediate between the more disordered DOPC-rich membrane and the ordered membrane enriched in DPPC and cholesterol. c) Confocal microscopy image showing the localisation of the Ld marker Rh-DOPE in the membrane of the hemifused GUVs. D) Fluorescence intensity of Rh-DOPE in ROIs A and B indicated in "c". The fluorescence intensity likely denotes that Rh-DOPE in ROI B is only present in one monolayer. This region of the membrane matches with the region displaying intermediate GP values in a and b.

6.5 Phase dynamics at the hemifusion diaphragm

Finally, a low proportion (n=3) of the fusion events recorded show dynamical changes in the membrane phase at an apparently extended hemifusion diaphragm (Fig. 6.7). Although the low number of observations does not allow us to do a statistical analysis, we observe two interesting opposite phenomena.

In two of those events, we observe the complete exclusion of the L_o phase marker from the membrane region where the GUVs get in contact (Fig. 6.7a-b, Supplementary movie 6.3). The exclusion of the L_o marker occurs simultaneously to an expansion and flattening of the contact region and a decrease of the relative fluorescence intensity of Rh-DOPE. The relative fluorescence intensity of the latter dye is however slightly higher (~70%) than 50%, which will be expected for a single L_d dye monolayer. This fluorescence intensity data makes it difficult to confidently define the configuration adopted by the membrane. A possible scenario is that the observed structure is an expanded hemifusion diaphragm with a DOPC monolayer labelled with Rh-DOPE and a DPPC/Chol monolayer from which the Npy dye is excluded due to the interleaflet coupling processes observed in the previous section. We speculate that the higher levels of Rh-DOPE fluorescence might be due to some extent of interleaflet lipid transfer, or a local enhancement of the fluorescence intensity due to a lipid condensation in this region of the membrane. The expanded hemifusion diaphragm dominated by the L_d phase show a very short life and it is formed just before the GUVs fully fuse. In these events, we do not detect migration of dyes from one GUV to the opposite. The dye exclusion and phase dynamics associated with it are restricted to the presumed hemifusion diaphragm and the L_d - L_o phase boundaries locate at the edges of it, where the bilayer at the hemifusion diaphragm meets the bilayers of the L_d and L_o GUVs, meet forming a Y-like junction.

The other movie shows a similar membrane behaviour at the contact region but in this case, the L_d marker is the one excluded from the membrane at the GUV-GUV interface (Fig. 6.7c, Supplementary movie 6.4). Contrary to the previous two observations, where the exclusion of the L_o dye from the hemifusion diaphragm happened suddenly, here we observe that the exclusion of the L_d marker starts at one edge of the region where the two GUVs are in contact and it gradually advances towards the other edge. This gradual exclusion of the Rh-DOPE is likely due to a slow expansion of a hemifusion diaphragm in this region of the GUVs. The relative fluorescence intensity of the Npy decreases by approximately half, which indicates that only a single labelled L_o monolayer is present in this region of the membrane. The opposite monolayer would be formed by DOPC but, contrary to what we observed before, here the L_o monolayer would be dominant, increasing the order of the DOPC leaflet *via* interleaflet coupling and causing the exclusion of the L_d marker.

In this event, the hemifusion diaphragm does not become flattened but the L_o GUV pushes and bends the Ld GUV. In addition, the fusion process is not completed but the GUVs remain adhered by the hemifusion diaphragm. The deformation of the L_d GUV by the L_o GUV might indicate that the former vesicle is not tense enough for the fusion pore to open and expand. We also observe a lipid transfer from the Ld to the L_o GUV. This leads to the formation of an asymmetric domain in the L_o GUV as indicated by the relative intensity levels of each fluorophore. In that region of the L_o GUV, the Npy relative fluorescence drops down to nearly 50% and the Rh fluorescence rise reaching about 50% of its maximum value shown in the L_d GUV (Fig. 6.7c inset). These fluorescence intensity values are characteristic of an asymmetric membrane with one Rh-DOPE-labelled L_d monolayer and one Npy-labelled L_o monolayer. This asymmetric domain is transient, the Rh-DOPE-labelled membrane retreats to its original GUV and the previously asymmetric domain recovers its L_o symmetric appearance. Eventually, the phase boundaries locate at the edges of the hemifusion diaphragm and the membranes seem to reach an equilibrium state.

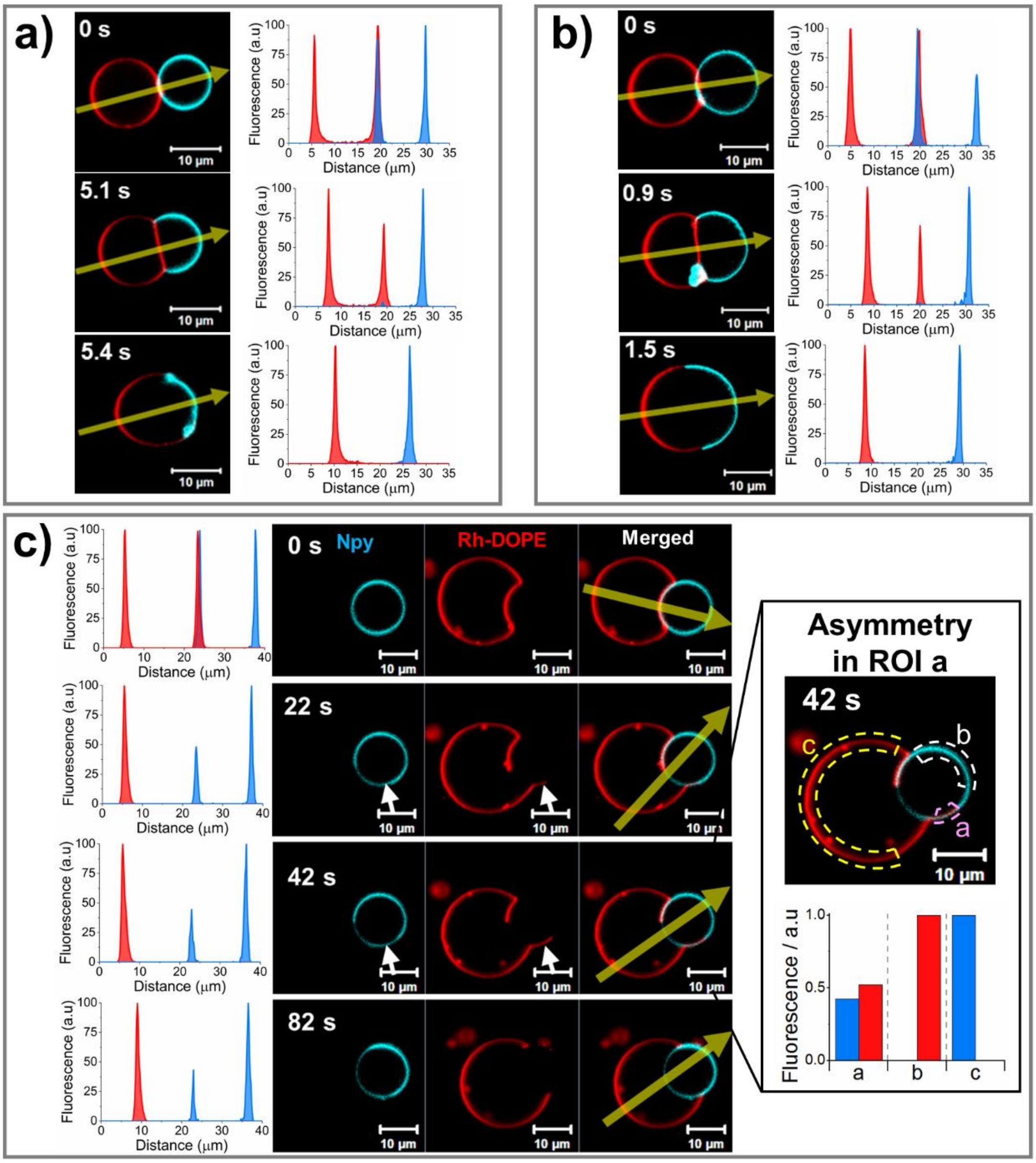

Figure 6.7. Phase behaviour at the hemifusion diaphragm. a and b) Confocal microscopy micrographs showing Naphthopyrene (Npy) exclusion from the contact region before fusion. Plots show the fluorescence intensity profile of Npy and Rh-DOPE across the yellow arrow indicated in the micrographs. c) Confocal microscopy micrographs showing Rh-DOPE exclusion from the hemifusion diaphragm. The dye exclusion advances gradually from one edge to the other. The plots in the left show the fluorescence intensity profile of Npy and Rh-DOPE across the yellow arrow indicated in the micrographs. White arrows indicate apparent asymmetric domains that arise from the transfer of lipids from the L_d GUV into the L_o GUV. Inset in c): The fluorescence intensity analysis in that region of the membrane (ROI a) shows a membrane domain where the relative intensity of each dye is approximately 50% of their maximum fluorescence intensity (ROI b=Npy_{max}; ROI c=Rh_{max}).

6.6 Discussion

Biological membranes present lateral heterogeneities which result in the emergence of lipid domains or lipid rafts. These domains have been proposed to be involved in lipid and protein sorting in the plasma membrane as well as many different signal transduction pathways [20, 269, 270]. In cell membranes, lipid domains are transient and nanoscopic (<200 nm) and hence difficult to characterise experimentally using common fluorescence microscopy [17, 257, 258]. For this reason, biomimetic model membranes, especially GUVs, which can display larger microdomains, have been extensively employed to study the lateral organisation of lipids within phase separated membranes. Studies using model membranes have identified various parameters that significantly contribute to the final organisation of lipids in domains including the length and unsaturation degree of the lipid acyl chains, the preferential segregation of cholesterol into ordered phases, the line tension at the phase boundaries and the temperature [19, 262, 263]. Additionally, phase separated model membranes are very useful tools for investigating lipid-protein interactions and the lateral organisation of transmembrane proteins within lipid membranes, as they can reveal preferential affinity by a particular membrane phase or even by the domain boundary [271-274].

Membrane phase separation can also be of great importance in synthetic biology as a spatiotemporal regulation system of membrane-protein interactions and membrane remodelling processes. For this purpose, strategies to produce phase separation in initially homogeneous membranes are desirable. A suitable method to achieve that goal is membrane fusion. Dreher *et al* recently showed that phase separation can lead to the division of a L_d/L_o GUV into two single-phased daughter vesicles, one formed by the disordered phase and the other by the ordered phase [260]. They then used DNA-triggered membrane fusion to induce phase separation in the daughter GUVs and repeat the division process [260].

Here we employ 30 nm SiO_2 NPs to mediate fusion between L_d DOPC GUVs and L_o DPPC/Chol (7:3) GUVs. The fusion of such GUVs generates phase separated GUVs. Laurdan imaging showed that the lipids in the L_d phase of the fused GUVs are more tightly packed than in the initial pure DOPC GUVs. These results indicate some degree of lipid redistribution across the fused membrane as dictated by the tie lines of the phase diagram where the disordered phase is enriched in DOPC, but not purely DOPC, and the ordered phase is predominantly formed by DPPC and cholesterol. Remarkably, the hemifusion between a DOPC GUV and a DPPC/Chol vesicle leads to the formation of asymmetric membrane domains and reveals a modulation of the physical state of the inner membrane leaflet induced by the outer monolayer in the asymmetric domain. Generally, we see a disorganisation of the formerly L_o inner leaflet induced by the migration of DOPC molecules from the outer leaflet of L_d GUV into the outer monolayer of the initially L_o GUV (Fig. 6.8). Only one observation seems to indicate an opposite behaviour where the L_o phase dominates over the L_d opposite leaflet.

To our knowledge, this is the first time that asymmetric domain formation and interleaflet coupling are imaged in real-time in GUVs and during fusion processes. Enoki and Feigenson developed a method by which they created asymmetric GUVs *via* hemifusion of the vesicles with a supported lipid bilayer (SLB) [275]. Using this method, they have seen that L_o domains of the inner monolayer induce L_o domains in an otherwise L_d outer monolayer, however, they only show the final membrane configuration but the process leading to the interleaflet coupling is not revealed [275, 276]. In their system, the L_o domains modulate the lipid order in the opposing leaflet whereas our results show the opposite tendency. This disparity is continuously repeated in the literature. For instance, L_o domains in the outer leaflet of SLBs have been seen to induce phase separation in the inner leaflet [277, 278]. However, the substrate where SLBs are formed can have a significant influence on the dynamical behaviour of the lipids in the inner leaflet, so unsupported model membranes, such as vesicles or pore-spanning planar bilayers, are better systems for these investigations. Chiantia and London showed that long-chain sphingomyelin (SM) in the outer leaflet of vesicles decreases the lateral diffusion of DOPC lipids in the inner monolayer [279]. They also saw that the interleaflet coupling is stronger when the PC lipids in the inner monolayer have one saturated acyl chain and attribute the coupling effect to the interaction between acyl chains at the bilayer midplane [279].

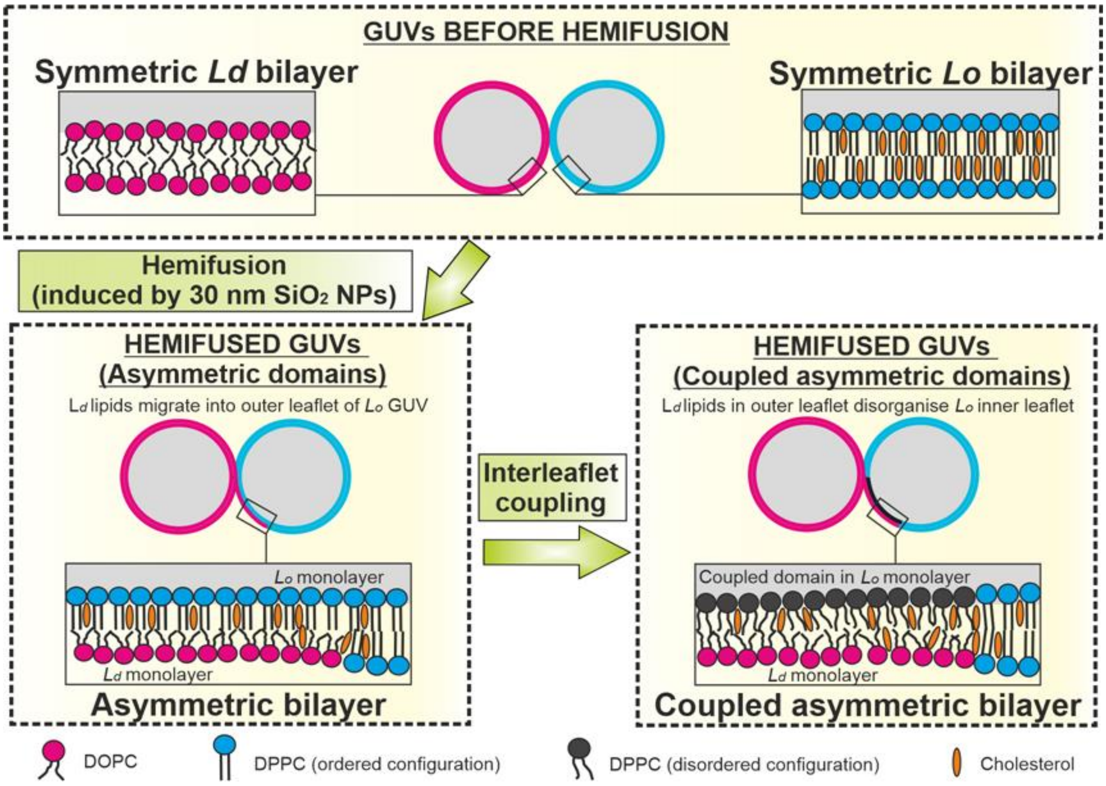

Figure 6.8. Schematic representation of asymmetric domain formation followed by interleaflet coupling during hemifusion between a L_d GUV and a L_o GUV. The process begins with the interaction of two symmetric GUVs, one L_d (formed by DOPC) and the other L_o (formed by DPPC and cholesterol), with 30 nm SiO_2 NPs. This interaction leads to the hemifusion of their membranes and consequently, DOPC molecules begin to migrate into the outer monolayer of the L_o GUV leading to the formation of an asymmetric domain. After the asymmetric domain is formed, the disordered outer leaflet induces a disorganising effect in the inner monolayer leading to a final configuration where the physical state of the leaflets in the asymmetric domain is coupled. (Note that the Ld monolayer in the asymmetric domain is also expected to contain some DPPC molecules but this was excluded from the illustration for clarity purposes. The cholesterol dynamics are also unknown but it is expected to partition preferentially into L_o domains).

A disorganisation effect of ordered domains by disordered lipids in the opposite leaflet, analogous to what we observe in most of our results, was reported by Heberle in asymmetric LUVs where the outer leaflet was composed of DPPC and the inner leaflet of POPC [280]. Using small-angle neutron scattering (SANS), they observed that the L_d inner monolayer induced a significant decrease in the lipid packing density of the gel domains in the outer leaflet [280]. Similarly, in a recent work, St. Clair *et al* have shown that while symmetric LUVs formed by a mixture of SM, POPC and cholesterol are phase separated, in asymmetric LUVs with SM/POPC/Chol in the outer leaflet but a POPC/Chol inner monolayer the formation of L_o domains is completely suppressed [281]. Wang and London also reported the ability of DOPC/Chol L_d inner leaflet of asymmetric LUVs to destabilise and destroy ordered domains in the outer monolayer containing SM [282]. This disorganisation of the outer leaflet L_o domains is however less pronounced when its content in SM increases [282]. Collins and Keller studied asymmetric pore spanning planar membranes formed by a L_d inner leaflet and an outer leaflet with a lipid composition within the L_d-L_o coexistence region of the phase diagram and showed that increasing or decreasing the fraction of high-T_m lipid in the outer monolayer induces or suppresses, respectively, the formation of bilayer domains [283].

Membrane asymmetry is a fundamental property of cell membranes with significant biological implications. The best-known cellular process controlled by the membrane asymmetry is the display of PS lipids in the outer leaflet in apoptotic cells as a signal to be consumed by phagocytes [256, 284, 285]. Moreover, the exposure of PS is related to other forms of cell death, platelet coagulation, and many biological processes including immune response, neuronal maintenance and muscle development [284, 285]. At the molecular level, membrane asymmetry has been seen to control the orientation of protein transmembrane domains (TMDs) inserted the bilayer so the thinner parts of the TMDs are located in the outer leaflet, rich in SM and more densely packed, whereas the thicker regions are preferentially located in the inner monolayer where lipids are relatively loosely packed [9, 286].

Membrane asymmetry has represented a problem for understanding the formation of domains in the plasma membrane, since only the outer monolayer presents the appropriate lipid composition to form such structures, but they exist in both leaflets [256, 287]. The reason behind the formation of bilayer domains is that both leaflets are coupled, so one monolayer can modulate the physical state of the other and thus determine the physicochemical properties of the membrane bilayer [256, 258]. In cells, the interleaflet coupling is thought to represent a lipid-mediated route to transfer information across the membrane different from the classical signal transduction mechanisms mediated by transmembrane proteins [256, 258, 284, 288]. For example, the binding of bacterial toxins to their receptors would promote the formation of L_o domains in the outer leaflet rich in long acyl chain sphingolipids. Those long acyl chain lipids would then interact with lipids in the inner monolayer and induce them to form L_o domains *via* interleaflet coupling. Consequently, lipids such as PS or phosphorylated phosphatidylinositols (PIPs), also known as phosphoinositides, can accumulate in those domains and recruit cytosolic proteins which then initiate intracellular signalling cascades [288].

The mechanisms governing the interleaflet coupling phenomena are still not clear. Investigations on asymmetric model membranes have suggested that interleaflet coupling might involve many different physicochemical parameters such as line tension, acyl chain interdigitation, membrane fluctuations, curvature and differential lateral stress [255, 258, 284]. Moreover, while several studies have reported a similar behaviour to what we observed in most of our experiments, with the disordered leaflet modulating the physical state of the ordered leaflet [280-282], many others show the ordered leaflet dominating the physical state of L_d monolayers [275-279]. The type of model membrane employed in interleaflet coupling studies as well as the varying lipid composition and experimental conditions used in different investigations are probably the principal causes behind the apparently contradictory results.

It is then evident that membrane asymmetry and interleaflet coupling are fundamental properties of cell membranes. Nevertheless, there is still a long way to go in order to fully understand the role that these properties play in the membrane structure and functions. From what we observed in our results, GUVs of different lipid composition undergoing hemifusion represent a potential experimental system to create asymmetric membrane domains and observe in real-time they organise as well as how the membrane leaflets modulate each other's physical state.

6.7 Conclusions

To summarise, in this chapter we employed 30 nm SiO_2 NPs to generate phase separated GUVs from two single-phased vesicles. Compared to fusion between two DOPC GUVs, we observed similar fusion efficiency but mechanistic differences, being the most notable the lack of gentle membrane merging events. Finally, we detected the formation of asymmetric membrane domains in hemifused GUVs and were able to image in real-time interleaflet coupling phenomena occurring within those domains.

Chapter 7:
Conclusions and outlook

Throughout this thesis, we have analysed varying responses of model lipid membranes to the non-specific contact with inorganic engineered nanomaterials (AgNPs and SiO_2 NPs) with a twofold aim: to provide information about the influence of the medium conditions on the nature and consequences of the interactions between NPs and lipid membranes; and to explore the inherent potential of NPs to replicate the activity of proteins involved in membrane remodelling processes, in particular membrane fusion.

7.1 Impact of medium conditions on the interactions between NPs and biomimetic lipid membranes

7.1.1 Summary

In **Chapter 3** we studied the influence of the ionic strength of the medium in the colloidal stability and membrane interaction of AgNPs. For this purpose, we performed parallel experiments in buffer with either 150 mM NaCl (physiological ionic strength) or 300 mM glucose (low ionic strength). Using DLS and DELSA we detected a weak NP agglomeration in physiological ionic strength buffer produced by the screening of the negative surface charge of the NPs by the Na^+ ions. The analysis of the aggregation kinetics indicated that most of the NP clusters remain suspended within the experimental incubation times. In contrast, AgNPs suspended in glucose buffer remained monodispersed. We also found that the AgNPs-membrane interactions strongly depend on the medium ionic strength. While colloidally stable AgNPs in glucose buffer had a negligible effect on the membrane, at physiological salt concentrations the weakly aggregated AgNPs induced sporadic but significant membrane perturbations. Under these latter conditions, we observed a small population of vesicles that display a significant change in their mechanical properties with lower bending rigidity and higher membrane tension. We argue that this low-probability mechanomodulation by small clusters of AgNPs interacting with the membrane is closely related to the transient poration and structural remodelling of some vesicle membranes detected under the same physiological ionic strength conditions.

In **Chapter 4** we investigated the impact of a protein corona on the interaction between SiO_2 NPs of two different sizes, 18 nm and 30 nm, and model membranes. To form a simplified protein corona, we incubated the SiO_2 NPs in a solution of bovine serum albumin. Although the BSA corona obtained is much simpler than the biomolecular coronas formed *in vivo*, it provides information about the modulation of the fundamental NP-membrane interactions when a protein layer covers the NP surface and eliminates the heterogeneity of coronas formed in complex serums which can introduce large variability to the interaction mechanisms.

Both types of bare SiO_2 NPs induced dose-dependent leakage of CF from LUVs, but the data showed differences that suggest distinct interaction mechanisms. The BSA corona induced significant changes in the CF leakage produced by the NPs, but while in the case of the smaller SiO_2 NPs, the NPs with corona produce greater levels of dye release than the bare SiO_2 NPs, the BSA corona minimised the leakage caused by the 30 nm SiO_2 NPs. The different interaction mechanisms were clearly confirmed by confocal microscopy. After being exposed to 18 nm SiO_2 NPs, DOPC GUVs exhibited a crumpled membrane with microsized permanent holes and a significantly tighter lipid packing. The same SiO_2 NPs coated with a BSA corona were wrapped by the membrane and produced a gradual shrinkage of the GUVs also accompanied by a denser packing of the lipids. Finally, in this chapter we observed for the first time the fusion ability of 30 nm SiO_2 NPs, confirming our initial hypothesis. This fusogenic activity was suppressed by the BSA corona. When exposed to 30 nm SiO_2 NPs with

BSA corona, the GUVs adhere to each other forming vesicle clusters but we did not detect any lipid exchange between the membranes of different GUVs. This, on one hand, confirms that the fusion is driven by the interaction of the SiO_2 NPs with two closely localised GUVs and, on the other hand, indicates that the protein corona reduces the adhesion strength between 30 nm SiO_2 NPs and lipid membranes. In conclusion, we observed that the BSA corona weakens the ability of NP to interact with the membrane and this causes a profound impact on the membrane responses to those interactions, yet the inherent physical properties of the NPs are still a key factor that determines the interaction mechanism.

7.1.2 Outlook

The studies of the interaction between NPs and model membranes have generated substantial progress on the understanding of the behaviour of NPs at the nanobio interface. However, there are still significant missing links between minimalistic well-controlled experimental systems and the actual biological context. This makes it challenging to predict the NP fate within biological systems and, consequently, to synthesise safe-by-design nanomaterials that perform the desired functions without harmful side effects. In addition, studies on NP-membrane interactions focused on the evaluation and prediction of potential cytotoxicity outcomes often obviate subtle impacts which can have greater biological relevance than expected when tested in more complex systems.

The work presented in this thesis evidences the importance of the environmental conditions on the interplay between NPs and lipid membranes. *In vivo*, NPs are expected to encounter different biological fluids with varying characteristics (pH, ionic strength, macromolecular crowding...) which will likely modify their physicochemical properties and biointeractions [71]. Hence, understanding the effect of the biological medium on the behaviour of NPs is critical to developing safe and effective nanomaterials. The extensive work produced on the effect of the protein corona on interactions of NPs and model membranes has provided valuable information for subsequential use of these materials *in vivo*. Generally, these investigations have reported that protein coronas reduce the adhesion strength between NPs and membranes and therefore change the resulting membrane perturbations. Nonetheless, many aspects of the formation, structure and protein composition of the corona itself remain obscure, and the effect of other biomolecules, such as lipids or nucleic acids, coating the NP surface has not been explored in-depth yet.

The influence of other properties of the medium, such as the ionic strength or macromolecular crowding, on the biological interactions of NPs are however strikingly underrepresented in the literature. These properties of the medium are likely to have important effects on the physicochemical characteristics of the NPs and their interactions with cell membranes and other biological entities. Hence, more attention has to be driven towards employing new experimental conditions that replicate a more realistic biological medium, with for example different ions, proteins and macromolecular crowding agents, and allow a better prediction of the NP behaviour in complex biological organisms.

Moreover, despite the experimental advantages and the ability to mimic fundamental properties of cell membranes that lipid vesicles present, other important structural and physicochemical characteristics of membranes are not well represented in these model systems. These include aspects such as the limited variety of lipids forming the membrane and the absence of proteins and glycolipids and other structural features such as membrane asymmetry. Within this framework, giant plasma membrane vesicles (GPMVs) obtained directly from cell membranes arise as an excellent model to study membrane structure, membrane fluidity and membrane interactions with nanomaterials, proteins and other biomolecules. This system maintains the structural and biophysical complexity of cell membranes, with an intricate mixture of lipids and membrane proteins diffusing through the membrane, which make them an intermediate model system between lipid vesicles and cells, with the experimental advantages of the former and nearly the compositional complexity of the latter [289, 290]. Albeit their nearly native composition, GPMVs also present some limitations including loss of native membrane asymmetry, state of chemical equilibrium in contrast to the constantly modified live cell membrane and protein crosslinking and damage induced by some methods employed to obtain them [289-292].

Membrane asymmetry is a fundamental property of cell membranes which is generally overlooked in the study of the membrane responses to NPs. The principal reason behind this experimental gap is that the most conventional methods to prepare lipid vesicles (and most model membranes) yield symmetric membranes, even though much effort is being put to develop new protocols to produce asymmetric LUVs and GUVs [275, 280, 293-297]. A recent study has shown that membrane asymmetry only has a minor impact on the interaction between silica NPs and lipid vesicles [232]. However, more investigations are needed before final conclusions can be drawn, since the asymmetric distribution of the lipids between the membrane leaflets is known to affect the mechanical and dynamical properties of the membrane, which in turn are fundamental players in the NP-membrane interactions.

Finally, the mechanical properties of the cell are defined by the close interplay between the plasma membrane and an actin cortex which covers the cytoplasmic surface of the membrane. The actin cortex has been successfully reconstituted inside GUVs. Such GUVs with cytoskeleton are extensively studied in bottom-up synthetic biology and could represent the next step of cell model systems. Nevertheless, these systems have not been used yet in studies on the biointeractions of NPs.

7.2 Engineered nanomaterials as protein mimics

7.2.1 Summary

In **Chapter 5** we investigated in detail the fusogenic activity of 30 nm SiO_2 NPs. Initially, we evaluated the fusion activity using a classic method based on Förster FRET to measure the lipid mixing between LUVs after exposure to varying concentrations of NPs. From these data, we observed an increase in lipid mixing dependent on the NP concentration. Then, using confocal microscopy we observed a direct connection between membrane tension and fusion efficiency and identified regions on the surface of the GUVs with enhanced fluorescence intensity that indicate the ability of the NPs to induce high local membrane curvature. Notably, real-time confocal fluorescence microscopy revealed three distinct mechanistic pathways for membrane fusion characterised by the intermediate configurations adopted by the membranes during the process. These pathways were classified as direct full fusion, hemifusion-fusion and gentle membrane merging. Finally, we proposed a mechanistic model to explain the different fusion possibilities where membrane tension is placed as the principal driver of the process.

After having confirmed the fusogenic activity of 30 nm SiO_2 NPs, in **Chapter 6** we performed a proof-of-concept study in which we employed those SiO_2 NPs to generate phase separated membranes by fusing two single-phased GUVs. Using fluorescence dyes that partition preferentially into liquid disordered or liquid ordered membrane phases we observed membrane domains formed in the fused vesicles. Using spectral imaging of Laurdan-labelled GUVs we analysed how the lipid packing varies in each membrane phase between single phased GUVs and phase separated GUVs. Real-time imaging of hemifused L_d and L_o GUVs showed striking dynamical phenomena involving the formation of asymmetric domains and interleaflet coupling processes.

7.2.2 Outlook

The results showed here demonstrate that 30 nm SiO_2 NPs promote fusion between two DOPC vesicles and between a DOPC and a DPPC/Chol membrane. Nevertheless, some questions remain open and further investigations are needed to improve our understanding and control of the process. First, the conditions of the medium can alter the interaction mechanism between the NPs and the membrane and therefore affect the fusogenic activity. As shown in **Chapter 4**, the formation of a protein corona inhibits the fusogenic activity of these SiO_2 NPs. In addition, as we saw in **Chapter 3**, the ionic strength of the medium can have important impacts on the interplay between the NPs and the membrane. Under different ionic strength conditions, the fusion efficiency of 30 nm SiO_2 NPs might be affected due to changes in the adhesion energy induced by the ionic strength of the medium. The new ionic strength might therefore shift the critical size range within which SiO_2 NPs can mediate fusion. If this were the case, the size of the NPs should be adjusted to match the new critical size. However, more work is required to test whether NPs of other sizes, even if they are within that new critical size range, are able to mediate fusion or on the contrary, they induce different effects. Moreover, the presence of divalent cations, such as Ca^{2+}, which are known to both promote fusion themselves and help other fusogens to do their work [108, 110, 225], is another factor to account for in future studies.

Secondly, different membrane compositions can also affect the process. We showed that changing the composition of only one GUV from DOPC to DPPC/Chol does not reduce the fusogenic activity but in the same experiments, we did not see any fusion between two L_o GUVs. We were unable to provide quantitative data on L_o-L_o fusions because the fluorescence spectra of the L_o partitioning dyes to which we had access overlapped and so their signal could not be separated into different imaging channels. For those experiments, L_o partitioning dyes which emit in the red or far-red region of the fluorescence spectrum are desirable, however, only a few examples of such dyes are found in the literature, including the modified Nile red dye NR12S [298] and the far-red emitting fluorescent phospholipid analogue DSPE-PEG-KK114 [299]. Beyond the bending rigidity, the surface charge of the membrane is known to modulate the strength of the NP-membrane interactions [75]. Thus, this opens a future investigation to explore how changing the proportion of charged (positively and negatively) lipids influences the fusion efficiency and the intermediate configurations adopted by the membranes during the process. This study might provide new insight on the mechanisms by which SiO_2 NPs mediate membrane fusion and might even allow to potentially gain some control or predictability over the fusion process. For instance, that investigation could help to favour one of the fusion pathways detected in **Chapter 5** over the others, or it could serve to develop a method to arrest the fusion process at the hemifusion stage to create stabilised hemifused GUVs with asymmetric domains such as the observed in **Chapter 6.**

The application of engineered nanomaterials in synthetic biology is not limited to membrane fusion. Other membrane remodelling and shaping processes can be induced by the contact of NPs with lipid membranes. Examples of these membrane transformations are the formation of ILVs produced by AgNPs observed in **Chapter 3** of this thesis, and the tubular protrusions induced by cationic NPs encapsulated within GUVs observed by Yu and Granick [107]. In addition, NPs could potentially be used to mediate protein-free division of artificial cells. In a recent study, Steinkuhler *et al.* have shown that His-tagged GFP proteins adhered to the membrane can generate membrane curvature and depending on the degree of coverage they can divide a “mother” GUV into two daughter vesicles [300]. That system does not rely on a specific division activity of the proteins used, but on the curvature induced by the crowding of those proteins onto the membrane. Hence, a similar curvature-driven division is likely to be achieved by the binding of NPs to the membrane. In conclusion, there is a vast range of unexplored possibilities for using engineered nanomaterials as bioinspired nanomachines in synthetic biology.

References

[1] Alberts, B., Johnson, A., Lewis, J., Morgan, D., Raff, M., Roberts, K., Walter, P., Wilson, J., and Hunt, T. (2015) *Molecular Biology of the Cell*, 6th ed., Garland Science, Taylor and Francis Group,, New York.

[2] Beales, P. A., Ciani, B., and Cleasby, A. J. (2015) Nature's Lessons in Design: Nanomachines to Scaffold, Remodel and Shape Membrane Compartments, *Physical Chemistry Chemical Physics 17*, 15489-15507.

[3] Singer, S. J., and Nicolson, G. L. (1972) The Fluid Mosaic Model of the Structure of Cell Membranes, *Science 175*, 720- 731.

[4] van Meer, G., Voelker, D. R., and Feigenson, G. W. (2008) Membrane Lipids: Where They Are and How They Behave, *Nature Reviews Molecular Cell Biology 9*, 112-124.

[5] Seddon, A. M., Casey, D., Law, R. V., Gee, A., Templer, R. H., and Ces, O. (2009) Drug Interactions with Lipid Membranes, *Chemical Society Reviews 38*, 2509-2519.

[6] Fadeel, B., and Xue, D. (2009) The Ins and Outs of Phospholipid Asymmetry in the Plasma Membrane: Roles in Health and Disease, *Critical Reviews in Biochemistry and Molecular Biology 44*, 264-277.

[7] Verkleij, A. J., Zwaal, R. F. A., Roelofsen, B., Comfurius, P., Kastelijn, D., and Vandeene.Ll. (1973) The Asymmetric Distribution of Phospholipids in the Human Red Cell Membrane. A Combined Study Using Phospholipases and Freeze-Etch Electron Microscopy., *Biochimica Et Biophysica Acta 323*, 178-193.

[8] Devaux, P. F. (1991) Static and Dynamic Lipid Asymmetry in Cell-Membranes, *Biochemistry 30*, 1163-1173.

[9] Lorent, J. H., Levental, K. R., Ganesan, L., Rivera-Longsworth, G., Sezgin, E., Doktorova, M. D., Lyman, E., and Levental, I. (2020) Plasma Membranes are Asymmetric in Lipid Unsaturation, Packing and Protein Shape, *Nature Chemical Biology 16*, 644-652.

[10] Eeman, M., and Deleu, M. (2010) From Biological Membranes to Biomimetic Model Membranes, *Biotechnologie Agronomie Societe Et Environnement 14*, 719-736.

[11] Janmey, P. A., and Kinnunen, P. K. J. (2006) Biophysical Properties of Lipids and Dynamic Membranes, *Trends in Cell Biology 16*, 538-546.

[12] Boal, D. (2012) *Mechanics of the Cell*, 2nd ed., Cambridge University Press, Cambridge.

[13] Shearman, G. C., Ces, O., Templer, R. H., and Seddon, J. M. (2006) Inverse Lyotropic Phases of Lipids and Membrane Curvature, *Journal of Physics-Condensed Matter 18*, S1105-S1124.

[14] Israelachvili, J. N. (2011) *Intermolecular and Surface Forces*, 3rd ed., Academic Press

[15] Frolov, V. A., Shnyrova, A. V., and Zimmerberg, J. (2011) Lipid Polymorphisms and Membrane Shape, *Cold Spring Harbor Perspectives in Biology 3*: a004747

[16] Tenchov, R., Bird, R., Curtze, A. E., and Zhou, Q. (2021) Lipid Nanoparticles-From Liposomes to mRNA Vaccine Delivery, a Landscape of Research Diversity and Advancement, *ACS nano*. DOI: 10.1021/acsnano.1c04996

[17] Cebecauer, M., Amaro, M., Jurkiewicz, P., Sarmento, M. J., Sachl, R., Cwiklik, L., and Hof, M. (2018) Membrane Lipid Nanodomains, *Chemical Reviews 118*, 11259-11297.

[18] Elson, E. L., Fried, E., Dolbow, J. E., and Genin, G. M. (2010) Phase Separation in Biological Membranes: Integration of Theory and Experiment, *Annual Review of Biophysics, Vol 39 39*, 207-226.

[19] Veatch, S. L., and Keller, S. L. (2005) Miscibility Phase Diagrams of Giant Vesicles Containing Sphingomyelin, *Physical Review Letters 94*, 148101

[20] Simons, K., and Toomre, D. (2000) Lipid Rafts and Signal Transduction, *Nature Reviews Molecular Cell Biology 1*, 31-39.

[21] Baumgart, T., Hess, S. T., and Webb, W. W. (2003) Imaging Coexisting Fluid Domains in Biomembrane Models Coupling Curvature and Line Tension, *Nature 425*, 821-824.

[22] Yoon, Y. Z., Hale, J. P., Petrov, P. G., and Cicuta, P. (2010) Mechanical Properties of Ternary Lipid Membranes Near a Liquid-Liquid Phase Separation Boundary, *Journal of Physics-Condensed Matter 22*.

[23] Garcia-Saez, A. J., and Schwille, P. (2010) Surface Analysis of Membrane Dynamics, *Biochimica Et Biophysica Acta-Biomembranes 1798*, 766-776.

[24] Ces, O., and Mulet, X. (2006) Physical Coupling Between Lipids and Proteins: a Paradigm for Cellular Control, *Signal Transduction 6*, 112-132.

[25] Kozlovsky, Y., and Kozlov, M. M. (2002) Stalk Model of Membrane Fusion: Solution of Energy Crisis, *Biophysical Journal 82*, 882-895.

[26] Helfrich, W. (1973) Elastic Properties of Lipid Bilayers: Theory and Possible Experiments, *Zeitschrift Fur Naturforschung C-a Journal of Biosciences C 28*, 693-703.

[27] Zimmerberg, J. (2006) Membrane Biophysics, *Current Biology 16*, R272-R276.

[28] Le, M. T., Litzenberger, J. K., and Prenner, E. J. (2011) Biomimetic Model Membrane Systems Serve as Increasingly Valuable In Vitro Tools, In *Advances in Biomimetics* (George, A., Ed.), pp 251-276, InTech.

[29] Akbarzadeh, A., Rezaei-Sadabady, R., Davaran, S., Joo, S. W., Zarghami, N., Hanifehpour, Y., Samiei, M., Kouhi, M., and Nejati-Koshki, K. (2013) Liposome: Classification, Preparation, and Applications, *Nanoscale Research Letters 8*, 1-9

[30] Dimova, R., and Marques, C. M. (2019) *The Giant Vesicle Book*, 1st ed., CRC Press.

[31] Gopfrich, K., Platzman, I., and Spatz, J. P. (2018) Mastering Complexity: Towards Bottom-up Construction of Multifunctional Eukaryotic Synthetic Cells, *Trends in Biotechnology 36*, 938-951.

[32] Kretschmer, S., Ganzinger, K. A., Franquelim, H. G., and Schwille, P. (2019) Synthetic Cell Division via Membrane-Transforming Molecular Assemblies, *Bmc Biology 17*, 1-10

[33] Walde, P., Cosentino, K., Engel, H., and Stano, P. (2010) Giant Vesicles: Preparations and Applications, *Chembiochem 11*, 848-865.

[34] Fenz, S. F., and Sengupta, K. (2012) Giant Vesicles as Cell Models, *Integrative Biology 4*, 982-995.

[35] Stano, P. (2017) Minimal Cellular Models for Origins-of-Life Studies and Biotechnology, In *The Biophysics of Cell Membranes* (Epand, R. M., and Ruysschaert, J.-M., Eds.) 1st ed., Springer, Singapore.

[36] Commission Recommendation of 18 October 2011 on the Definition of Nanomaterial, In *Official Journal of the European Communities*, pp 38-40.

[37] Nel, A., Xia, T., Madler, L., and Li, N. (2006) Toxic Potential of Materials at the Nanolevel, *Science 311*, 622-627.

[38] Qiu, T. A., Clement, P. L., and Haynes, C. L. (2018) Linking Nanomaterial Properties to Biological Outcomes: Analytical Chemistry Challenges in Nanotoxicology for the Next Decade, *Chemical Communications 54*, 12787-12803.

[39] Albanese, A., Tang, P. S., and Chan, W. C. W. (2012) The Effect of Nanoparticle Size, Shape, and Surface Chemistry on Biological Systems, *Annual Review of Biomedical Engineering, 14*, 1-16.

[40] Oberdorster, G., Stone, V., and Donaldson, K. (2007) Toxicology of Nanoparticles: A Historical Perspective, *Nanotoxicology 1*, 2-25.

[41] Farnoud, A. M., and Nazemidashtarjandi, S. (2019) Emerging Investigator Series: Interactions of Engineered Nanomaterials with the Cell Plasma Membrane; What Have We Learned from Membrane Models?, *Environmental Science-Nano 6*, 13-40.

[42] Lewinski, N., Colvin, V., and Drezek, R. (2008) Cytotoxicity of Nanoparticles, *Small 4*, 26-49.

[43] Srivastava, V., Gusain, D., and Sharma, Y. C. (2015) Critical Review on the Toxicity of Some Widely Used Engineered Nanoparticles, *Industrial & Engineering Chemistry Research 54*, 6209-6233.

[44] Vance, M. E., Kuiken, T., Vejerano, E. P., McGinnis, S. P., Hochella, M. F., Rejeski, D., and Hull, M. S. (2015) Nanotechnology in the Real World: Redeveloping the Nanomaterial Consumer Products Inventory, *Beilstein Journal of Nanotechnology 6*, 1769-1780.

[45] Calderon-Jimenez, B., Johnson, M. E., Bustos, A. R. M., Murphy, K. E., Winchester, M. R., and Baudrit, J. R. V. (2017) Silver Nanoparticles: Technological Advances, Societal Impacts, and Metrological Challenges, *Frontiers in Chemistry 5, 6*.

[46] Sotiriou, G. A., and Pratsinis, S. E. (2011) Engineering Nanosilver as an Antibacterial, Biosensor and Bioimaging Material, *Current Opinion in Chemical Engineering 1*, 3-10.

[47] Piella, J., Bastus, N. G., and Puntes, V. (2017) Modeling the Optical Responses of Noble Metal Nanoparticles Subjected to Physicochemical Transformations in Physiological Environments: Aggregation, Dissolution and Oxidation, *Zeitschrift Fur Physikalische Chemie-International Journal of Research in Physical Chemistry & Chemical Physics 231*, 33-50.

[48] Li, Y. N., Chang, Y. T., Lian, X. F., Zhou, L. Q., Yu, Z. Q., Wang, H. X., and An, F. F. (2018) Silver Nanoparticles for Enhanced Cancer Theranostics: In Vitro and In Vivo Perspectives, *Journal of Biomedical Nanotechnology 14,* 1515-1542.

[49] Klasen, H. J. (2000) A Historical Review of the Use of Silver in the Treatment of Burns. II. Renewed Interest for Silver, *Burns 26*, 131-138.

[50] Pal, S., Tak, Y. K., and Song, J. M. (2007) Does the Antibacterial Activity of Silver Nanoparticles Depend on the Shape of the Nanoparticle? A Study of the Gram-Negative Bacterium *Escherichia coli*, *Applied and Environmental Microbiology 73*, 1712-1720.

[51] Sondi, I., and Salopek-Sondi, B. (2004) Silver Nanoparticles as Antimicrobial Agent: a Case Study on E. coli as a Model for Gram-Negative Bacteria, *Journal of Colloid and Interface Science 275*, 177-182.

[52] Morones, J. R., Elechiguerra, J. L., Camacho, A., Holt, K., Kouri, J. B., Ramirez, J. T., and Yacaman, M. J. (2005) The Bactericidal Effect of Silver Nanoparticles, *Nanotechnology 16*, 2346-2353.

[53] Li, W.-R., Xie, X.-B., Shi, Q.-S., Zeng, H.-Y., Ou-Yang, Y.-S., and Chen, Y.-B. (2010) Antibacterial Activity and Mechanism of Silver Nanoparticles on Escherichia coli, *Applied Microbiology and Biotechnology 85*, 1115-1122.

[54] Fabrega, J., Fawcett, S. R., Renshaw, J. C., and Lead, J. R. (2009) Silver Nanoparticle Impact on Bacterial Growth: Effect of pH, Concentration, and Organic Matter, *Environmental Science & Technology 43*, 7285-7290.

[55] Nanda, A., and Saravanan, M. (2009) Biosynthesis of Silver Nanoparticles from Staphylococcus aureus and its Antimicrobial Activity Against MRSA and MRSE, *Nanomedicine-Nanotechnology Biology and Medicine 5*, 452-456.

[56] Panacek, A., Kolar, M., Vecerova, R., Prucek, R., Soukupova, J., Krystof, V., Hamal, P., Zboril, R., and Kvitek, L. (2009) Antifungal Activity of Silver Nanoparticles Against Candida spp, *Biomaterials 30*, 6333-6340.

[57] Lara, H. H., Ayala-Nunez, N. V., Ixtepan-Turrent, L., and Rodriguez-Padilla, C. (2010) Mode of Antiviral Action of Silver Nanoparticles Against HIV-1, *Journal of Nanobiotechnology 8*, 1.

[58] Lu, L., Sun, R. W.-Y., Chen, R., Hui, C.-K., Ho, C.-M., Luk, J. M., Lau, G. K. K., and Che, C.-M. (2008) Silver Nanoparticles Inhibit Hepatitis B Virus Replication, *Antiviral Therapy 13*, 253-262.

[59] Xiang, D.-x., Chen, Q., Pang, L., and Zheng, C.-l. (2011) Inhibitory Effects of Silver Nanoparticles on H1N1 Influenza A Virus In Vitro, *Journal of Virological Methods 178*, 137-142.

[60] Jain, P. K., Huang, X. H., El-Sayed, I. H., and El-Sayed, M. A. (2008) Noble Metals on the Nanoscale: Optical and Photothermal Properties and Some Applications in Imaging, Sensing, Biology, and Medicine, *Accounts of Chemical Research 41*, 1578-1586.

[61] Evanoff, D. D., and Chumanov, G. (2005) Synthesis and Optical Properties of Silver Nanoparticles and Arrays, *Chemphyschem 6*, 1221-1231.

[62] Austin, L. A., Mackey, M. A., Dreaden, E. C., and El-Sayed, M. A. (2014) The Optical, Photothermal, and Facile Surface Chemical Properties of Gold and Silver Nanoparticles in Biodiagnostics, Therapy, and Drug Delivery, *Archives of Toxicology 88*, 1391-1417.

[63] Schlucker, S. (2009) SERS Microscopy: Nanoparticle Probes and Biomedical Applications, *Chemphyschem 10*, 1344-1354.

[64] Kim, I. Y., Joachim, E., Choi, H., and Kim, K. (2015) Toxicity of Silica Nanoparticles Depends on Size, Dose, and Cell Type, *Nanomedicine-Nanotechnology Biology and Medicine 11*, 1407-1416.

[65] Petushkov, A., Ndiege, N., Salem, A. K., and Larsen, S. C. (2010) Toxicity of Silica Nanomaterials: Zeolites, Mesoporous Silica, and Amorphous Silica Nanoparticles, In *Advances in Molecular Toxicology* (Fishbein, J. C., Ed.), pp 223-266, Elsevier.

[66] Tang, L., and Cheng, J. J. (2013) Nonporous Silica Nanoparticles for Nanomedicine Application, *Nano Today 8*, 290-312.

[67] Yang, Y. N., Zhang, M., Song, H., and Yu, C. Z. (2020) Silica-Based Nanoparticles for Biomedical Applications: From Nanocarriers to Biomodulators, *Accounts of Chemical Research 53*, 1545-1556.

[68] Contini, C., Schneemilch, M., Gaisford, S., and Quirke, N. (2018) Nanoparticle-Membrane Interactions, *Journal of Experimental Nanoscience 13*, 62-81.

[69] Carlson, C., Hussain, S. M., Schrand, A. M., Braydich-Stolle, L. K., Hess, K. L., Jones, R. L., and Schlager, J. J. (2008) Unique Cellular Interaction of Silver Nanoparticles: Size-Dependent Generation of Reactive Oxygen Species, *Journal of Physical Chemistry B 112*, 13608-13619.

[70] Mukherjee, S. G., O'Claonadh, N., Casey, A., and Chambers, G. (2012) Comparative In Vitro Cytotoxicity Study of Silver Nanoparticle on two Mammalian Cell Lines, *Toxicology in Vitro 26*, 238-251.

[71] Nel, A. E., Madler, L., Velegol, D., Xia, T., Hoek, E. M. V., Somasundaran, P., Klaessig, F., Castranova, V., and Thompson, M. (2009) Understanding Biophysicochemical Interactions at the Nano-Bio Interface, *Nature Materials 8*, 543-557.

[72] Rascol, E., Devoisselle, J. M., and Chopineau, J. (2016) The Relevance of Membrane Models to Understand Nanoparticles-Cell Membrane Interactions, *Nanoscale 8*, 4780-4798.

[73] Behzadi, S., Serpooshan, V., Tao, W., Hamaly, M. A., Alkawareek, M. Y., Dreaden, E. C., Brown, D., Alkilany, A. M., Farokhzad, O. C., and Mahmoudi, M. (2017) Cellular Uptake of Nanoparticles: Journey Inside the Cell, *Chemical Society Reviews 46*, 4218-4244.

[74] Kettiger, H., Quebatte, G., Perrone, B., and Huwyler, J. (2016) Interactions Between Silica Nanoparticles and Phospholipid Membranes, *Biochimica Et Biophysica Acta-Biomembranes 1858*, 2163-2170.

[75] Zuraw-Weston, S., Wood, D. A., Torres, I. K., Lee, Y., Wang, L. S., Jiang, Z. W., Lazaro, G. R., Wang, S. Y., Rodal, A. A., Hagan, M. F., Rotello, V. M., and Dinsmore, A. D. (2019) Nanoparticles Binding to Lipid Membranes: From Vesicle-Based Gels to Vesicle Tubulation and Destruction, *Nanoscale 11*, 18464-18474.

[76] Lipowsky, R., and Dobereiner, H. G. (1998) Vesicles in Contact with Nanoparticles and Colloids, *Europhysics Letters 43*, 219-225.

[77] Le Bihan, O., Bonnafous, P., Marak, L., Bickel, T., Trepout, S., Mornet, S., De Haas, F., Talbot, H., Taveau, J. C., and Lambert, O. (2009) Cryo-Electron Tomography of Nanoparticle Transmigration into Liposome, *Journal of Structural Biology 168*, 419-425.

[78] Strobl, F. G., Seitz, F., Westerhausen, C., Reller, A., Torrano, A. A., Brauchle, C., Wixforth, A., and Schneider, M. F. (2014) Intake of Silica Nanoparticles by Giant Lipid Vesicles: Influence of Particle Size and Thermodynamic Membrane State, *Beilstein Journal of Nanotechnology 5*, 2468-2478.

[79] Zhang, S. W., Nelson, A., and Beales, P. A. (2012) Freezing or Wrapping: The Role of Particle Size in the Mechanism of Nanoparticle-Biomembrane Interaction, *Langmuir 28*, 12831-12837.

[80] Contini, C., Hindley, J. W., Macdonald, T. J., Barritt, J. D., Ces, O., and Quirke, N. (2020) Size Dependency of Gold Nanoparticles Interacting with Model Membranes, *Communications Chemistry 3*.

[81] Deserno, M. (2004) Elastic Deformation of a Fluid Membrane upon Colloid Binding, *Physical Review E 69*.

[82] Michel, R., and Gradzielski, M. (2012) Experimental Aspects of Colloidal Interactions in Mixed Systems of Liposome and Inorganic Nanoparticle and Their Applications, *International Journal of Molecular Sciences 13*, 11610-11642.

[83] Chithrani, B. D., Ghazani, A. A., and Chan, W. C. W. (2006) Determining the Size and Shape Dependence of Gold Nanoparticle Uptake into Mammalian Cells, *Nano Letters 6*, 662-668.

[84] Moghadam, B. Y., Hou, W. C., Corredor, C., Westerhoff, P., and Posner, J. D. (2012) Role of Nanoparticle Surface Functionality in the Disruption of Model Cell Membranes, *Langmuir 28*, 16318-16326.

[85] Dubavik, A., Sezgin, E., Lesnyak, V., Gaponik, N., Schwille, P., and Eychmuller, A. (2012) Penetration of Amphiphilic Quantum Dots through Model and Cellular Plasma Membranes, *Acs Nano 6*, 2150-2156.

[86] Werner, M., Auth, T., Beales, P. A., Fleury, J. B., Hook, F., Kress, H., Van Lehn, R. C., Muller, M., Petrov, E. P., Sarkisov, L., Sommer, J. U., and Baulin, V. A. (2018) Nanomaterial Interactions with Biomembranes: Bridging the Gap Between Soft Matter Models and Biological Context, *Biointerphases 13*, 028501.

[87] Metin, C. O., Bonnecaze, R. T., Lake, L. W., Miranda, C. R., and Nguyen, Q. P. (2014) Aggregation Kinetics and Shear Rheology of Aqueous Silica Suspensions, *Applied Nanoscience 4*, 169-178.

[88] Chen, K. L., Mylon, S. E., and Elimelech, M. (2006) Aggregation Kinetics of Alginate-Coated Hematite Nanoparticles in Monovalent and Divalent Electrolytes, *Environmental Science & Technology 40*, 1516-1523.

[89] Huynh, K. A., and Chen, K. L. (2011) Aggregation Kinetics of Citrate and Polyvinylpyrrolidone Coated Silver Nanoparticles in Monovalent and Divalent Electrolyte Solutions, *Environmental Science & Technology 45*, 5564-5571.

[90] Li, S., and Malmstadt, N. (2013) Deformation and Poration of Lipid Bilayer Membranes by Cationic Nanoparticles, *Soft Matter 9*, 4969-4976.

[91] Cedervall, T., Lynch, I., Lindman, S., Berggard, T., Thulin, E., Nilsson, H., Dawson, K. A., and Linse, S. (2007) Understanding the Nanoparticle-Protein Corona Using Methods to Quantify Exchange Rates and Affinities of Proteins for Nanoparticles, *Proceedings of the National Academy of Sciences of the United States of America 104*, 2050-2055.

[92] Nienhaus, K., and Nienhaus, G. U. (2019) Towards a Molecular-Level Understanding of the Protein Corona around Nanoparticles - Recent Advances and Persisting Challenges, *Current Opinion in Biomedical Engineering 10*, 11-22.

[93] Zhang, H. Y., Peng, J. X., Li, X., Liu, S. J., Hu, Z. Y., Xu, G. J., and Wu, R. A. (2018) A Nano-Bio Interfacial Protein Corona on Silica Nanoparticle, *Colloids and Surfaces B-Biointerfaces 167*, 220-228.

[94] Mohammad-Beigi, H., Hayashi, Y., Zeuthen, C. M., Eskandari, H., Scavenius, C., Juul-Madsen, K., Vorup-Jensen, T., Enghild, J. J., and Sutherland, D. S. (2020) Mapping and Identification of Soft Corona Proteins at Nanoparticles and Their Impact on Cellular Association, *Nature Communications 11*.

[95] Garcia-Alvarez, R., and Vallet-Regi, M. (2021) Hard and Soft Protein Corona of Nanomaterials: Analysis and Relevance, *Nanomaterials 11*.

[96] Monopoli, M. P., Aberg, C., Salvati, A., and Dawson, K. A. (2012) Biomolecular Coronas Provide the Biological Identity of Nanosized Materials, *Nature Nanotechnology 7*, 779-786.

[97] Lundqvist, M., Stigler, J., Elia, G., Lynch, I., Cedervall, T., and Dawson, K. A. (2008) Nanoparticle Size and Surface Properties Determine the Protein Corona with Possible Implications for Biological Impacts, *Proceedings of the National Academy of Sciences of the United States of America 105*, 14265-14270.

[98] Monopoli, M. P., Walczyk, D., Campbell, A., Elia, G., Lynch, I., Bombelli, F. B., and Dawson, K. A. (2011) Physical-Chemical Aspects of Protein Corona: Relevance to in Vitro and in Vivo Biological Impacts of Nanoparticles, *Journal of the American Chemical Society 133*, 2525-2534.

[99] Ro, D. K., Paradise, E. M., Ouellet, M., Fisher, K. J., Newman, K. L., Ndungu, J. M., Ho, K. A., Eachus, R. A., Ham, T. S., Kirby, J., Chang, M. C. Y., Withers, S. T., Shiba, Y., Sarpong, R., and Keasling, J. D. (2006) Production of the Antimalarial Drug Precursor Artemisinic Acid in Engineered Yeast, *Nature 440*, 940-943.

[100] Gaut, N. J., and Adamala, K. P. (2021) Reconstituting Natural Cell Elements in Synthetic Cells, *Advanced Biology 5*(3), 2000188. https://doi.org/10.1002/adbi.202000188

[101] Schwille, P., Spatz, J., Landfester, K., Bodenschatz, E., Herminghaus, S., Sourjik, V., Erb, T. J., Bastiaens, P., Lipowsky, R., Hyman, A., Dabrock, P., Baret, J. C., Vidakovic-Koch, T., Bieling, P., Dimova, R., Mutschler, H., Robinson, T., Tang, T. Y. D., Wegner, S., and Sundmacher, K. (2018) MaxSynBio: Avenues Towards Creating Cells from the Bottom Up, *Angewandte Chemie-International Edition 57*, 13382-13392.

[102] Yewdall, N. A., Mason, A. F., and van Hest, J. C. M. (2018) The Hallmarks of Living Systems: Towards Creating Artificial Cells, *Interface Focus 8* (5), 20180023

[103] Van de Cauter, L., Fanalista, F., van Buren, L., De Franceschi, N., Godino, E., Bouw, S., Danelon, C., Dekker, C., Koenderink, G. H., and Ganzinger, K. A. (2021) Optimized cDICE for Efficient Reconstitution of Biological Systems in Giant Unilamellar Vesicles, *Acs Synthetic Biology 10*, 1690-1702.

[104] Kotov, N. A. (2010) Inorganic Nanoparticles as Protein Mimics, *Science 330*, 188-189.

[105] Manea, F., Houillon, F. B., Pasquato, L., and Scrimin, P. (2004) Nanozymes: Gold-Nanoparticle-Based Transphosphorylation Catalysts, *Angewandte Chemie-International Edition 43*, 6165-6169.

[106] Hafez, M. E., Ma, H., Ma, W., and Long, Y. T. (2019) Unveiling the Intrinsic Catalytic Activities of Single-Gold-Nanoparticle-Based Enzyme Mimetics, *Angewandte Chemie-International Edition 58*, 6327-6332.

[107] Yu, Y., and Granick, S. (2009) Pearling of Lipid Vesicles Induced by Nanoparticles, *Journal of the American Chemical Society 131*, 14158-14159.

[108] Tahir, M. A., Guven, Z. P., Arriaga, L. R., Tinao, B., Yang, Y. S. S., Bekdemir, A., Martin, J. T., Bhanji, A. N., Irvine, D., Stellacci, F., and Alexander-Katz, A. (2020) Calcium-Triggered Fusion of Lipid Membranes Is Enabled by Amphiphilic Nanoparticles, *Proceedings of the National Academy of Sciences of the United States of America 117*, 18470-18476.

[109] Martens, S., and McMahon, H. T. (2008) Mechanisms of Membrane Fusion: Disparate Players and Common Principles, *Nature Reviews Molecular Cell Biology 9*, 543-556.

[110] Sudhof, T. C., and Rothman, J. E. (2009) Membrane Fusion: Grappling with SNARE and SM Proteins, *Science 323*, 474-477.

[111] Kozlov, M. M., and Chernomordik, L. V. (2015) Membrane Tension and Membrane Fusion, *Current Opinion in Structural Biology 33*, 61-67.

[112] Chernomordik, L. V., and Kozlov, M. M. (2008) Mechanics of Membrane Fusion, *Nature Structural & Molecular Biology 15*, 675-683.

[113] Lu, T., and Guo, H. X. (2019) How the Membranes Fuse: From Spontaneous to Induced, *Advanced Theory and Simulations 2*, 10.

[114] Rautu, S. A., Orsi, D., Di Michele, L., Rowlands, G., Cicuta, P., and Turner, M. S. (2017) The role of optical projection in the analysis of membrane fluctuations, *Soft Matter 13*, 3480-3483.

[115] Faizi, H. A., Reeves, C. J., Georgiev, V. N., Vlahovska, P. M., and Dimova, R. (2020) Fluctuation Spectroscopy of Giant Unilamellar Vesicles Using Confocal and Phase Contrast Microscopy, *Soft Matter 16*, 8996-9001.

[116] Anderson, T. H., Min, Y. J., Weirich, K. L., Zeng, H. B., Fygenson, D., and Israelachvili, J. N. (2009) Formation of Supported Bilayers on Silica Substrates, *Langmuir 25*, 6997-7005.

[117] Stetefeld, J., McKenna, S. A., and Patel, T. R. (2016) Dynamic Light Scattering: a Practical Guide and Applications in Biomedical Sciences, *Biophysical Reviews 8*, 409-427.

[118] Hassan, P. A., Rana, S., and Verma, G. (2015) Making Sense of Brownian Motion: Colloid Characterization by Dynamic Light Scattering, *Langmuir 31*, 3-12.

[119] Dynamic light scattering: an introduction in 30 minutes., In *DLS Tech. Note*, pp 1-8, Malvern: Malvern Instruments. 2012.

[120] Norde, W. (2003) *Colloids and Interfaces in Life Sciences*, Marcel Dekker, Inc, New York.

[121] Kaszuba, M., Corbett, J., Watson, F. M., and Jones, A. (2010) High-Concentration Zeta Potential Measurements Using Light-Scattering Techniques, *Philosophical Transactions of the Royal Society a-Mathematical Physical and Engineering Sciences 368*, 4439-4451.

[122] Fonte, P., Andrade, F., Araujo, F., Andrade, C., das Neves, J., and Sarmento, B. (2012) Chitosan-Coated Solid Lipid Nanoparticles for Insulin Delivery, In *Nanomedicine: Cancer, Diabetes, and Cardiovascular, Central Nervous System, Pulmonary and Inflammatory Diseases* (Düzgüneş, N., Ed.), pp 295-314, Academic Press.

[123] Munjanja, B., and Sanganyado, E. (2015) UV–Visible Absorption, Fluorescence, and Chemiluminescence Spectroscopy, In *Handbook of Food Analysis* (Nollet, L. M. L., and Toldra, F., Eds.), pp 1417-1432, CRC Press.

[124] Higson, S. (2004) *Analytical Chemistry*, Oxford University Press, Oxford.

[125] Munjanja, B., and Sanganyado, E. (2015) UV–Visible Absorption, Fluorescence, and Chemiluminescence Spectroscopy, In *Handbook of Food Analysis* (Nollet, L. M. L., and Toldra, F., Eds.), pp 1417-1432, CRC Press.

[126] Lakowicz, J. R. (2006) *Principles of Fluorescence Spectroscopy*, 3rd ed., Springer US.

[127] Valeur, B., and Berberan-Santos, M. N. (2013) *Molecular Fluorescence : principles and applications*, 2nd ed., Wiley-VCH, Weinheim.

[128] Sun, Y. S., Wallrabe, H., Seo, S. A., and Periasamy, A. (2011) FRET Microscopy in 2010: The Legacy of Theodor Forster on the 100th Anniversary of his Birth, *Chemphyschem 12*, 462-474.

[129] Algar, W. R., Hildebrandt, N., Vogel, S. S., and Medintz, I. L. (2019) FRET as a Biomolecular Research Tool: Understanding its Potential While Avoiding Pitfalls, *Nature Methods 16*, 815-829.

[130] Claxton, N. S., Fellers, T. J., and Davidson, M. W. (2006) Microscopy, Confocal, In *Encyclopedia of Medical Devices and Instrumentation* (Webster, J. G., Ed.), John Wiley & Sons, Inc.

[131] Muller, M. (2006) *Introduction to Confocal Fluorescence Microscopy*, Vol. 69, SPIE Press.

[132] Loren, N., Hagman, J., Jonasson, J. K., Deschout, H., Bernin, D., Cella-Zanacchi, F., Diaspro, A., McNally, J. G., Ameloot, M., Smisdom, N., Nyden, M., Hermansson, A. M., Rudemo, M., and Braeckmans, K. (2015) Fluorescence Recovery After Photobleaching in Material and Life Sciences: Putting Theory into Practice, *quarterly Reviews of Biophysics 48*, 323-387.

[133] Pincet, F., Adrien, V., Yang, R., Delacotte, J., Rothman, J. E., Urbach, W., and Tareste, D. (2016) FRAP to Characterize Molecular Diffusion and Interaction in Various Membrane Environments, *Plos One 11*.

[134] Subburaj, Y., Gallego, R. S., and García-Sáez, A. J. (2006) Membrane Dynamics: Fluorescence Spectroscopy, In *Encyclopedia of Analytical Chemistry*, John Wiley & Sons, Ltd.

[135] Soumpasis, D. M. (1983) Theoretical Analysis of Fluorescence Photobleaching Recovery Experiments, *Biophysical Journal 41*, 95-97.

[136] Bouvrais, H. (2012) Bending Rigidities of Lipid Bilayers: Their Determination and Main Inputs in Biophysical Studies, In *Advances in Planar Lipid Bilayers and Liposomes* (Iglič, A., Ed.), pp 1-75, Academic Press.

[137] Brochard, F., and Lennon, J. F. (1975) Frequency Spectrum of Flicker Phenomenon in Erythrocytes, *Journal De Physique 36*, 1035-1047.

[138] Dimova, R. (2014) Recent Developments in the Field of Bending Rigidity Measurements on Membranes, *Advances in Colloid and Interface Science 208*, 225-234.

[139] Helfrich, W., and Servuss, R. M. (1984) Undulations, Steric Interaction and Cohesion of Fluid Membranes, *Nuovo Cimento Della Societa Italiana Di Fisica D-Condensed Matter Atomic Molecular and Chemical Physics Fluids Plasmas Biophysics 3*, 137-151.

[140] Pecreaux, J., Dobereiner, H. G., Prost, J., Joanny, J. F., and Bassereau, P. (2004) Refined Contour Analysis of Giant Unilamellar Vesicles, *European Physical Journal E 13*, 277-290.

[141] Purushothaman, S., Cicuta, P., Ces, O., and Brooks, N. J. (2015) Influence of High Pressure on the Bending Rigidity of Model Membranes, *Journal of Physical Chemistry B 119*, 9805-9810.

[142] Booth, A., Marklew, C. J., Ciani, B., and Beales, P. A. (2019) In Vitro Membrane Remodeling by ESCRT is Regulated by Negative Feedback from Membrane Tension, *iScience 15*, 173-184.

[143] Yoon, Y. Z., Hong, H., Brown, A., Kim, D. C., Kang, D. J., Lew, V. L., and Cicuta, P. (2009) Flickering Analysis of Erythrocyte Mechanical Properties: Dependence on Oxygenation Level, Cell Shape, and Hydration Level, *Biophysical Journal 97*, 1606-1615.

[144] Chen, R. F., and Knutson, J. R. (1988) Mechanism of Fluorescence Concentration Quenching of Carboxyfluorescein in Liposomes - energy-transfer to nonfluorescent dimers, *Analytical Biochemistry 172*, 61-77.

[145] Weber, G., and Farris, F. J. (1979) Synthesis and Spectral Properties of a Hydrophobic Fluorescent-Probe: 6-propionyl-2-(dimethylamino)naphthalene, *Biochemistry 18*, 3075-3078.

[146] Parasassi, T., Conti, F., and Gratton, E. (1986) Time-Resolved Fuorescence Emission-Spectra of Laurdan in Phospholipid-Vesicles by Multifrequency Phase and Modulation Fluorometry, *Cellular and Molecular Biology 32*, 103-108.

[147] Sezgin, E., and Schwille, P. (2012) Model Membrane Platforms to Study Protein-Membrane Interactions, *Molecular Membrane Biology 29*, 144-154.

[148] Parasassi, T., De Stasio, G., Dubaldo, A., and Gratton, E. (1990) Phase Fluctuation in Phospholipid-Membranes Revealed by Laurdan Fluorescence, *Biophysical Journal 57*, 1179-1186.

[149] Parasassi, T., De Stasio, G., Ravagnan, G., Rusch, R. M., and Gratton, E. (1991) Quantitation of Lipid Phases in Phospholipid-Vesicles by the Generalized Polarization of Laurdan Fluorescence, *Biophysical Journal 60*, 179-189.

[150] Amaro, M., Reina, F., Hof, M., Eggeling, C., and Sezgin, E. (2017) Laurdan and Di-4-ANEPPDHQ Probe Different Properties of the Membrane, *Journal of Physics D-Applied Physics 50*.

[151] Sezgin, E., Waithe, D., de la Serna, J. B., and Eggeling, C. (2015) Spectral Imaging to Measure Heterogeneity in Membrane Lipid Packing, *Chemphyschem 16*, 1387-1394.

[152] Owen, D. M., Rentero, C., Magenau, A., Abu-Siniyeh, A., and Gaus, K. (2012) Quantitative Imaging of Membrane Lipid Order in Cells and Organisms, *Nature Protocols 7*, 24-35.

[153] Angelova, M. I., and Dimitrov, D. S. (1986) Liposome Electroformation, *Faraday Discussions 81*, 303-311.

[154] Dimitrov, D. S., and Angelova, M. I. (1988) Lipid Swelling and Liposome Formation Mediated by Electric-Fields, *Bioelectrochemistry and Bioenergetics 19*, 323-336.

[155] Angelova, M. I., Soleau, S., Meleard, P., Faucon, J. F., and Bothorel, P. (1992) Preparation of Giant Vesicles by External AC Electric-Fields. Kinetics and applications, *Trends in Colloid and Interface Science VI 89*, 127-131.

[156] Kim, T. H., Kim, M., Park, H. S., Shin, U. S., Gong, M. S., and Kim, H. W. (2012) Size-Dependent Cellular Toxicity of Silver Nanoparticles, *Journal of Biomedical Materials Research Part A 100A*, 1033-1043.

[157] Xue, Y. Y., Zhang, T., Zhang, B. Y., Gong, F., Huang, Y. M., and Tang, M. (2016) Cytotoxicity and Apoptosis Induced by Silver Nanoparticles in Human Liver HepG2 Cells in Different Dispersion Media, *Journal of Applied Toxicology 36*, 352-360.

[158] Zou, Z. Z., Chang, H. C., Li, H. L., and Wang, S. M. (2017) Induction of Reactive Oxygen Species: an Emerging Approach for Cancer Therapy, *Apoptosis 22*, 1321-1335.

[159] Bastus, N. G., Merkoci, F., Piella, J., and Puntes, V. (2014) Synthesis of Highly Monodisperse Citrate-Stabilized Silver Nanoparticles of up to 200 nm: Kinetic Control and Catalytic Properties, *Chemistry of Materials 26*, 2836-2846.

[160] Bastus, N. G., Casals, E., Vazquez-Campos, S., and Puntes, V. (2008) Reactivity of Engineered Inorganic Nanoparticles and Carbon Nanostructures in Biological Media, *Nanotoxicology 2*, 99-112.

[161] Diegoli, S., Manciulea, A. L., Begum, S., Jones, I. P., Lead, J. R., and Preece, J. A. (2008) Interaction Between Manufactured Gold Nanoparticles and Naturally Occurring Organic Macromolecules, *Science of the Total Environment 402*, 51-61.

[162] Cumberland, S. A., and Lead, J. R. (2009) Particle Size Distributions of Silver Nanoparticles at Environmentally Relevant Conditions, *Journal of Chromatography A 1216*, 9099-9105.

[163] Velegol, D. (2007) Assembling Colloidal Devices by Controlling Interparticle Forces, *Journal of Nanophotonics 1*, 012502.

[164] Prathna, T. C., Chandrasekaran, N., and Mukherjee, A. (2011) Studies on aggregation behaviour of silver nanoparticles in aqueous matrices: Effect of Surface Functionalization and Matrix Composition, *Colloids and Surfaces a-Physicochemical and Engineering Aspects 390*, 216-224.

[165] Jang, M. H., Lee, S., and Hwang, Y. S. (2015) Characterization of Silver Nanoparticles under Environmentally Relevant Conditions Using Asymmetrical Flow Field-Flow Fractionation (AF4), *Plos One 10*, e0143149.

[166] Leite, N. B., Aufderhorst-Roberts, A., Palma, M. S., Connell, S. D., Neto, J. R., and Beales, P. A. (2015) PE and PS Lipids Synergistically Enhance Membrane Poration by a Peptide with Anticancer Properties, *Biophysical Journal 109*, 936-947.

[167] Bergstrom, C. L., Beales, P. A., Lv, Y., Vanderlick, T. K., and Groves, J. T. (2013) Cytochrome c Causes Pore Formation in Cardiolipin-Containing Membranes, *Proceedings of the National Academy of Sciences of the United States of America 110*, 6269-6274.

[168] Montis, C., Generini, V., Boccalini, G., Bergese, P., Bani, D., and Berti, D. (2018) Model Lipid Bilayers Mimic Non-Specific Interactions of Gold Nanoparticles with Macrophage Plasma Membranes, *Journal of Colloid and Interface Science 516*, 284-294.

[169] Reynwar, B. J., Illya, G., Harmandaris, V. A., Muller, M. M., Kremer, K., and Deserno, M. (2007) Aggregation and Vesiculation of Membrane Proteins by Curvature-Mediated Interactions, *Nature 447*, 461-464.

[170] Spangler, E. J., Kumar, P. B. S., and Laradji, M. (2018) Stability of Membrane-Induced Self-Assemblies of Spherical Nanoparticles, *Soft Matter 14*, 5019-5030.

[171] van den Bogaart, G., Hermans, N., Krasnikov, V., de Vries, A. H., and Poolman, B. (2007) On the Decrease in Lateral Mobility of Phospholipids by Sugars, *Biophysical Journal 92*, 1598-1605.

[172] Amjad, O. A., Mognetti, B. M., Cicuta, P., and Di Michele, L. (2017) Membrane Adhesion through Bridging by Multimeric Ligands, *Langmuir 33*, 1139-1146.

[173] Booth, A., Marklew, C. J., Ciani, B., and Beales, P. A. (2019) In Vitro Membrane Remodelling by ESCRT is Regulated by Negative Feedback From Membrane Tension, *iScience 15*, 173-184.

[174] Karatekin, E., Sandre, O., Guitouni, H., Borghi, N., Puech, P. H., and Brochard-Wyart, F. (2003) Cascades of Transient Pores in Gant Vesicles: Line Tension and Transport, *Biophysical Journal 84*, 1734-1749.

[175] Akimov, S. A., Volynsky, P. E., Galimzyanov, T. R., Kuzmin, P. I., Pavlov, K. V., and Batishchev, O. V. (2017) Pore Formation in Lipid Membrane II: Energy Landscape Under External Stress, *Scientific Reports 7*, 12509.

[176] Fuertes, G., Garcia-Saez, A. J., Esteban-Martin, S., Gimenez, D., Sanchez-Munoz, O. L., Schwille, P., and Salgado, J. (2010) Pores Formed by Bax alpha 5 Relax to a Smaller Size and Keep at Equilibrium, *Biophysical Journal 99*, 2917-2925.

[177] Delay, M., Dolt, T., Woellhaf, A., Sembritzki, R., and Frimmel, F. H. (2011) Interactions and Stability of Silver Nanoparticles in the Aqueous Phase: Influence of Natural Organic Matter (NOM) and Ionic Strength, *Journal of Chromatography A 1218*, 4206-4212.

[178] Montis, C., Maiolo, D., Alessandri, I., Bergese, P., and Berti, D. (2014) Interaction of Nanoparticles with Lipid Membranes: a Multiscale Perspective, *Nanoscale 6*, 6452-6457.

[179] Churchman, A. H., Wallace, R., Milne, S. J., Brown, A. P., Brydson, R., and Beales, P. A. (2013) Serum Albumin Enhances the Membrane Activity of ZnO Nanoparticles, *Chemical Communications 49*, 4172-4174.

[180] Lee, Y. K., Choi, E. J., Webster, T. J., Kim, S. H., and Khang, D. (2015) Effect of the Protein Corona on Nanoparticles for Modulating Cytotoxicity and Immunotoxicity, *International Journal of Nanomedicine 10*, 97-112.

[181] Wei, X., Qu, X., Ding, L., Hu, J., and Jiang, W. (2016) Role of Bovine Serum Albumin and Humic Acid in the Interaction between SiO2 Nanoparticles and Model Cell Membranes, *Environmental Pollution 219*, 1-8.

[182] Di Silvio, D., Maccarini, M., Parker, R., Mackie, A., Fragneto, G., and Bombelli, F. B. (2017) The Effect of the Protein Corona on the Interaction between Nanoparticles and Lipid Bilayers, *Journal of Colloid and Interface Science 504*, 741-750.

[183] Anderson, C. R., Gnopo, Y. D. M., Gambinossi, F., Mylon, S. E., and Ferri, J. K. (2018) Modulation of Cell Responses to Ag-(MeO(2)MA-co-OEGMA): Effects of Nanoparticle Surface Hydrophobicity and Serum Proteins on Cellular Uptake and Toxicity, *Journal of Biomedical Materials Research Part A 106*, 1061-1071.

[184] Lesniak, A., Salvati, A., Santos-Martinez, M. J., Radomski, M. W., Dawson, K. A., and Aberg, C. (2013) Nanoparticle Adhesion to the Cell Membrane and Its Effect on Nanoparticle Uptake Efficiency, *Journal of the American Chemical Society 135*, 1438-1444.

[185] Yi, P., and Chen, K. L. (2013) Interaction of Multiwalled Carbon Nanotubes with Supported Lipid Bilayers and Vesicles as Model Biological Membranes, *Environmental Science & Technology 47*, 5711-5719.

[186] Wang, Q. Y., Lim, M. H., Liu, X. T., Wang, Z. W., and Chen, K. L. (2016) Influence of Solution Chemistry and Soft Protein Coronas on the Interactions of Silver Nanoparticles with Model Biological Membranes, *Environmental Science & Technology 50*, 2301-2309.

[187] Romer, W., Berland, L., Chambon, V., Gaus, K., Windschiegl, B., Tenza, D., Aly, M. R. E., Fraisier, V., Florent, J. C., Perrais, D., Lamaze, C., Raposo, G., Steinem, C., Sens, P., Bassereau, P., and Johannes, L. (2007) Shiga Toxin Induces Tubular Membrane Invaginations for its Uptake into Cells, *Nature 450*, 670-U673.

[188] Praper, T., Sonnen, A. F. P., Kladnik, A., Andrighetti, A. O., Viero, G., Morris, K. J., Volpi, E., Lunelli, L., Serra, M. D., Froelich, C. J., Gilbert, R. J. C., and Anderluh, G. (2011) Perforin Activity at Membranes Leads to Invaginations and Vesicle Formation, *Proceedings of the National Academy of Sciences of the United States of America 108*, 21016-21021.

[189] Solon, J., Gareil, O., Bassereau, P., and Gaudin, Y. (2005) Membrane Deformations Induced by the Matrix Protein of Vesicular Stomatitis Virus in a Minimal System, *Journal of General Virology 86*, 3357-3363.

[190] Lamaziere, A., Burlina, F., Wolf, C., Chassaing, G., Trugnan, G., and Ayala-Sanmartin, J. (2007) Non-Metabolic Membrane Tubulation and Permeability Induced by Bioactive Peptides, *Plos One 2*, e201.

[191] Sandre, O., Moreaux, L., and Brochard-Wyart, F. (1999) Dynamics of Transient Pores in Stretched Vesicles, *Proceedings of the National Academy of Sciences of the United States of America 96*, 10591-10596.

[192] Jaalouk, D. E., and Lammerding, J. (2009) Mechanotransduction Gone Awry, *Nature Reviews Molecular Cell Biology 10*, 63-73.

[193] Gerhold, K. A., and Schwartz, M. A. (2016) Ion Channels in Endothelial Responses to Fluid Shear Stress, *Physiology 31*, 359-369.

[194] Yasuda, N., Miura, S. I., Akazawa, H., Tanaka, T., Qin, Y., Kiya, Y., Imaizumi, S., Fujino, M., Ito, K., Zou, Y., Fukuhara, S., Kunimoto, S., Fukuzaki, K., Sato, T., Ge, J. B., Mochizuki, N., Nakaya, H., Saku, K., and Komuro, I. (2008) Conformational Switch of Angiotensin II Type 1 Receptor Underlying Mechanical Stress-Induced Activation, *Embo Reports 9*, 179-186.

[195] Soubias, O., Teague, W. E., Hines, K. G., and Gawrisch, K. (2014) The Role of Membrane Curvature Elastic Stress for Function of Rhodopsin-Like G Protein-Coupled Receptors, *Biochimie 107*, 28-32.

[196] Zhang, Y. L., Frangos, J. A., and Chachisvilis, M. (2009) Mechanical Stimulus Alters Conformation of Type 1 Parathyroid Hormone Receptor in Bone Cells, *American Journal of Physiology-Cell Physiology 296*, C1391-C1399.

[197] Chen, K. D., Li, Y. S., Kim, M., Li, S., Yuan, S., Chien, S., and Shyy, J. Y. J. (1999) Mechanotransduction in Response to Shear Stress - Roles of Receptor Tyrosine Kinases, Integrins, and Shc, *Journal of Biological Chemistry 274*, 18393-18400.

[198] Hoffman, B. D., Grashoff, C., and Schwartz, M. A. (2011) Dynamic Molecular Processes Mediate Cellular Mechanotransduction, *Nature 475*, 316-323.

[199] De Pascalis, C., and Etienne-Manneville, S. (2017) Single and Collective Cell Migration: the Mechanics of Adhesions, *Molecular Biology of the Cell 28*, 1833-1846.

[200] Yamamoto, K., and Ando, J. (2018) Emerging Role of Plasma Membranes in Vascular Endothelial Mechanosensing, *Circulation Journal 82*, 2691-2698.

[201] Halder, G., Dupont, S., and Piccolo, S. (2012) Transduction of Mechanical and Cytoskeletal Cues by YAP and TAZ, *Nature Reviews Molecular Cell Biology 13*, 591-600.

[202] Low, B. C., Pan, C. Q., Shivashankar, G. V., Bershadsky, A., Sudol, M., and Sheetz, M. (2014) YAP/TAZ as Mechanosensors and Mechanotransducers in Regulating Organ Size and Tumor Growth, *Febs Letters 588*, 2663-2670.

[203] Casals, E., Gonzalez, E., and Puntes, V. F. (2012) Reactivity of Inorganic Nanoparticles in Biological Environments: Insights into Nanotoxicity Mechanisms, *Journal of Physics D-Applied Physics 45*, 443001.

[204] Lesniak, A., Fenaroli, F., Monopoli, M. R., Aberg, C., Dawson, K. A., and Salvati, A. (2012) Effects of the Presence or Absence of a Protein Corona on Silica Nanoparticle Uptake and Impact on Cells, *Acs Nano 6*, 5845-5857.

[205] Vakurov, A., Brydson, R., and Nelsont, A. (2012) Electrochemical Modeling of the Silica Nanoparticle-Biomembrane Interaction, *Langmuir 28*, 1246-1255.

[206] Sakuma, Y., Taniguchi, T., and Imai, M. (2010) Pore Formation in a Binary Giant Vesicle Induced by Cone-Shaped Lipids, *Biophysical Journal 99*, 472-479.

[207] Chernomordik, L. V., Zimmerberg, J., and Kozlov, M. M. (2006) Membranes of the World Unite!, *Journal of Cell Biology 175*, 201-207.

[208] Kozlovsky, Y., Chernomordik, L. V., and Kozlov, M. M. (2002) Lipid Intermediates in Membrane Fusion: Formation, Structure, and Decay of Hemifusion Diaphragm, *Biophysical Journal 83*, 2634-2651.

[209] Lei, G. H., and MacDonald, R. C. (2003) Lipid Bilayer Vesicle Fusion: Intermediates Captured by High-Speed Microfluorescence Spectroscopy, *Biophysical Journal 85*, 1585-1599.

[210] Wang, B., Zhang, L. F., Bae, S. C., and Granick, S. (2008) Nanoparticle-Induced Surface Reconstruction of Phospholipid Membranes, *Proceedings of the National Academy of Sciences of the United States of America 105*, 18171-18175.

[211] Akimov, S. A., Molotkovsky, R. J., Kuzmin, P. I., Galimzyanov, T. R., and Batishchev, O. V. (2020) Continuum Models of Membrane Fusion: Evolution of the Theory, *International journal of molecular sciences 21*.

[212] Meher, G., and Chakraborty, H. (2019) Membrane Composition Modulates Fusion by Altering Membrane Properties and Fusion Peptide Structure, *Journal of Membrane Biology 252*, 261-272.

[213] Wang, L., Hartel, N., Ren, K. X., Graham, N. A., and Malmstadt, N. (2020) Effect of protein corona on nanoparticle-plasma membrane and nanoparticle-biomimetic membrane interactions, *Environmental Science-Nano 7*, 963-974.

[214] Nguyen, V. H., and Lee, B. J. (2017) Protein Corona: a New Approach for Nanomedicine Design, *International Journal of Nanomedicine 12*, 3137-3151.

[215] Wang, F. J., Yu, L., Monopoli, M. P., Sandin, P., Mahon, E., Salvati, A., and Dawson, K. A. (2013) The Biomolecular Corona is Retained During Nanoparticle Uptake and Protects the Cells from the Damage Induced by Cationic Nanoparticles until Degraded in the Lysosomes, *Nanomedicine-Nanotechnology Biology and Medicine 9*, 1159-1168.

[216] Yin, H., Chen, R., Casey, P. S., Ke, P. C., Davis, T. P., and Chen, C. Y. (2015) Reducing the Cytotoxicity of ZnO Nanoparticles by a Pre-Formed Protein Corona in A Supplemented Cell Culture Medium, *Rsc Advances 5*, 73963-73973.

[217] Gebauer, J. S., Malissek, M., Simon, S., Knauer, S. K., Maskos, M., Stauber, R. H., Peukert, W., and Treuel, L. (2012) Impact of the Nanoparticle-Protein Corona on Colloidal Stability and Protein Structure, *Langmuir 28*, 9673-9679.

[218] Mahl, D., Greulich, C., Meyer-Zaika, W., Koller, M., and Epple, M. (2010) Gold Nanoparticles: Dispersibility in Biological Media and Cell-Biological Effect, *Journal of Materials Chemistry 20*, 6176-6181.

[219] Barbalinardo, M., Caicci, F., Cavallini, M., and Gentili, D. (2018) Protein Corona Mediated Uptake and Cytotoxicity of Silver Nanoparticles in Mouse Embryonic Fibroblast, *Small 14*, 1801219.

[220] Jahn, R., Lang, T., and Sudhof, T. C. (2003) Membrane Fusion, *Cell 112*, 519-533.

[221] Lira, R. B., Robinson, T., Dimova, R., and Riske, K. A. (2019) Highly Efficient Protein-free Membrane Fusion: A Giant Vesicle Study, *Biophysical Journal 116*, 79-91.

[222] Loffler, P. M. G., Ries, O., Rabe, A., Okholm, A. H., Thomsen, R. P., Kjems, J., and Vogel, S. (2017) A DNA-Programmed Liposome Fusion Cascade, *Angewandte Chemie-International Edition 56*, 13228-13231.

[223] Nikolaus, J., Stockl, M., Langosch, D., Volkmer, R., and Herrmann, A. (2010) Direct Visualization of Large and Protein-Free Hemifusion Diaphragms, *Biophysical Journal 98*, 1192-1199.

[224] Mora, N. L., Boyle, A. L., Kolck, B. J. v., Rossen, A., Pokorna, S., Koukalova, A., Sachl, R., Hof, M., and Kros, A. (2020) Controlled Peptide-Mediated Vesicle Fusion Assessed by Simultaneous Dual-Colour Time-Lapsed Fluorescence Microscopy, *Scientific reports 10*, 3087-3087.

[225] Mondal Roy, S., and Sarkar, M. (2011) Membrane Fusion Induced by Small Molecules and Ions, *Journal of lipids 2011*, 528784-528784.

[226] Bolognesi, G., Friddin, M. S., Salehi-Reyhani, A., Barlow, N. E., Brooks, N. J., Ces, O., and Elani, Y. (2018) Sculpting and Fusing Biomimetic Vesicle Networks Using Optical Tweezers, *Nature Communications 9*, 1-11.

[227] Vivek, A., Bolognesi, G., and Elani, Y. (2020) Fusing Artificial Cell Compartments and Lipid Domains Using Optical Traps: A Tool to Modulate Membrane Composition and Phase Behaviour, *Micromachines 11*, 388

[228] Rorvig-Lund, A., Bahadori, A., Semsey, S., Bendix, P. M., and Oddershede, L. B. (2015) Vesicle Fusion Triggered by Optically Heated Gold Nanoparticles, *Nano Letters 15*, 4183-4188.

[229] Haluska, C. K., Riske, K. A., Marchi-Artzner, V., Lehn, J. M., Lipowsky, R., and Dimova, R. (2006) Time Scales of Membrane Fusion Revealed by Direct Imaging of Vesicle Fusion with High Temporal Resolution, *Proceedings of the National Academy of Sciences of the United States of America 103*, 15841-15846.

[230] Struck, D. K., Hoekstra, D., and Pagano, R. E. (1981) Use of Resonance Energy Transfer to Monitor Membrane Fusion, *Biochemistry 20*, 4093-4099.

[231] Ibarguren, M., Bomans, P. H. H., Ruiz-Mirazo, K., Frederik, P. M., Alonso, A., and Goni, F. M. (2015) Thermally-Induced Aggregation and Fusion of Protein-Free Lipid Vesicles, *Colloids and Surfaces B-Biointerfaces 136*, 545-552.

[232] Nazemidashtarjandi, S., and Farnoud, A. M. (2019) Membrane Outer Leaflet is the Primary Regulator of Membrane Damage Induced by Silica Nanoparticles in Vesicles and Erythrocytes, *Environmental Science-Nano 6*, 1219-1232.

[233] Ewins, E., Lira, R. B., Zhang, W. Y., Yuan, J. Y., Antonietti, M., Robinson, T., and Dimova, R. (2019) Poly(Ionic Liquid) Nanoparticles Selectively Disrupt Biomembranes, *Advanced Science 6*.

[234] Shillcock, J. C., and Lipowsky, R. (2005) Tension-Induced Fusion of Bilayer Membranes and Vesicles, *Nature Materials 4*, 225-228.

[235] Liu, X. J., Tian, F. L., Yue, T. T., Zhang, X. R., and Zhong, C. L. (2017) Pulling Force and Surface Tension Drive Membrane Fusion, *Journal of Chemical Physics 147*.

[236] Kliesch, T. T., Dietz, J., Turco, L., Halder, P., Polo, E., Tarantola, M., Jahn, R., and Janshoff, A. (2017) Membrane Tension Increases Fusion Efficiency of Model Membranes in the Presence of SNAREs, *Scientific Reports 7*.

[237] Cevc, G., and Richardsen, H. (1999) Lipid Vesicles and Membrane Fusion, *Advanced Drug Delivery Reviews 38*, 207-232.

[238] Tanaka, T., and Yamazaki, M. (2004) Membrane Fusion of Giant Unilamellar Vesicles of Neutral Phospholipid Membranes Induced by La3+, *Langmuir 20*, 5160-5164.

[239] Wang, L., Seeley, E. S., Wickner, W., and Merz, A. J. (2002) Vacuole Fusion at a Ring of Vertex Docking Sites Leaves Membrane Fragments within the Organelle, *Cell 108*, 357-369.

[240] Mattie, S., McNally, E. K., Karim, M. A., Vali, H., and Brett, C. L. (2017) How and why Intralumenal Membrane Fragments Form during Vacuolar Lysosome Fusion, *Molecular Biology of the Cell 28*, 309-321.

[241] Heo, P., Park, J. B., Shin, Y. K., and Kweon, D. H. (2017) Visualization of SNARE-Mediated Hemifusion between Giant Unilamellar Vesicles Arrested by Myricetin, *Frontiers in Molecular Neuroscience 10*, 93

[242] Michel, R., Kesselman, E., Plostica, T., Danino, D., and Gradzielski, M. (2014) Internalization of Silica Nanoparticles into Fluid Liposomes: Formation of Interesting Hybrid Colloids, *Angewandte Chemie-International Edition 53*, 12441-12445.

[243] Arribas Perez, M., Moriones, O. H., Bastus, N. G., Puntes, V., Nelson, A., and Beales, P. A. (2019) Mechanomodulation of Lipid Membranes by Weakly Aggregating Silver Nanoparticles, *Biochemistry 58*, 4761-4773.

[244] Raphael, R. M., and Waugh, R. E. (1996) Accelerated Interleaflet Transport of Phosphatidylcholine Molecules in Membranes under Deformation, *Biophysical Journal 71*, 1374-1388.

[245] Doktorova, M., Heberle, F. A., Marquardt, D., Rusinova, R., Sanford, R. L., Peyear, T. A., Katsaras, J., Feigenson, G. W., Weinstein, H., and Andersen, O. S. (2019) Gramicidin Increases Lipid Flip-Flop in Symmetric and Asymmetric Lipid Vesicles, *Biophysical Journal 116*, 860-873.

[246] Gardner, J. M., and Abrams, C. F. (2018) Lipid Flip-Flop vs. Lateral Diffusion in the Relaxation of Hemifusion Diaphragms, *Biochimica Et Biophysica Acta-Biomembranes 1860*, 1452-1459.

[247] D'Agostino, M., Risselada, H. J., Endter, L. J., Comte-Miserez, V., and Mayer, A. (2018) SNARE-Mediated Membrane Fusion Arrests at Pore Expansion to Regulate the Volume of an Organelle, *Embo Journal 37*, e99193.

[248] Coomer, C. A., Carlon-Andres, I., Iliopoulou, M., Dustin, M. L., Compeer, E. B., Compton, A. A., and Padilla-Parra, S. (2020) Single-Cell Glycolytic Activity Regulates Membrane Tension and HIV-1 Fusion, *Plos Pathogens 16*, e1008359.

[249] Bassereau, P., Jin, R., Baumgart, T., Deserno, M., Dimova, R., Frolov, V. A., Bashkirov, P. V., Grubmuller, H., Jahn, R., Risselada, H. J., Johannes, L., Kozlov, M. M., Lipowsky, R., Pucadyil, T. J., Zeno, W. F., Stachowiak, J. C., Stamou, D., Breuer, A., Lauritsen, L., Simon, C., Sykes, C., Voth, G. A., and Weikl, T. R. (2018) The 2018 Biomembrane Curvature and Remodeling Roadmap, *Journal of Physics D-Applied Physics 51*, 343001.

[250] Risselada, H. J., Smirnova, Y., and Grubmuller, H. (2014) Free Energy Landscape of Rim-Pore Expansion in Membrane Fusion, *Biophysical Journal 107*, 2287-2295.

[251] Ryham, R. J., Klotz, T. S., Yao, L. H., and Cohen, F. S. (2016) Calculating Transition Energy Barriers and Characterizing Activation States for Steps of Fusion, *Biophysical Journal 110*, 1110-1124.

[252] Smirnova, Y. G., Marrink, S. J., Lipowsky, R., and Knecht, V. (2010) Solvent-Exposed Tails as Prestalk Transition States for Membrane Fusion at Low Hydration, *Journal of the American Chemical Society 132*, 6710-6718.

[253] Risselada, H. J., Bubnis, G., and Grubmuller, H. (2014) Expansion of the Fusion Stalk and Its Implication for Biological Membrane Fusion, *Proceedings of the National Academy of Sciences of the United States of America 111*, 11043-11048.

[254] Anderson, R. G. W., and Jacobson, K. (2002) A Role for Lipid Shells in Targeting Proteins to Caveolae, Rafts, and Other Lipid Domains, *Science 296*, 1821-1825.

[255] Nickels, J. D., Smith, J. C., and Cheng, X. L. (2015) Lateral Organization, Bilayer Asymmetry, and Inter-Leaflet Coupling of Biological Membranes, *Chemistry and Physics of Lipids 192*, 87-99.

[256] St. Clair, J. R., Wang, Q., Li, G., and London, E. (2017) Preparation and Physical Properties of Asymmetric Model Membrane Vesicles, In *The Biophysics of Cell Membranes: Biological Consequences* (Epand, R. M., and Ruysschaert, J.-M., Eds.), pp 1-27, Springer Singapore, Singapore.

[257] Sezgin, E., Levental, I., Mayor, S., and Eggeling, C. (2017) The Mystery of Membrane Organization: Composition, Regulation and Roles of Lipid Rafts, *Nature Reviews Molecular Cell Biology 18*, 361-374.

[258] Sarmento, M. J., Hof, M., and Sachl, R. (2020) Interleaflet Coupling of Lipid Nanodomains - Insights From in vitro Systems, *Frontiers in Cell and Developmental Biology 8*, 284.

[259] Bezlyepkina, N., Gracia, R. S., Shchelokovskyy, P., Lipowsky, R., and Dimova, R. (2013) Phase Diagram and Tie-Line Determination for the Ternary Mixture DOPC/eSM/Cholesterol, *Biophysical Journal 104*, 1456-1464.

[260] Dreher, Y., Jahnke, K., Bobkova, E., Spatz, J. P., and Gopfrich, K. (2021) Division and Regrowth of Phase-Separated Giant Unilamellar Vesicles, *Angewandte Chemie-International Edition 60*, 10661-10669.

[261] Baumgart, T., Hunt, G., Farkas, E. R., Webb, W. W., and Feigenson, G. W. (2007) Fluorescence Probe Partitioning between Lo/Ld Phases in Lipid Membranes, *Biochimica Et Biophysica Acta-Biomembranes 1768*, 2182-2194.

[262] Veatch, S. L., and Keller, S. L. (2003) Separation of Liquid Phases in Giant Vesicles of Ternary Mixtures of Phospholipids and Cholesterol, *Biophysical Journal 85*, 3074-3083.

[263] Garcia-Saez, A. J., Chiantia, S., and Schwille, P. (2007) Effect of Line Tension on the Lateral Organization of Lipid Membranes, *Journal of Biological Chemistry 282*, 33537-33544.

[264] Sezgin, E., Gutmann, T., Buhl, T., Dirkx, R., Grzybek, M., Coskun, U., Solimena, M., Simons, K., Levental, I., and Schwille, P. (2015) Adaptive Lipid Packing and Bioactivity in Membrane Domains, *Plos One 10*, e0123930.

[265] Sezgin, E., Sadowski, T., and Simons, K. (2014) Measuring Lipid Packing of Model and Cellular Membranes with Environment Sensitive Probes, *Langmuir 30*, 8160-8166.

[266] Mills, T. T., Huang, J. Y., Feigenson, G. W., and Nagle, J. F. (2009) Effects of Cholesterol and Unsaturated DOPC Lipid on Chain Packing of Saturated Gel-Phase DPPC Bilayers, *General Physiology and Biophysics 28*, 126-139.

[267] Elani, Y., Purushothaman, S., Booth, P. J., Seddon, J. M., Brooks, N. J., Law, R. V., and Ces, O. (2015) Measurements of the Effect of Membrane Asymmetry on the Mechanical Properties of Lipid Bilayers, *Chemical Communications 51*, 6976-6979.

[268] Hossein, A., and Deserno, M. (2020) Spontaneous Curvature, Differential Stress, and Bending Modulus of Asymmetric Lipid Membranes, *Biophysical Journal 118*, 624-642.

[269] Binder, W. H., Barragan, V., and Menger, F. M. (2003) Domains and Rafts in Lipid Membranes, *Angewandte Chemie-International Edition 42*, 5802-5827.

[270] Lingwood, D., and Simons, K. (2010) Lipid Rafts As a Membrane-Organizing Principle, *Science 327*, 46-50.

[271] Booth, A., Marklew, C., Ciani, B., and Beales, P. A. (2020) The Influence of Phosphatidylserine Localisation and Lipid Phase on Membrane Remodelling by the ESCRT-II/ESCRT-III Complex, *Faraday Discussions*. DOI: 10.1039/D0FD00042F

[272] Bacia, K., Schuette, C. G., Kahya, N., Jahn, R., and Schwille, P. (2004) Snares Prefer Liquid-Disordered Over "Raft" (Liquid-Ordered) Domains when Reconstituted into Giant Unilamellar Vesicles, *Journal of Biological Chemistry 279*, 37951-37955.

[273] Marinko, J. T., Kenworthy, A. K., and Sanders, C. R. (2020) Peripheral Myelin Protein 22 Preferentially Partitions into Ordered Phase Membrane Domains, *Proceedings of the National Academy of Sciences of the United States of America 117*, 14168-14177.

[274] Yang, S.-T., Kiessling, V., and Tamm, L. K. (2016) Line Tension at Lipid Phase Boundaries as Driving Force for HIV Fusion Peptide-Mediated Fusion, *Nature Communications 7*.

[275] Enoki, T. A., and Feigenson, G. W. (2019) Asymmetric Bilayers by Hemifusion: Method and Leaflet Behaviors, *Biophysical Journal 117*, 1037-1050.

[276] Enoki, T. A., Wu, J., Heberle, F. A., and Feigenson, G. W. (2021) Investigation of the Domain Line Tension in Asymmetric Vesicles Prepared via Hemifusion, *Biochimica Et Biophysica Acta-Biomembranes 1863*, 183586.

[277] Kiessling, V., Crane, J. M., and Tamm, L. K. (2006) Transbilayer Effects of Raft-Like Lipid Domains in Asymmetric Planar Bilayers Measured by Single Molecule Tracking, *Biophysical Journal 91*, 3313-3326.

[278] Wan, C., Kiessling, V., and Tamm, L. K. (2008) Coupling of Cholesterol-Rich Lipid Phases in Asymmetric Bilayers, *Biochemistry 47*, 2190-2198.

[279] Chiantia, S., and London, E. (2012) Acyl Chain Length and Saturation Modulate Interleaflet Coupling in Asymmetric Bilayers: Effects on Dynamics and Structural Order, *Biophysical Journal 103*, 2311-2319.

[280] Heberle, F. A., Marquardt, D., Doktorova, M., Geier, B., Standaert, R. F., Heftberger, P., Kollmitzer, B., Nickels, J. D., Dick, R. A., Feigenson, G. W., Katsaras, J., London, E., and Pabst, G. (2016) Subnanometer Structure of an Asymmetric Model Membrane: Interleaflet Coupling Influences Domain Properties, *Langmuir 32*, 5195-5200.

[281] St Clair, J. W., Kakuda, S., and London, E. (2020) Induction of Ordered Lipid Raft Domain Formation by Loss of Lipid Asymmetry, *Biophysical Journal 119*, 483-492.

[282] Wang, Q., and London, E. (2018) Lipid Structure and Composition Control Consequences of Interleaflet Coupling in Asymmetric Vesicles, *Biophysical Journal 115*, 664-678.

[283] Collins, M. D., and Keller, S. L. (2008) Tuning Lipid Mixtures to Induce or Suppress Domain Formation across Leaflets of Unsupported Asymmetric Bilayers, *Proceedings of the National Academy of Sciences of the United States of America 105*, 124-128.

[284] Doktorova, M., Symons, J. L., and Levental, I. (2020) Structural and Functional Consequences of Reversible Lipid Asymmetry in Living Membranes, *Nature Chemical Biology 16*, 1321-1330.

[285] Shin, H. W., and Takatsu, H. (2020) Phosphatidylserine Exposure in Living Cells, *Critical Reviews in Biochemistry and Molecular Biology 55*, 166-178.

[286] Sharpe, H. J., Stevens, T. J., and Munro, S. (2010) A Comprehensive Comparison of Transmembrane Domains Reveals Organelle-Specific Properties, *Cell 142*, 158-169.

[287] Devaux, P. F., and Morris, R. (2004) Transmembrane Asymmetry and Lateral Domains in Biological Membranes, *Traffic 5*, 241-246.

[288] Skotland, T., and Sandvig, K. (2019) The Role of PS 18:0/18:1 in Membrane Function, *Nature Communications 10*, 1-10.

[289] Sezgin, E., Kaiser, H. J., Baumgart, T., Schwille, P., Simons, K., and Levental, I. (2012) Elucidating Membrane Structure and Protein Behavior using Giant Plasma Membrane Vesicles, *Nature Protocols 7*, 1042-1051.

[290] Levental, K. R., and Levental, I. (2015) Giant Plasma Membrane Vesicles: Models for Understanding Membrane Organization, In *Current Topics in Membranes* (Kenworthy, A. K., Ed.), pp 25-57, Academic Press.

[291] Del Piccolo, N., Placone, J., He, L. J., Agudelo, S. C., and Hristova, K. (2012) Production of Plasma Membrane Vesicles with Chloride Salts and Their Utility as a Cell Membrane Mimetic for Biophysical Characterization of Membrane Protein Interactions, *Analytical Chemistry 84*, 8650-8655.

[292] Sarabipour, S., Chan, R. B., Zhou, B. W., Di Paolo, G., and Hristova, K. (2015) Analytical Characterization of Plasma Membrane-Derived Vesicles Produced via Osmotic and Chemical Vesiculation, *Biochimica Et Biophysica Acta-Biomembranes 1848*, 1591-1598.

[293] Chiantia, S., Schwille, P., Klymchenko, A. S., and London, E. (2011) Asymmetric GUVs Prepared by M beta CD-Mediated Lipid Exchange: An FCS Study, *Biophysical Journal 100*, LO1-LO3.

[294] Pautot, S., Frisken, B. J., and Weitz, D. A. (2003) Engineering Asymmetric Vesicles, *Proceedings of the National Academy of Sciences of the United States of America 100*, 10718-10721.

[295] Hu, P. C. C., Li, S., and Malmstadt, N. (2011) Microfluidic Fabrication of Asymmetric Giant Lipid Vesicles, *Acs Applied Materials & Interfaces 3*, 1434-1440.

[296] Lu, L., Schertzer, J. W., and Chiarot, P. R. (2015) Continuous Microfluidic Fabrication of Synthetic Asymmetric Vesicles, *Lab on a Chip 15*, 3591-3599.

[297] Richmond, D. L., Schmid, E. M., Martens, S., Stachowiak, J. C., Liska, N., and Fletcher, D. A. (2011) Forming Giant Vesicles with Controlled Membrane Composition, Asymmetry, and Contents, *Proceedings of the National Academy of Sciences of the United States of America 108*, 9431-9436.

[298] Kucherak, O. A., Oncul, S., Darwich, Z., Yushchenko, D. A., Arntz, Y., Didier, P., Mely, Y., and Klymchenko, A. S. (2010) Switchable Nile Red-Based Probe for Cholesterol and Lipid Order at the Outer Leaflet of Biomembranes, *Journal of the American Chemical Society 132*, 4907-4916.

[299] Honigmann, A., Mueller, V., Hell, S. W., and Eggeling, C. (2013) STED Microscopy Detects and Quantifies Liquid Phase Separation in Lipid Membranes Using a New Far-Red Emitting Fluorescent Phosphoglycerolipid Analogue, *Faraday Discussions 161*, 77-89.

[300] Steinkuhler, J., Knorr, R. L., Zhao, Z., Bhatia, T., Bartelt, S. M., Wegner, S., Dimova, R., and Lipowsky, R. (2020) Controlled Division of Cell-Sized Vesicles by Low Densities of Membrane-Bound Proteins, *Nature communications 11*, 905-905.